流体包有物と微小鉱物形成からみたプレート境界付近の過去の地震断層の研究

（研究課題番号　13304038）

平成１３年度～平成１５年度科学研究費補助金

[基盤研究(A)(1)]

研　究　成　果　報　告　書

平成１６年３月

研究代表者　小川勇二郎

（筑波大学地球科学系）

はしがき

われわれは３ヵ年の基盤研究「流体包有物と微小鉱物形成からみたプレート境界付近の過去の地震断層の研究」を行った．その主たる目的は，プレート境界付近で生じる断層の生成条件とメカニズムを明らかにすることであり，そのうちの断層に伴う変形と流体移動に関しては，多くの成果をあげることが出来た．主たる武器は顕微ラマン分光装置，走査型電子顕微鏡，および流体包有物測定装置であり，これらを用いて，断層岩の構造，組織，伴う脈鉱物の観察，温度・圧力測定，鉱物同定などを行った．その過程で，鉱物同定の基礎となる顕微ラマン分光装置の設置と運転を行い，多くの基礎的データを所得した．それらのデータは日常的に増大し続けており，今後ともさまざまな研究に大いに役に立つと思われる．

主たるテーマに関しては，特に，付加体およびオフィオライト帯の内部に発達する多くの新しいタイプの断層を識別し，それらが，プレート発散および収斂地域におけるテクトニクスの理解にどのような意義を持っているかを明らかにすることが出来た．調査した地域は，スコットランドのサザンアプランズ付加体，アメリカ合衆国のコースタルレンジとワイオミングスラストベルト，ニュージーランドのヒクランギ付加体とトアラス付加体，オマーンオフィオライト，本邦の四万十付加体，嶺岡オフィオライト帯など世界の代表的付加体やプレート境界にわたった．

課題に直接関連する成果は，Ogawa(2002)，Takahashi et al. (2004)，Hirano et al. (2004)，Ogawa and Takahashi (2004)その他などに発表されており，また，関連する成果は，Hirano et al. (2002)，Tanaka and Ogawa (2004)，Kyono (2003)，Kimata et al. (2002)，Hirai et al. (2002,2003)，Li and Ogawa (2001, 2003) などに示されている．最大の成果は，海洋を構成していた岩石が陸上に取り込まれる時にどのような変形パタンを取るか，それらのステージにどのような流体が断層を流れるか，またそれらに伴ってどのような大小構造が形成されるかについて明らかにできたことであり，また堆積物の圧密による組織の急激な変化が，すでに海洋堆積物中で生じているなどについても明らかにした．また，堆積物の力学特性に関する基礎的研究も同時に行い，地震発生時の挙動に関しても詳しい実験的研究を行った．この中で，特に，Shinozaki and Ogawa (2002)，Ohta (2004)，Kawamura and Ogawa (2003)，遠藤 (2004)は特筆に価する．そのいくつかは，未だに国際誌にアクセプトされてはいないが，近々公表する予定である．これらの研究は，従来の知識を一新するもので，今回の一連の研究において初めて明らかにされたものも多い．

本報告では，研究の設定と概要を述べ，代表的研究論文を付し，成果報告書としたい．

本研究を行うに当たり，筑波大学の職員，学生からは絶大な助力を得た．心から感謝したい．また，本研究を推進する機会を与えてくださった日本学術振興会に感謝する．

平成１６年３月

研究代表者　小川　勇二郎

研究課題　流体包有物と微小鉱物形成からみたプレート境界付近の過去の地震断層の研究

研究組織

研究代表者　小川勇二郎（筑波大学地球科学系・教授）
研究分担者　木股　三善（筑波大学地球科学系・教授）
研究分担者　平井　寿子（筑波大学地球科学系・講師）
研究分担者　安間　了（筑波大学地球科学系・講師）
研究分担者　坂口　有人（海洋科学研究センター・研究員）

研究協力者　李　火銀（筑波大学大学院地球科学研究科・学生）
研究協力者　興野　純（筑波大学大学院地球科学研究科・学生）
研究協力者　平野　直人（筑波大学大学院地球科学研究科・学生）
研究協力者　大田　恭史（筑波大学大学院地球科学研究科・学生）
研究協力者　川村喜一郎（深田地質研究所・研究員）
研究協力者　内原　弓佳子（筑波大学大学院理工学研究科・学生）
研究協力者　高橋　明子（筑波大学大学院生命環境科学研究科・学生）
研究協力者　篠崎　良（筑波大学大学院生命環境科学研究科・学生）
研究協力者　田中　勝法（筑波大学大学院生命環境科学研究科・学生）
研究協力者　鈴木　清史（筑波大学地球科学系・非常勤研究員）
研究協力者　遠藤　良太（筑波大学大学院生命環境科学研究科・学生）
研究協力者　田中　千尋（筑波大学第一学群自然学類・学生）

研究経費

平成１３年度 29,500　千円
平成１４年度　4,400　千円
平成１５年度　5,000　千円

研究発表

（１）学会誌等（下線は、代表者および分担者）

２００１(平成１３）年度

Hirai, H., Uchihara, Y., Fujihisa, H., Sakashita, M., Katoh, E., Aoki, K., Nagashima, K., Yamamoto, Y. and Yagi, T. (2001) High-pressure structures of methane hydrate observed up to 8 GPa at room temperature. J. Chem. Phys. 115 [15], 7066-7070.

Hirai, H., Uchihara, Y., Fujihisa, H., Aoki, K., Yamamoto, Y. and Yagi, T. (2001) New structures of Methane hydrate under high pressure. *Advanced Materials '01*, Edited by Akaishi, M. et al., ICS PRESS, 21-122.

Kyono, A. and Kimata, M. (2001) The crystal structure of synthetic $TlAlSi_3O_8$: Influence of inert pair effect on thallium on feldspar structure. - Euro. Jour. Mineral., 13, 849-856.

Kyono, A. and Kimata, M. (2001) Refinement of the crystal structure of a synthetic non-stoichiometric Rb-feldspar. Mineral. Mag., 65, 523-531.

興野純、木股三善、清水雅浩（2001）$Tl6s^2$ 孤立電子対の結晶化学的挙動－鉱物種を限定する不活性電子対効果－．岩石鉱物科学, 30, 180-189.

Ogawa, Y. (2001) Duplex structure and their tectonic implication for the Southern Uplands accretionary complex. Trans. Royal Soc. Edinburgh, 91, 515-519.
Masalu, D.C.P., Ogawa, Y., and Kobayashi, K. (2001) Bathymetry of the Joban seamount chain, northwestern Pacific. Marine Geology, 173, 87-96.
Li, Hyou Yin and Ogawa, Y. (2001) Pore structure of sheared coals and related coalbed methane. Environmental Geology, 40, 1455-1461.
Hirano, N., Kawamura, K., Hattori, M., Saito, K., and Ogawa, Y. (2001) A new type of intra-plate volcanism; young alkali-basalts discovered from the subducting Pacific Plate, northern Japan Trench. Geophysical Research Letters, 28, (14), 2719-2722.

２００２（平成１４）年度

Hirai, H., Uchihara, Y., Kawamua, T., Yamamoto,Y. and Yagi, T. (2002) Pressure-indued phase changes of argon hydrate and methane hydrate at room temperature. Proc. Jpn. Acad. ser. B, 78 [3], 39-44.
Hirai, H., Uchihara, Y., Nishimura, Y., Kawamua,T., Yamamoto, Y. and Yagi, T. (2002) Structural changes of argon hydrate under high pressure. J. Phys. Chem. B, 106 [43], 11089-11092.
Hirai, H., Uchihara, Y., Fujihisa, H., Sakashita, M., Katoh, E., Aoki, K., Yamamoto, Y., Nagashima, K. and Yagi, T. (2002) High-pressure structures of methane hydrate. J. Physics: Condensed Matter, 14 [44], 11443-11446.
平井寿子、内原弓佳子 (2002) メタンハイドレートの高圧相転移、高圧力の科学と技術 12巻、1号、28-33頁.
Kyono, A. and Kimata, M. (2002) Crystal chemical behavior of Tl6s^2 lone electron pairs: Inert pair effect imposing constraints on the mineral species. – Trend in Geochem., 2, 43-58.
Kyono, A., Kimata, M., Matsuhisa, M., Miyashita, Y. and Okamoto, K. (2002) Low-temperature crystal structures of stibnite implying orbital overlap of 5s^2 inert pair electrons. - Phys. Chem. Mineral., 29, 254-260.
Kawamura, K., and Ogawa, Y. (2002) Progressive microfabric changes in unconsolidated pelagic and hemipelagic sediments down to 180 mbsf, northwest Pacific, ODP Leg 185, Site 1149. In Ludden, J.N., Plank, T., and Escutia, C. (Eds.), Proc. ODP, Sci. Results, 185 [Online]. Available from World Wide Web: http://www-odp.tamu.edu /publications/185_SR/003/003.htm.
Hirano, S., Ogawa, Y., and Saito, K. (2002) Long-lived early Cretaceous seamount volcanism in the Mariana Trench, Western Pacific Ocean. Marine Geology, 189, 371-397.
Tanaka, H., Wang, Chien-Ying, Chen, Wei-Min, Sakaguchi, A,, Ujiie, K., Ito, H. and Ando, M. (2002) Initial science report of shallow drilling penetrating in to the Chelungpu fault zone, Taiwan. Terrestrial Atmospheric and Oceanic Sciences. 13, 227-251.
Hashimoto, Y., Enjoji, M., Sakaguchi, A. and Kimura, G. (2002) P-T conditions of cataclastic deformation associated with underplating: An example from the Cretaceous Shimanto complex, Kii Peninsula, SW Japan. Earth Planets Space, 54, 1133-1138.

２００３(平成１５)年度 (2004年 in press を含む)

Herve, F., Fanning, M. C., Thomson, S. N., Pankhurst, R. J., Anma, R., Veloso, A. and Herrera, C. (2003) SHRIMP U-Pb and FT Pliocene ages of near-trench granites in Taitao peninsula, southern Chile. Short papers of IV South America Symposium on Isotope Geology, 190-193.
Motoki, A., Orihashi, Y., Hirata, D., Haller, M.J., Ramos, V.A., Schilling, M., Iwano, H., Cario, F.D. and Anma, R. (2003) U-Pb dating for single grain zircon using laser ablation ICP

massspectrometer and fission track ages of zircon for back-arc adakitic bodies, the Cerro Pampa and the Puesto Nuevo, Argentine Ptagonia., IV South America Symposium on Isotope Geology, Salvador, Brazil, August 24-27, Short papers of IV South America Symposium on Isotope Geology, 219-220.

Orihashi, Y., Motoki, A., Hirata, D., Haller, M. J., Ramos, V. A., Ota, T., Yoshida, H. and Anma, R. (2003) Zircon geochemistry of Mid-Miocene adakites in the southern Patagonian province, The 13th Goldschmidt Conference, Kurashiki, Japan, Spetember 7-12, Geochim. Cosmochim. Acta Spec. Suppl., A364-A364.

山本啓司・寺林　優・大麻広幸・金子慶之・安間　了 (2004) 岩国一柳井領家帯の泥質片岩と珪化岩に認められるコンピテンス較差. 地質学雑誌, 110巻, 第2号.

Hirai, H., Tanaka, T., Yamamoto, Y., Kawamura, T., Yagi, T. (2003) Retention of filled ice structure of methane hydrate up to 42 GPa. Phys. Rev. B, 68 [17], 172,102-1-172,102-4.

Kyono, A., Kimata, M. and Hatta, T. (2003) Aluminium position in Rb-feldspar as determined by X-ray photoelectron spectroscopy.– Naturwissenschaften, 90, 414-418.

Nishida, N., Kimata, M., Sugimoto, A., Kyono, A. and Hatta, T. (2003) Quantitative analysis of minerals containing various kinds of rare earth elements in large quantities: Chemical composition of thortveitite. – Recent Res. Devel. in Mineral., 3, 1-16.

Nishida, N., Kimata, M., Kyono, A. and Hatta, T. (2003) Quantitative analysis of light elements (carbon and nitrogen) and coexisting heavy elements in minerals: Nitrogen ammonioleucite. – Recent Res. Devel. in Mineral., 3, 17-31.

Nishida, N., Kimata, M., Kyono, A. and Hatta, T. (2003): Nano identification of ultra-micro inclusions: Native copper in sunstone.– Recent Res. Devel. in Mineral., 3, 33-46.

Li, Huoyin, Ogawa, Y., and Shimada, S. (2003) Mechanism of methane flow through sheared coals and its role on methane recovery. Fuel (Elsevier), 82, 1269-1277.

Ikesawa, E., Sakaguchi, A. and Kimura, G. (2003) Pseudotachylyte from an ancient accretionary complex: Evidence for melt generation during seismic slip anlong a master decollement?, Geology, 31, 637-640.

坂口有人, 四万十付加体異津メランジュの震源断層の特徴と流体移動に伴うセメンテーションによる固着すべりのアナログ実験. (2003) 地学雑誌、112、885-896.

Hashimoto, Y., Enjoji, M., Sakaguchi, A. and Kimura, G. (2003) In-situ pressure-temperature conditions of a tectonic melange: Constrains from fluid inclusion analysis of syn-melange veins. The Island Arc, 12, 357-365.

Kato, A., Sakaguchi, A., Yoshida, S., Mochizuki, H. and Kaneda, Y. (2003) Permeability measurements and precipitation sealing of basalt in the ancient exhumed fault in subduction zone, Bulletin of Earthquake Research Institute, University of Tokyo, 78, 83-89.

Hirai, H., Tanaka, T., Kawamura, T., Yamamoto, Y. and Yagi, T. (2004) Structural changes of gas hydrates and stability of a filled ice structure of methane hydrate up to 42 GPa, J. Phys. Chem. Solid., 64 (in press).

Takahashi, A., Ogawa, Y., Ohta, Y., and Hirano, N. (2004) The nature of faulting and deformation in the Mineoka Ophiolite, NW Pacific Rim. In: Dilek, Y. and Robinson, P. (eds), Geological Society of London, Special Publication, 128, "Ophiolite in Earth History", (in press).

Ogawa, Y. and Takahashi, A. (2004) Tectonic implications of Mineoka Ophiolite emplacement, central Japan: with special reference to spreading and obduction. Tectonophysics, (in press).

Hirano, N., Ogawa, Y., Saito, K, Yoshida, T., Sato, H. and Taniguchi, H. (2004) Multi-stage evolution of the Tertiary Mineoka Ophiolite in the NW Pacific as revealed by new geochemical and age constraints. In: Dilek, Y. and Robinson, P. (eds), Geological Society of London, Special Publication, 128, "Ophiolite in Earth History", (in press).

Ogawa, Y. and Vrolijk, P. (2004) Comment: Control of internal structure and fluid-migration pathways within the Barbados Ridge decollement zone by strike-slip faulting: Evidence from coherence and three-dimensional seismic amplitude imaging. GSABull, (in press).

Tanaka, C. and Ogawa, Y. (2004), DATA REPORT: Silica mineral crystallization with textural change of Cretaceous siliceous/Calcareous pelagic sedimentary rocks recovered from the NW Pacific, ODP Leg 185, Proc. ODP, Sci. Results, 185 [Online]. Available from World Wide Web: http://www-odp.tamu.edu /publications/185 (in press).

（2）報告書，学会発表等

(学会発表(一部))

Kawamura, K., Hosono, T., Allawati, H., Taniguchi, H. and Ogawa, Y. (2002) Vertical variation of magnetic susceptibility in layered gabbro in Oman Ophiolite: Younging direction determination at Sadam area. International Symposium of Istanbul Technical University, 2002,5.

Allawati, H. and Ogawa, Y. (2002) Flow and shear structures along the Moho in Northern Oman Mountains. International Symposium of Istanbul Technical University, 2002,5.

Ogawa, Y. and Asada, M. (2002) En echelon and conjugate strike-slip fault patterns on seabed indicated by sharp alignment of *Calyptogena* communities, NE Philippine Sea Plate boundary. WPGM Fluid redistribution process along active plate boundaries, Wellington, N.Z., 2002, 7.

Takami, Y. and Ogawa, Y. (2002) Large-scale fault pattern and submarine topography along the Sagami Trough on the NE Philippine Sea Plate subduction boundary as explained by Riedel shear box test. WPGM Tectonic and Surface, Wellington, N.Z., 2002, 7.

Shinozaki, R. and Ogawa, Y. (2003) Stress drop measured from fluid Inclusion analysis in the base of accretionary prism: example from Ordovician Southern Uplands Accretionary Prism, Scotland. GSA Annual Meeting, Seattle, 2003, 10.

Ogawa, Y., Hirano, N. and Shipboard Scientific Party KR03-07 (JAMSTEC) (2003) En echelon knolls on the Nosappu Fracture Zone, NW Pacific: A possible leaky transform fault zone. AGU Fall Meeting, San Francisco, V10 Crustal and Mantle Processes in Ophiolites and Ocean Crust Generation, 2003,12.

Lee, I. T. and Ogawa, Y. (2003) Deep-sea tsunami deposits in the Miocene Nishizaki Formation of Boso Peninsula, Central Japan. AGU Fall Meeting, OS22B, San Francisco, 2003,12.

Allawati, H. and Ogawa, Y. (2003) Structural geology of Northern Oman Ophiolite at Moho horizon in Shar area. AGU Fall Meeting, San Francisco, V10 Crustal and Mantle Processes in Ophiolites and Ocean Crust Generation, 2003,12.

遠藤良太・安間了(2004) 屋久島南西部に分布するメランジュの構造解析. (筑波大学生命環境科学研究科修士論文にもとづく) (手記)

平成１３年度～平成１５年度科学研究費補助金[基盤研究(A)(1)]
(研究課題番号　13304038)

研究成果報告書

流体包有物と微小鉱物形成からみたプレート境界付近の過去の地震断層の研究

目　次

研究成果の概要

小川　勇二郎　(筑波大学地球科学系)

われわれは３ヵ年の基盤研究「流体包有物と微小鉱物形成からみたプレート境界付近の過去の地震断層の研究」を行った．その主たる目的は，プレート境界付近で生じる断層の生成条件とメカニズムを明らかにすることであり，そのうちの断層にともなう変形と流体移動に関しては，多くの成果をあげることが出来た．主たる武器は顕微ラマン分光装置，走査型電子顕微鏡，および流体包有物測定装置であり，これらを用いて，断層岩の構造，組織，伴う脈鉱物の観察，温度・圧力測定，鉱物同定などを行った．その過程で，鉱物同定の基礎となる顕微ラマン分光装置の設置と運転を行い，多くの基礎的データを所得した．それらのデータは日常的に増大し続けており，今後とも大いに役に立つ．特に，付加体およびオフィオライト帯の内部に発達する多くの新しいタイプの断層を識別し，それらが，プレート収斂地域におけるテクトニクスの理解にどのような意義を持っているかを明らかにすることが出来た．調査した地域は，スコットランドのサザンアプランズ付加体，アメリカ合衆国のコースタルレンジ，ワイオミングスラストベルト，ニュージーランドのヒクランギ付加体とトアラス付加体，オマーンオフィオライト，本邦の四万十付加体，嶺岡オフィオライト帯など世界の代表的プレート境界にわたった．

そもそもプレート境界には３種類あるとされ，プレート収斂境界，発散境界，すれ違い境界である．最前者には，沈み込み境界と衝突境界がある．これらのほとんどすべての境界に関して，我々は現地調査を行った．即ち，プレート収斂境界のうち，沈み込み境界については，時代の古い方から，オルドビス紀のサザンアプランズ付加体，中生代のワイオミングスラストベルト，中生代から新生代のコースタルレンジ，ヒクランギ付加体とトアラス付加体，および四万十付加体，新生代の三浦・房総付加体，および現世の南海付加体である．また，衝突境界としては，原生代のスコットランドのアウターヘブリデスの断層帯，中生代のオマーンオフィオライトなどを調査し，また，すれ違い境界としては，コースタルレンジと嶺岡オフィオライト帯を調査した．

これらの調査の過程で，従来知られていた地質構造を確認するとともに，新しい発見を多く行った．そのほとんどは，国際学会で発表し，そのうちのいくつかはすでに国際誌に発表済みまたは投稿中である．

付加体にはさまざまな大小構造が知られているが，砂質と泥質では，その大小構造の有様をことにする．今回，前者として，サザンアプランズとワイオミングスラストベルトを選び，後者として四万十付加体の特に屋久島，および三浦・房総付加体を選んだ．それらの諸構造は，それぞれ，現世の南海付加体とバルバドス付加体に対応しており，それらとの比較研究も行った．その過程で四万十付加体の過去のプレート境界からシュードタキライト（地震の化石とも言われている）の発見もなされた．これは，分担者の一人の坂口とその指導学生による，世界初の快挙である．また，付加体内部における大小構造の記載的研究が，代表者によってサザンアプランズでなされ，各種の規模のデュープレックス構造が初めて発見された．さらに，その過去のプレート境界である，デコルマン帯に流れる流体の証拠である脈鉱物の流体包有物の研究から，代表者およびその学生によって，初めてバイモーダルの均質化温度が知られた．また，分担者の安間とその学生によって，四万十付加体の大小構造が詳しく記載され，構造変形に伴う著しいひずみが定量的に明らかにされ，過去のプレート運動に直接関連するものであることが分かった．また，今まで全く知られていなかった現世付加体の最先端部に関して，代表者とその研究協力者によって潜水船および潜水ロボットを用いて，詳しい観察と試料の採集，およびそれらの力学特性や変形履歴などが明らかにされた．一方，岩石と堆積物の基本的変形特性が，共同研究者と代表者の学生数名によって行われており，それらは，修士論文，博士論文として結実している．

最も基礎的な鉱物の同定，構造解析に関する研究は，分担者である木股および平井とその学生によって多方面にわたって研究されており，連綿として成果が続出している．特に，タリウムケイ酸塩の不対電子構造，メタンハイドレートの高圧相に関して，初めて明らかにされたのが特筆される．

以上のような成果を要約すると以下のようになる．

1．　本邦および海外の代表的付加体やオフィオライト帯を調査し，過去の地震断層またはその延長と思われる地域の地質構造の詳細を明らかにした．

2．　それらのうち，サザンアプランズのオルドビス紀付加体中に，海洋性岩石が断層で陸源性岩石と接する部分の構造解析と流体の温度圧力と移動様式を明らかにした．また同シルル紀付加体部分での構造様式と流体移動を調査し，今後の重要な研究地点の予備知識をえることが出来た．

3．　屋久島の四万十付加体の詳細を明らかにし，多くの構造相を示し，特にメランジュの詳細な構造を把握した．

4．　嶺岡オフィオライト構造体の構造，変形，変質，流体移動を調べ，その変形・流体条件，流体移動，テクトニクスを明らかにし，さらに国際協力のもとでの新たな進展を見た．

5．　フランシスカン帯におけるオフィオライトの産状と付加体，変成岩などの関係をフィールドで明らかにし，今後の研究の足がかりをつかんだ．

6．　高圧ガスハイドレートの新しい相を発見した．

7．　微小鉱物（１μ）の同定をルーティン化した．

キーワード

プレートテクトニクス (plate tectonics)，地震断層 (seismogenic fault)，流体包有物 (fluid inclusion)，ラマン分光分析 (Raman spectroscopy)．

Duplex structures and their tectonic implication for the Southern Uplands accretionary complex

Yujiro Ogawa

ABSTRACT: Various order duplex structures are described from oceanic sequences of basaltic and associated pelagic–hemipelagic sedimentary rocks in the Ordovician (northern) part of the Southern Uplands accretionary complex. The general structure of the terrane as a whole strikes ENE, but each component lithological tract strikes NE or more northerly, oblique to the regional trend, making an *en echelon* outcrop pattern. Further oblique relationships between structures and lithologies can be mapped at larger scales, up to 1 km scale or more. These duplex structures are thought to be originally SE-verging, now partly overturned to the NW. Differences in the *en echelon* geometry, either sinistral or dextral, are explained by variable plunge of the original structures.

Peach & Horne's first regional map of the Southern Uplands suggests an *en echelon* pattern of lithologies, implying large-scale duplex structures across the whole terrane. Here, the duplex structures are regarded as ubiquitous at both regional and smaller scales, suggesting considerable horizontal shortening. This was accommodated by such structures during underplating and out-of-sequence thrusting, in all parts of the accretionary prism, but particularly in the deeper tectono-stratigraphic levels. The duplex structures are characteristic of ancient décollement zones.

KEY WORDS: Décollement, *en echelon* pattern, geological structure, oceanic sequence, underplating.

The Southern Uplands of Scotland is widely thought to be one of the oldest recognised accretionary complexes (McKerrow *et al.* 1977; Leggett *et al.* 1979, 1982; Hepworth *et al.* 1982; Leggett 1987), although there is still some controversy over its precise palaeogeographic setting. The terrane has been extensively studied since the now-classical work by Peach & Horne (1899), who proposed many overturned fold-and-thrust structures based on the outcrop patterns of oceanic sequences composed of basaltic and pelagic lithologies. These include radiolarian bedded chert and a black shale known as the Glenkiln Shale. The large-scale fold structures proposed by Peach & Horne are actually uncommon, and generally consistent S-ward younging in steeply dipping strata means that most of the repetitions of the same lithologies are likely to arise from thrust faulting. In recent years much more detailed stratigraphy has been obtained (Armstrong *et al.* 1996, 1999; Floyd 1996), and overall S-ward younging of the ages of each tract has been confirmed. This contradiction between the N-ward younging of the strata and the S-ward younging of the structural tracts means that the Southern Uplands Terrane satisfies the geometry of an accretionary complex (Ogawa 1998).

Several published geological maps and cross-sections of this terrane imply a large-scale duplex structure (e.g. British Geological Survey 1985, 1986), and a few examples have been demonstrated in detail, for example SW of Stranraer (British Geological Survey 1992; Stone 1995) and the structural profiles based on biostratigraphical data in the SW Southern Uplands and in the Peebles and Hawick areas (Rushton *et al.* 1996). This paper describes several examples of typical duplex structures and discusses their regional significance. Three areas have been mapped in detail: the first is the Wandel area, 5 km NE of Abington; the second is at Hunt Law in the Leadhills area, 10 km SE of Abington; the third is the Glen App coastal area, S of Ballantrae (Ogawa 1998) (Fig. 1). In each area, the lithological outcrop pattern is not parallel to the general trend of the structural tract in which it is contained. The former is commonly more northerly than the latter, thus producing an *en echelon* structurally defined outcrop pattern.

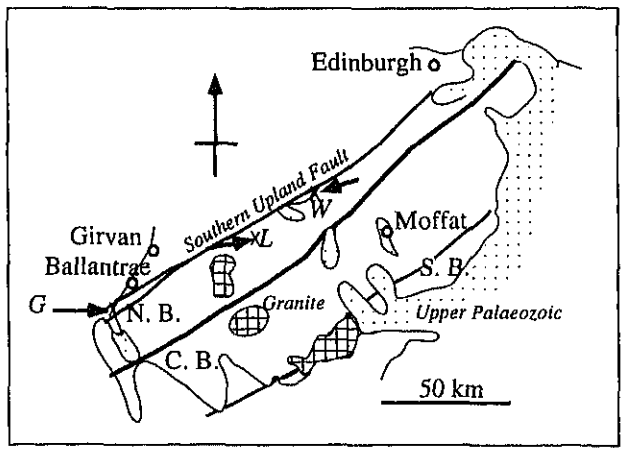

Figure 1 Index map showing study areas: Glen App (*G*), Leadhills (*L*) and Wandel (*W*) areas; *N.B., C.B.* and *S.B.* are northern belt, central belt and southern belt of the Southern Uplands terrane, respectively.

1. Description of duplex structures

1.1. Wandel area

This area lies within the northernmost tract of the Southern Uplands (Leggett *et al.* 1982), and the strata correspond to part of the Marchburn Formation (Floyd 1996). In the upper reaches of the Hawkwood Burn, which flows from the NE to merge with the Wandel Water, several bedded chert bodies [NS 973 259] have yielded fossils of Llanvirn age (Armstrong *et al.* 1990). The disposition of these strata (Fig. 2) indicates a

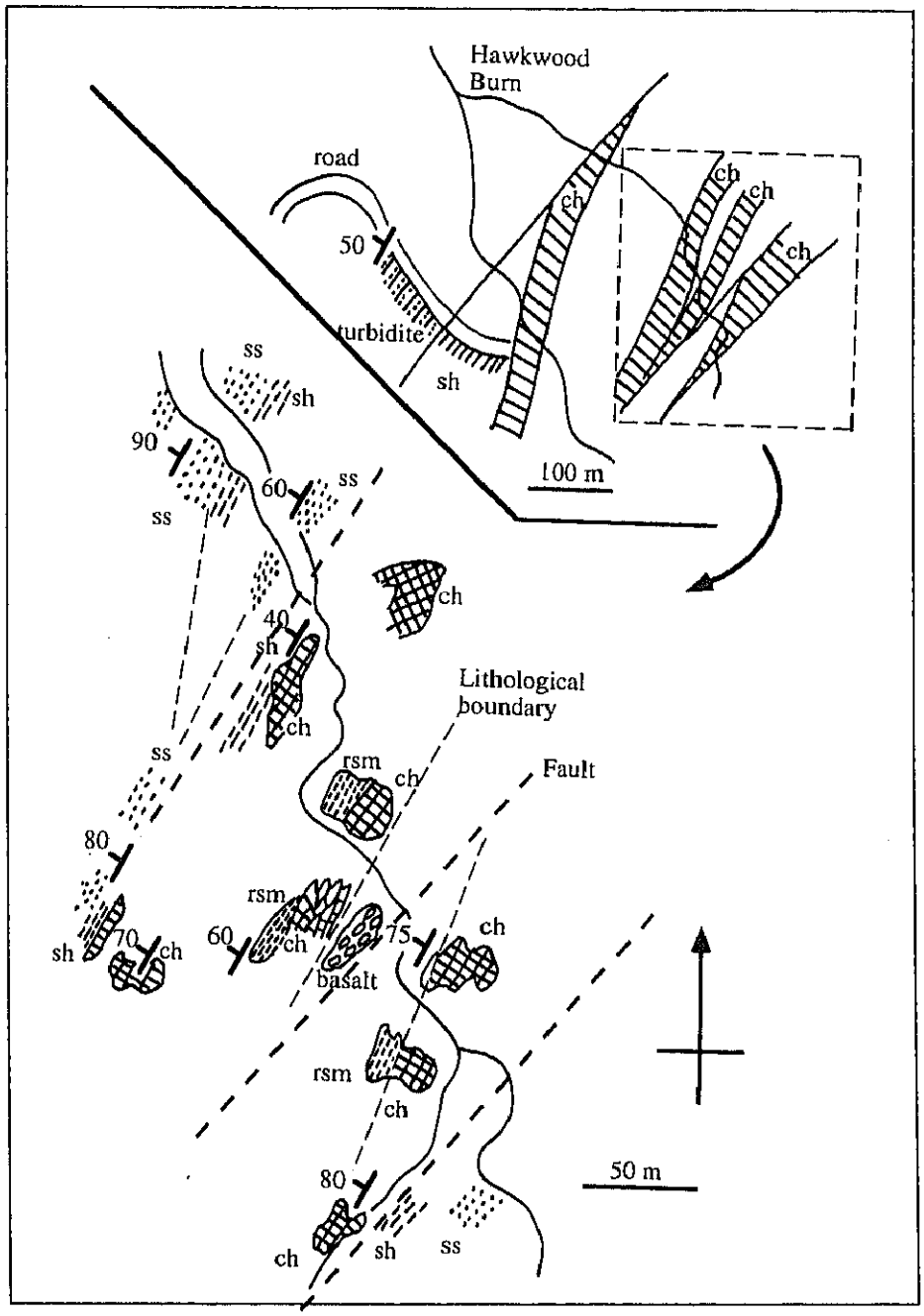

Figure 2 Lithological map of the upper reaches of the Hawkwood Burn, Wandel area; note the oblique relation to the general trend of the chert-dominant zone; ch—chert, rsm—red siliceous mudstone, ss—sandstone, sh—shale.

repetition of the same succession, from chert to turbidite through mudstone with steep dips but consistent N-ward younging. Brecciated basaltic rock of within-plate basalt affinity occurs adjacent to one of the chert bodies. The illustrations in Clarkson *et al.* (1993) and Armstrong *et al.* (1990) both suggest a general ENE strike for the chert bodies; however, careful mapping indicates that this is not the case. Each chert bed can be traced along a NE or even a NNE strike, oblique to the general trend of the belt (Fig. 2). There are several outcrops each containing minor faults and folds which define smaller-scale duplex structures, all with a SE vergence and consisting of horses (imbricated thrust packets) each several tens of metres long.

There could also be duplex structures of a greater order of magnitude, on a scale of 1 km, recognisable by the oblique distribution of chert-dominant zones within the Marchburn Formation structural tract (inset Fig. 2).

1.2. Leadhills area

Hunt Law is on the northern side of a ridge which divides the Strathclyde region to the NE from the Dumfries and Galloway region to the SW. Leadhills is well known as the location of now-defunct lead mines. Near Leadhills, along the upper reaches of the Snar Water, excellent exposures are developed [NS 871 157] (Borthwick 1993), and three chert beds are recognisable in the tributary valley draining into the Snar Water from Hunt Law (Fig. 3). The chert beds seemingly alternate with N-ward-younging turbidite sandstone and mudstone, assigned to the Kirkcolm Formation (Floyd 1996). Basaltic rocks are also exposed, but their relationships to the chert

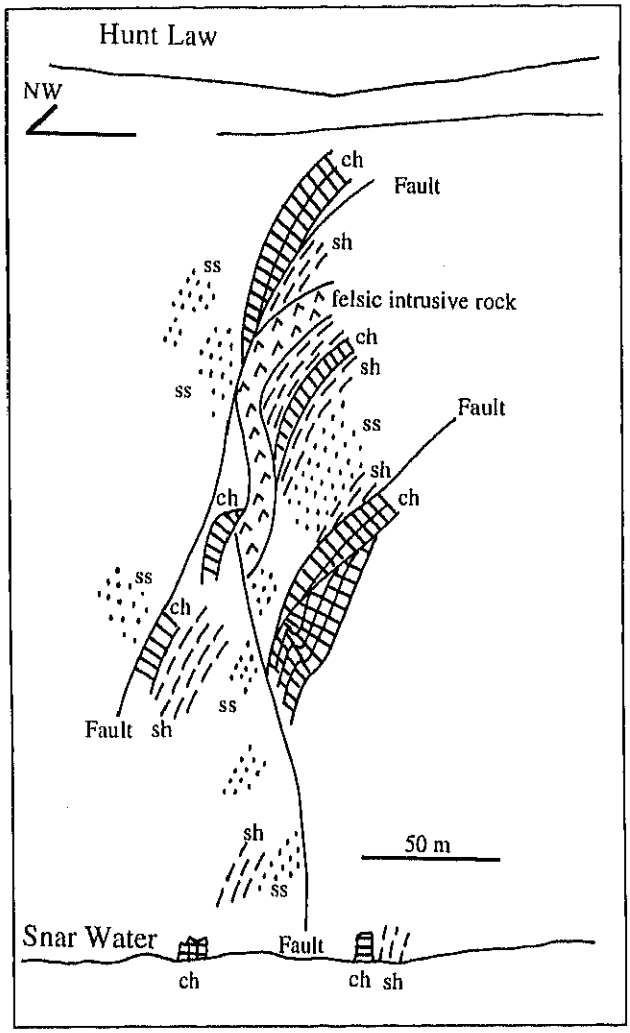

Figure 3 Lithological sketch, looking NE of the chert-dominant zone exposed on the hillside at Hunt Law, Leadhills area.

and turbidites are not clear. The chert bodies can be traced to the NE, slightly oblique to the overall NNE structural trend of the tract. Thrusts occur between the chert and turbidite lithologies and dip steeply NW, implying a SE vergence, and apparently link into duplex structures of several horses, each on the scale of tens of metres. Along strike to the E, in the Abington area, Leggett *et al.* (1982) recorded many repetitions of the same sequence from basalt to turbidite through pelagic lithologies within 100 m widths. These repetitions are also considered here to be enclosed within a thrust duplex system.

1.3. Glen App coastal area

This area lies in the NW of the Southern Uplands between the Stinchar Valley Fault to the N and the Glen App Fault to the S. A very complicated lithology distribution is mapped in detail along the coast (Fig. 4) (Ogawa 1998), although poor exposure prevents a similar analysis inland. The characteristic lithological association of basaltic and cherty rocks within red siliceous mudstone (Currarie Formation) is traceable in a series of *en echelon* outcrops [NX 05 75–06 79] (fig. 2 in Ogawa 1998). Ogawa (1998) identified several stages of deformation but the most important, first, stage is duplexing to create several horses on a scale of hundreds of metres. The readily traceable, red-coloured sedimentary rocks best show the disposition of the duplex along the faults. Overall, the structural geometry is interpreted as a mélange formed along a large décollement zone between the subducting and over-riding plates (Fig. 4; fig. 13 in Ogawa 1998). It is the component, much smaller-scale duplex structures that are seen in outcrop. All of the observed thrust duplexes are S-ward verging but downward facing, hence the original vergence must be S-ward with hinterland-dipping duplex style (Fig. 4). An important feature is that intensely folded turbidites are caught up between the décollement zones dominated by red siliceous mudstone.

2. Discussion and conclusion

From the detailed mapping outlined above, the following conclusions can be deduced: (1) the regional trend of each tract is ENE, whereas each individual bed strikes obliquely to the NE or NNE; (2) chert to turbidite sequences are repeated many times by thrust faults; (3) basaltic rocks are sporadically associated with the bedded radiolarian chert and siliceous mudstone, which are thought to be of pelagic to hemipelagic origin; (4) chert-dominant bodies are distributed in an *en echelon* pattern, not only on a local scale but also on a regional scale, as demonstrated by previous mapping.

The classical work by Peach & Horne (1899) led to a regional map covering the whole of the Southern Uplands Terrane and illustrating oblique relations between the general direction of the tracts and their component strata. Peach & Horne interpreted the contradiction in terms of folding rather than thrusting, and previously published geological maps on the scale of 1:50,000 (e.g. British Geological Survey 1978, 1992) and 1:250,000 (British Geological Survey 1985, 1986) indicate a similar arrangement. The structural relationships shown by these previously published geological maps range in scale from tens of kilometres to less than 1 km, whereas those described in this paper range in scale down to tens of metres, and locally down to the 1 m scale. At all scales, oblique relations between the general trend of the tracts and the detailed lithology are confirmed. It is considered here that these relationships arose when the oceanic sequence, which forms the lower tectonostratigraphic horizon during accretionary prism formation, was accreted by means of duplex formation during underplating. The red siliceous mudstone with basalt and chert bodies along many duplex structures is thought to represent the décollement zones (Fig. 5). The structure was then further dislocated by later, out-of-sequence thrusts at a shallower level to form the whole accretionary complex. Most of the beds in the northern belt of the Southern Uplands dip at high angles, and may be overturned, as in the Glen App coastal area (Fig. 4), but the basic duplex structure is still preserved.

Geological bodies are, of course, arranged in three dimensions, whereas they are exposed largely on two-dimensional surfaces. However, from the sections described above, it is clear that the features are indeed three-dimensional duplexes. In some areas, the *en echelon* pattern of lithology is dextral, but in others it is sinistral. The difference arises from variable plunge direction. If the S-ward-younging, hinterland-dipping duplex plunges E, dextral *en echelon* relationships appear, but if the plunge is to the W, the relationships are sinistral (Fig. 6).

These duplex structures are seen not only in the areas discussed here, but also elsewhere in the Southern Uplands. From the work of Peach & Horne (1899), and from many of the recent geological maps published on a scale of 1:50,000, it is reasonable to deduce that most of the pelagic lithologies exposed in the area lie within duplex structures without any significant large folds. The duplex structures are the product of intense lateral shortening by means of imbricated thrust

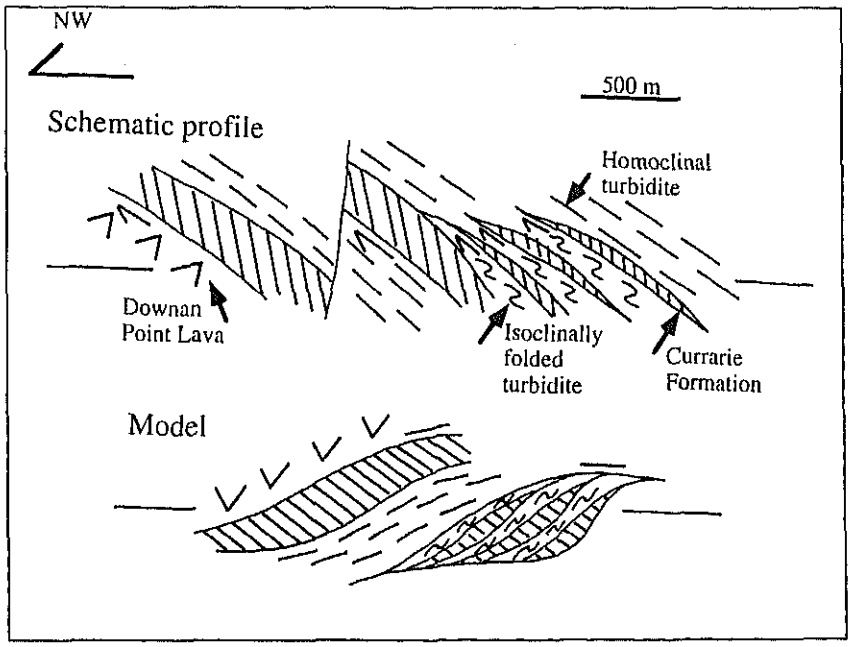

Figure 4 Largely overturned and faulted present schematic profile of the Glen App coastal area, S of Ballantrae, showing the distribution of the Currarie Formation (Currarie Formation is shown hatched; red siliceous mudstone with basalt and chert), and the model at the time of the accretionary prism stage; a 1 km-scale duplex structure is reconstructed in the model.

packets (horses), bounded by a floor-thrust below and a roof-thrust above. Similar structures are seen in other ancient accretionary complexes that have been mapped in detail, such as the Shimanto belt (Murata 1991; Hashimoto & Kimura 1998), and Miura–Boso peninsulas (Yamamoto *et al.* 2000; Hirono & Ogawa 1998) of Japan, the Franciscan complex of the U.S. West Coast (Kimura *et al.* 1996), and in Kodiak Island, Alaska (Sample & Fisher 1986; Sample & Moore 1987). In these examples, the structures are thought to have formed by underplating of the accretionary prism, in particular along décollement zones between the subducting and over-riding plates. Hence, the Southern Uplands could also be an underplated prism, and it is likely that further detailed mapping will establish many more examples of duplex structure.

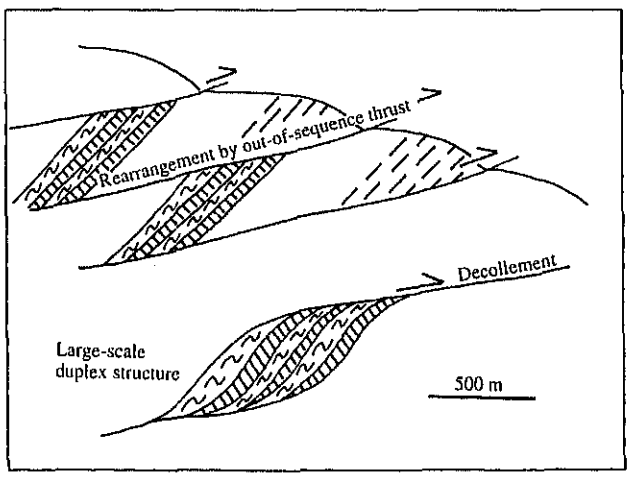

Figure 5 Model of large-scale duplex structure formation along the décollement zone in an accretionary prism; note that the oceanic sequence, pelagic rock-dominant lithology alternates with folded terrigenous strata (shown as S-shaped turbidites) to form a duplex structure first, then is rearranged at the shallower levels by out-of-sequence thrusts.

3. Acknowledgements

I am grateful to Professor Alastair H. F. Robertson, Dr Jeremy K. Leggett and Professor Euan N. K. Clarkson, who gave me the opportunity to visit the Southern Uplands. The field

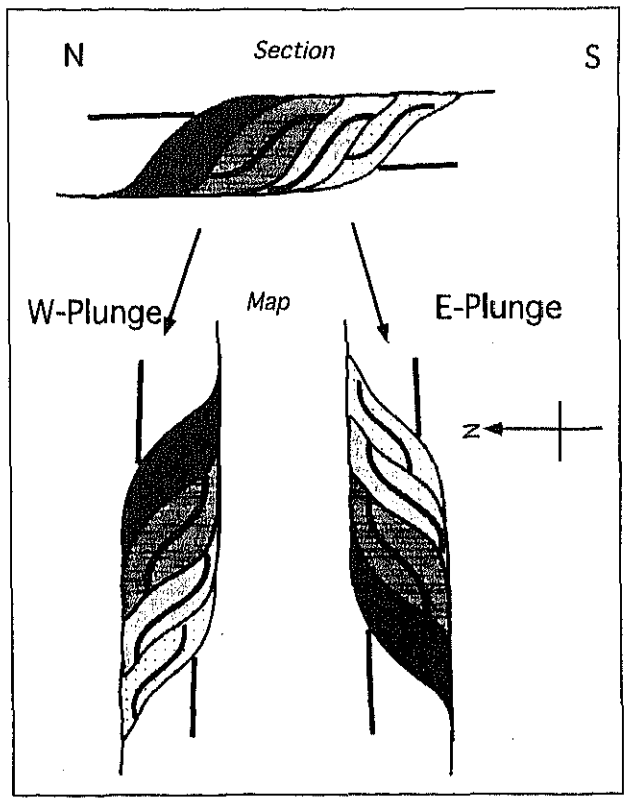

Figure 6 Schematic disposition of two-dimensional figure for a duplex structure; the original E–W section (top) is rotated vertically and plunges either E (right) or W (left).

expenses were provided by the British Council and Japanese Ministry of Education, Science, Culture and Sports (Grant-in-aid A-10304037) to which I express my gratitude. An early draft was reviewed and revised by Dr Alex Maltman, Dr Robert Cheeney, and in particular Dr Phil Stone, to whom I am grateful. The field survey was assisted by Than Tin Aung and Toshiyuki Kurihara whom I thank very much.

4. References

Armstrong, H. A., Clarkson, E. N. K. & Owen, A. W. 1990. A new Lower Ordovician conodont faunule from the Northern Belt of the Southern Uplands. *Scottish Journal of Geology* **26**, 47–52.

Armstrong, H. A., Owen, A. W., Scrutton, C. T., Clarkson, E. N. K. & Taylor, C. M. 1996. Evolution of the Northern Belt, Southern Uplands: implications for the Southern Uplands Controversy. *Journal of the Geological Society, London*, **153**, 197–205.

Armstrong, H. A., Owen, A. W. & Floyd, J. D. 1999. Rare earth geochemistry of Arenig cherts from the Ballantrae Ophiolite and Leadhills Imbricate Zone, southern Scotland: implications for origin and significance to the Caledonian Orogeny. *Journal of the Geological Society, London* **156**, 549–60.

Borthwick, G. W. 1993. Leadhills and Wanlockhead. *In* McAdam, A. D., Clarkson, E. N. K., & Stone, P. (eds) *Scottish Borders geology—An excursion guide*, 192–200. Edinburgh: Scottish Academic Press.

British Geological Survey 1978. *Biggar, Sheet 24(W), Solid Edition, 1:50,000*. Keyworth, Nottingham: BGS.

British Geological Survey 1985. *Clyde, Sheet 55°N-06°W, 1:250 000 Series, Solid Geology*. Keyworth, Nottingham: BGS.

British Geological Survey 1986. *Borders, Sheet 55°N-04°W, 1:250 000 Series, Solid Geology*. Keyworth, Nottingham: BGS.

British Geological Survey 1992. *The Rhins of Galloway, Sheet 1 and 3 with parts of 7 and 4W (Scotland), Solid Edition, 1:50,000*. Keyworth, Nottingham: BGS.

Clarkson, E. N. K., Harper, D. A. T., Owen, A. W. & Taylor, C. M. 1993. Biggar. *In* McAdam, A.D., Clarkson, E.N.K. & Stone, P. (eds) *Scottish Borders geology—An excursion guide*, 181–91. Edinburgh: Scottish Academic Press.

Floyd, J. D. 1996. Lithostratigraphy of the Ordovician rocks in the Southern Uuplands: Crawford Group, Moffat Shale Group, Leadhills Supergroup. *Transactions of the Royal Society of Edinburgh: Earth Sciences* **86**, 153–65.

Hashimoto, Y. & Kimura, G. 1998. Underplating process from melange formation to duplexing: Example from the Cretaceous Shimanto Belt, Kii Peninsula, southwest Japan. *Tectonics* **18**, 92–107.

Hepworth, B. C., Oliver, G. J. H. & McMartry, M. J. 1982. Sedimentology, volcanism, structure and metamorphism of the northern margin of a Lower Palaeozoic accretionary complex; Bail Hill–Abington area of the Southern Uplands of Scotland. *In* Leggett, J. K. (ed.) *Trench-forearc geology, Geological Society, London, Special Publication* **10**, 521–33.

Hirono, T. & Ogawa, Y. 1998. Duplex arrays and thickening of accretionary prisms—an example from Boso Peninsula, Japan. *Geology* **26**, 779–82.

Kimura, G., Maruyama, S., Isozaki, Y. & Terabayashi, M. 1996. Well-preserved underplating structure of the jadeitized Franciscan complex, Pacheco Pass, California. *Geology* **24**, 75–8.

Leggett, J. K. 1987. The Southern Uplands as an accretionary prism: the importance of analogues in reconstructing palaeogeography. *Journal of the Geological Society, London* **144**, 737–52.

Leggett, J. K., McKerrow, W. S. & Eales, M. H. 1979. The Southern Uplands of Scotland; a Lower Palaeozoic accretionary prism. *Journal of the Geological Society, London* **136**, 755–70.

Leggett, J. K., McKerrow, W. S. & Casey, D. M. 1982. The anatomy of a Lower Palaeozoic accretionary forearc: The Southern Uplands of Scotland. *In* Leggett, J. K. (ed.) *Trench-forearc geology, Geological Society, London, Special Publication* **10**, 494–520.

McKerrow, W. S., Leggett, J. K. & Eales, M. H. 1977. Imbricate thrust model for the Southern Uplands of Scotland. *Nature* **267**, 237–9.

Murata, A. 1991. Duplex structures of the Uchinohae formation in the Shimanto Terrane, Kyushu, Southwest Japan. *Journal of the Geological Society of Japan* **97**, 39–52.

Ogawa, Y. 1998. Tectono-stratigraphy of the Glen App area, Southern Uplands, Scotland: anatomy of an Ordovician accretionary complex. *Journal of the Geological Society, London* **155**, 651–62.

Peach, B. N. & Horne, J. 1899. The Silurian Rocks of Britain, Volume 1: Scotland. *Memoir of the Geological Survey of the United Kingdom*. Glasgow: HMSO.

Rushton, A. W. A., Stone, P. & Hughes, R. A. 1996. Biostratigraphical control of thrust models for the Southern Uplands of Scotland. *Transactions of the Royal Society of Edinburgh: Earth Sciences* **86**, 137–52.

Sample, J. & Fisher, D. 1986. Duplex accretion and underplating in an ancient accretionary complex, Kodiak and adjacent islands, Alaska. *Geology* **14**, 160–3.

Sample, J. & Moore, J. C. 1987. Structural style and kinematics of an underplated slate belt, Kodiak and adjacent islands, Alaska. *Geological Society of America Bulletin* **99**, 7–20.

Stone, P. 1995. *Geology of the Rhins of Galloway district. Memoir of the British Geological Survey, sheets 1 and 3 (Scotland)*. Keyworth, Nottingham: BGS.

Yamamoto, Y., Ohta, Y. & Ogawa, Y. 2000. Implication for the two-stage layer-parallel faults in the context of Izu forearc collision zone: examples from the Miura accretionary prism, central Japan. *Tectonophysics* **325**, 133–44.

YUJIRO OGAWA, Institute of Geoscience, University of Tsukuba, Tsukuba 305-8571, Japan
e-mail: yogawa@arsia.geo.tsukuba.ac.jp

MS received 27 October 1999. Accepted for publication 3 July 2000.

High-pressure structures of methane hydrate observed up to 8 GPa at room temperature

H. Hirai and Y. Uchihara
Institute of Geoscience, University of Tsukuba, 1-1 Tennoudai, Tsukuba, Ibaraki 305-8571, Japan

H. Fujihisa, M. Sakashita, E. Katoh, and K. Aoki
National Institute of Materials and Chemical Research, 1-1-1 Higashi, Tsukuba, Ibaraki 305-8565, Japan

K. Nagashima and Y. Yamamoto
National Institute for Resources and Environment, 16-1 Onogawa, Tsukuba, Ibaraki 305-8569, Japan

T. Yagi
Institute of Solid State Physics, Tokyo University, 5-1-5 Kashiwanoha, Kashiwa, Chiba 277-8581, Japan

(Received 7 December 2000; accepted 25 July 2001)

Three high-pressure structures of methane hydrate, a hexagonal structure (str.A) and two orthorhombic structures (str.B and str.C), were found by *in situ* x-ray diffractometry and Raman spectroscopy. The well-known structure I (str.I) decomposed into the str.A and fluid at 0.8 GPa. The str.A transformed into the str.B at 1.6 GPa, and the str.B further transformed into the str.C at 2.1 GPa which survived above 7.8 GPa. The fluid solidified as ice VI at 1.4 GPa, and the ice VI transformed to ice VII at 2.1 GPa. The structural changes occurring with increasing pressure were observed reversibly with decreasing pressure. The symmetric stretching vibration, ν_1, of the methane molecule observed in the Raman spectra changed along with the structural changes. The bulk moduli, K_0, for the str.I, str.A, and str.C were calculated to be 7.4, 9.8, and 25.0 GPa, respectively. The difference in the bulk moduli implies the difference in fundamental structure of the high-pressure structures. © *2001 American Institute of Physics.* [DOI: 10.1063/1.1403690]

I. INTRODUCTION

Methane hydrate, containing guest methane molecules in cages of hydrogen bonded water molecules, lies globally under the oceans.[1] Methane hydrate is called "burning ice" and is a promising natural resource, while at the same time methane is a greenhouse gas that plays the most prominent role in global warning. In addition, outer planets and their satellite such as Uranus and Ganymede are thought to be composed partly of ice and methane hydrate. Many studies, therefore, have been carried out from wide viewpoints such as phase relations[2–4] crystal structures,[5–12] physical properties,[2,13] and nature of hydrogen bonding.[14] Most of these studies, except for a few,[14–16] were made at low temperature under ambient pressure. Therefore, high-pressure studies above 1 GPa have to be more intensively pursued to explore new materials in water-methane system, as well as, to survey their possible occurrence on the outer planets. Recently, the present authors reported an *in situ* x-ray diffraction study of methane hydrate at pressures of up to 5.5 GPa using a diamond anvil cell (DAC).[17] This study showed that the structure I (str.I) of methane hydrate survived until 2.3 GPa by changing its cage occupancy. Another high-pressure study by x-ray diffractometry and Raman spectroscopy reported transformations to a hexagonal structure via the structure II.[18] The other work by neutron and x-ray diffractometry described existence of a hexagonal structure and a orthorhombic structure.[19] The discrepancy in the transition behavior is probably affected by kinetic conditions such as compression rate and the initial state of the sample. Therefore, further experiments with a reduced compression rate are required, as are those at higher-pressure regions.

In order to clarify the structure changes for clathrate hydrate, it is necessary to pursue not only the fundamental structure (the framework built up by cages) but also the vibration state of the guest molecules. For this purpose, it is required for the specimens to be characterized by x-ray diffractometry and Raman spectroscopy. The Raman spectrum resulting from the totally symmetric stretching vibration, ν_1, of enclathrated methane can be used as a probe for their cage size and the occupancy.[20–22] In this study, both *in situ* observations of x-ray diffractometry (XRD) and Raman spectroscopy were carried out for the same samples, and three high-pressure structures, a hexagonal structure (str.A) and two orthorhombic structures (str.B and str.C) were found at higher pressure. As well, the fundamental structure of the str.A was examined.

II. EXPERIMENT

A lever and spring-type DAC was used in the high-pressure experiments. In order to control pressures lower than 2 GPa and the compression rate, several pairs of soft springs were used. Pressure measurements were made by the ruby fluorescence method. The accuracy of the present measurement system is 0.1 GPa, taking the resolution of the spectrometer and the analytical procedure into account. The pressure measurements were carried out several times, and an average of three reasonable values among them was

0021-9606/2001/115(15)/7066/5/$18.00 © 2001 American Institute of Physics

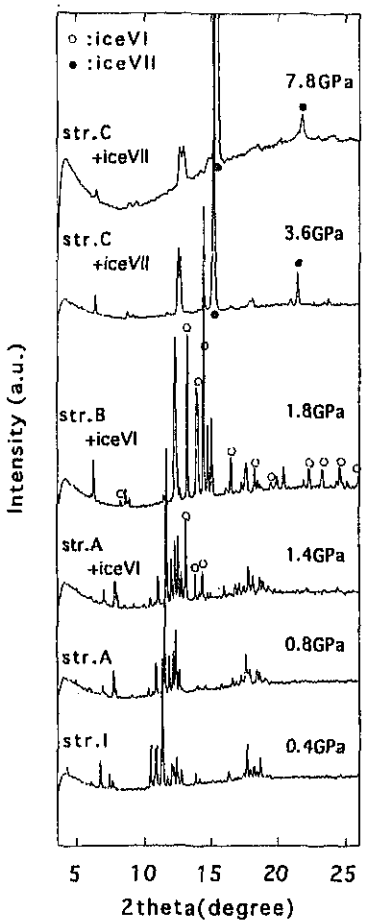

FIG. 1. XRD patterns observed with pressure changes. At 0.4 GPa, typical XRD of the str.I is shown. At 0.8 GPa, the str.A is observed as a crystalline phase. At 1.4 GPa, the str.A and ice VI (marked by open circles) are observed. At 1.8 GPa, the str.B and ice VI are observed. At 3.6 GPa, the str.C and ice VII (marked by solid circles) are observed. At 7.8 GPa, the str.C is still observed.

adopted. The XRD experiment was performed using synchrotron radiation (SR) on a BL-18C at Photon Factory, High Energy Accelerator Research Organization (KEK). The monochromatized beam with a wavelength of 0.6198 Å was used. Methane hydrate powder prepared using a conventional ice-gas interface method under the conditions of 15 MPa and −3 °C was used as the initial material. This powder consisted of almost pure methane hydrate and contained a maximum of a few vol % of ice I_h according to a combustion analysis. The sample powder was put into a gasket hole in a vessel cooled by liquid nitrogen to prevent decomposition of the sample. The sample was sealed by loading the anvils slightly up to 0.2–0.3 GPa at the low temperature. Then the DAC was placed under room temperature. The sample was held as solid state during the procedure. All measurements were conducted at room temperature. Particular attention was paid to reducing the rates of compression or decompression. The mean rate was approximately 0.1 GPa per 10 mins. Raman spectroscopy was performed by using the 488 nm line of an argon ion laser with incident power of 400 mW at tube. A single monochromator and CCD-detector were used in the optical system. The calibration of wave number was carried out by using ten Ne emission lines in the

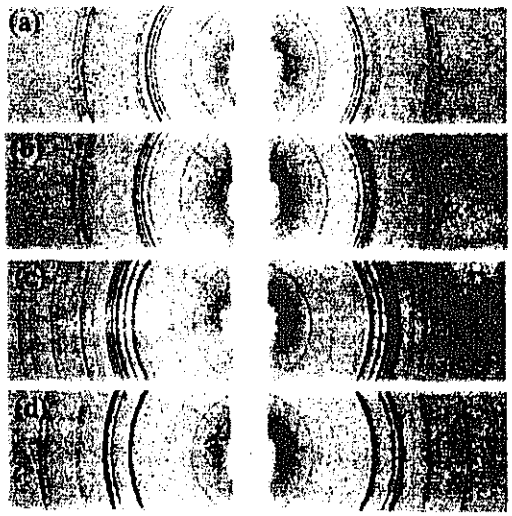

FIG. 2. Representative XRD patterns. (a) The str.I at 0.4 GPa; (b) the str.A at 0.8 GPa; (c) the str.B and ice VI (spotty rings) at 1.8 GPa; and (d) the str.C and ice VII at 3.6 GPa.

range from 1000 cm^{-1} to 3500 cm^{-1}, and by fitting the deviations between the standard and the observed values with third order polynomial.

III. RESULTS

Figure 1 shows XRD patterns observed with changes in pressure. At 0.4 GPa, a typical XRD pattern of the str.I was observed. The XRD pattern represented clear powder rings [Fig. 2(a)]. The *d*-values and relative intensities agreed with those of the established crystal structure I.[6] At 0.8 GPa, a hexagonal structure (str.A) was observed in the XRD pattern. Under an optical microscope, relatively larger crystals and thin fluid layer between the crystals were observed. The XRD pattern of the str.A was spotty at this time, suggesting grain growth in the fluid. At 1.4 GPa, ice VI (marked by open circles) appeared besides the str.A, and the fluid disappeared. At 1.6 GPa, the str.A transformed into the str.B. At 2.1 GPa, the str.B further transformed into the str.C, and ice VI transformed into ice VII (marked by solid circles). At 7.8 GPa, the str.C still remained, although the diffraction intensities were rather weakened. Solid methane, phase I or phase A, were not observed in the pressure region examined.[23] The structural changes of methane hydrate occurring with increasing pressure were observed reversibly with decreasing pressure. The representative XRD patterns of the str.I, str.A, str.B, and str.C were given in Fig. 2. The XRD patterns of the str.A reverted from the str.B represented relatively homogeneous rings [Fig. 2(b)] than those observed at the decomposition from the str.I.

The changes in fundamental structure were clarified by the XRD data mentioned above. In order to examine changes in the state of the guest methane molecule along with the structural change, the Raman spectrum resulting from the totally symmetric stretching vibration (ν_1) of enclathrated methane was measured. Figure 3 shows Raman spectra observed with changes in pressure. For the str.I, a typical doublet peak was observed at 2904 cm^{-1} and 2919 cm^{-1} at 0.4

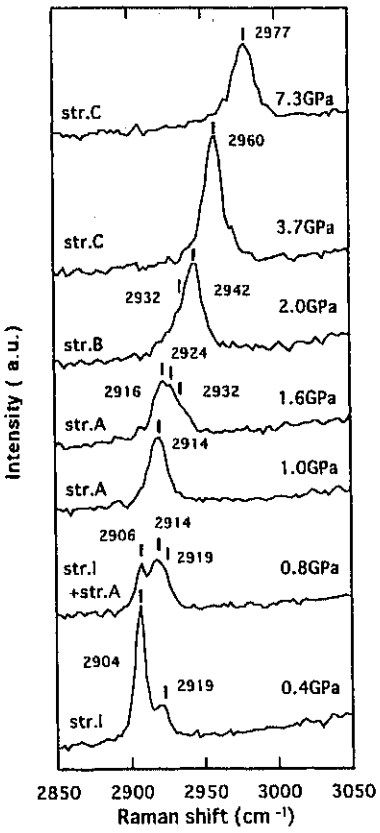

FIG. 3. Raman spectra from ν_1 of methane molecule along with the structural change.

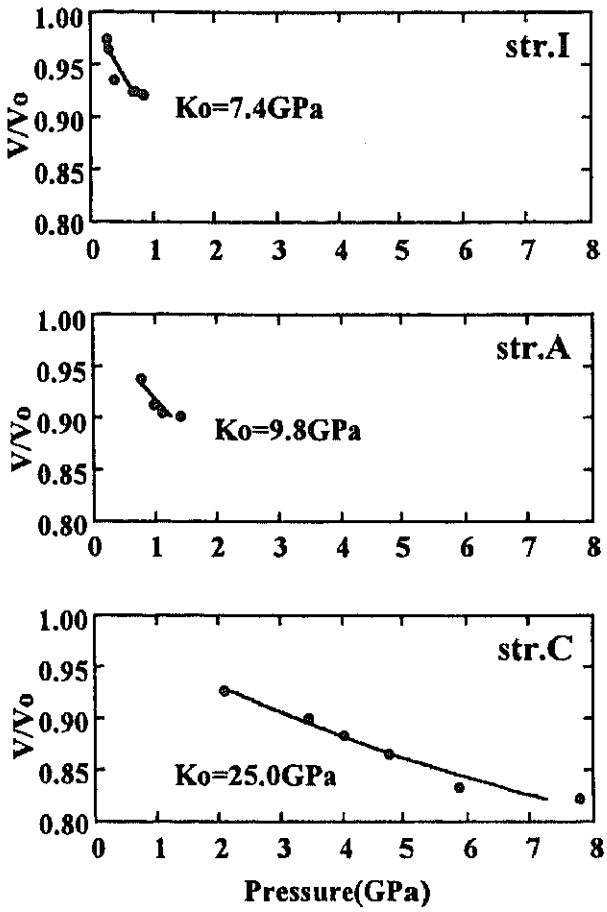

FIG. 4. Variations in the volume ratio with pressure for the str.I, str.A, and str.C.

GPa (Fig. 3). The intensity ratio of the former to the latter peak was 2.9 as an average within the measurements. The former peak, 2904 cm^{-1}, was coincident with those reported previously; on the other hand, the latter one, 2919 cm^{-1}, was a little higher than those reported, 2914–2915 cm^{-1}.[20,21,18] The previously reported data were obtained at ambient pressure[20,21] or at 0.125 GPa,[18] while the present data were obtained at higher than 0.4 GPa. A certain pressure effect might occur,[22] although the reason for the shift is not clear at the present time. At the transition from the str.I to str.A, the peak for the str.A began to appear between the doublet peak of the str.I at 0.8 GPa (Fig. 3). After the transition, an apparent single peak for the str.A was observed at 2914 cm^{-1} at 1.0 GPa (Fig. 3). With increasing pressure, the peak of the str.A split into two or three peaks at 1.6 GPa (Fig. 3). At 2.0 GPa, a peak for the str.B was observed at 2942 cm^{-1}. An apparent single peak for the str.C shifted to 2977 cm^{-1} at 7.3 GPa. The observed changes of ν_1 vibration of the methane molecule in the Raman spectra corresponded to the structural changes observed in the XRD patterns (Fig. 1).

The variations in volume ratios (V/V_0) with pressure for the str.I, str.A, and str.C were obtained. Fitting by Birch–Murnaghan's equation of state as $K_0'=4$, the bulk moduli, K_0, were calculated for the str.I, str.A, and str.C to be 7.4 GPa, 9.8 GPa, and 25.0 GPa, respectively (Fig. 4). There is a smaller difference between the str.I and the str.A, suggesting that the fundamental structure of the str.A is composed of cages while the bulk modulus for the str.C is much larger which is comparable to that of ice VII. This implies that the str.C is different from those of cage structure. The bulk modulus for the str.B was not calculated because there was insufficient data for fitting due to the narrow pressure range.

IV. DISCUSSION

In the previous study by the present authors,[17] where the compression rate was rather higher, methane hydrate decomposed into ice VII and solid methane (phase I) at 2.3 GPa. While, in the present study, three high-pressure structures were clearly found. The transition behavior is thought to be considerably affected by the compression rate and the starting material. The study by other authors[18] reported that the str.I transformed into the structure II at 0.1 GPa, and the structure II transformed into a hexagonal structure at 0.6 GPa. The structure II was not observed within the present experiments performed. The other study[19] described that at 0.9 GPa the str.I transformed to a hexagonal structure, and that at 2.0 GPa the hexagonal structure transformed to an orthorhombic structure. These hexagonal and orthorhombic structures (named as MH-II and MH-III) are thought to correspond to the present str.A and str.C, respectively, on the basis of the same unit cell parameters, the indexing, and the pressure range of existence. While the str.B was not found in that study. The str.B, in the present study, existed only in a narrow pressure range from 1.6 GPa to 2.1 GPa, but this structure was observed in good reproducibility with increas-

TABLE I. The observed and calculated d-values for the str.A at 0.8 GPa. The observed unit cell parameters: $a=12.004$ Å, $c=10.046$ Å.

$h\,k\,l$	d-obs. (Å)	d-calc. (Å)	Dev.	$h\,k\,l$	d-obs. (Å)	d-calc. (Å)	Dev.
1 0 0	10.226	10.337	−0.011	2 0 4	2.249	2.246	0.001
0 0 1	9.932	9.975	−0.004	2 2 3		2.221	
1 0 1	7.133	7.178	−0.006	4 1 1	2.205	2.200	0.002
1 1 0	5.952	5.968	−0.003	3 2 2	2.143	2.142	0.000
1 1 1	5.109	5.121	−0.002	2 1 4	2.107	2.102	0.002
0 0 2	4.988	4.988	0.000	5 0 0	2.073	2.067	0.003
2 0 1	4.575	4.589	−0.003	5 0 1		2.024	
1 0 2	4.478	4.492	−0.003	3 0 4	2.025	2.020	0.002
2 1 0	3.900	3.907	−0.002	0 0 5		1.995	
2 1 1		3.638		3 3 0	1.993	1.989	0.002
2 0 2	3.585	3.589	−0.001	4 2 0	1.956	1.953	0.002
3 0 0	3.446	3.446	0.000	3 3 1		1.951	
0 0 3	3.328	3.325	0.001	3 2 3	1.933	1.931	0.001
3 0 1	3.257	3.257	0.000	4 2 1		1.917	
1 0 3		3.165		2 2 4		1.913	
2 1 2	3.080	3.076	0.001	5 0 2	1.914	1.910	0.002
2 2 0	2.987	2.984	0.001	1 1 5		1.892	
1 1 3	2.907	2.905	0.001	3 1 4		1.882	
3 1 0	2.861	2.867	−0.002	4 1 3	1.868	1.867	0.001
2 2 1		2.859		5 1 0		1.857	
2 0 3	2.802	2.796	0.002	3 3 2		1.848	
3 1 1		2.755		4 2 2		1.819	
2 1 3	2.536	2.532	0.002	4 0 4	1.783	1.794	−0.004
3 1 2		2.486		2 1 5	1.781	1.777	0.002
1 0 4	2.436	2.424	0.005				
3 2 0	2.373	2.371	0.001				
4 0 2		2.294					

ing and decreasing pressure. And the XRD pattern was clearly distinguished from those of the str.A and str.C (Fig. 2). The str.B is certainly present as a high-pressure structure of methane hydrate. The discrepancy among these studies might be affected mainly by compression rate and the initial state of the sample.

The diffraction lines observed in the str.A were indexed by a primitive hexagonal lattice (Table I) with the unit cell parameters of $a=12.004$ Å and $c=10.046$ Å at 0.8 GPa. A hexagonal clathrate hydrates with a space group of $P6/mmm$ have been previously reported at ambient pressure, which accommodate a large guest molecule, methyl cyclohexane-d_4 in the large 20-hedra cage and small help gas, H_2S.[8] And a structural refinement of the hexagonal structure accommodating a large 2,2-dimethylpentane molecule was performed.[24] The framework of these clathrate hydrates is the same as that of dodecasil 1H,[25,26] which is a clathrate compound of silica. The dodecasil 1H also accommodates a large guest molecule of piperidine. The framework of the hexagonal structure is composed of three different cages, one 20-hedra cage [$5^{12}6^8$] (X-cage), three 12-hedra cages [5^{12}] (Y-cage), and two modified 12-hedra cages [$4^35^66^3$] (Z-cage)[5,25] within a unit cell. The ideal composition of the structure is $1X3Y2Z/34H_20$, when one guest molecule is contained in each cage. The number of the guest molecules is 6 for 34 water in this case. Table I shows the observed d-values and the calculated ones using crystal parameters of dodecasil 1H. Both d-values exhibit good agreement, which indicates that the fundamental structure of the present str.A is similar to those of the low-pressure hexagonal structure reported.[8,24,25] The recent high-pressure study[18] of methane hydrate also reported that the hexagonal structure observed in that study was similar to the low-pressure one. The low-pressure hexagonal structures reported are stabilized by accommodating the large guest molecule in their large 20-hedra cage. In order to stabilize the structure only by small methane molecules, it is expected that two or more methane molecules are accommodated in the 20-hedra. According to Udachin *et al.*,[24] the dimensions of a free ellipsoid in the 20-hedra are 6.84, 6.84, and 8.59 Å, while the van der Waals diameter of methane molecule is 4.1 to 4.3 Å. Thus two methane molecules can be easily accommodated in the 20-hedra with sufficient intermolecular distance and also distance from the cage. On the other hand, it seems rather difficult for three methane molecules to be accommodated without superimposing each other. A preliminary structural analysis based on the low-pressure hexagonal structure suggested that the fundamental structure of the str.A might not totally be the same as that of the hexagonal structure but may be somewhat modified. A detailed refinement of the str.A should be the subject for future research.

As for two orthorhombic structures, the str.B and str.C, the unit cell parameters tentatively determined were $a=4.806$, $b=8.140$, $c=7.935$ at 1.80 GPa and $a=4.644$, $b=7.967$, $c=7.572$ at 4.80 GPa, respectively. Although these orthorhombic structures have similar unit cell parameters, they exhibit clearly different XRD patterns described above. The str.B might be a related structure of the str.A

consisting of cages, because the transition from the str.A to str.B was not clearly distinguished under the optical microscope. The str.C corresponded to the body-centered orthorhombic structure reported[19] because of the same unit cell parameters and the body-center indexing. The str.C survived above 7.8 GPa. The bulk modulus is comparable to that of ice VII. These suggest that the str.C is probably a denser structure such as H_2–H_2O clathrate[14] rather than other structures consisting of cages.

The present work, employing a combination of x-ray diffactometry with Raman spectroscopy, has developed an understanding of the behavior of methane hydrate under high pressure. The results suggest that further new materials in the water–methane system might be present under higher pressure, and that methane hydrate might exist on the outer planets and their satellites.

[1] K. A. Kvenvolden, Chem. Geol. **71**, 41 (1988).
[2] E. D. Sloan, Jr., *Clathrate Hydrates of Natural Gases* (Dekker, New York, 1990), pp. 25–55.
[3] D. W. Davidson, in *Water: A Comprehensive Treaties*, edited by F. Franks (Plenum, New York, 1973), Vol. 2, pp. 115–234.
[4] L. A. Stern, S. H. Kirby, and W. B. Durham, Science **273**, 1843 (1996).
[5] G. A. Jeffrey, in *Inclusion Compounds*, edited by J. L. Atwood, J. E. D. Davies, and D. D. MacNichol (Academic, London, 1984), Vol. I, pp. 135–190.
[6] R. K. McMullan and G. A. Jeffrey, J. Chem. Phys. **42**, 2725 (1965).
[7] T. C. W. Mak and R. K. McMullan, J. Chem. Phys. **42**, 2732 (1965).
[8] J. A. Ripmeester, J. S. Tse, and C. I. Ratcliffe, Nature (London) **325**, 135 (1987).
[9] D. W. Davidson, Y. P. Handa, C. I. Ratcliff, J. S. Tse, and B. M. Powell, Nature (London) **311**, 142 (1984).
[10] J. A. Ripmeester and C. I. Ratcliffe, J. Phys. Chem. **92**, 337 (1988).
[11] J. S. Tse, C. I. Ratcliff, C. I. Powell, V. F. Sears, and Y. P. Handa, J. Phys. Chem. A **101**, 4491 (1997).
[12] W. F. Kuhs, B. Chazallon, and P. G. Radaelli, J. Inclusion Phenom. Mol. Recognit. Chem. **19**, 65 (1997).
[13] D. W. Davidson, *Natural Gas Hydrates: Properties, Occurrence and Recovery*, edited by J. L. Cox (Butterworths, Boston, 1983).
[14] W. L. Vos, L. W. Finger, and R. J. Hemley, Chem. Phys. Lett. **257**, 524 (1996).
[15] Y. A. Dyadin, E. Y. Aladko, and E. G. Larionov, Mendeleev Commun. **1**, 34 (1997).
[16] H. T. Lotz and J. A. Schouten, J. Chem. Phys. **111**, 10242 (1999).
[17] H. Hirai, T. Kondo, M. Hasegawa, T. Yagi, Y. Yamamoto, K. Nagashima, M. Sakashita, H. Fujihisa, and K. Aoki, J. Phys. Chem. B **104**, 1429 (2000).
[18] I-Ming Chou, A. Sharma, R. C. Burruss, A. F. Goncharov, R. J. Hemley, L. A. Stern, and S. H. Kirby, Proc. Natl. Acad. Sci. U.S.A. **97**, 13484 (2000).
[19] J. S. Loveday, R. J. Nelmes, M. Guthrie, S. A. Belmonte, D. R. Allan, D. D. Klug, J. S. Tse, and Y. P. Handa, Nature (London) **410**, 661 (2001).
[20] A. K. Sum, R. C. Burruss, and E. D. Sloan, J. Phys. Chem. B **101**, 7371 (1997).
[21] S. Subramanian and E. D. Sloan., Chem. Eng. Sci. **55**, 1981 (2000).
[22] S. Nakano, M. Moritoki, and K. Oogaki, J. Chem. Eng. Data **44**, 254 (1999).
[23] In our previous study (Ref. 17), the methane hydrate decomposed into ice VII and solid methane, phase I, at 2.3 GPa.
[24] K. A. Udachin, C. I. Ratcliffe, G. D. Enright, and L. A. Ripmeester, Supramol. Chem. **8**, 173 (1997).
[25] H. Gerke and H. Gies, Z. Kristallogr. **166**, 11 (1984).
[26] F. Liebau, H. Gies, R. P. Gunawardane, and B. Marler, Zeolites **6**, 373 (1986).

Eur. J. Mineral.
2001, 13, 849–856

This paper was presented at the EMPG VIII meeting in Bergamo, Italy (April 2000)

The crystal structure of synthetic $TlAlSi_3O_8$: Influence of the *inert-pair effect* of thallium on the feldspar structure

ATSUSHI KYONO* and MITSUYOSHI KIMATA

Institute of Geoscience, University of Tsukuba, Tennodai 1-1-1, Tsukuba, Ibaraki, 305-8571, Japan
*e-mail: kyono@esca.geo.tsukuba.ac.jp

Abstract: The crystal structure of synthetic Tl feldspar, $TlAlSi_3O_8$, was determined based on single-crystal X-ray diffraction data; monoclinic, $a = 8.882(3)$, $b = 13.048(2)$, $c = 7.202(2)$ Å, $\beta = 116.88(1)°$, $V = 744.5(4)Å^3$, $Z = 4$, space group $C2/m$ ($R = 7.33\%$ for 462 observed reflections). The underlying framework is similar to Rb feldspar, $RbAlSi_3O_8$, and can be regarded as isotypic with sanidine. The structure accommodates Tl^+ cations occupying the M site coordinated by nine O atoms. The more expanded Tl polyhedra as compared to the Rb polyhedra, in spite of the small ion radius of Tl^+ relative to Rb^+, result from the behavior of the stereoactive lone-pair electrons of Tl^+ called "*inert-pair effect*". The difference in centroid–central atom distance in the TlO_9 polyhedron suggests that the lone-pair electrons are orienting parallel to the [001] direction in the feldspar structure. Therefore, Tl found as a trace element in analyses of natural K-feldspar can be considered as an actual constituent of this mineral. The syntheses of the present Tl-feldspar, $TlAlSi_3O_8$, together with Tl-leucite, $TlAlSi_2O_6$, and the chemical analogue of kalsilite, $TlAlSiO_4$, shed new light on the crystal chemistry of potassium aluminosilicate minerals.

Key-words: thallium, feldspar, crystal structure, lone-pair electrons, stereochemical activity, *inert-pair effect*.

Introduction

Thallium is commonly distributed as a trace element in the Earth's crust (*e.g.* Rb 90, Sr 375, Cs 3, Ba 425, Sb 0.2, Pb 13, Bi 0.2, and Tl 0.5 ppm; Mason & Moore, 1982), but sulfides represent the overwhelming majority (over 30 defined species) of known thallium minerals (Clark, 1993) because of the chalcophile property of this element. Silicate minerals containing Tl as a trace element, for example feldspars and micas with Tl contents in the ppm range, were reported by Badolov & Rabinovich (1966) and Heinrichs *et al.* (1980). Extracting crystal-chemical information about Tl behavior from silicate minerals in nature, however, is still a far from routine process and quantitative studies are rare (Mason & Moore, 1982). The first synthesis of thallium aluminosilicates by Krogh *et al.* (1991) provided $Tl_{1.1}AlSiO_4$, with a determination of the crystal structure by Rietveld analysis. More recently, new thallium aluminosilicates like Tl-leucite ($TlAlSi_2O_6$) have been synthesized by Kyono *et al.* (1999) and the crystal structure of synthetic $TlAlSiO_4$ has been accurately re-determined by single-crystal X-ray diffraction (Kyono *et al.*, 2000). Our initial interest in these aluminosilicates stems from the "*inert-pair effect*" of Tl^+, which produces an irregular coordination environment of anions around this atom (West, 1999). Application of the *inert-pair effect* to mineralogy was made to understand the crystal structure of derbylite, where the $[SbO_3]^{3-}$ complex is a distorted tetrahedron with the lone electron pair occupying a missing vertex (Moore & Araki, 1976); in these cases the bonding is well described by the valence-shell electron-pair repulsion (VSEPR) model (Gillespie, 1972) with the lone-pair electrons at one of the four tetrahedral ligand positions to give the configuration MX_3E. Recently, the crystal-structure refinement of $TlAlSiO_4$ has clarified the substantial *inert-pair effect* of

DOI: 10.1127/0935-1221/2001/0013/0849

0935-1221/01/0013/0849 $ 2.00
© 2001 E. Schweizerbart'sche Verlagsbuchhandlung, D-70176 Stuttgart

the Tl atom on this structure, and the extremely distorted Tl-O polyhedra have an implication for the rare occurrence of Tl aluminosilicate minerals in nature (Kyono *et al.*, 2000).

The present work was aimed at synthesis and single-crystal X-ray structural refinement of Tl feldspar ($TlAlSi_3O_8$) in order to elicit the *inert-pair effect* of thallium on the feldspar structure and to understand its bearing on the crystallization of Tl minerals in nature.

Experimental methods and data analysis

The $TlAlSi_3O_8$ crystal was synthesized from a powdered sample of low-albite ($Ab_{98.8}An_{1.0}$) from Minas Gerais, Brazil, under hydrothermal conditions. The starting material was mixed with $TlNO_3$ in a 1 : 1 weight ratio and poured into a 5 cm^3 silver tube. Water was then added in a suitable volume to

Table 1. X-ray powder diffraction data of synthetic Tl feldspar.

h	k	l	I/I_0	d_{obs}(Å)	d_{calc}(Å)*
0	2	0	44	6.46	6.52
0	0	1	20	6.37	6.41
1	1	$\bar{1}$	20	5.90	5.94
0	2	1	26	4.55	4.57
2	0	0	64	3.94	3.96
1	1	1			3.96
1	3	0	36	3.80	3.81
1	3	$\bar{1}$	70	3.63	3.64
2	2	$\bar{1}$	80	3.62	3.63
1	1	$\bar{2}$	92	3.45	3.46
2	2	0	100	3.372	3.385
2	0	$\bar{2}$	20	3.327	3.339
0	0	2	54	3.197	3.209
1	3	1	78	2.992	3.003
2	2	$\bar{2}$	20	2.977	2.972
0	4	1	18	2.900	2.907
3	1	$\bar{1}$	24	2.895	2.884
1	3	$\bar{2}$	42	2.760	2.770
3	1	$\bar{2}$	32	2.669	2.676
2	4	$\bar{1}$	36	2.606	2.613
3	1	0	22	2.582	2.588
1	1	2	18	2.536	2.544
3	3	$\bar{1}$	2	2.444	2.445
1	5	$\bar{1}$	12	2.424	2.430
2	0	$\bar{3}$	8	2.383	2.387
3	3	$\bar{2}$	18	2.310	2.314
1	1	$\bar{3}$			2.313
3	3	0	8	2.255	2.257
2	2	$\bar{3}$	6	2.241	2.242
1	3	2	6	2.234	2.228
1	5	1	6	2.207	2.209
3	1	$\bar{3}$	10	2.198	2.194
4	0	$\bar{1}$	16	2.191	2.192
4	0	$\bar{2}$	16	2.189	2.183
0	6	0	16	2.169	2.174
0	0	3	4	2.137	2.139
3	1	1	10	2.097	2.099
4	2	$\bar{2}$	12	2.073	2.070
1	3	$\bar{3}$	14	2.066	2.068
0	6	1	4	2.054	2.059
3	3	$\bar{3}$	20	1.978	1.980
4	0	0	24	1.977	1.980
2	2	2	24	1.975	1.978
3	5	$\bar{1}$	2	1.956	1.956
2	4	$\bar{3}$	2	1.931	1.926
3	3	1	14	1.914	1.910
2	6	0	8	1.907	1.906
4	2	0	2	1.895	1.895
3	5	0	6	1.854	1.856
1	1	3	4	1.846	1.845
2	6	$\bar{2}$	4	1.821	1.822
1	7	0	10	1.814	1.814
2	0	$\bar{4}$	14	1.793	1.797
1	7	$\bar{1}$	14	1.792	1.795
0	4	3	10	1.790	1.789
1	5	$\bar{3}$	2	1.749	1.746
1	3	3	2	1.709	1.713
4	0	1	8	1.690	1.689
3	1	2	2	1.684	1.683
4	4	$\bar{3}$	2	1.681	1.681
3	5	1	8	1.649	1.648
4	2	1	6	1.635	1.635
4	2	$\bar{4}$	2	1.618	1.617
5	3	$\bar{3}$	8	1.574	1.575
2	4	$\bar{4}$			1.574
0	2	4	2	1.560	1.558
3	7	$\bar{2}$	6	1.540	1.540
2	6	2	6	1.502	1.501
6	0	$\bar{2}$	2	1.478	1.479
0	8	2	2	1.454	1.454
6	2	$\bar{2}$	4	1.442	1.442
1	1	4			1.441
2	4	3	8	1.439	1.439
6	2	$\bar{3}$	4	1.420	1.421
1	9	$\bar{1}$	4	1.417	1.416
1	9	1	2	1.370	1.368
5	5	0	4	1.355	1.354
1	9	$\bar{2}$	2	1.344	1.344
3	9	$\bar{1}$	4	1.301	1.301
2	8	2	2	1.283	1.282
7	1	$\bar{3}$	2	1.258	1.258
6	0	$\bar{5}$	2	1.244	1.243

* d_{cal} based on refined cell parameters: a = 8.881(2), b = 13.044(3) Å, c = 7.196(2)Å, β = 116.89(2)°, V = 743.6(3) Å^3.

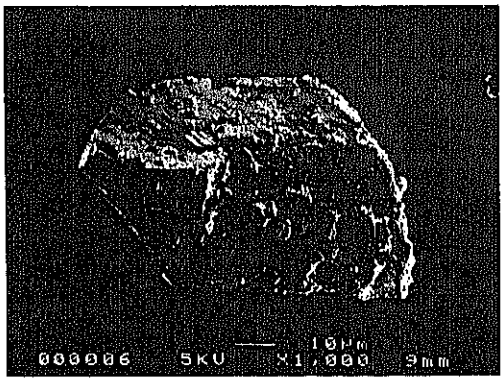

Fig. 1. SEM photograph of synthetic Tl feldspar.

give a 70% filling ratio before sealing up the tube. These silver tubes were inserted into the autoclave. The whole was heated up to 550°C during 5 days: the maximum pressure reached under such conditions was around 70 MPa. The experiments were stopped by air-cooling of the autoclaves to room temperature within the furnace. The totally crystallized precipitate was filtered and washed thoroughly with distilled water in order to completely dissolve the $TlNO_3$ covering the surface of the products. The synthesized Tl-feldspar crystals are translucent and colorless, up to 0.5 mm in size (Fig.1). The X-ray powder diffraction pattern (Table 1) of the crystals was indexed on a monoclinic lattice derived from that of the sanidine structure (Ribbe, 1963).

The chemical homogeneity of the synthetic Tl-feldspar was confirmed by electron-microprobe analysis, which was performed with the wavelength-dispersion spectroscopy (WDS) on a JEOL superprobe (JXA-8621), operated at 20 kV and 10 nA beam current, with a beam size of 10 μm. Synthetic lorandite (Berlepsch, 1996) was used as Tl standard. Na and K are below detection in the studied crystals and the average of six analyses made at different positions of a single-crystal sample is SiO_2 40.63, Al_2O_3 12.25, Tl_2O 46.42, sum 99.30 wt.%, leading to the empirical formula $Tl_{0.960}Al_{1.055}Si_{2.969}O_8$, which is close to endmember of $TlAlSi_3O_8$.

X-ray single-crystal investigations were pursued on an Enraf-Nonius CAD4 diffractometer utilizing graphite monochromated Mo$K\alpha$ radiation. Intensities were recorded using the standard $\omega/2\theta$ scan technique. Absorption (ψ scan method), Lorentz, and polarization corrections were applied to the intensities with the SDP program (Enraf-Nonius, 1983). All calculations for refinement were done with the SHELXL-97 program (Sheldrick, 1997); the crystal data and refinement information are given in Table 2. The initial model for Tl-feldspar was taken from the structure of sanidine (Ribbe, 1963). The refined atomic coordinates and displacement parameters for Tl feldspar are presented in Table 3.

Table 2. Crystal data for synthetic Tl feldspar.

Empirical formula	$TlAlSi_3O_8$
Formula weight	443.62
Wavelength (Å)	0.71073
Crystal system	monoclinic
Space group	*C2/m*
a (Å)	8.882(3)
b (Å)	13.048(2)
c (Å)	7.202(2)
β (°)	116.88(1)
V (Å^3)	744.5(4)
Z	4
F(000)	800.0
D_{calc} (g/cm^3)	3.958
μ (mm^{-1})	22.31
Crystal size (mm^3)	0.12×0.05×0.05
Max θ, deg.	25
h, *k*, *l* ranges	-10→9, 0→15, 0→8
Total reflections	749
Unique reflections	693
$\|F\| \geq 4\sigma_F$	462
Parameters	64
Final *R* (%)	7.33
Final *S*	1.140

$R = \Sigma \| |F_o| - |F_o| | / \Sigma |F_o|$
$S = [\Sigma w (|F_o| - |F_c|)^2 / (m - n)]^{1/2}$, for *m* observations and *n* parameters

Infrared spectra were obtained using FTIR spectroscopy (Herschel FT/IR-300, JASCO) over the range 1400-400 cm^{-1} (Fig. 2). Samples were ground into a powder for about 5 min by hand in an agate mortar and pestle, and absorption experiments were performed using the standard pellet technique. The powder was diluted with KBr in the ratio 1:400 for the middle infrared region. A total of 128 scans were averaged at a nominal resolution of 4 cm^{-1}. The instrument was equipped with a Ge-coated KBr beamsplitter and a MCT detector.

Results and discussion

Description of the crystal structure

On the basis of 25 reflection data with $2\theta > 25°$, the unit-cell parameters were determined on the diffractometer as a = 8.882(3), b = 13.048(2), c =

Table 3. Atomic parameters and their estimated standard deviations for Tl feldspar

atom	x	y	z	U_{11}	U_{22}	U_{33}	U_{12}	U_{13}	U_{23}	U_{eq}(Å^2)
Tl	0.2968	0	0.1568	0.0620	0.1163	0.0483	0	0.0230	0	0.0763
	0.0003	0	0.0004	0.0018	0.0031	0.0017	0	0.0013	0	0.0015
T_1	0.0081	0.1928	0.2222	0.0409	0.0716	0.0274	0.0017	0.0174	0.0015	0.0459
	0.0013	0.0010	0.0016	0.0052	0.0081	0.0049	0.0050	0.0041	0.0049	0.0028
T_2	0.7223	0.1227	0.3395	0.0412	0.0637	0.0349	0.0020	0.0221	0.0019	0.0448
	0.0012	0.0010	0.0016	0.0053	0.0075	0.0056	0.0048	0.0046	0.0048	0.0027
OA_1	0	0.1494	0	0.0879	0.0548	0.0167	0	0.0306	0	0.0505
	0	0.0032	0	0.0294	0.0236	0.0159	0	0.0180	0	0.0100
OA_2	0.6767	0	0.2817	0.0599	0.0359	0.0991	0	0.0306	0	0.0670
	0.0059	0	0.0094	0.0259	0.0224	0.0384	0	0.0268	0	0.0133
OB	0.8279	0.1606	0.2212	0.0559	0.0743	0.0369	0.0031	0.0155	-0.0035	0.0578
	0.0038	0.0027	0.0045	0.0166	0.0218	0.0141	0.0152	0.0131	0.0147	0.0078
OC	0.0410	0.3163	0.2603	0.0495	0.0648	0.0310	-0.0032	0.0111	-0.0143	0.0511
	0.0036	0.0023	0.0042	0.0151	0.0191	0.0131	0.0135	0.0118	0.0130	0.0070
OD	0.1730	0.1284	0.4076	0.0887	0.0546	0.0195	-0.0026	0.0215	-0.0068	0.0554
	0.0044	0.0023	0.0039	0.0211	0.0181	0.0126	0.0153	0.0137	0.0117	0.0076

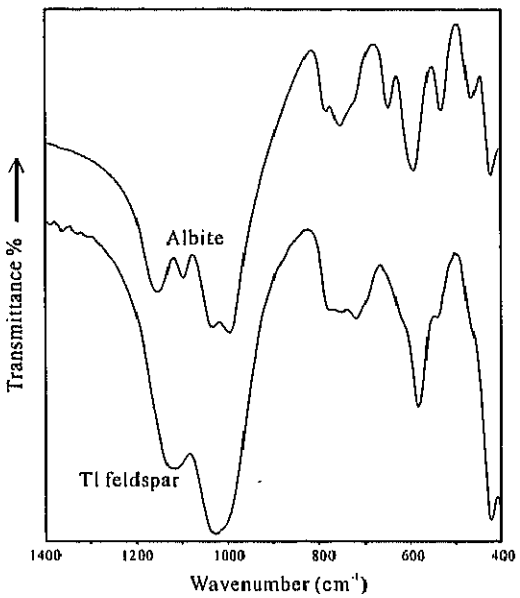

Fig. 2. IP powder spectra between 400 and 1400 cm^{-1} for albite (starting materials) and synthetic Tl feldspar.

7.202(2) Å, β = 116.88(1)°, V = 744.5(4) Å^3 (Table 2). It is worth noting that $TlAlSi_3O_8$ has a larger unit-cell volume than $RbAlSi_3O_8$ (Gasperin, 1971; Voncken *et al.* 1993; Koval'skii *et al.* 2000) although the ionic radius of the Tl^+ cation is slightly smaller than that of Rb^+ (Shannon, 1976). The structure was solved and refined in the space group *C2/m*. Conventional refinements of diffraction data yielded reasonable interatomic distances and angles for tetrahedral framework, but the *R* value was very large (about 10%) when the reflection data were used from 2° to 70° in 2θ. After omitting the high-angle reflections (2θ > 50°) on account of extreme weakness of these intensities, the *R* value dropped drastically to about 7%, and the final agreement factor is *R* = 7.33% (Table 2). However, more prudent calculations did not give a better *R* factor owing to the rugged surface of crystals. The average structure finally obtained can be effectively utilized to outline the crystal-chemical features of feldspar structures.

Although the framework structure for the Tl-feldspar is topologically equivalent to that for Rb-feldspar of the sanidine type (Gasperin, 1971), the isotropic displacement factors of Tl and OA_2 ions are much larger than those of Rb and OA_2 in the Rb feldspar (Gasperin, 1971). These factors dominate the characteristic structure of Tl-feldspar (Table 2). The difference between these two isotypes probably demands some stereochemical explanation from the *inert-pair effect* on the feldspar structure. The mean T_1-O and T_2-O distances in the present Tl-feldspar indicate a highly disordered (Al,Si) distribution (Table 4), and a slight difference in (Al,Si) ordering between Tl and Rb feldspars (Table 5). The IR spectrum of the Tl-feldspar (Fig. 2) supports such a disordered (Al,Si) distribution, because the broader peaks are attributed to strong disorder of Al and Si atoms (Smith & Brown, 1988). The contrast with the highly ordered (Al,Si) distribution in the low-albite starting material (Fig. 2) implies that Tl-feldspar has crystallized after dissolution of low-albite in the hydrothermal solution. The SEM photograph suggesting a possibly euhedral morphology of Tl-feldspar is corroborative evidence of such crystallization (Fig. 1).

Table 4. Interatomic distances (Å), angles (°) and bond valences (b.v.).

	Tl feldspar	Rb feldspar*		Tl feldspar	Rb feldspar*
$T_1 - OA_1$	1.669 (17)	1.633	OA_1-T_1-OB	106.8 (13)	107.6
OB	1.651 (33)	1.629	OA_1-T_1-OC	114.9 (18)	112.9
OC	1.638 (32)	1.644	OA_1-T_1-OD	103.6 (13)	106.5
OD	1.693 (33)	1.634	OB-T_1-OC	110.5 (17)	110.6
mean	**1.663**	**1.635**	OB-T_1-OD	111.6 (17)	110.9
			OC–T_1-OD	*109.3 (15)*	*108.3*
			mean	**109.5**	**109.5**
$T_2 - OA_2$	1.658 (19)	1.633	OA_2-T_2-OB	107.4 (23)	110.7
OB	1.605 (33)	1.627	OA_2-T_2-OC	106.9 (19)	105.4
OC	1.650 (30)	1.634	OA_2-T_2-OD	106.0 (23)	109.5
OD	1.629 (27)	1.635	OB-T_2-OC	112.4 (16)	109.7
mean	**1.636**	**1.632**	OB-T_2-OD	113.4 (17)	110.9
			OC – T_2-OD	109.8 (16)	111.0
			mean	**109.3**	**109.4**
	Tl feldspar	**b.v.**	Rb feldspar*		
Tl – OA_1×2	3.055 (27)	**0.184**	3.068		
OA_2	3.074 (46)	**0.087**	2.95		
OB×2	3.210 (31)	**0.121**	3.169		
OC×2	3.090 (30)	**0.167**	3.124		
OD×2	3.012 (29)	**0.207**	3.041		
mean	**3.090**	**Σ 0.766**	**3.084**		

* Gasperin (1971)

Table 5. The Al content of individual tetrahedra and their angular distortions.

	Site occupancy		Angular distortion	
	t_1	t_2	T_1	T_2
Tl feldspar	0.261	0.239	3.92	3.07
Rb feldspar (Gasperin, 1971)	0.251	0.249	2.35	2.13

Site occupancies were calculated as $t_i = 0.25 + (<T_i–O> - <<T–O>>)/const$, where 'const' ≡ <<Al–O>> – <<Si–O>>; it is equal to 0.125 Å for K-rich feldspars (Kroll & Ribbe, 1983).

TlO_9 and RbO_9 polyhedra

There is a very strong possibility that the structural difference between $TlAlSi_3O_8$ and $RbAlSi_3O_8$ feldspars is mainly caused by the behavior of the lone-pair electrons of the Tl^+ ion (West, 1999). Brown (1988) had already mentioned that for the main heavy elements in lower oxidation states (such as Tl^+, Pb^{2+}, Sb^{3+}, Bi^{3+}) low coordination numbers are invariably associated with stereochemical activity of the lone pair, in particular that Tl^+ offers a dramatic illustration of this effect, and that the weaker bonding bases show a tendency for the coordination number to rise and for the distortion to diminish as the base strength is reduced. In the Tl-feldspar structure Tl^+ is found to be coordinated by nine oxygen atoms of the framework (Fig. 3). The poly hedral volume, centroid–central atom distances and sphericity parameters for $M^+_xM^{2+}_{1-x}Si_{2+x}Al_{2-x}O_8$ feldspars (Makovicky & Balic-Zunic, 1998) calculated with the program IVTON (Balic-Zunic & Vickovic, 1996) are listed in Table 6. These results suggest that the geometry characteristic of this TlO_9 polyhedron departs from the correlation between ion radii and distortion parameters (Fig. 4). Particular attention must be paid to the fact that the Tl coordination polyhedron has the largest volume of all alkali polyhedra in feldspar structures (Table 6). In general, the shortest M-O distance is M-OA_2 due to the OA_2 oxygen depending on the repulsive power of M cations from each other (Smith & Brown, 1988). However, the Tl-OA_2 bond distance is 3.074 Å and not the minimum (Table 4). The uniqueness of this polyhedral environment is plainly shown in Fig. 4, which indicates that despite of great allowance of T-OA_2-T angles in monoclinic feldspars (*Kimata et al., 1996*) the Tl-OA_2 bond distance of Tl-feldspar is disproportionately longer. The unusual Tl polyhedron evidently derives from the uniqueness of Tl-OA_2 bond distance revealed by Fig. 4. Therefore bond elongation of the Tl-OA_2 distance is regarded as due to the influence of the distorted ligand field caused by the *inert-pair effect* of Tl lone-pair electrons.

Table 6. Selected polyhedral distortion parameters.

Chemical formula	Polyhedron	V(Å^3)	r(Å)	s	d(Å)	Reference
$TlAlSi_3O_8$	TlO_9	47.31	3.089	0.991	0.134	This study
$NaAlSi_3O_8$	NaO_9	40.21	2.903	0.925	0.114	Harlow (1982)
$Ba_2Al_2Si_2O_8$	BaO_9	41.19	2.925	0.952	0.023	Newnham & Megaw (1960)
$KAlSi_3O_8$	KO_9	43.43	2.986	0.961	0.051	Scambos *et al.* (1987)
$RbAlSi_3O_8$	RbO_9	46.68	3.082	0.982	0.089	Gasperin (1971)

V: volume of coordination polyhedron
r: mean distance from centroid to ligands
s: sphericity of coordination polyhedron
d: centroid – central atom distance

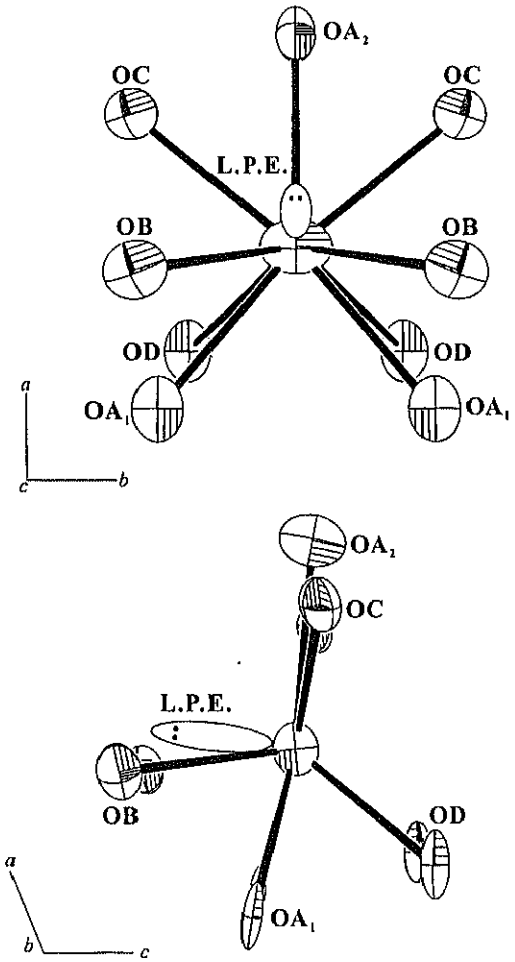

Fig. 3. Anisotropic thermal-vibration ellipsoids of TlO_9 polyhedra in projection on [001] and [010]. Polarized Tl $6s^2$ lone pair electrons (L.P.E) are shown schematically.

The bond-valence arrangement calculated from the parameters of Brese & O'Keeffe (1991) is shown in Table 4. The bond-valence sum around the Tl site does not fully satisfy the formal charge for Tl^+ (= 1.000). This deficiency, as similarly calculated in $TlAlSiO_4$ (Kyono *et al.*, 2000), reveals that the coordination polyhedron of Tl can be electrostatically established for the crystal structure by some other factors except for bond valence. The result of statistical analysis that the bond valences of lone pair cations are not only correlated with bond length but also with bond angles (Wang & Liebau, 1996) can provide a plausible explanation for the total bond valence contribution to the central Tl^+ cation. Therefore a reasonable explanation for the present deficiency in the total bond valence must await clarification of the relationship between the bond valence and the position of the lone pair with respect to the nucleus.

Orientation of inert-pair electrons in Tl-feldspar

The displacement of the central atom from the 'best' center of the ligand arrangement can be used as a measure of stereochemical activity for the s^2 lone pair of the central atom (Andersson & Åström, 1972). The direction of the displacement is assumed to be opposite to the orientation of the lone pair on this atom (Balic-Zunic & Makovicky, 1996). The TlO_9 polyhedron shows a remarkable difference in centroid–central atom distance with respect to MO_9 polyhedra in other feldspars (Table 6), and the cause for the deviation has apparently to be sought in the existence of the Tl $6s^2$ lone pair. The assumed orientation of the Tl lone-pair electrons calculated from the IVTON data points approximately in the [001] direction, which makes the following angles with the crystal axes: 112.40°, 90.00°, 4.48°. From the Tl atom through the centroid of TlO_9 polyhedron, the Tl $6s^2$ lone pair points between the three oxygen atoms, OA_2 and two OB (Fig. 3).

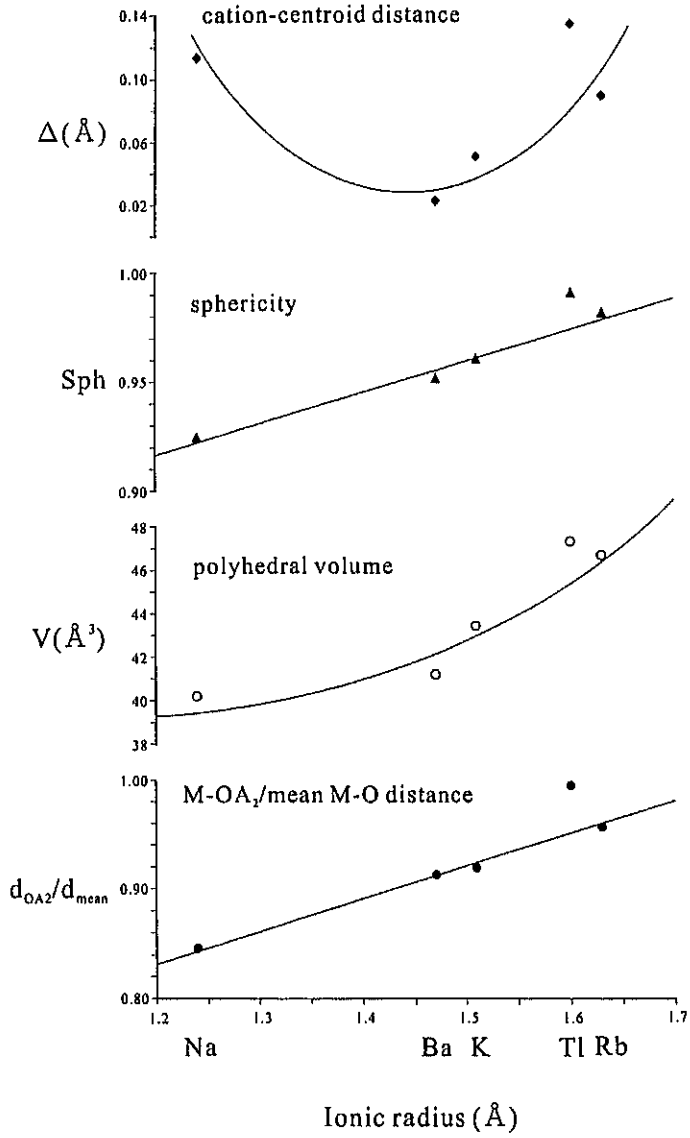

Fig. 4. Ionic radii for Na, Ba, K, Tl and Rb *vs.* their individual polyhedral parameters in feldspar. Values are taken from Table 4 and 6.

Implications for mineralogy

The synthesis and crystal structure of $TlAlSi_3O_8$ feldspar, together with Tl-leucite $TlAlSi_2O_6$ (Kyono *et al.*, 1999) and the chemical analogue of kalsilite, $TlAlSiO_4$ (Kyono *et al.*, 2000), provide us with new insights into the crystal chemistry of feldspars and potassium aluminosilicate minerals in general. When Tl^+ is geochemically offered to growing feldspars, the structure can easily accommodate this cation despite of expanded Tl polyhedra caused by the *inert-pair effect* of Tl $6s^2$ lone pair. Therefore, the present synthesis of $TlAlSi_3O_8$ has an implication for the occurrence of feldspars enriched in Tl^+ in nature. The rarity of Tl-rich feldspars in nature may be due not to crystal-chemical constraints but to geochemical ones. In any event, the low Tl contents reported in analyses of K-feldspars from granitic pegmatites (Černý, 1994) can be considered as an actual constituent of the feldspar structure.

Acknowledgements: The manuscript benefited from the insightful comments of A. Blasi, University of Milano, Italy. Structural data collection, EMPA and IR-absorption experiments were performed in the Chemical Analysis Center, University of Tsukuba, and N. Nishida and H. Nakazono are acknowledged for technical assistance. We are grateful to T. Balic-Zunic, University of Copenhagen, Denmark and I. Vickovic, University of Zagreb, Croatia for providing their IVTON program. We also want to thank P. Berlepsch, University of Copenhagen, Denmark who kindly provided the Tl standard of EMP analysis.

References

Andersson, S. & Åström, A. (1972): Solid state chemistry. Proceedings of the 5th Material Research Symposium, p. 3-14.

Badolov, S.T. & Rabinovich, A.V. (1966): The geochemistry of indium and thallium in the Karamazar ore region (the Uzbek and Tadzhik republics). *Geochem. Inter.*, **3**, 1095-1101.

Balic-Zunic, T. & Makovicky, E. (1996): Determination of the centroid or 'the best center' of a coordination polyhedron. *Acta. Cryst.*, **B52**, 78-81.

Balic-Zunic, T. & Vickovic, I. (1996): IVTON – program for the calculation of geometrical aspects of crystal structures and some crystal chemical applications. *J. Appl. Cryst.*, **29**, 305-306.

Berlepsch, P. (1996): Crystal structure and crystal chemistry of the homeotypes edenharterite ($TlPbAs_3S_6$) and jentschite ($TlPbAs_2SbS_6$) from Lengenbach, Binntal (Switzerland). *Schweiz. Mineral. Petrogr. Mitt.*, **76**, 147-157.

Brese, N.E. & O'Keeffe, M. (1991): Bond-valence parameters for solids. *Acta Cryst.*, **B47**, 192-197.

Brown, I.D. (1988): What factors determine cation coordination numbers? *Acta Cryst.*, **B44**, 545-553.

Černý, P. (1994): Evolution of feldspars in granitic pegmatites. *In* Parsons, I. (ed.), Feldspars and their reactions, *NATO ASI Series*, **C421**, 501-504, Kluwer, London.

Clark, A.M. (1993): Hey's mineral index: mineral species, varieties and synonyms, 3rd ed. Champman & Hall, London, 848 p.

Enraf-Nonius (1983): Structure determination package (SDP). Enraf-Nonius, Delft, The Netherlands.

Gasperin, M. (1971): Structure cristalline de $RbAlSi_3O_8$. *Acta Cryst.*, **B27**, 854-855.

Gillespie, R.J. (1972): Molecular geometry. Van Nostrand-Reinhold, London, 6-15.

Harlow, G.E. (1982): The anorthoclase structures: the effects of temperature and composition. *Am. Mineral.*, **67**, 975-996.

Heinrichs, H., Schulz-Dobrick, B., Wedepohl, K.H. (1980): Terrestrial geochemistry of Cd, Bi, Tl, Pb, Zn and Rb. *Geochim. Cosmochim. Acta*, **44**, 1519-1533.

Kimata, M., Saito, S., Shimizu, M., Iida, I., Matsui, T. (1996): Low-temperature crystal structures of orthoclase and sanidine. *N. Jb. Mineral. Abh.*, **171**, 199-213.

Koval'skii, A.M., Kotel'nikov, A.R., Bychkov, A.M., Chichagov, A.V., Samokhvalova, O.L. (2000): Synthesis and X-ray diffraction study of (K,Rb)-feldspar solid solution: preliminary data. *Geochem. Inter.*, **38**, 220-224.

Krogh, A.I.G., Krogh, A.E., Norby, P., Colella, C., de'Gennaro, M. (1991): Synthesis and structure of an ABW type thallium aluminosilicate. *Zeolites*, **11**, 149-154.

Kroll, H. & Ribbe, P.H. (1983): Lattice parameters, composition and Al,Si order in alkali feldspars. Feldspar Mineralogy, 2nd ed. *Reviews in Mineralogy*, **2**, 57-99.

Kyono, A., Kimata, M., Shimizu, M. (2000): The crystal structure of $TlAlSiO_4$. The role of the inert-pair effect in the exclusion of Tl from silicate minerals. *Am. Mineral.*, **85**, 1287-1293.

Kyono, A., Kimata, M., Shimizu, M., Saito, S., Nishida, N., Hatta, T. (1999): Synthesis of thallium-leucite ($TlAlSi_2O_6$) pseudomorph after analcime. *Mineral. Mag.*, **63**, 75-83.

Makovicky, E. & Balic-Zunic, T. (1998): New measure of distortion for coordination polyhedra. *Acta Cryst.*, **B54**, 766-773.

Mason, B. & Moore, C.B. (1982): Principles of geochemistry, 4th ed. Wiley, New York, 350 p.

Moore, P.B. & Araki T. (1976): Derbylite, $Fe_4^{3+}Ti_3^{4+}Sb^{3+}O_{13}(OH)$, a novel close-packed oxide structure. *N. Jb. Miner. Abh.*, **126**, 292-303.

Newnham, R.E. & Megaw, H.D. (1960): The crystal structure of celsian (barium feldspar). *Acta Cryst.*, **13**, 303-313.

Ribbe, P.H. (1963): A refinement of the structure of sanidinized orthoclase. *Acta Cryst.*, **B16**, 426-427.

Scambos, T.A., Smyth, J.R., McCormick, T.C. (1987): Crystal structure refinement of high-sanidine from the upper mantle. *Am. Mineral.*, **72**, 973-978.

Shannon, R.D. (1976): Revised effective ionic radii and systematic studies of interatomic distances in halides and chalcogenides. *Acta Cryst.*, **A32**, 751-768.

Sheldrick, G.M (1997): SHELXL-97. Program for refinement of crystal structures. Univ. Göttingen, Germany.

Smith, J.V. & Brown, W.L. (1988): Feldspar minerals, I. crystal structures, physical, chemical and microtextural properties, 2nd ed. Springer-Verlag, Berlin, 828 p.

Voncken, J.H.L., Konings, R.J.M., Van der Eerden, A.M.J., Jansen, J.B.H., Schuiling, R.D., Woensdregt, C.F. (1993): Crystal morphology and X-ray powder diffraction of the Rb-analogue of high sanidine, $RbAlSi_3O_8$. *N. Jb. Miner. Mh.*, **1993**, 10-16.

Wang, X. & Liebau, F. (1996): Studies on bond and atomic valences. I. Correlation between bond valence and bond angles in Sb^{III} chalcogen compounds: The influence of lone-electron pairs. *Acta Cryst.*, **B52**, 7-15.

West, A.R. (1999): Basic Solid State Chemistry, 2nd ed. John Wiley & Sons, LTD, 480 p.

Received 20 May 2000
Modified version received 26 February 2001
Accepted 12 March 2001

ELSEVIER

Marine Geology 173 (2001) 87–96

MARINE GEOLOGY
INTERNATIONAL JOURNAL OF MARINE GEOLOGY, GEOCHEMISTRY AND GEOPHYSICS

www.elsevier.nl/locate/margeo

Bathymetry of the Joban Seamount Chain, Northwestern Pacific

D.C.P. Masalu[a,*], Y. Ogawa[b], K. Kobayashi[c]

[a]*Ocean Research Institute, University of Tokyo, 1-15-1 Minamidai, Nakano-Ku, Tokyo 164, Japan*
[b]*Institute of Geoscience, University of Tsukuba, Tsukuba, Ibaraki 305, Japan*
[c]*Japan Marine Science and Technology Center, 2-15 Natsushima-cho, Yokosuka, Kanagawa 237, Japan*

Received 9 March 2000; accepted 1 December 2000

Abstract

We conducted a detailed bathymetric survey of a chain of seamounts named the Joban Seamount Chain (JSC), extending N53°E over a distance of about 394 km on the ocean floor located east of the southern Japan trench. We surveyed a total of nine seamounts in the JSC and obtained their precise shapes and locations. Two of the seamounts, Hitachi and Futaba seamounts, were newly found and named. Two seamounts, Ryofu and Futaba, seem to lie in another line parallel to the JSC, which probably also includes Katori seamount. Two other seamounts, Iwaki and Hitachi seamounts, were classified as guyots and Iwaki has a terrace on its northeastern side. Another isolated guyot, Daigo-Kashima, is located close to the southeast of Daiyon-Kashima seamount. The origin of the JSC remains uncertain owing to the lack of reliable ages, but formation at a congregation of hotspots or some combination with fissure eruption appear to be possible candidates. © 2001 Elsevier Science B.V. All rights reserved.

Keywords: Seamount; Guyot; Seamount chain; Bathymetry; Morphology

1. Introduction

We conducted a systematic geophysical survey of a seamount chain, Joban Seamount Chain (JSC), in the Northwestern Pacific during cruises KH90-1 and KH92-3 (Figs. 1 and 2) of the R/V *Hakuho-maru* of the Ocean Research Institute, University of Tokyo (Kobayashi, 1991, 1993) to map in detail its bathymetry using the SeaBeam system. The JSC is situated to the east of the southern end of the Japan Trench (Fig. 1), and extends N53°E over a distance of about 394 km, which is inconsistent with an origin from a fixed hotspot and models of motion of the early Mesozoic Pacific plate. The JSC is composed of eleven seamounts: (from northeast) Ryofu, Soma, Mizunagidori, Iwaki, Futaba, Hitachi, Daiyon-Kashima, Daisan-Kashima, Daini-Kashima, Katori, and Daiichi-Kashima seamounts. Except for Daiichi-Kashima and Katori seamounts, which were surveyed by the KAIKO project, the remaining nine seamounts were mapped by our cruises. To enhance our understanding of the JSC, we also surveyed a seamount called Daigo-Kashima, located about 74 km to the southeast of Daiyon-Kashima seamount (Fig. 1). The GEBCO chart and satellite geoid map indicate another seamount west of Daigo-Kashima, which was confirmed by our reconnaissance survey, but no other seamounts have been found in its northeastern extension in any available maps. Daigo-Kashima seamount is isolated and not obviously related to any chain.

* Corresponding author. Now at: Institute of Marine Sciences, University of Dar Es Salaam, P.O. Box 668, Mizingani Road, Zanzibar, Tanzania.
E-mail address: masalu@zims.udsm.ac.tz (D.C.P. Masalu).

0025-3227/00/$ - see front matter © 2001 Elsevier Science B.V. All rights reserved.
PII: S0025-3227(00)00162-6

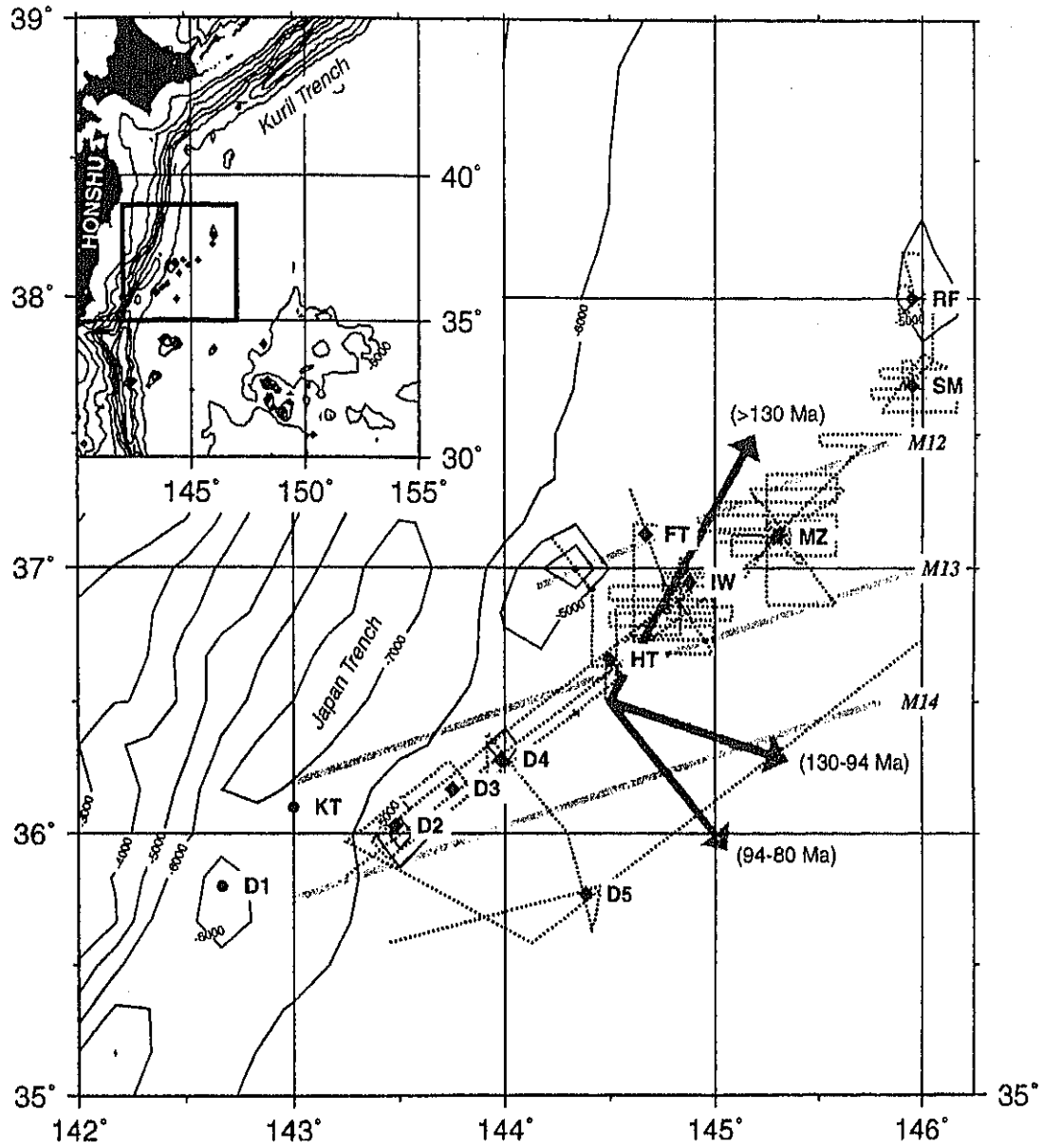

Fig. 1. Index map showing the Joban Seamount Chain (JSC) and neighboring seamounts. D1, Daiichi-Kashima; KT, Katori; D2, Daini-Kashima; D3, Daisan-Kashima; D4, Daiyon-Kashima; IW, Iwaki; FT, Futaba; MZ, Mizunagidori; RF, Ryofu; SM, Soma; D5, Daigo-Kashima. M12, M13 and M14 are magnetic anomaly lineations based on Nakanishi et al. (1989), which are equivalent to 137, 139 and 140 Ma, respectively, by the Harland et al. (1989) timescale. Bathymetry based on GEBCO (General Bathymetric Chart of the Oceans) data. Dotted lines are ship tracks of surveys during cruises KH90-1 (Leg 1) and KH92-3. Thick arrows show expected hotspot trends for the respective ages in brackets (Henderson, 1985), pointing towards the younging direction. Inset at upper right shows the JSC within its regional context.

The existence of JSC has been known (e.g. Charts 6312 and 1009 of the Hydrographic Department of Japan, 1968), but had not been surveyed in detail before our cruises. Cruise KH90-1 marked the first extensive geophysical survey on the JSC and yielded much new information about this seamount chain.

The purpose of this paper is to present the results of our surveys, including the precise locations and description of the morphology of the JSC seamounts

based on the newly obtained SeaBeam bathymetric data. These data are not only an important contribution in the mapping and understanding of the bathymetry of the world's ocean-floor, but also are important in unraveling the tectonics and evolution history of the Pacific plate, and in investigation of the origin of the abundant Northwestern Pacific seamounts.

1.1. Previous work on the Joban Seamount Chain

Several previous studies have been done on the JSC. Daiichi-Kashima seamount (Fig. 1) has been studied extensively under the KAIKO project (Le Pichon et al., 1987; Kobayashi et al., 1987; Cadet et al., 1987; Tani, 1986), which followed up a study by Mogi and Nishizawa (1980) and their findings of normal-faulted features parallel to the Japan trench. After reconstruction, the original seamount body was found to be a guyot (Tani, 1986). This seamount was found to be capped by about 100 m of limestone (Cadet et al., 1987; Pautot et al., 1987). The round flat top of the original seamount has a diameter of about 18 km with a depth of 3500 m. The eastern flank of Daiichi seamount is 7000 m deep, indicating that it is down in the trench slope, and its crestal height is about 3500 m. The cap limestones were studied by Konishi (1989), who concluded that they were of Albian age (ca. 112–97 Ma). Basalts from Daiichi-Kashima seamount were dated by the ^{40}Ar–^{39}Ar method to be about 120 Ma (Takigami et al., 1989). A paleomagnetic study of Daiichi-Kashima seamount suggests that a considerable part of its top is non-magnetic (Ueda, 1985), which is consistent with the presence of a limestone cap.

Katori seamount was also studied by the KAIKO project and was found to have two peaks with water depths of 4129 and 4241 m, with a narrow but flat crest (KAIKO I Research Group, 1985). The depth contour 4500 m is elongated in a direction of N60°W, which is roughly perpendicular to the trend of the JSC. The flank of Katori is about 7000 m, so its height is about 3000 m. A paleomagnetic study suggests that Katori seamount has different components of magnetization in its top and bottom parts (Ueda, 1985).

Daini-Kashima and Ryofu seamounts have been dated by the K–Ar method to be about 81 and 70–72 Ma, respectively (Ozima et al., 1970; Kaneoka, 1971). Uyeda and Richards (1966) studied the paleomagnetism of Ryofu seamount and concluded that its top part may be weakly or completely non-magnetized. Furthermore, paleomagnetic studies suggest that Mizunagidori seamount has a small magnetic anomaly (Tomoda, 1974; Masalu et al., 1993).

1.2. Seamounts in the Northwestern Pacific

The Northwestern Pacific seafloor is characterized by a great abundance of seamounts, most of which are guyots (Van Waasbergen and Winterer, 1993; Sager et al., 1993; Winterer et al., 1993; Lincoln et al., 1993). However, the origin of Northwest Pacific seamounts, which tend to align in chains similar to those known to have been formed by hotspot volcanism, is uncertain. Two hypotheses have been proposed for their origin. The first hypothesis, unusual widespread volcanic pulses, is based upon results from Deep Sea Drilling Project cores on intrusive and volcanogenic sediments. At least two widespread Cretaceous volcanic events have been postulated: Aptian to Cenomanian (~115–95 Ma) and Campanian-Maestrichtian (~80–65 Ma) (Rea and Vallier, 1983; Schlanger et al., 1981; Winterer, 1976; Tarduno et al., 1991). The second hypothesis, formation at a congregation of hotspots, is based on the trends of numerous seamount chains and their age data that have been used to document the motion of the Pacific plate relative to hotspots (Henderson, 1985; Duncan and Clague, 1985; Engebretson et al., 1985; Fleitout and Moriceau, 1992). These models suggest that most of the western Pacific seamounts were probably formed as the Pacific plate drifted over a congregation of hotspots presently located in the southeast Pacific, an area which has been dubbed the 'superswell' (McNutt and Fischer, 1987; McNutt et al., 1990; Wolfe and McNutt, 1991).

2. Results of the surveys

The bathymetric map of the JSC and nearby seamounts based on the data collected during cruises KH90-1 and KH92-3 is presented in Fig. 2. The map provides precise locations and shapes of the JSC seamounts.

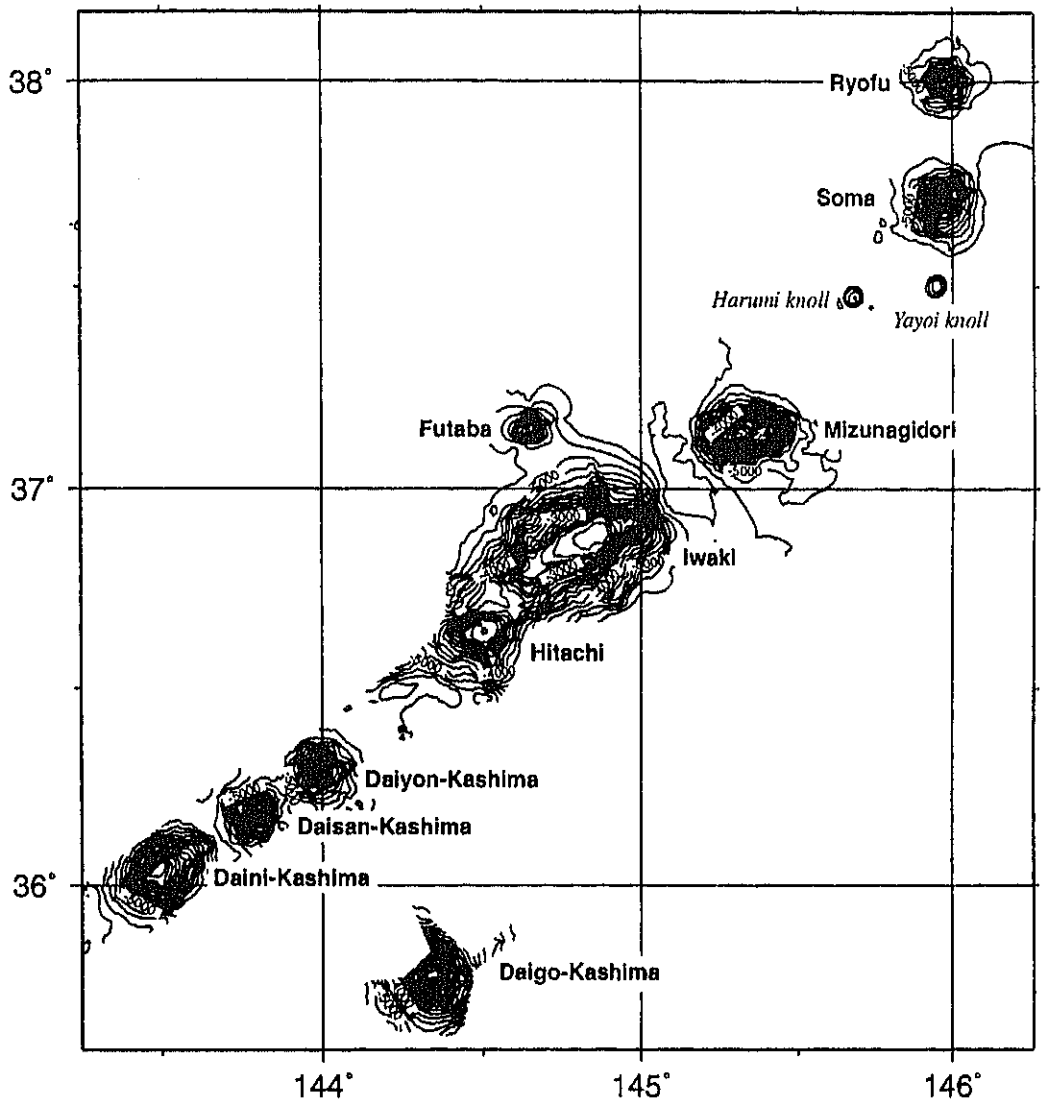

Fig. 2. Bathymetric map of the Joban Seamount Chain and nearby seamounts produced from SeaBeam bathymetric data collected by cruises KH90-1 and KH92-3. Contour interval is 100 m.

2.1. Topography and nomenclature of the Joban Seamount Chain

In the bathymetric chart No. 6312 (Tohoku Nippon) of the Hydrographic Department, Maritime Safety Agency of Japan (1968), five seamounts are shown to exist east of the Japan Trench at latitudes of 35°40′N–37°10′N, to the southeast off the coast of Ibaraki Prefecture (Japan). They are, from southwest to northeast, Daiichi-Kashima, Katori, Daini-Kashima, Daisan-Kashima and Daiyon-Kashima seamounts. We confirmed that these seamounts exist and form a linear chain (Fig. 2) trending N53°E (Kobayashi, 1991, 1993). This seamount chain extends further to the northeast to include Hitachi, Iwaki, Bosei, Soma and Ryofu seamounts. Another seamount, Daigo-Kashima, is located on the southeast of this line.

Soma was named by the scientific party onboard cruise KH92-3 (Kobayashi, 1993) after a Pacific coast city in the north of Joban District, northeastern Honshu, Japan. The name 'Bosei' is after chart No. 1009; however, the name 'Mizunagidori' was first proposed by Tomoda (1974) for this seamount when

Table 1
Main characteristics of seamounts in the Joban Seamount Chain

Seamount	Location	Crestal depth (m)	Flank depth (m)	Height (m)	Diameter (km)	Volume (km^3)	Remarks
Ryofu	37°59.9′N 145°58.5′E	2880	5360	2400	18	215	Conical seamount
Soma	37°42.9′N 145°57.5′E	2180	5400–5500	~3200	24	555	Crestal ridge trending NE
Mizunagidori	37°08.8′N 145°17.5′E	2300	5400–5800	~3500	33	1069	Sharp ridge trending N60°E, oblate shape in W–E direction
Futaba	37°08.8′N 144°39.0′E	3600	~5400	~2000	14	110	Small, conical, found in cruise KH90-1
Iwaki	36°53.0′N 144°46.0′E	1700	~5400	~3700	60	2282	Corrected position, guyot, top inclines SW, oblate shape along N60°E
Hitachi	36°39.5′N 144°29.5′E	2360	5660	3300	18	488	Guyot found in cruise KH90-1
Daigo-Kashima	35°48.0′N 144°21.0′E	1500	5600	4100	40	1144	Classified as guyot
Daiyon-Kashima	36°17.6′N 143°59.0′E	2800	5500	2600	24	341	Conical seamount
Daisan-Kashima	36°11.0′N 143°47.0′E	3100	5800	2700	11	315	Conical star-fish seamount
Daini-Kashima	36°03.0′N 143°39.0′E	2800	5800	3000	30	626	Conical seamount
Yayoi Knoll	37°30.2′N 145°57.0′E	4840	5540	~700	7.5	10	Conical, sharp crest
Harumi Knoll	37°29.0′N 145°41.0′E	4750	5500	~830	7.5	12	Conical, sharp crest

he surveyed it in 1969, although later detailed work by Murauchi and others using the R/V *Bosei-Maru* proposed the name 'Bosei', which has been adopted by the Ocean Topography Nomenclature Committee. Two knolls were discovered on the area between Mizunagidori and Soma seamounts and were named Harumi and Yayoi by the scientific party onboard cruise KH92-3. Hitachi seamount was newly found during cruise KH90-1 and was named by the scientific party onboard Leg 1 of Cruise KH90-1, after the nearest city in the east coast of northeastern Honshu, Japan (Kobayashi, 1991).

We found that Iwaki seamount is not situated at the location shown in map No. 6312 but slightly to the southeast and just on the line of the chain (Kobayashi, 1991). Moreover, in the Hydrographic Department maps, Iwaki seamount is shown to have two peaks. We confirmed the existence of only one peak on this seamount (Fig. 2). We found a peak to the northwest of Iwaki seamount, but it does not seem to be a part of this seamount. Rather, it seems to be an independent seamount and was named 'Futaba' by the scientific party onboard Leg 1 of cruise KH90-1, after the geological town in Fukushima Prefecture which yielded a Dinosaur remain, 'Futaba-Suzuki-Ryu'.

The name 'Joban' was proposed by the scientific

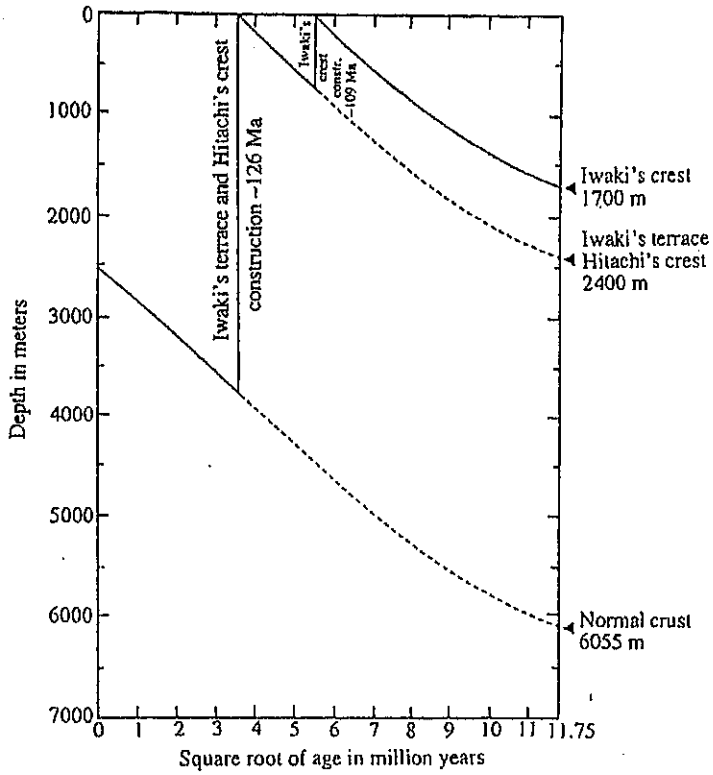

Fig. 3. Estimation of ages of guyot seamounts. Backtracking of the flat top and terrace of Iwaki and Hitachi seamounts to sea-level against a crustal age depth curve (Parsons and McKenzie, 1977).

party onboard Leg 1 of cruise KH90-1 for this linear chain of seamounts trending along N53°E direction, from Daiichi-Kashima to Soma seamount (Kobayashi, 1991, 1993). This name is after the nearest Japanese old local territory name. Futaba and Ryofu seamounts lie slightly out of the JSC (Fig. 2). They seem to lie in another line nearly parallel to the JSC that probably also includes Katori seamount as its southwestern end (Fig. 1).

2.2. *Seamount morphology*

The JSC is composed of both peaked and flat-topped (guyot) seamounts (Fig. 2). The principle morphological characteristics of the JSC seamounts are summarized in Table 1. Three seamounts, Iwaki, Hitachi and Daigo-Kashima have flat tops and were classified as guyots (Kobayashi, 1991, 1993). Ryofu, Soma and Mizunagidori seamounts have crestal ridges that are oriented in the northeast direction, which is the trend of the JSC. Ryofu, Soma, Daiyon-Kashima, Daisan-Kashima, Daigo-Kashima and Futaba seamounts and the Harumi and Yayoi knolls have nearly round plan view, thus they are conical. On some of the seamounts studied, i.e. Ryofu, Soma, Mizunagidori, Hitachi, Daisan-Kashima, Daini-Kashima, Daigo-Kashima and Futaba, several ridges that run in different directions down the slopes of the seamounts can be observed. Some of these ridges are separated by cliffs, for example, on Daisan-Kashima and Daini-Kashima seamounts. The ridges may imply exposure of ancient lava flows.

Mizunagidori seamount has an oblate shape elongated in the east–west direction and has two peaks. The smaller peak, which is located at the east, has a crestal depth of 2700 m. A moat with depths ranging between 5800 and 5900 m surrounds Mizunagidori seamount on the southwestern side (Fig. 2).

Iwaki seamount is elongated along the trend of the JSC. The flat top plain of Iwaki, which is at a depth of 1700 m, is also very elongated. The 2000 m contour

line has a southwest–northeast diameter of about 21 km, whereas the northwest–southeast diameter is only about 9 km. A gentle slope spreads from the flat top, down in the southwest direction. The shallowest part of the crest of Iwaki seamount is located at the northeastern side. Based upon the steep slope at northeast below the flat crest, we suggest that this might be a reef, which was probably well developed on a dominant wind side. After the steep crestal slope on the northeast side, a terrace or level bench in the flank of a seamount exists at about 2400 m. Hitachi seamount, which has a flat top at a depth of 2400 m, is located very close to Iwaki seamount and the two share contours deeper than 3500 m (Fig. 2).

3. Discussion

3.1. Origin of the Joban Seamount Chain

The trend of the JSC (Figs. 1 and 2) is oblique to the N68°E trend of magnetic anomaly lineations of the surrounding ocean-floor. Hence it is unlikely that the JSC formed on a spreading center. The trend of the JSC is also inconsistent with the expected hotspot trend (Fig. 1) for the available dates of the seamounts, which calls for further investigation of the chain. Other viable possible origins of the JSC are: formation at a single stationary hotspot, which requires evidence of age progression along the chain, fissure eruption along a weak zone, amorphous volcanic pulse, which requires evidence of a wide spread of volcanic products of the same age, and ridge–hotspot interaction (Morgan, 1978; Schilling, 1991), which can produce seamount chains with orientations intermediate between the orientation of the ridge and a fixed intraplate hotspot. As in the case of formation of a seamount chain at a single stationary hotspot, seamount chains produced by the ridge–hotspot interaction require evidence of a general age progression along the chain. Unfortunately, only few radiometric dates are available for the JSC seamounts.

3.1.1. Age estimations for guyot seamounts

A flat top and a level bench of a seamount are geomorphic features that are formed at or near sea-level (Hess, 1946; Hamilton, 1956; Tucholke and Smoot, 1990). Approximate dates of these features can be derived by backtracking them to sea-level against an appropriate age–depth curve (Tucholke and Smoot, 1990).

Iwaki and Hitachi seamounts reside on 138 and 139 Ma crust, respectively (Fig. 1). Observed seafloor depth around these seamounts is about 5800 m whereas the expected depth based on the crustal age–depth relationship curve (Parsons and McKenzie, 1977) is about 6055 m. The discrepancy between the two values can be accounted for by sediment thickness. After backtracking Iwaki's crest (1700 m) in time, it was found to be at sea level when the crust upon which Iwaki resides was about 29 My old (Fig. 3); so, the crest was constructed about 109 Ma. Similarly, Iwaki's terrace (2400 m) was at sea level when the crust was about 12 My old; therefore, it was constructed about 126 Ma. Applying the same method we obtained, an age of about 127 Ma for Hitachi seamount (Fig. 3). These results suggest that the two seamounts formed approximately simultaneously about 127–126 Ma, and about 109 Ma Iwaki's crest was constructed, presumably of limestone. These ages are close to the ^{40}Ar–^{39}Ar age of 120 Ma for basaltic samples from nearby Daiichi-Kashima guyot (Takigami et al., 1989).

The terrace on the northeast of Iwaki seamount is at the same level of 2400 m as the southwestern part of the flat top of this seamount, which dips gently to the southwest (Fig. 2). The 2400-m level is also consistent with the flat top of Hitachi seamount (Fig. 2) suggesting that the two seamounts were truncated at sea-level along their present 2400-m level about 127–126 Ma with subsequent reef-growth on Iwaki until about 109 Ma.

3.1.2. Possible origin of the seamounts

A study of the flat top of Hitachi seamount shows that for level contours from 2600 to 2800 m (Fig. 2), the northwest–southeast diameters are shorter than the northeast–southwest diameters. This may suggest that the primary body of this seamount is elongated along the northeast–southwest consistent with the trend of the JSC and Iwaki seamount.

The two seamounts appear to be very similar morphologically, which suggests that they were probably formed by the same mechanism. Their general elongation along the trend of the JSC may suggest a fissure eruption origin. Rupture of the lithosphere,

which caused the fissure eruption may have been caused by tensions that probably developed in it during a Mid-Cretaceous rotation of the Pacific plate, which has been postulated by Jarrard and Sasajima (1980). A similar mechanism of origin has been proposed for seamounts in other locales such as the Line Island chain in the central Pacific (Sager and Keating, 1984) when the Pacific plate changed its drifting direction at about 43 Ma. Another excellent example of tensional ridge volcanism is the Puka Puka ridges (Lynch, 1999).

However, careful investigation of Fig. 2 reveals that the trends of some of the seamounts, e.g. Hitachi, Iwaki, Mizunagidori and Soma, particularly their crestal part, seems to be slightly different by about 10–20° from the trend of the JSC. The seamounts look en-echelon, which can be seen also in ridge–hotspot interaction as in the Musicians seamounts. Since the ocean floor upon which the seamounts were built was fairly young at the time of volcanism, the model of formation of the JSC by ridge–hotspot interaction also seems to be viable.

On the other hand, paleomagnetic study of the JSC suggests that Iwaki and Hitachi seamounts may be Early-Cretaceous in age, consistent with our age estimations based on depth, whereas the rest of the studied seamounts appear to be Mid- to Late-Cretaceous in age (Masalu et al., 1993). Because Iwaki and Hitachi seamounts (guyots) are located in the middle of the JSC (Fig. 2), this argues against the formation of the JSC by a single stationary hotspot as well as by ridge–hotspot interaction. This variation of paleomagnetic ages also argues against the hypothesis of amorphous volcanic pulses, which requires evidence of widespread volcanic products of the same age. Furthermore, the hypothesis of amorphous volcanic pulses cannot explain satisfactorily why seamounts in the JSC are aligned in a linear chain. The observation that Ryofu, Futaba and Katori seamounts (Figs. 1 and 2) appear to lie in another linear chain parallel to the JSC and the inferred mixing of volcanic products of different ages in the chain may suggest formation of the JSC at a congregation of hotspots. Our data set, in particular with the lack of sufficient reliable dates for the JSC seamounts, does not allow us to categorically disprove or accept any of the hypotheses discussed above; but as far as the origin of the JSC is concerned, we are in favor of formation at a congregation of hotspots, or some combination with ridge–hotspot interaction. The origin of the JSC will only be resolved with the availability of sufficient reliable ages of the chain.

4. Summary and conclusions

We have mapped the bathymetry and confirmed the existence of a linear chain of seamounts trending along N53°E, located east of the Japan trench. This seamount chain was named 'Joban' by the scientific party on board Leg 1 of cruise KH90-1. Our results provide precise shapes and locations of the JSC seamounts. We surveyed a total of nine seamounts in the JSC, two of which, Hitachi and Futaba seamounts, were newly found and named by Leg 1 of cruise KH90-1. Two seamounts, Ryofu and Futaba seamounts, appear to lie in another line parallel to the JSC that probably also includes Katori seamount. Two seamounts, Iwaki and Hitachi seamounts, are guyots and Iwaki has a terrace on its northeast side. These seamounts were probably formed approximately simultaneously about 127–126 Ma.

The JSC appears not to have been formed by a single hotspot, although our data, in particular the absence of sufficient reliable dates for the JSC seamounts, do not allow us to unequivocally disprove or accept any of the four possible hypotheses of origin discussed: congregation of hotspots, amorphous volcanic pulses, fissure eruption and ridge–hotspot interaction; but we are in favor of origin at a congregation of hotspots, or some combination with ridge–hotspot interaction.

Acknowledgements

We would like to express our sincere thanks to the captain, staff, crew and the scientific party onboard Cruises KH90-1 and KH92-3 of the R/V *Hakuho-maru* (Ocean Research Institute/University of Tokyo) for the invaluable assistance and cooperation they accorded us during the surveys. We also wish to express our special thanks and gratefully acknowledge the constructive review comments by David J.W. Piper (editor-in-chief), Rodey Batiza, Jean Paul

Cadet, Nicolus Binard, Michael A. Arthur, and an anonymous reviewer. This study has been supported partly by the Japan Society for the Promotion of Science (JSPS) through a fellowship to D.C.P.M. GMT-System (Wessel and Smith, 1991) was used in preparing most of the figures in this manuscript.

References

Cadet, J.-P., Kobayashi, K., Lallemand, S., Jolivet, L., Aubouin, J., Boulegue, J., Dubois, J., Hotta, H., Ishii, T., Konishi, K., Niitsuma, N., Shimamura, H., 1987. Deep submersible dives in the Japan and Kuril Trenches. Earth Planet. Sci. Lett. 83, 313–327.

Chart number 1009 (Tohoku), 1968. Hydrographic Department, Maritime Safety Agency of Japan.

Chart number 6312 (Tohoku), 1968. Hydrographic Department, *Maritime Safety Agency of Japan.*

Duncan, R.A., Clague, D.A., 1985. Pacific plate motion recorded by linear volcanic chains. In: Nairn, A.E.M., Stehli, F.G., Uyeda, S. (Eds.), The Ocean Basins and Margins, vol. 7A. Plenum Press, New York, pp. 89–121.

Engebretson, D.C., Cox, A., Gordon, R.G., 1985. Relative motions between oceanic and continental plates in the Pacific basin. GSA Special Paper, Geological Society of America, 206, 3300 Penrose Place, P.O. Box 9140, Boulder, CO 80301, USA.

Fleitout, L., Moriceau, C., 1992. Short-wavelength geoid, bathymetry and the convective pattern beneath the Pacific Ocean. Geophys. J. Int. 110, 6–28.

Hamilton, E.L., 1956. Sunken Islands of the mid-Pacific mountains. *Mem. Geol. Soc. Am. 64, 97 pp.*

Harland, W.B., Armstrong, R.L., Cox, A.V., Craig, L.E., Smith, A.G., Smith, D.G., 1989. A Geologic Time Scale 1989. Cambridge University Press, New York, 263 pp.

Henderson, L.J., 1985. Motion of the Pacific plate relative to the hotspots since the Jurassic and model of oceanic plateaus of the Farallon plate. PhD dissertation, Northwestern University, Evanston, IL, 321 pp.

Hess, H.H., 1946. Drowned ancient islands of the Pacific Basin. Am. J. Sci. 244, 772–791.

Jarrard, R.D., Sasajima, S., 1980. Paleomagnetic synthesis for southeast Asia: constraints on plate motions. In: Hayes, D.E. (Ed.). The Tectonic and Geologic Evolution of Southeast Asian Seas and Islands. Geophys. Monogr. Ser., vol. 23. AGU, Washington, DC, pp. 293–317.

KAIKO 1 Research Group, 1985. Topography of Trenches and Troughs Around Japan. University of Tokyo Press, Tokyo.

Kaneoka, I., 1971. K–Ar ages of seamounts along the Japan trench and the effect of acid leaching on the K–Ar age of a dredge submarine rock. Geochem. J. 5, 113–120.

Kobayashi, K., Cadet, J.-P., Aubouin, J., Boulegue, J., Dubois, J., Von Huene, R., Jolivet, L., Kanazawa, T., Kasahara, J., Koizumi, K., Lallemand, S., Nakamura, Y., Pautot, G., Suyehiro, K., Tani, S., Tokuyama, H., Yamazaki, T., 1987. Normal faulting of the Daiichi-Kashima Seamount in the Japan Trench revealed by the KAIKO I cruise, Leg 3. Earth Planet. Sci. Lett. 83, 257–266.

Kobayashi, K., 1991. Preliminary Report of the Hakuho Maru Cruise KH90-1, Ocean Research Institute University of Tokyo, 174 pp.

Kobayashi, K., 1993. Preliminary Report of the Hakuho Maru Cruise KH92-3, Ocean Research Institute University of Tokyo, 137 pp.

Konishi, K., 1989. Limestone of the Daiichi Kashima Seqmount and the fate of a subducting guyot: fact and speculation from the Kaiko "Nautile" dives. Tectonophysics 160, 249–265.

Le Pichon, X., Kobayashi, K., Cadet, J.-P., Iiyama, T., Nakamura, K., Pautot, G., Renard, V., The KAIKO scientific crew, 1987. Project KAIKO — introduction. Earth Planet. Sci. Lett. 83, 183–185.

Lincoln, J.M., Pringle, M.S., Premoli-Silva, I., 1993. Early and late Cretaceous volcanism and reef-building in the Marshall Islands. In: Pringle, M.S., Sager, W.W., Sliter, W.V., Stein, S. (Eds.), The Mesozoic Pacific: Geology, Tectonics and Volcanism. Geophys. Monogr. Ser., vol. 77. AGU, Washington, DC, pp. 279–305.

Lynch, M.A., 1999. Linear ridge groups: evidence for tensional cracking in the Pacific Plate. J. Geophys. Res. 104, 29,321–29,333.

Masalu, D.C.P., Tamaki, K., Kobayashi, K., 1993. Paleomagnetism of the Joban Seamount Chain, Northwestern Pacific. J. Geomag. Geoelectr. 45, 503–534.

McNutt, M.K., Fischer, K.M., 1987. The south Pacific superswell. In: Keating, B.H., Fryer, P., Batiza, R., Boehlert, G.W. (Eds.), Seamounts, Islands and Atolls. Geophys. Monogr. Ser., vol. 43. AGU, Washington DC, pp. 25–34.

McNutt, M.K., Winterer, E.I., Sager, W.W., Natland, J.H., Ito, G., 1990. The Darwin Rise: a Cretaceous superswell?. Geophys. Res. Lett. 17, 1101–1104.

Mogi, A., Nishizawa, K., 1980. Breakdown of a seamount on the slope of the Japan Trench. Proc. Jpn. Acad. 56, 257–259.

Morgan, W.J., 1978. Rodrigues, Darwin, Amsterdam, a second type of hotspot island. J. Geophys. Res. 83, 5355–5360.

Nakanishi, M., Tamaki, K., Kobayashi, K., 1989. Mesozoic magnetic anomaly lineations and seafloor spreading history of the Northwestern Pacific. J. Geophys. Res. 94, 15,437–15,462.

Ozima, M., Kaneoka, I., Aramaki, S., 1970. K–Ar ages of submarine basalts dredged from seamounts in the Western Pacific area and discussion of oceanic crust. Earth Planet. Sci. Lett. 8, 237–249.

Parsons, B., McKenzie, D., 1977. Mantle convection and the thermal structure of the plates. J. Geophys. Res. 83, 4485–4496.

Pautot, G., Nakamura, K., Huchon, P., Angelier, J., Bourgois, J., Fujioka, K., Kanazawa, T., Nakamura, Y., Ogawa, Y., Seguret, M., Takeuchi, A., 1987. Deep-sea submersible survey in the Suruga, Sagami and Japan Trenches: preliminary results of the 1985 KAIKO cruise Leg 2. Earth Planet. Sci. Lett. 83, 300–312.

Rea, D.K., Vallier, T.L., 1983. Two Cretaceous volcanic episodes in the western Pacific Ocean. Geol. Soc. Am. Bull. 94, 1430–1437.

Sager, W.W., Keating, B.H., 1984. Paleomagnetism of Line Islands seamounts: evidence for late Cretaceous and early tertiary volcanism. J. Geophys. Res. 89, 11,135–11,151.

Sager, W.W., Duncan, R.A., Handschumacher, D.W., 1993. Paleomagnetism of the Japanese and Marcus–Wake Seamounts, Western Pacific Ocean. In: Pringle, M.S., Sager, W.W., Sliter, W.V., Stein, S. (Eds.), The Mesozoic Pacific: Geology, Tectonics and Volcanism. Geophys. Monogr. Ser., vol. 77. AGU, Washington, DC, pp. 401–435.

Schlanger, S.O., Jenkyns, H.C., Premoli-Silva, I., 1981. Volcanism and vertical tectonics in the Pacific basin related to global Cretaceous transgressions. Earth Planet. Sci. Lett. 52, 435–449.

Schilling, J.-G., 1991. Fluxes and excess temperatures of mantle plumes inferred from their interaction with migrating mid-ocean ridges. Nature 352, 397–403.

Tarduno, J.A., Sliter, W.V., Kroenke, L., Leckie, M., Mayer, H., Mahoney, J.J., Musgrave, R., Storey, M., Winterer, E.L., 1991. Rapid formation of Ontong Java Plateau by Aptian mantle plume volcanism. Science 254, 399–403.

Takigami, Y., Kaneoka, I., Ishii, T., Nakamura, Y., 1989. ^{40}Ar–^{39}Ar ages of igneous rocks recovered from Diichi-Kashima and Erimo seamounts during the KAIKO project. Palaeogeogr. Palaeoclimatol. Palaeoecol. 71, 71–81.

Tani, S., 1986. Detailed topographic study of the Daiichi-Kashima seamount. Paleogeogr. Paleoclimatol. Paleoecol. 71, 31–48.

Tomoda, Y., 1974. Reference Book for Gravity, Magnetic and Bathymetric Data of the Pacific Ocean and Adjacent Seas, 1963–71. University of Tokyo Press, Tokyo, 158 pp.

Tucholke, B., Smoot, N.C., 1990. Evidence for age and evolution of Corner seamounts and Great Meteor Seamount Chain from multibeam bathymetry. J. Geophys. Res. 95, 17,555–17,569.

Ueda, Y., 1985. Geomagnetic study on seamounts Daiiti-Kashima and Katori with special reference to a subduction process of Daiiti-Kashima. J. Geomag. Geoelectr. 37, 601–625.

Uyeda, S., Richards, M.L., 1966. Magnetization of four Pacific seamounts near the Japanese Islands. Bull. Earthquake Res. Inst., Univ. Tokyo 44, 179–213.

van Waasbergen, R.J., Winterer, E.L., 1993. Summit geomorphology of western Pacific guyots. In: Pringle, M.S., Sager, W.W., Sliter, W.V., Stein, S. (Eds.), The Mesozoic Pacific, Geology, Tectonics and Volcanism. Geophys. Monogr. Ser., vol. 77. AGU, Washington, DC, pp. 335–366.

Wessel, P., Smith, W.H.F., 1991. Free software helps map and display data. EOS Trans. AGU 72, 445–446.

Winterer, E.L., Duncan, R.A., McNutt, M.K., Natland, J.H., Premoli-Silva, I., Sager, W.W., Sliter, W.V., Van Waasbergen, R., Wolfe, C.J., 1993. Cretaceous guyots in the northwest Pacific: an overview of their geology and geophysics. In: Pringle, M.S., Sager, W.W., Sliter, W.V., Stein, S. (Eds.), The Mesozoic Pacific, Geology, Tectonics and Volcanism. Geophys. Monogr. Ser., vol. 77. AGU, Washington, DC.

Winterer, E.L., 1976. Anomalies in the tectonic evolution of the Pacific. In: Sutton, G.H., Manghnani, M.H., Moberly, R. (Eds.), The Geophysics of the Pacific Ocean Basin and its Margin. Geophys. Monogr. Ser., vol. 19. AGU, Washington, DC, pp. 269–278.

Wolfe, C.J., McNutt, M.K., 1991. Compensation of Cretaceous seamounts of the Darwin Rise, northwest Pacific Ocean, . J. Geophys. Res. 96, 2363–2374.

Pore structure of sheared coals and related coalbed methane

Huoyin Li · Yujiro Ogawa

Abstract Coalbed methane is considered to be one of the major contributors to global warming. Geological prospecting of the rich-storage zone of methane is an important precondition for gas recovery projects. Shear zones along coal seams have long been considered as a major place where gas outbursts occur during mining, but they also have a positive aspect in coalbed methane prospecting and production because of their great quantity of fractures and high methane content. Mercury penetrating experiments on a series of variously sheared coal samples from the Pingdingshan coalfield, China, were performed. The results showed that tectonically sheared coals possess three to eight times more porosity and two to ten times more specific surface area than their normal counterparts Moreover, brittlely deformed coals possess larger average fracture apertures representing a good condition for methane extraction, whereas ductilely deformed coals show a fracture aperture even smaller than normal coals, which can explain why intensely sheared coals become difficult for methane extraction. The occurrence of a large number of tectonic fractures in a shear zone will make it easier for an artificial fracture to increase the permeability of coals in methane production. Therefore, except for locally ductile deformation areas, shear zones along coal seams are the best source and reservoir for methane gas production and, if this methane is extracted, it will help not only the reservoir but also protect the earth against global warming.

Received: 3 January 2001 / Accepted: 20 March 2001
Published online: 28 June 2001
© Springer-Verlag 2001

H. Li (✉)
Doctoral Program in Geoscience,
University of Tsukuba, Tsukuba 305-8571, Japan
E-mail: lhy@arsia.geo.tsukuba.ac.jp
Tel.: +81-298-536139
Fax: +81-298-519764

Y. Ogawa
Institute of Geoscience, University of Tsukuba,
Tsukuba 305-8571, Japan

Keywords Global warming · Coalbed methane (CBM) · Shear zone · Mercury penetration

Introduction

Coalbed methane released from coal mines, particularly from underground mining, is presumed to be one of the major contributors to global warming (Fig. 1). To effectively control the emission of greenhouse gas, and make good use of methane gas as an energy source, various studies for recovery and utilization of coalbed methane are under way all over the world (John 2000). Shear zones along coal seams, which can contain a large number of fractures and therefore much gas, have long been looked upon as a major factor for a catastrophic failure or "outburst" of gas and coal in coalfields during coal extraction (Shepherd and others 1981; Dumpleton 1990; Peng 1991; Beamish and Crosdale 1998). Shear zones are widespread in various ranks of coal seams, and are commonly named detachments, bedding plane faults and soft-coal bands (Yu and Li 1981; Frodsham and Gayer 1999). The mechanism of formation has been argued to be either a flexural slip process or major thrusting corresponding to regional compressive stress (Bustin 1982; Kang and Li 1995; Frodsham and Gayer 1999). Because a shear zone is generally distributed in the middle of the seam (Fig. 2), a large volume of methane within the shear zone could be prevented from escaping by the surrounding hard coals which are characterized by unusually low vertical permeability and thus similar to the cap rock of the conventional natural gas reservoirs. In mining production, coalbed methane (CBM) has been considered a type of disaster gas, which greatly threatens safe production in coal mines, and thus it has been released to the atmosphere for a long time. This situation must, to a certain extent, have aggravated global warming because the methane gas has a greater greenhouse effect than carbon dioxide gas (John 2000). From the geological point of view, important observations about outbursts accepted by most researchers are: (1) most of the outbursts occur in the sheared coal layers within a tectonically deformed zone (Shepherd and others 1981; Cao 1994; Bibler and others 1998), and (2) outburst coals contain three to ten times more methane than non-deformed coals (Shepherd and others 1981; Hargravs 1983;

Li 1995). In addition, the comparison of gas content between shear zone and normal coal also reflects the fact that sheared coals contain more gas compared with normal coals (Table 1). Hokao (1982) proposed that geologically sheared (kneaded) coals can give out ten times more gas than hard coals when they are broken to pieces.
Although the occurrence of a shear zone within a coal seam represents a mining disaster, it might be regarded more positively in coalbed methane prospecting and production because of the great quantity of fractures and higher methane content. From the gas production point of view, the most important structural features of coals are the storage capacity and permeability. For coalbed methane extraction, knowledge of the properties of fractures is essential for planning production and exploration because of the fractures' influence on recovery of methane and the local and regional flow of methane. The shear zone along a coal seam, because of its extensively developed fractures compared with surrounding normal hard coal, which is hardly destroyed and thus plays a role in sealing gas, might be considered a potentially significant coalbed methane reservoir or a "gas river" (Fig. 3).
To explain the influence of tectonic pressure on coal properties, measurements were made on a series of coal samples exhibiting various degrees of tectonic deformation. Field work was also undertaken. Coal samples were collected from the bedding shear zones where outbursts frequently occur and from the normal hard coal where outbursts occur infrequently. Mercury porosimetry studies on coal samples have been performed to gain a better understanding of: (1) porosity and specific surface area, which reflect storage capacity, and (2) average fracture aperture, which indicates the permeability of coals.

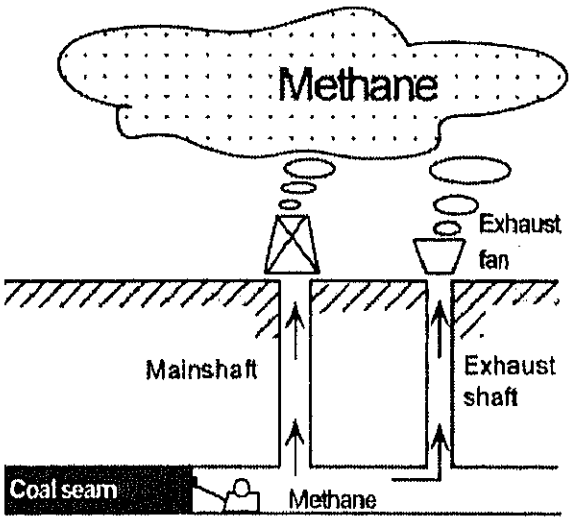

Fig. 1
Diagrammatic illustration of an underground coal mine where a great quantity of coalbed methane is released to the atmosphere during coal extraction

Geological setting of the samples

Coal samples were taken from the lower Permian Wu coal seam of the Pingdingshan coalfield in Henan Province, China. In the coalfield, the main coal-bearing measures are dominated by strike-parallel compressional structures,

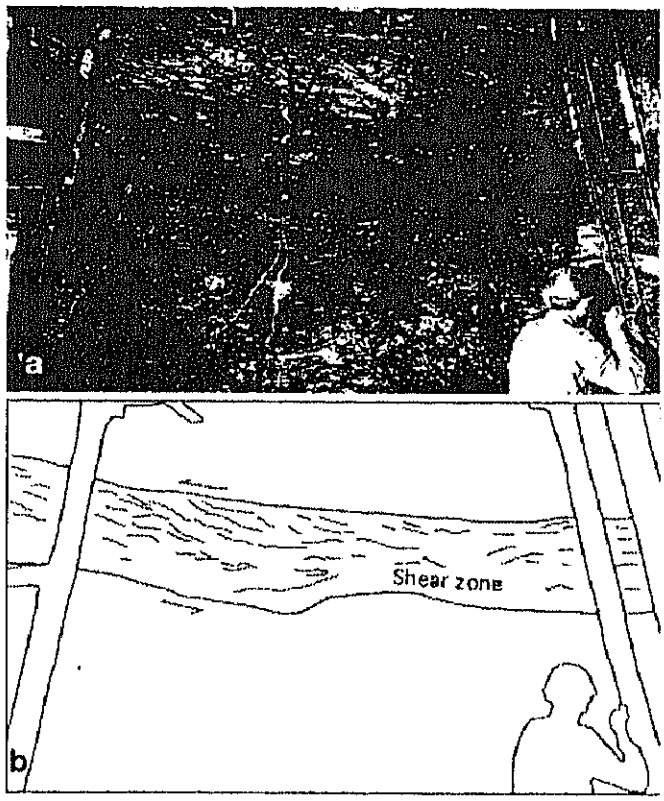

Fig. 2
Photograph showing a bedding shear zone, which is generally distributed in the middle of the coal seam and characterized by a great quantity of fractures (*dark band* is a bedding shear zone, indicating a sinistral shear sense)

Table 1
Comparison of coalbed methane contents between sheared coals and their normal counterparts in an underground mine (Pingdingshan no. 10 mine, unpublished data)

Locality	Depth (m)	Thickness (m) seam/shear zone	CBM content in shear zone (m^3/t)	CBM content in normal coal (m^3/t)
Wu 12130	487	5.8/1.8	11.83	7.44
Wu 12130	484	5.5/1.9	12.21	6.34
Wu 14131	483	5.4/0.9	12.15	6.52
Wu 14131	485	5.3/1.1	12.22	7.21
Wu 20080	511	5.6/2.5	13.42	8.22
Wu 20080	508	5.7/2.3	14.51	8.56
Wu 20090	520	5.4/0.8	13.87	8.34
Wu 20090	521	5.5/0.6	12.98	8.05

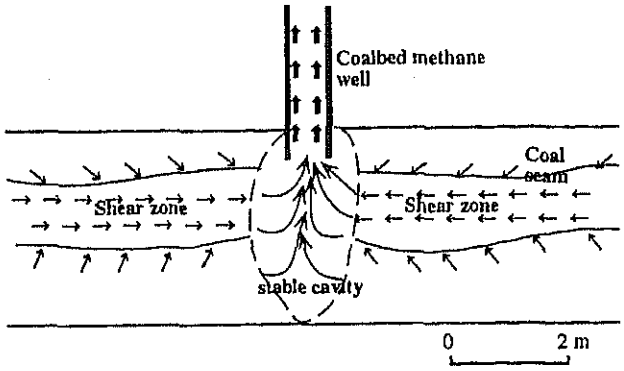

Fig. 3
Model of methane flow in a coal seam with a shear zone which becomes a "gas river" during methane extraction

which have been interpreted to have occurred during the Indosinian (late Triassic) orogenic compression (Geological Survey of Henan Province 1990). Within the Wu seam, there appears to be a widespread bedding shear zone where more than 90% of the outbursts of gas occur, the largest of which displaced 54 t of coal and expelled 3,487 m^3 of methane. The gas content of outburst coal was estimated at 64.57 m^3/t of coal, whereas the gas content of normal coal was about 10 m^3/t of coal. The bedding shear zone has traditionally been called a "soft-coal band" by mining workers in the Pingdingshan coal district because of the absence of bedding planes and the occurrence of friable coals with a thickness of 0.9–2.5 m. According to the underground mining data, the width of the shear zone significantly affects the relative amount of gas emission, which increases as the thickness of the shear zone increases (Table 2).

The shear zone is not consistent with a simple bedding fault, but rather a complexly deformed band locally overprinted by ductile shearing fabrics. In general, normal coals exhibit bedding plane structures with smooth and conchoidal fractures, whereas sheared coals were dull and blocky with a granular texture. Deformed coals were classified into microstructural classes based on their particle size and texture as cataclastic-angular coal, cataclastic-granular coal, foliated coal and mylonitic coal (Fig. 4). The former two are considered to be developed in a brittle mechanism and are widely distributed in the shear zone, whereas the latter two are developed during the ductile deformation process and have been subjected to more intense deformation. The ductile shearing structures commonly occur where the coal dips steeply (30–40°) at an angle close to the direction of maximum shear stress developed within a horizontal compressional stress field (Ramsay and Huber 1987). Intense shearing may locally transform coal into mylonites or foliated fabrics which, under ground weight or abutment pressure, become impermeable to gas and are usually considered as a "tectonic screen", which blocks methane migration, and thus prevents methane extraction. Although the number of fissures may be very high, connection between them no longer exists. From the experiences of gas drainage in underground mines, although the rate of gas extraction within a shear zone is commonly higher than from normal coals, locally the most noted problem that has been met is that a drill rod is often gripped and unable to turn and that drilled holes close quickly like quicksand after drilling, due to the great gas pressure and intensely sheared coals where ductile structures often occur. For this reason, gas extraction in such an area becomes very difficult and the rate of gas extraction is relatively lower than in brittlely deformed areas, despite the great volume of gas content.

Experimental methods and results

Studies on the pore structures of variously ranked normal coals using the method of mercury penetration have been carried out by many researchers (Zwietering and van Krevelen 1954; Toda 1973; Spitzer 1981), but there is little literature about the application of this method on tectonically deformed coals, except for the work of Wang and Yang (1980). This situation may be due to the fact that almost all researchers tend to determine the internal chemical structure and properties of coal with this method rather than investigating the fractures of geological disturbance related to the coalbed methane. In this study, the mercury penetration method was used to investigate the fracture characters of the various deformed coals compared with normal coals to reveal the porosity, specific surface area and the distribution of fracture aperture in coals. The porosity and specific surface area of coal were considered to be related to the content of free and adsorbed gas, and the average fracture aperture to the permeability of coals.

Experimental conditions

Measurements were carried out using a macropores Unit 120 under pressures of 0–1 atm and an automated high-

Table 2
Relationship between the relative amount of gas emission and the thickness of shear zone in advance faces

Working faces	Depth (m)	Thickness of coal seam (m)	Thickness of shear zone (m)	Relative amount of gas emission (m^3/t)
Wu 12130	487	5.8	1.8	15.68
Wu 12130	484	5.5	1.9	16.56
Wu 14131	483	5.4	0.9	9.04
Wu 14131	485	5.3	1.1	10.45
Wu 20080	511	5.6	2.5	18.54
Wu 20080	508	5.7	2.3	17.34
Wu 20090	520	4.8	0.8	10.31
Wu 20090	521	4.9	0.6	10.55

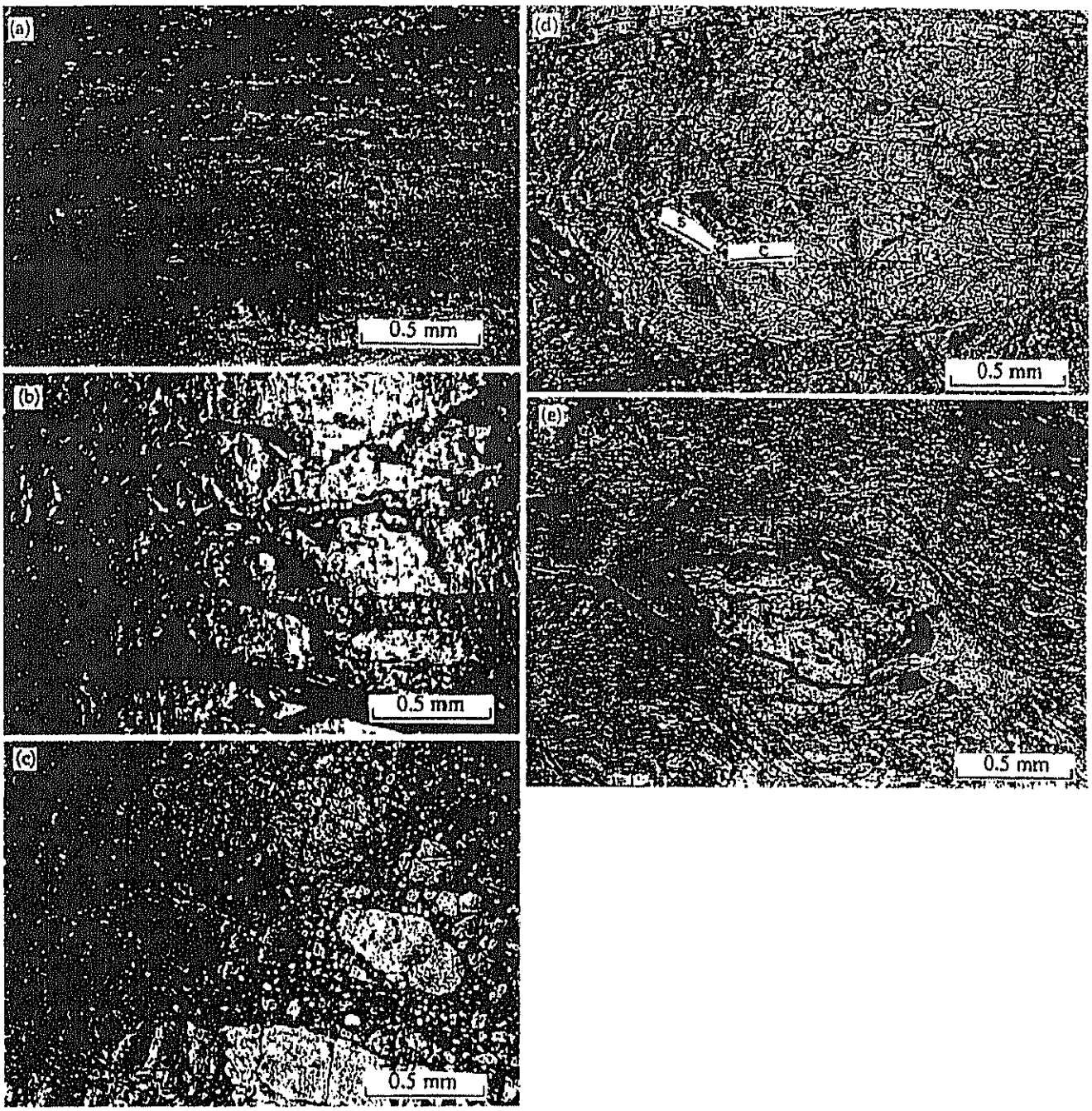

Fig. 4
Microphotographs showing variously deformed coals. a Normal coal exhibiting bedding plane structure and scarce fractures. b Cataclastic–angular coal displaying angular structure and wide fracture aperture. c Cataclastic–granular coal which has been rotated and ground by stress and exhibits granular fragments of variable size. d Foliated coal characterized by a slightly elongate shape of most of the grains similar to s–c structures. e Mylonitic coal which has been intensely sheared shows σ-structures (porphyroclasts are founded by inertinite-rich coal and matrix is founded by vitrinite-rich coal)

pressure Mercury Porosimeter 2000 under a maximum operational pressure of 2,000 atm. Eleven samples collected from the shear zone and hard coals were measured (Fig. 5). The calculation of the main parameters with coals are described below.

Fracture aperture

According to Washburn's (1921) method, fracture aperture was calculated from the relation:

$$W = -2\sigma\cos\theta/P \quad (1)$$

where σ is the mercury surface tension, θ the mercury contact angle and P the pressure. When σ=485 dyne/cm and θ=140° (to the coal), this formula gives:

$$W = 7.5/P(\text{W in } \mu\text{ m, P in atm}). \quad (2)$$

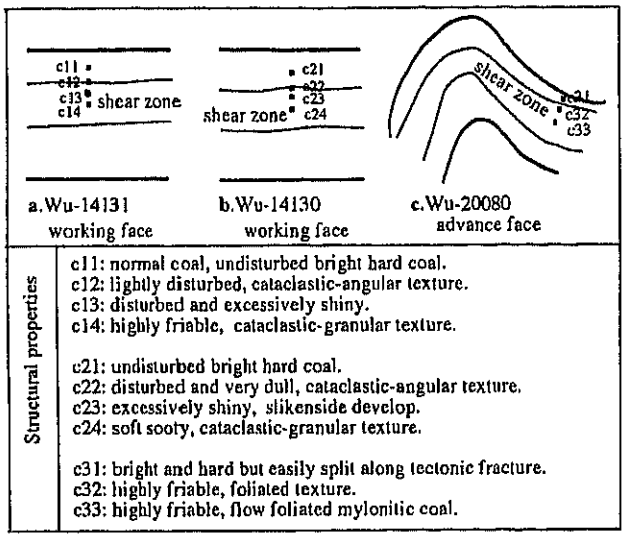

Fig. 5
Locality and structural properties of samples with brittle deformation *a* and *b*, and ductile deformation *c*

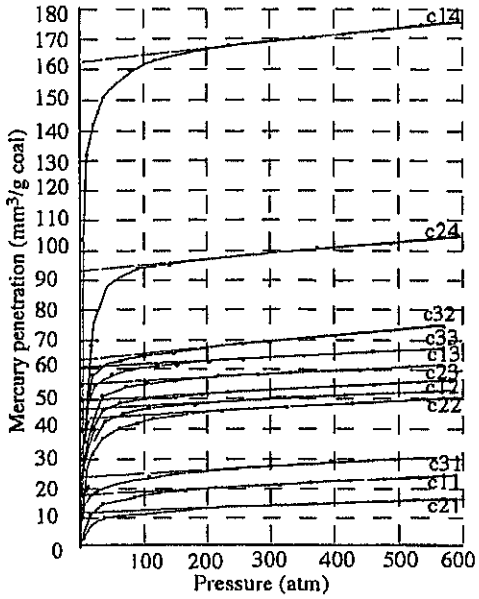

Fig. 6
Diagram illustrating mercury penetration with increasing pressure for various deformed and non-deformed samples

Specific pore surface

To calculate the specific pore surface from mercury penetration, the Rootare method (Rootare and Prenzlow 1967) was employed:

$$S = \frac{0.0192}{m} \int_0^{L_{max}} PdL \qquad (3)$$

where 0.0192 is the porosity meter constant, 0 the mercury level of the dilatometer at the starting stage, L the cumulative shift of the mercury level in the dilatometer, m the mass of the sample and P the pressure.

Coal compressibility

Because of the high compressibility of the coal substance, as compared with other solid materials, a correction was necessary. The experimental results which were expressed from 0 atm were plotted against pressure. The compressibility of coals can be calculated by the following formula:

$$K = \frac{1}{P} \times \frac{\Delta v}{v} \times \frac{1}{1.013 \times 10^{16}} cm^2 \cdot dyne^{-1} \qquad (4)$$

where v is the volume of sample, P the pressure and Δv the change of volume corresponding to P.

Results and discussion

Figure 6 shows that almost all samples show a straight line above 200 atm, suggesting that the apparent growth of the pore volume at pressures over 200 atm is due entirely to the compressibility of coal rather than to the occurrence of a number of real fractures. At the critical pressure (200 atm), the amount of mercury pressed into the normal coal sample appears to approach a volume of 0.013–0.025 cm^3/g, whereas it varies from 0.048 to 0.166 cm^3/g with the various deformed coals. This tendency evidently shows that the sheared coals contain three to eight times more pore volume than the normal hard coals.

Figure 7 shows the frequency distribution of the porosity, specific surface area, average fracture aperture and compressibility of samples, implying that because of the variable nature of the fracture aperture, a large volume does not necessarily imply that the pore surface is also large. The specific surface area of coal rises as the pore volume increases and decreases the average aperture. While the pore volume determines the free gas present, the pore surface is closely bonded with the shape and size of the fractures and determines the amount of adsorbed gas present. Therefore, the foliated and mylonitized coals (Fig. 5c) with more surface area contain more adsorbed gas, whereas the cataclastic coals, because of greater porosity, possess more free gas. Furthermore, the relatively smaller fracture aperture of the foliated and mylonitized coals (Fig. 7c) represents a lower permeability and can explain why the rate of gas extraction from such an area is always remarkably lower than that from the cataclastic coal. This may also explain why the outburst of gas always occurs in the foliated and mylonitized coal areas despite the pre-drainage of gas being undertaken.

The compressibility analysis (Fig. 7d) of various coals also shows that the compressibility rose with the increasing fracture level, implying that the intensely deformed coals also contain many more smaller microfractures (less than 0.075 μm corresponding to more than 200 atm) compared with the normal coals. These microfractures are not accessible to mercury even at very high pressure, but they are accessible to gas. This tendency further indicates that tectonically deformed coals possess a potentially significant capacity of gas storage. Because of the relative

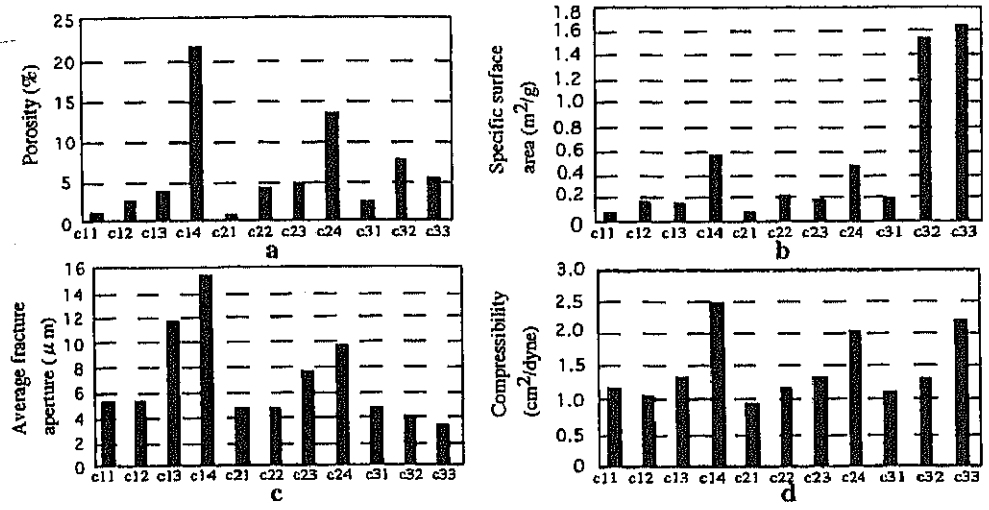

Fig. 7
Histograms indicating a the porosity, b specific surface area, c average fracture aperture and d compressibility of samples

thickness of deformed coal layers and its granular texture, migration and accumulation of large quantities of gaseous and liquid hydrocarbons may be anticipated.

Conclusions

Coalbed methane, which has many times the greenhouse effect of carbon dioxide gas, is still being released in the atmosphere in almost all underground coal mines over the world. The project of coalbed methane recovery and utilization can, to a certain extent, mitigate global warming, besides improving coal mine safety.

A shear zone along coal seams, commonly called a soft-coal band, and referable to as a detachment or bedding fault, is widely distributed throughout the world's coalfields. The coals in the shear zones are on average much weaker than those from the non-deformed coals, and contain a great quantity of methane gas. Sheared coals were further classified into microstructural classes based on their particular size and texture as cataclastic series, which widely occur in a shear zone, and mylonitic series, developing in a locally steeply dipping area. According to the present study on mercury penetration, it is known that cataclastic coals possess higher porosity, a larger fracture aperture and smaller specific surface area compared with mylonitic coals, which show smaller porosity, smaller fracture aperture and higher specific area. The former represent a high methane storage capacity and a good condition for gas extraction, whereas the latter show abundant adsorbed gas and difficult conditions for gas extraction, which can explain why more intensely sheared coals become difficult for methane extraction and why gas outburst always occurs in these areas.

For a coalbed methane exploitation, the coals serve both as a source and reservoir for methane gas. Tectonically deformed coals can commonly promote both effects due to their higher storage capacity and permeability to methane gas, but locally it is difficult to extract methane due to unusually small fracture apertures, such as within the limb of a subordinate fold. The occurrence of a large number of tectonic fractures in a shear zone will make it easier for artificial breaks such as hydro-fracturing to increase the permeability of coals in methane production. Therefore, except for locally intensely sheared coals, the tectonically deformed coal bands, especially bedding shear zones along coal seams, are the best source and reservoir for methane gas. Geological studies on these tectonically fractured bands in coal seams would provide a beneficial precondition to exploit coalbed methane in the future and thus help protect the earth from global warming.

Acknowledgements The authors wish to thank Dr. W Lin and Dr. M Takahashi of the Geological Survey of Japan for assisting with the mercury penetration experiment and data processing. Pingdingshan Coal Administration is thanked for providing opportunities to study the shear zones within coal seams in their collieries.

References

Beamish BB, Crosdale PJ (1998) Instantaneous outbursts in underground coal mines: an overview and association with coal type. Int J Coal Geol 35:27-55

Bibler CJ, Marshall JS, Pilcher, RC (1998) Status of worldwide coal mine methane emissions and use. Int J Coal Geol 35:283-310

Bustin RM (1982) The effect of shearing on quality of some coals in the southeastern Canadian Cordillera. Can Inst Min Metall Bull 75:76-83

Cao Y (1994) The knowledge and practice for prediction of gas outburst by gas geology. J China Coal Soc Suppl 20:76-78

Dumpleton S (1990) Outbursts in the South Wales coalfield: their occurrence in three dimensions and a method for identifying potential outburst zones. Min Eng 1990:322-329

Frodsham K, Gayer RA (1999) The impact of tectonic deformation upon coal seams in the South Wales coalfield, UK. Int J Coal Geol 38:297-332

Geological Survey of Henan Province (1990) Depositional models of coal-bearing sequences in the Henan Province. China Geological University Press, Beijing

Hargravs AJ (1983) Instantaneous outbursts of coal and gas: a review. Proc Aust Inst Min Metall 285:1-37

Hokao Z (1982) Prediction, method and countermeasure of gas outburst. Uchida Rokakuho Press, Tokyo
John R (2000) Greenhouse challenge of Australian coal mining industry. In: Proc Asia-Pacific workshop on coal mining technology 2000 Symp. Japan Coal Energy Center, Tokyo, pp 219–230
Kang J, Li W (1995) Remark on the Guodishan fault in Pingdingshan coalfield. J China Coal Soc 20:132–141
Li H (1995) Application of the deformation coefficients of fold in forecasting outburst of coal and gas. Henan Geol 13:304–308
Peng L (1991) The main types of bedding faults and its geological significance. Proc 4th Academic Discussion of Jiaozuo Mining Institute. Jiaozuo, China, pp 26–45
Ramsay J, Huber M (1987) The techniques of modern structural geology, vol 2: folds and fractures. Academic Press, London, pp 445–502
Rootare HM, Prenzlow CF (1967) Surface area from mercury porosimeter measurements. J Phys Chem 71:2733–2736
Shepherd J, Rixon LK, Griffiths L (1981) Outbursts and geological structures in coal mines: a review. Int J Rock Mech Min Sci Geomech Abstr 18:267–283
Spitzer Z (1981) Mercury porosimetry and its application to the analysis of coal pore structure. Power Technol 29:177–186
Toda Y (1973) Report of study on pore structure of coals and their carbonized products. National Research Institute for Pollution and Resources no 5, Tsukuba, Japan, pp 36–46
Wang Y, Yang S (1980) Some characteristics of coal seam with hazard of outburst. J China Coal Soc 1:47–53
Washburn EW (1921) Note on a method of determining the distribution of pore sizes in a porous material. Proc Natl Acad Sci USA 7:115–116
Yu L, Li W (1981) Study on composition of hydrocarbon in coal seams liable to outbursts. J China Coal Soc 4:1–8
Zwietering P, van Krevelen D (1954) Chemical structure and properties of coal-pore structure. Fuel 33:331–337

GEOPHYSICAL RESEARCH LETTERS, VOL. 28, NO. 14, PAGES 2719-2722, JULY 15, 2001

A new type of intra-plate volcanism; young alkali-basalts discovered from the subducting Pacific Plate, northern Japan Trench

N. Hirano[1], K. Kawamura[2], M. Hattori[3], K. Saito[4] and Y. Ogawa[5]

Abstract. Alkali pillow basalts were collected from the toe of the oceanward slope of the northern Japan Trench. These alkali-basalts formed as a result of a low degree of partial melting of Pacific Ocean mantle and rapid rise of the magma (no fractionation in shallow magma chambers). Reconstructing Pacific Plate motion based on ^{40}Ar-^{39}Ar age dates of 5.95±0.31 Ma for these basalts indicates that they erupted outboard of outer swell or forebulge of the Japan Trench in the NW Pacific. We suggest that these alkali-basalts represent a new form of intra-plate volcanism, whereby magmatic activity occurs off the forebulge of the downgoing Pacific slab, perhaps using conduits related to fracturing of the slab during bending prior to subduction.

1. Introduction

Alkali-basalts occur on various parts on the surface of the earth, most particularly in continental and hotspot areas. These alkali-basalts are products of deep-origin magma from the upper mantle or lower depths. Occurrences of such alkali-basalt are also documented from tectonically unique locations, such as along deep fractures in oceanic crust.

Alkali olivine basalt and trachyandesite representative of the ocean island basalt series have been documented around the Japan Trench on the Joban, Erimo and Takuyo Seamounts [*Kobayashi et al.*, 1987; *Cadet et al.*, 1987]. The ^{40}Ar-^{39}Ar ages of these volcanic rocks range from 120 Ma (Daiichi-Kashima Seamount in the Joban Seamount Chain) to 104 Ma (Erimo Seamount) [*Takigami et al.*, 1989], indicating that these are the products of Cretaceous off-ridge seamount volcanism (Fig. 1A). In contrast, the bathymetry of the study area does not show any evidence for a large volcanic edifice or seamount, but only a small mound (Fig. 1B).

This paper describes an occurrence of young alkali-basalt on the downgoing oceanic slab of a subduction zone. We present the geologic setting, major and trace element compositions, and ^{40}Ar-^{39}Ar age of these basaltic rocks. We then discuss the tectonic and geophysical implications for this first documentation of alkali-basaltic magmatism outboard of outer swell of a subducting oceanic slab.

2. Occurrence and description of samples

Continuous outcrops of pillow basalt were documented and sampled at depths of 7325 to 7360 m on the oceanward slope toe of the northern Japan Trench (39°23' N, 144°16' E) during JAMSTEC (Japan Marine Science and Technology Center) *R/V Kairei/ROV KAIKO* cruise KR97-11. The slope is characterized by trench-parallel (N-S) normal faults with some NNW or NNE faults, due to warping of the downgoing Pacific Plate (the age of the Pacific Plate here is Early Cretaceous [*Kobayashi et al.*, 1998]) (Fig. 1). These normal faults bound horst and graben structures that are approximately 5 km in horizontal extent with 100 to 500 m vertical separations [*Ogawa and Kobayashi*, 1993;

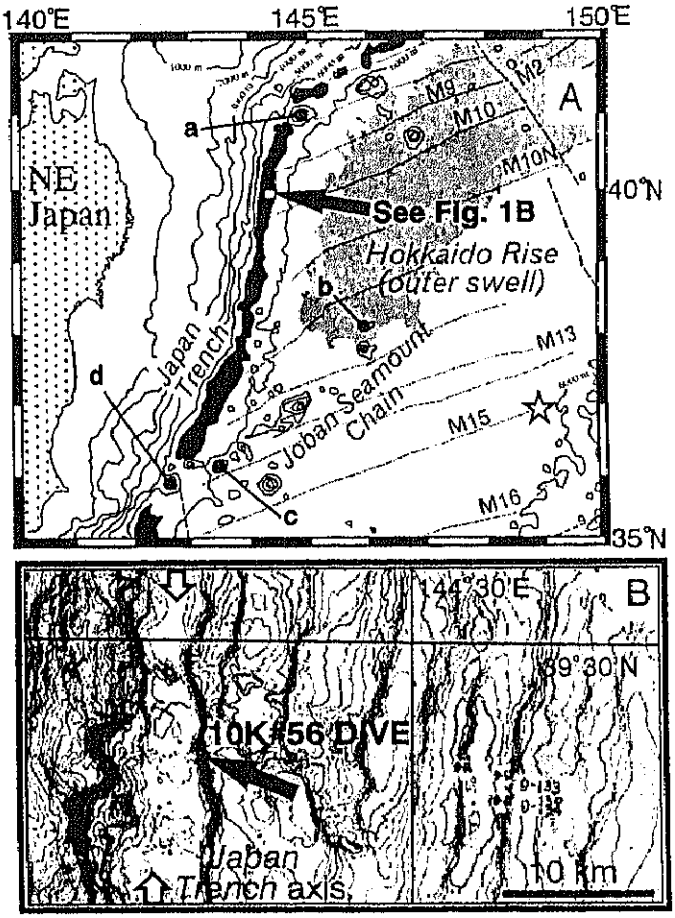

Figure 1. Index maps of the dive site. A: The general bathymetric map of the northwest Pacific ocean floor based on Kobayshi et al. (1998). Black area is trench floor deeper than 7000 m, and grey-shaded area is the outer swell (<5400 m in depth). Radiometric ages of Erimo (a), Ryofu (b), Daini-Kashima (c) and Daiichi-Kashima (d) Seamounts are obtained as follows respectively; (a) 104 Ma and (d) 120 Ma ^{40}Ar-^{39}Ar age [*Takigami et al.*, 1989], (b) 70-72 Ma and (c) 81 Ma K-Ar age [*Ozima et al.*, 1977]. The approximate eruption site is plotted as asterisk. B: Seabeam bathymetric map of the dive site 10K#56 by R/V *KAIREI* at the northern Japan Trench. Contour interval is 250 m. Trench axis is shown by white arrow.

[1]Doctral Program in Geoscience, University of Tsukuba, Tsukuba, Japan. Now at Ocean Research Institute, University of Tokyo, Tokyo, Japan.
[2]Fukada Geological Institute, Tokyo, Japan
[3]Japan Marine Science and Technology Center, Yokosuka, Japan
[4]Department of Earth and Environmental Sciences, Faculty of Science, Yamagata University, Yamagata, Japan
[5]Institute of Geoscience, University of Tsukuba, Tsukuba, Japan

Copyright 2001 by the American Geophysical Union.

Paper number 2000GL012426.
0094-8276/01/2000GL012426$05.00

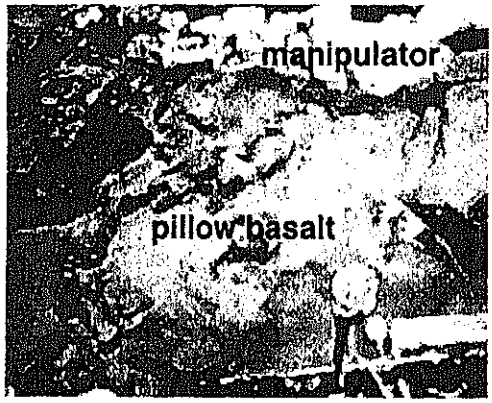

Figure 2. Outcrop photograph of the pillow basalt taken by R/V *KAIREI* video record, indicating a large pillow structure. The field of view is approximately 1 m in length.

Ogawa et al., 1996]. There is no distinct seamount topography associated with the alkali pillow basalt outcrops, however a subdued mound-like feature (100 to 200 m hight, 1 to 2 km in diameter) is recognized using seabeam sonar bathymetric mapping (Fig. 1B).

The ROV *KAIKO* was used to sample rocks from the toe of the oceanward slope (downgoing Pacific Plate) of the subduction zone. The slopes have an average dip of 25° but are locally very steep, forming escarpments along which there are exposures of

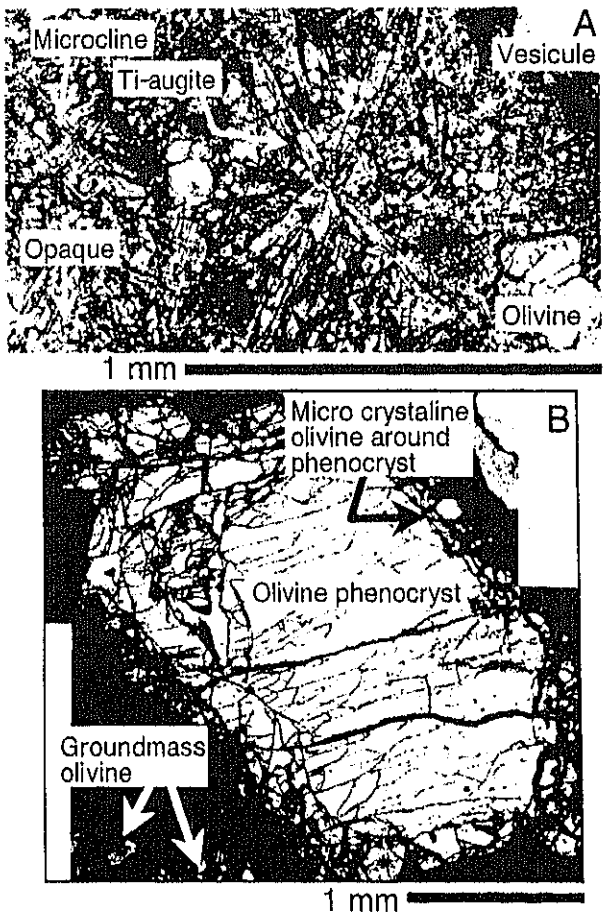

Figure 3. Photomicrographs of thin section of sample (10K#56 R-002). A: groundmass. B: Olivine phenocryst surrounded by micro crystalline olivine.

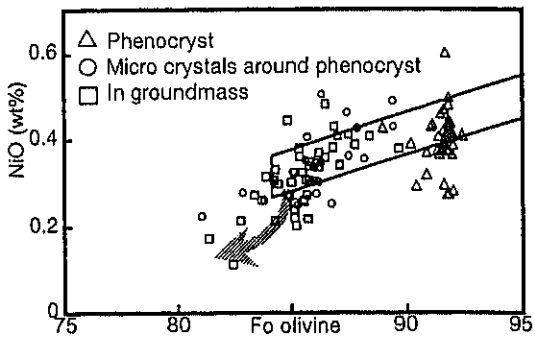

Figure 4. Fo value vs. NiO plot of olivine from 10K#56 R-001 and R-002. Open box zone is mantle olivine array after *Takahashi et al.* (1987). Arrows show trends of olivine fractional crystallization after *Sato* (1977).

alkali pillow basalt outcrops at depths of 7325 to 7360 m. The cliffs are covered with thin drapings of soft, black, muddy sediments. The total thickness of the basalt outcrops is more than 35 m. The outcrops are alternations of pillow lava (Fig. 2) and hyaloclastite.

Two samples, 10K#56 R-001 and R-002, were collected from pillow lava outcrops at around 7360 m depth (Fig. 2). Both samples exhibit curved foliations, representing the surface of a pillow of around 30 cm in diameter. The samples contain a large proportion of vesicles, reaching 10-30 volume percent. The rocks and minerals, which have a dendritic texture, are very fresh, even in vesicles. Large olivine phenocrysts make up from 1.0 % to 2.4 % in volume (R-001 and R-002, respectively), and the groundmass is composed of olivine, Ti-augite, microcline and opaque minerals (Fig. 3A). The olivine phenocrysts (Fo values, 90-93, and NiO contents, 0.3-0.5 wt%) (Fig. 3B) are more primitive in origin than those in the groundmass (Fo values, 80-90, and NiO contents, 0.1-0.5 wt%), and have compositions in equilibrium with the mantle olivine array [*Sato*, 1977; *Takahashi et al.*, 1987] (Fig. 4). Small crystalline olivines around phenocrysts have the same composition as groundmass olivines. Potassium rich contents of microcline, and Ti-augite (TiO_2; 2.0 to 5.0 wt%) characterize the highly alkaline magma. Ilmenite is the most common opaque mineral in the groundmass (Fig.3A). Bulk chemical compositions (Table 1 and 2), trace elements spidergram (Fig. 5A) and REE pattern (Fig. 5B) show that these rocks are enriched in incompatible elements and can be characterized as potassium-rich alkali-basalts, shoshonites.

3. ^{40}Ar-^{39}Ar dating

Sample 10K#56 R-002 was irradiated in the Japan Material Testing Reactor (JMTR) along with three flux monitors (HD-B1 biotite) and synthetic salts to permit the corrections for interfering isotopes. The sample was subjected to eight step-heating intervals by induction heating. The method of Ar isotopic analysis follows *Saito et al.* (1991). Precision limits represent propagated measurement and J-value uncertainties and are reported throughout this paper at the 2σ level. The detailed data can be obtained through URL [http://www.f2.dion.ne.jp/~nhirano/JT/].

In order to obtain a plateau age in age-spectrum, we need consistent age over three continuous fractions at 2σ level. A plateau age of 5.95±0.31 Ma for the sample 10K#56 R-002 was calculated in the age spectrum (Fig. 6a). The J-value error was not used in the age spectrum, and was included at the last stage of age calibration as a plateau age. In addition, we obtained a well-defined isochron using the inverse isochron method (Fig. 6b), and the derived isochron age (5.69±0.43 Ma) is in accord with the plateau age.

Table 1. Bulk compositions of 10K#56 R-001 and R-002 by XRF analysis.

sample		major element (wt%)												
		SiO_2	TiO_2	Al_2O_3	Fe_2O_3	FeO	MnO	MgO	CaO	Na_2O	K_2O	P_2O_5	H_2O+	H_2O-	Total
R-001	bulk	48.22	2.56	10.30	6.38	4.23	0.14	11.68	7.47	2.95	3.17	0.78	1.76	0.36	100.00
	groundmass[a]	48.84	2.72	11.60	10.44	-	0.13	8.23	7.68	3.04	3.88	0.83	1.23	1.39	100.00
R-002	bulk	48.45	2.84	11.26	6.12	4.36	0.13	7.83	8.14	3.28	3.63	0.84	2.49	0.64	100.00
	groundmass[a]	49.27	2.84	12.18	10.00	-	0.12	6.61	7.61	3.13	4.11	0.87	1.47	1.81	100.00

sample		trace element (ppm)													
		Ba	Ce	Co	Cr	Ga	Nb	Ni	Pb	Rb	Sr	Th	V	Y	Zr
R-001	bulk	1202.3	94.4	56.7	527.8	17.7	36.6	418.1	7.2	47.0	1076.5	2.0	140.1	14.2	243.0
	groundmass[a]	1176.8	-	154.0	424.0	-	37.4	163.1	6.9	56.2	1212.4	4.7	-	18.8	263.8
R-002	bulk	1209.5	108.7	46.7	400.5	20.2	40.3	227.8	7.3	53.1	1092.4	2.0	143.4	15.3	259.9
	groundmass[a]	1191.2	-	129.0	353.0	-	39.4	117.2	7.3	59.0	1140.4	4.9	-	19.7	273.8

[a] Data for the samples separated the olivine phenocryst from the groundmass. In this data[a], Fe_2O_3 show the total Fe-oxide.

Table 2. REE compositions of the bulk samples by the ICP-MS analysis. Analyzed by Dr. M. Komuro and Ms. K. Fujii, Institute of Geoscience, University of Tsukuba (personal communication).

	ppm													
	Y	La	Ce	Pr	Nd	Sm	Eu	Gd	Tb	Dy	Ho	Er	Tm	Yb	Lu
R-001	19.17	54.07	106.95	12.03	49.35	9.41	2.98	7.74	1.00	4.63	0.77	1.83	0.23	1.41	0.19
R-002	20.78	58.69	114.28	12.97	53.61	10.02	3.22	8.38	1.08	4.72	0.88	1.93	0.23	1.46	0.20

4. Tectonic interpretation and geophysical implication

The alkali-basalts documented here are very young, much younger than the ocean floor in this area (identified isochron M9 or M10; around 130 Ma [*Gradstein et al.*, 1994; *Kobayashi et al.*, 1998]). Seamounts in this region are also Cretaceous, with ages ranging from 120-104 Ma. In contrast, the rocks analyzed in this study have ages of 5.95±0.31 Ma (latest Miocene), and are found in small-volumes along seafloor escarpments rather than on seamounts or large volcanic constructions. By performing a plate tectonic reconstruction we have determined that there is no plausible hotspot that could have produced these basalts. We have reconstructed the eruption location of these basalts using the ^{40}Ar-^{39}Ar age of 5.95±0.31 Ma and the present "absolute" motion of the Pacific Plate (10.29 cm/yr to 295.26 degrees [*Gripp and Gordon*, 1990]). Using this method we have derived a position of approximately 612±32 km ESE off the northern Japan Trench, now approximately at 37°N, 149°E. As the volcanic front in the NE Japan Arc has scarcely shifted since the latest Miocene [*Ohki et al.*, 1993], the kinematics of the Pacific slab at 5-6 Ma are the same as at present. According to the bathymetric chart of the northwest Pacific, this area corresponds to a site just oceanward of the current outer swell or forebulge (Hokkaido rise), with an inferred paleo-depth of ~6000 m (asterisk in Fig. 1A).

Enriched incompatible element concentrations and REE pattern indicate that the magma source for these alkali-basalts formed as a result of low degree of partial melting. Disequilibrium between olivine phenocrysts and groundmass olivines suggest that the phenocrysts may be xenocrysts transported from deep in the mantle with rapid rise of the alkali-basaltic magma. If a fracture occurs or is rejuvenated in the

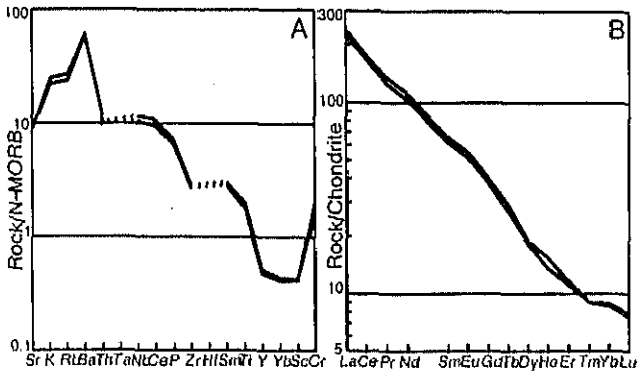

Figure 5. Spidergrams of trace element concentrations in samples 10K#56 R-001 and R-002. A: Normalized by average MORB [*Pearce*, 1982, 1983]. B: Chondrite-normalized REE pattern [*Evensen et al.*, 1978]. U, Ta and Hf were not analyzed.

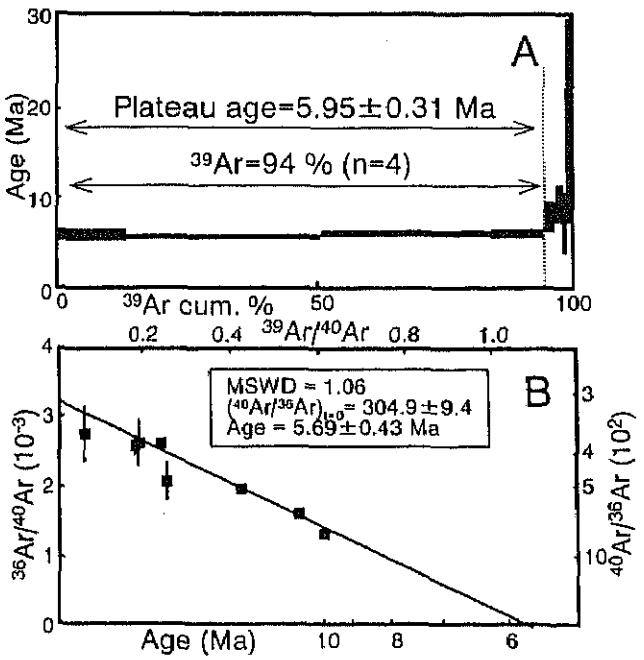

Figure 6. Age determination results by ^{40}Ar-^{39}Ar method of sample 10K#56 R-002. Correction factors and J-value are as follows; $(^{36}Ar/^{37}Ar)_{Ca}$ = (3.744±0.082)×10^{-4}, $(^{39}Ar/^{37}Ar)_{Ca}$ = (9.30±0.44)×10^{-4} and J = (3.412±0.063)×10^{-3}. Calculated using decay constants and potassium isotope ratios from *Steiger and Jager* (1977).

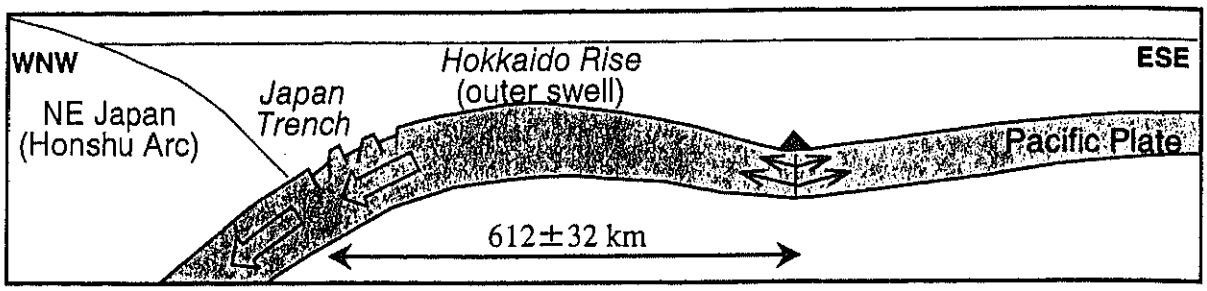

Figure 7. A model of possible alkali-basalt eruption on the old oceanic crust toward the subduction zone. Fracturing of Pacific Plate toward the outer swell may result in the formation of conduits for magma flow to the surface.

oceanic lithosphere, magma from the lowest part where fracture reached may erupt to the seafloor. It can be also assumed that melting was induced by decompression in the upper mantle. The occurrence, mineralogical and chemical characteristics of the basalt samples documented here show that the magma could have ascended toward the surface in this way.

We suggest a possible scenario for the formation and eruption of this new type of intra-plate alkali-basalt (Fig. 7). 1) The oceanic crust undergoes lithosphere scale orthogonal flexure as it begins to enter the outer swell. 2) Extension on the inside of the lithosphere folding on this large-scale causes decompression melting in the upper portions of the lower mantle. 3) Fracturing during folding results in the formation of conduits for magma flow to the surface. If these processes are intrinsic to the subduction of oceanic crust, alkali-basalts should be common in forebuldge regions worldwide.

Geophysical investigations may reveal more about this new type of intra-plate volcanism, specifically about the relationship between subduction and the formation and eruption of alkali-basalts on the outer swell or forebuldge of a subducting slab. If orthogonal flexure, decompression melting, and fracturing occur in the downgoing slab as it enters the subduction zone, they should impart specific physical characteristics (density, velocity, faults and fractures) to the crust and lithospheric mantle. Seismic tomography, seismic reflection/refraction surveys, gravity, and earthquake seismicity should all reflect these changes to the oceanic slab as it moves through the forebulge into the subduction zone.

Acknowledgments. We owe much to the crew of the mother vessel R/V *KAIREI* of JAMSTEC and ROV operation team, particularly Captain H. Tanaka and Commander T. Fukui. We highly appreciate the staff of the Institute for Material Research, Tohoku University (Oarai Branch) for irradiating samples in the Japan Material Testing Reactor (JMTR). Drs. T. Ishii and H. Sato of Ocean Research Institute, University of Tokyo, Dr. N. Iwata, Faculty of Science, Yamagata University, and Dr. T. Yoshida, Faculty of Science, Tohoku University, and Dr. K. Komuro and Ms. K. Fujii, Institute of Geoscience, University of Tsukuba, for chemical analysis and age determination. Discussions by Prof. K. Miyano and Dr. M. Kurosawa of Institute of Geoscience, University of Tsukuba are also greatly appreciated. Early draft was critically reviewed and revised by Dr. D. Curewitz of Ocean Research Institute, University of Tokyo, to whom we are grateful.

References

Cadet, J. P., K. Kobayashi, J. Aubouin, J. Boulegue, C. Deplus, R. Von Huene, L. Jolivet, T. Kanazawa, J. Kasahara, K. Koizumi, S. Lallemand, Y. Nakamura, G. Pautoto, K. Suyehiro, S. Tani, H. Tokuyama and T. Yamazaki, The Japan Trench and its juncture with the Kuril Trench: cruise results of the Kaiko project, Leg 3, *Earth Planet. Sci. Lett.*, 83, 267-284, 1987.

Evensen, N. M., Hamilton, P. J. and O'Nions, R. K., Rare-earth abundances in chondritic meteorites, *Geochim. Cosmochim. Acta*, 42, 1199-1212, 1978.

Gradstein, F. M., F. P. Agterberg, J. G. Ogg, J. Hardenbol, P. V. Veen, J. Thierry and Z. Huang, A Mesozoic time scale, *J. Geophys. Res.*, 99, 24051-24074, 1994.

Gripp, A. E. and R. G. Gordon, Current plate velocities relative to the hotspots incorporating the NUVEL-1 global plate motion model, *Geophys. Res. Lett.*, 17, 1109-1112, 1990.

Kobayashi, K., J. P. Cadet, J. Aubouin, J. Boulegue, J. Dubois, R. Von Huene, L. Jolivet, T. Kanazawa, J. Kasahara, K. Koizumi, S. Lallemand, Y. Nakamura, G. Pautot, K. Suyehiro, S. Tani and H. Tokuyama, T. Yamazaki, Normal faulting of the Daiichi-Kashima Seamount in the Japan Trench revealed by the Kaiko I cruise, Leg 3., *Earth Planet. Sci. Lett.*, 83, 257-266, 1987.

Kobayashi, K., M. Nakanishi, K. Tamaki and Y. Ogawa, Outerslope faulting associated with the eastern Kuril and Japan Trenches, *Geophysical Journal International*, 134, 356-372, 1998.

Ogawa, Y. and K. Kobayashi, Mud ridge on the crest of the outer swell off Japan Trench. *Marine Geology*, 111, 1-6, 1993.

Ogawa, Y., K. Kobayashi, H. Hotta and K. Fujioka, Tension cracks on the oceanward slopes of the northern Japan and Mariana Trenches, *Marine Geology*, 114, 111-123, 1996.

Ohki, J., Watanabe, N., Shuto, K., and Itaya, T., Shifting of the volcanic fronts during Early to Late Miocene in the northeast Japan arc, *The Island Arcs*, 2, 87-93, 1993.

Ozima, M., Honda, M. and Saito, K., 40Ar/39Ar ages of guyots in the western Pacific and discussion of their evolution, *Earth Planet. Sci. Lett.*, 51, 475-485, 1977.

Pearce, J. A., Trace element characteristics of lavas from destructive plate boundaries, in *Andesites*, edited by R. S. Torpe, pp.525-548, John Wiley and Sons, New York, 1982.

Pearce, J. A., Role of the sub-continental lithosphere in magma ganasis at active continental margins, in Continental Basalts and Mantle Xenoliths, edited by C. J. Hawkesworth and M. J. Norry, pp.230-249, Shiva, Nantwich, 1983.

Saito, K., Otomo, I. and Takai, T., K-Ar dating of the Tanzawa tonalitic body and some restrictions on the collision tectonics in the south Fossa Magna, cantral Japan, *J. Geomag. Geoelectr.*, 43, 921-935, 1991.

Sato, H., Nickel content of basaltic magma: identification of primary magmas and a measure of the degree of olivine fractionation, *Lithos*, 10, 113-120, 1977.

Steiger, R. H. and Jager, E., 1977, Subcommission on geochronology: convection on the use of decay constants in geo- and cosmochronology, *Earth Planet. Sci. Lett.*, 36, 359-362.

Takahashi, K., K. Uto and J. G. Schilling, Primary magma compositions and Mg/Fe ratio of their mantle residues along Mid Atlantic Ridge 29 -N to 73-N, *Technical Report of ISEI, Okayama Univ.*, 1-4, 1987.

Takigami, Y, I. Kaneoka, T. Ishi, Y. Nakamura, 40Ar-39Ar ages of igneous rocks recovered from Daiichi-Kashima and Erimo Seamounts during the KAIKO project, *Palaeogeography, Palaeoclimatology, Palaeoecology*, 71, 71-81, 1989.

N. Hirano, Ocean Research Institute, University of Tokyo, 1-15-1 Minamidai, Nakano, Tokyo, 164-8639, Japan. (nhirano@ori.u-tokyo.ac.jp)
K. Kawamura, Fukada Geological Institute, Tokyo, Japan.
M. Hattori, Japan Marine Science and Technology Center, Yokosuka, Japan.
K. Saito, Department of Earth and Environmental Sciences, Faculty of Science, Yamagata University, Yamagata, Japan.
Y. Ogawa, Institute of Geoscience, University of Tsukuba, 1-1-1 Tennoudai, Tsukuba, 305-8571, Japan. (yogawa@arsia.geo.tsukuba.ac.jp)

(Received October 03, 2000; revised April 19, 2001;
accepted May 02, 2001.)

Ludden, J.N., Plank, T., and Escutia, C. (Eds.)
Proceedings of the Ocean Drilling Program, Scientific Results Volume 185

Progressive Microfabric Changes in Unconsolidated Pelagic and Hemipelagic Sediments Down to 180 mbsf, Northwest Pacific, ODP Leg 185, Site 1149[1]

Kiichiro Kawamura[2] and Yujiro Ogawa[3]

ABSTRACT

During Ocean Drilling Program Leg 185, we studied progressive changes of microfabrics of unconsolidated pelagic and hemipelagic sediments in Holes 1149A and 1149B in the northwest Pacific at 5818 m water depth. We paid particular attention to the early consolidation and diagenetic processes without tectonic deformation before the Pacific plate subduction at the Izu-Bonin Trench. Shape, size, and arrangement of pores were analyzed by scanning electron microscope (SEM) and were compared to anisotropy of magnetic susceptibility (AMS) data. The microfabric in Unit I is nondirectional fabric and is characterized by large peds of ~10–100 µm diameter, which are made up of clay platelets (mainly illite) and siliceous biogenic fragments. They are ovoid in shape and are mechanically packed by benthic animals. Porosity decreases from 0 to 60 meters below seafloor (mbsf) in Unit I (from 60% to 50%) in association with macropore size decreases. The microfabric of coarser grain particles other than clay in Unit II is characterized by horizontal preferred orientation because of depositional processes in Subunit IIA and burial compaction in Subunit IIB. On the other hand, small peds, which are probably made of fragments of fecal pellets and are composed of smectite and illite (3–30 µm diameter), are characterized by random orientation of clay platelets. The clay platelets in the small peds in Subunit IIA are in low-angle edge-to-face (EF) or face-to-

[1]Kawamura, K., and Ogawa, Y., 2002.Progressive microfabric changes in unconsolidated pelagic and hemipelagic sediments down to 180 mbsf, northwest Pacific, ODP Leg 185, Site 1149. *In* Ludden, J.N., Plank, T., and Escutia, C. (Eds.), *Proc. ODP, Sci. Results*, 185, 1–29 [Online]. Available from World Wide Web: <http://www-odp.tamu.edu/publications/185_SR/VOLUME/CHAPTERS/003.PDF>. [Cited YYYY-MM-DD]
[2]Fukada Geological Institute, Honkomagome 2-13-12, Tokyo 113-0021, Japan. kichiro@fgi.or.jp
[3]Institute of Geoscience, University of Tsukuba 1-1-1, Tennodai, Tsukuba 305-8571, Japan.

Initial receipt: 9 October 2001
Acceptance: 31 May 2002
Web publication: 16 September 2002
Ms 185SR-003

face (FF) contact. These peds are electrostatically connected by long-chained clay platelets, which are interconnected by high-angle EF contact. Breaking of these long chains by overburden pressure diminishes the macropores, and the clay platelets in the peds become FF in contact, resulting in decreases in the volume of the micropores between clay platelets. Thus, porosity in Subunits IIA and IIB decreases remarkably downward. The AMS indicates random fabric and horizontal preferred orientation fabric in Units I and II, respectively. This result corresponds to that of SEM microfabric observations.

In Subunit IIB, pressure solutions around radiolarian tests and clinoptilolite veins with normal displacement sense are seen distinctively below ~170 mbsf, probably in correspondence to the transition zone from opal-A to opal-CT.

INTRODUCTION

Argillaceous sediments change their internal microfabrics drastically at shallow burial depths by compaction resulting from particle reorientation. This process is associated with pore volume decreases (Bennett et al., 1981). The compaction model in previous studies is summarized as follows, from shallow to deep. First, clay platelets are linked by edge-to-edge (EE), edge-to-face (EF), or stepped face-to-face (FF) contact in a random arrangement, forming a long flocculation chain. This structure is called "cardhouse" fabric. Next, during further burial, such contacts in flocculations change to FF contact, forming preferred horizontal orientation (Bennett and Hulbert, 1986). These fabric changes in argillaceous sediments have been detected by shallowing of inclination of remanent magnetization, which is mostly a result of small magnetite grains of single-domain size being reoriented in preferred horizontal orientation because of compaction (Anson and Kodama, 1987; Deamer and Kodama, 1990).

At the sediment/water interface, argillaceous sediments do not have a homogeneous cardhouse fabric but have heterogeneous fabrics because of bioturbation, bottom-current disturbance, crystallization, dissolution of minerals, and so on (Reynolds and Gorsline, 1992; Bennett et al., 1991). For example, fine-grained particles are aggregated into heterogeneous fabrics by various processes as follows. Benthic animals that eat organic materials in mud make an aggregation of fine-grained particles in their own gut (Reynolds and Gorsline, 1992). Agitation by bioturbation and bottom currents at the sediment/water interface re-aggregates the fine-grained particles as a result of organic matter's adsorption and electrostatic attraction (Bennett et al., 1991; Stolzenbach et al., 1992). Then, the fine-grained particles are reoriented from EF and EE contact to FF contact by shear stress caused by the internal flow that occurs because of bioturbation and bottom-current disturbance even at the sediment/water interface. This idea was already well developed by O'Brien and Slatt (1990) and Bennett et al. (1991).

Through these complicated processes at the sediment/water interface and at shallow burial depths, fine-grained particles are eventually aggregated to what are called "peds" (Yong, 1972; Collins and McGown, 1974; Reynolds and Gorsline, 1992). Although the peds play an important role in the early compaction process of argillaceous sediments (Yong, 1972; Velde, 1996), real examples from the deep sea have not been well studied except by Collins and McGown (1974), Reynolds and Gorsline (1992), and Kawamura et al. (1999). In the present study, we

will describe detailed microfabrics of the argillaceous sediments of 180-m-long cored sediments recovered from the northwest Pacific in view of peds and their interrelational development. Polarized microscope, scanning electron microscope (SEM), and magnetic fabric analyses by measuring anisotropy of magnetic susceptibility (AMS) were used for microfabric observations. Grain-size distribution and X-ray diffraction (XRD) were also conducted in this study. A new concept for the early phase of the compaction process, which gives more importance to biologic process that forms peds at various depths, is given here.

MATERIAL AND METHODS

During Ocean Drilling Program (ODP) Leg 185 at Site 1149 (Holes 1149A and 1149B), we recovered 180 m of sediments (lithologic Unit I and Subunits IIA and IIB) from the northwest Pacific, at 31°20.519′N, 143°21.078′E (Hole 1149A; 5818 m water depth) and at 31°20.532′N, 143°21.060′E (Hole 1149B; 5818 m water depth) (Fig. F1). Unit I (0–118.2 meters below seafloor [mbsf]) is composed of argillaceous hemipelagic sediments (late Miocene–late Pliocene in age), including many volcanic glass fragments, feldspar grains, and siliceous biogenic tests. Subunit IIA (118.2–149.5 mbsf) is characterized by brown pelagic clay, including small amounts of volcanic glass fragments and siliceous biogenic tests. Subunit IIB (149.5–180 mbsf) is composed of dominantly brown pelagic clay. The lowermost part of Subunit IIB includes zeolitic (clinoptilolite) pelagic clay below 175 mbsf. The age of Unit II is unknown because of the lack of index fossils, but comparable lithology at Deep Sea Drilling Project (DSDP) Leg 20, Hole 196 (30°1.162′N, 148°5.748′E; 6194 m water depth), ~500 km east of Site 1149, is considered to be Late Cretaceous in age (Shipboard Scientific Party, 2000). Below Subunit IIB, Cretaceous chert and marlstone continue down to ~400 mbsf, above basaltic rocks.

Tube samples (each ~3 cm diameter, 5 cm in length), two samples per each core, were packed on board with certain orientation in cylindric plastic cases to keep them wet until they were divided into SEM and AMS samples on shore.

F1. Bathymetric map of Site 1149, p. 15.

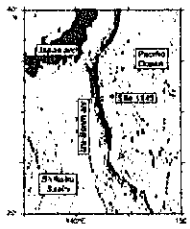

Physical Properties

Since the grain density, porosity, and void ratio of Subunit IIB from Hole 1149A were not measured during Leg 185, we measured grain density (g/cm^3) (ρ_g) of four samples from Subunit IIB (Samples 185-1149A-18H-2, 65–67 cm; 18H-4, 75–77 cm; 19X-1, 40–42 cm; and 20X-1, 88–90 cm) using a pycnometer. The porosity (η) and void ratio (e) were calculated from the above grain density, the water content by dry weight (W), and the dry bulk density (g/cm^3) (ρ_d) reported by Shipboard Scientific Party (2000) as follows:

Void ratio in Equation (1) (Lambe and Whiteman, 1969),

$$e = \{[(1 + W)/\rho_d][\rho_g\rho_w]\} - 1, \quad (1)$$

and porosity,

$$\eta = e/(1 + e), \quad (2)$$

where ρ_w = density of seawater (typical average value) = 1.024 g/cm^3.

AMS

The AMS samples were obtained from the tube samples through the insertion of 7-cm^3 plastic cubes in the right orientations. The remains of the samples were used for smear slide observations, grain-size analysis, and XRD analysis. AMS of the cube samples was measured using a AGICO KLY-3 magnetic susceptometer at a setting of 0.04 mT low magnetic field.

The AMS is geometrically represented by a magnetic susceptibility ellipsoid with three principal axes: the maximum (K_{max}), intermediate (K_{Int}), and minimum (K_{min}) magnetic susceptibility. In general, the ellipsoid is controlled by arrangement of magnetic particles in the sediments (Tarling and Hrouda, 1993). The following parameters were used in this study to represent the shape of the magnetic susceptibility ellipsoid in Equations (3) (Jelinek, 1981), (4) (Stacey et al., 1960), and (5) (Basley and Buddington, 1960):

$$P'=\exp(\mathrm{SQR}\{2[(\eta_1-\eta m)^2+(\eta_2-\eta m)^2+(\eta_3-\eta m)^2]\}), \quad (3)$$

$$F = K_{Int}/K_{min}, \text{ and} \quad (4)$$

$$L = K_{max}/K_{Int}, \quad (5)$$

where

η_1 = $\ln(K_{max})$;
η_2 = $\ln(K_{Int})$;
η_3 = $\ln(K_{min})$,
ηm= $(\eta_1 + \eta_2 + \eta_3)/3$;
P' = corrected anisotropy degree;
F = foliation; and
L = lineation parameter.

The declinations of the K_{max}, K_{Int}, and K_{min} of the AMS were corrected to magnetic north using the on board measured paleomagnetic data (Shipboard Scientific Party, 2000).

Because all the minerals in marine sediments contribute to the AMS in various degrees, it is important to define the kind of mineral most responsible for the measured magnetic fabric by the following two methods. Both vibrating sample magnetometer (VSM) measurements and SEM energy-dispersive spectrometer (EDS) analyses were used for this purpose. The VSM of Molspin Co. Ltd. measures susceptibility in high magnetic fields (K_{hf}) of 500–1000 mT. The K_{hf} is generally a result of magnetic minerals, mainly paramagnetic, not ferrimagnetic minerals (Housen and Sato, 1995; Housen, 1997). On the other hand, low field susceptibility (K_{lf}) in the sediments measured at 0.04 mT by the KLY-3 can be subdivided into components that are contributed by both ferrimagnetic and paramagnetic minerals (Housen and Sato, 1995; Housen, 1997). The ratio of K_{hf}/K_{lf} is inversely proportional to the relative contribution extent of the ferrimagnetic minerals to the K_{lf} (Housen and Sato, 1995; Housen, 1997).

Additionally, ferrimagnetic minerals were separated by a hand magnet from the sediment samples dispersed into distilled water in order to

observe their individual shape. The collected ferrimagnetic minerals were attached to SEM stubs using carbon tape and then coated with carbon. Their chemical composition was analyzed using EDS.

Grain-Size Analysis

The grain-size distribution was obtained using a CIRAS1064 laser diffraction grain-size analyzer. A wet sediment weight of ~0.1 g for each sample was dispersed into boiled water in a glass beaker and then left for 24 hr than was further dispersed by an ultrasonic vibrator for 30–60 s just before measurement.

XRD Analysis

The XRD analysis was conducted for samples finer than 5 μm diameter on a polished glass slide. Three slides were analyzed for each sample in this study; the first slide sample was untreated, the next one was boiled in a dilute HCl (6 N) solution for 1 hr, and the last one was treated with ethylene glycol. CuK_α was used under 40-kV and 15-mA conditions by a RIGAKU RAC-A system.

Using HCl treatment, the kaolinite (001) (7 Å) peak could be identified from the original doublet peaks of kaolinite (001) and chlorite (002) because chlorite in the samples was dissolved by this treatment. Through the ethylene glycol treatment, the smectite (001) (12 Å) peak was found shifted from the original doublet peaks of chlorite (001) and smectite (001) to 15 Å. From the relative extent of each peak area, the component ratio of clay minerals was calculated in each sample qualitatively (Oinuma, 1968; Aoki and Kohyama, 1998) as follows: smectite (15 Å) = 1.0, illite (10 Å) = 3.6, chlorite (7 Å) = 3.6, and kaolinite (7 Å) = 3.6.

Preparation of Samples for SEM and Polarized Microscope

The SEM samples and thin section samples were prepared by the freeze-drying method (Takizawa et al., 1995) in order to avoid microfabric disturbance under the air-drying process that is due to the effect of surface tension of pore water. The sediment from Unit I that was subjected to the air-drying method suffered 25%–40% volume shrinkage, whereas that from Unit II suffered ~60%. As a result, the microfabrics in both units were completely distorted (Fig. F2).

The freeze-drying method was conducted as follows. First, the pore water in the sediment was replaced by ethanol and then by *t*-butyl alcohol for several months. Next, *t*-butyl alcohol in the pores was quickly frozen by liquid nitrogen and sublimated in the vacuum desiccator. Thus, the freeze-dried samples retained the original microfabrics without any texture disruption and were best for SEM observation. The samples were coated by Au-Pd to observe the microfabrics by SEM at a setting of 15 kV and ~80 μA.

The embedded method for preparation of thin sections was conducted as follows. First, the pore water in the sediment was replaced by ethanol and then by propylene oxide for several months. Next, propylene oxide was further replaced by resin Quetol 651 from Nisshin EM Co. Ltd. Finally, the sediments were fixed under 60°C for 24 hr for thin sections.

F2. Comparison between freeze-drying and air-drying, p. 16.

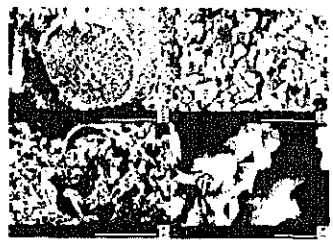

RESULTS

Physical Properties

Grain density of four samples (185-1149A-18H-2, 65–67 cm; 18H-4, 75–77 cm; 19X-1, 40–42 cm; and 20X-1, 88–90 cm) are mostly the same, with values of 2.60, 2.60, 2.61, and 2.59 g/cm^3, respectively. The average grain density of the four samples is 2.60 g/cm^3. The porosity and void ratio calculated by this average grain density and the physical properties (Shipboard Scientific Party, 2000) are shown in Figure F3 and Table T1.

Magnetic Susceptibility and AMS

Although the magnetic susceptibility of the samples from Hole 1149A is a constant ~0.001 SI throughout Units I and II, it changes from 0.001 to 0.002 SI at three stratigraphic horizons: 120.76 mbsf (Sample 185-1149A-14H-2, 106–108 cm) in Subunit IIA, ~135 mbsf (Sample 15H-2, 116–118 cm; 130.36 mbsf, and Sample 15H-7, 36–38 cm; 137.06 mbsf) in Subunit IIB, and 170.68 mbsf (Sample 20X-1, 88–90 cm) in Subunit IIB (Fig. F3; Table T2). This change of magnetic susceptibility at these three horizons reflects the variation in content, kind, and amount of the magnetic minerals.

The magnetic minerals contributing to the magnetic susceptibility and their anisotropy are assumed to be ferrimagnetic minerals of detritic origin because of the following two reasons. The first is that the ratio of K_{hf}/K_{lf}, which reflects contribution percentage of paramagnetic minerals at low magnetic field, is <10% (Fig. F4A), suggesting that the AMS is >90% to the ferrimagnetic minerals. The second comes from a result of SEM-EDS analyses where ferrimagnetic minerals were observed as detritic shapes of ~10 µm diameter by SEM (Fig. F4B, F4C) and the chemical compositions of the minerals are predominantly O and Fe with small amounts of Ti by EDS (Fig. F4B, F4C).

The P' value <1.02 of Unit I indicates the low anisotropy degree of the magnetic susceptibility ellipsoid (Fig. F3). Although the individual ferrimagnetic mineral grains in the sediments have their own shape and AMS, the results of the AMS measurements in Unit I show low degrees of anisotropy. This means that the ferrimagnetic mineral grains probably arrange in a low degree of preferred horizontal orientation, which is mostly random in the sediment.

On the other hand, Unit II is characterized by higher P' and F values with steep K' inclination, reflecting that the ferrimagnetic mineral grains are arranged into preferred horizontal orientation (Fig. F3). The degree of the horizontal arrangement becomes more distinct from ~118 mbsf, which is the boundary between Unit I and Subunit IIA. The P' and F values in Unit II become maximum at 170.68 mbsf (Sample 185-1149A-20X-1, 88–90 cm) (Fig. F3).

The AMS of samples from Hole 1149B are characterized by low P' and F values, high L value, and low angle of K_{min} inclination (Fig. F3; Table T2). These are quite different than those from the same depths in mbsf from Hole 1149A. As the primary magnetic fabric is formed by sedimentation processes usually yielding ellipsoids with $F > L$ and K_{min} inclination >70° (Tarling and Hrouda, 1993), the results from Hole 1149B suggest that these sediments have suffered some deformation through

F3. Magnetic susceptibility, AMS, and K_{min}, p. 17.

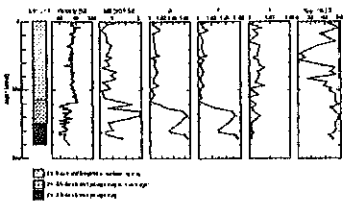

T1. Physical properties of Subunit IIB, p. 28.

T2. Magnetic susceptibility and AMS data, p. 29.

F4. Percentage of low magnetic susceptibility, p. 18.

secondary effects such as bioturbation, tectonic deformation, or drilling disturbance.

Grain Size

The grain-size distribution of each sample is shown in Figure F5. The patterns in Unit I are characterized by a peak at ~10 µm diameter and a wider range in size from ~0.1 to 100 µm than that in Unit II. Some of the patterns are polymodal, having more than two peaks at ~10 µm and 25–50 µm diameter, owing to the fine particles of clay minerals and the coarse particles of volcanic glass fragments and siliceous biogenic tests.

On the other hand, the size range of Unit II is finer than that of Unit I. The grain-size distribution patterns of Subunit IIA are characterized by better sorting, with the range in size being from 0.1 to 30 µm diameter and a sharp peak of ~10 µm. Those of Subunit IIB are characterized by further finer and acuter size range from 0.1 to 25 µm and a peak of ~5 µm diameter.

The above-mentioned tendency of fining and better sorting downward may reflect a more pelagic environment in the older section.

XRD Analysis

Results of the XRD analysis and clay composition are shown in Figures F6 and F7, respectively. The samples in Unit I are predominantly composed of illite, whereas those in Unit II are mainly composed of smectite and illite. Kaolinite decreases downward through Unit I to Unit II.

In the sample at 176.9 mbsf (Sample 185-1149B-3R-5, 60–62 cm), clinoptilolite (9 Å) was detected. The relative peak area of clinoptilolite (9 Å) to illite peak increases with burial depth, suggesting better crystallization in the deeper section. Opal-CT (4.04 Å) was detected in the sample at 179.51 mbsf (Sample 185-1149A-21X-1, 41–43 cm) close to the bottom of Unit II. According to correlation with results from DSDP Leg 20, Site 196, this horizon may be Cretaceous in age and corresponds to the transition zone from opal-A to opal-CT (Shipboard Scientific Party, 2000).

Microfabrics of Units I and II

Unit I

The microfabrics of Unit I are characterized by random arrangement of sedimentary particles (Fig. F8).

The coarse-grained particles, mainly volcanic glass fragments, are concentrated in many pipes, which are ~100 µm diameter and are considered to be burrows (Fig. F8C, F8D). The coarse-grained particles show preferred orientation along the extension direction of the pipe. As the extension direction of pipes are random in the sediment, the total orientation of the coarse-grained particles is also random.

Fine-grained particles, clay platelets, biogenic tests, and single grains are mechanically aggregated in ovoid forms of ~10–100 µm diameter as peds (Fig. F8A, F8B). Some of the biogenic tests and single grains are pressed mechanically into the ped. In the ped, some of the clay platelets are flocculated by low- to high-angle EF contact, although most of them are aggregated by low-angle EF and FF contacts. The peds are in contact with each other either directly or through bridges made of

F5. Grain-size distribution patterns, p. 19.

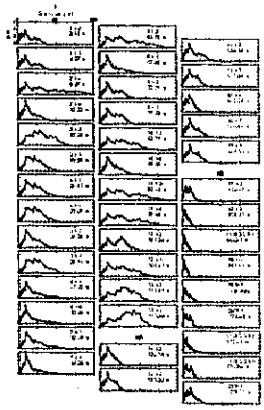

F6. Results of XRD, p. 20.

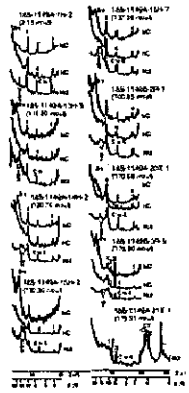

F7. Ratio of clay mineral composition, p. 21.

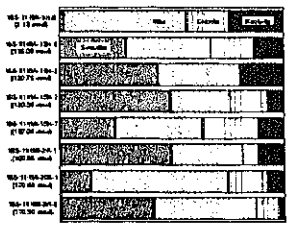

F8. Microfabrics of Unit I, p. 22.

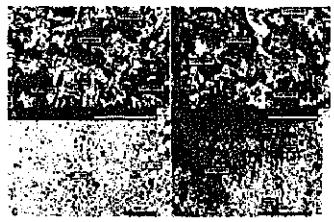

coarse-grained particles in low to high angles (Fig. F8A, F8B). The macropores at ~10–50 µm diameter could be seen between peds (Fig. F8A, F8B). The size of the macropores in the shallow depth (Sample 185-1149A-1H-2, 63–65 cm; 2.13 mbsf) is slightly larger than that in the deeper depth (Sample 7H-1, 79–81 cm; 52.49 mbsf) (Fig. F8A, F8B).

Radiolarian tests are well preserved in all microfabrics throughout Unit I, but there are different types between the inside and outside of the burrow. Inside the burrow, many radiolarian tests are filled with fine sediments (Figs. F2B, F8C), whereas those outside the burrows are vacant (Fig. F8C). This suggests that the radiolarian tests filled their own inside pore spaces with fine sediments as a result of activities of benthic animals during burrowing.

Unit II

The microfabrics are characterized by dimensional preferred horizontal orientation of coarse-grained particles of ~10–100 µm length (Figs. F9C, F10B, F10C, F10D), although the compositions of coarse-grained particles are different in Subunits IIA and IIB. In Subunit IIA, such coarse-grained particles, mainly quartz and feldspar, form thin layers of ~0.5–1.0 mm thickness at sporadic depths (Fig. F9D). These laminations may result from episodic pulses of low density, low-velocity turbidity currents, and/or of volcanic ash falling. High P' and F values in Subunit IIA probably result from these laminations. On the other hand, the coarse-grained particles in Subunit IIB are mainly composed of fragments of biogenic tests and fecal pellets showing preferred horizontal orientation (Fig. F10B, F10D) formed in association with mechanical compaction by overburden pressure.

Although the grains of preferred horizontal orientation obtained from AMS analysis in Subunits IIA and IIB are consistent with the orientation of the coarse-grained particles, the fine-grained particles show random fabric under high-magnification SEM (Figs. F9A, F9B, F10A, F10C). At 125.30 mbsf (Sample 185-1149A-14H-5, 110–112 cm) and 125.30 mbsf (Sample 14H-5, 110–112 cm) of Subunit IIA, clay platelets (mainly smectite and illite) contact at low angle in EF and FF fashion. Those clay platelets are aggregated to small spheres of ~3–30 µm diameter as peds (Fig. F9A, F9B). The small peds are connected by long chains of clay platelets at high-angle EF contact (Fig. F9C). Many macropores of ~5–10 µm diameter are present between the small peds behind the long connectors so that the microfabrics in Subunit IIA are porous.

On the other hand, the boundary of the small peds is unclear at 150.47 mbsf (Sample 185-1149A-17H-3, 77–79 cm), 164.8 mbsf (Sample 19X-1, 40–42 cm), and 170.68 mbsf (Sample 20X-1, 88–90 cm) of Subunit IIB (Fig. F10A). Elongated small peds of wedge shape are aligned along the bedding plane. The microfabrics are in direct contact with each other (Fig. F10A). Therefore, some of the sediments in Subunit IIB are not porous. In the small ped, several clay platelets contact in FF to form small units as paper-stacking structure at a smaller scale (10 µm) (Fig. F10A, F10C). The orientation of small units is random in the ped a mosaic fabric in larger scale (100 m) (Fig. F10B, F10C).

Palynomorphs are seen at 170.68 mbsf (Sample 185-1149A-20X-1, 88–90 cm) and 179.51 mbsf (Sample 21X-1, 41–43 cm), the bottom of Subunit IIB (Fig. F11). There is a growth ring as an internal microstructure (Figs. F10B, F11A), and the surface microstructure is composed of many micropores (Fig. F11D). Some of the palynomorphs are in a closed ellipsoidal form with a long axis parallel to the bedding plane

F9. Microfabrics of Subunit IIA, p. 23.

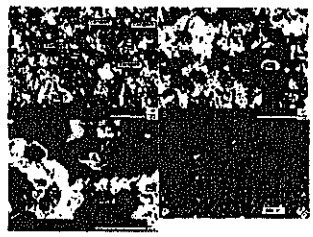

F10. Microfabrics of Subunit IIB, p. 24.

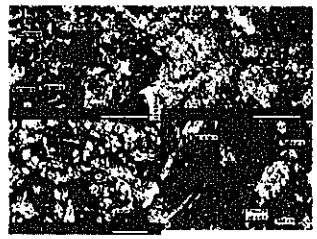

F11. Palynomorphs, vertical views, p. 25.

(Fig. F11C). Because their original shapes are commonly spherical (O'Brien and Slatt, 1990), these ellipsoidal forms indicate the minimum amount of compaction that took place during burial. This further supports the assumption that this initially flocculated sediment has suffered vertical flattening and transformed to shale as explained by O'Brien and Slatt (1990).

The radiolarian tests in Subunit IIB are quite different in the degree of preservation from those in Unit I and Subunit IIA, although the latter are not well preserved. Those in Subunit IIB are not only poorly preserved but are also recrystallized by diagenesis, as marked by opal-CT fillings detected by XRD analysis (Fig. F10D). Furthermore, under the polarized microscope, the bright area surrounding the radiolarian tests can be recognized as pressure solution (Fig. F10D). The degree of brightness and width of the pressure solution increase with burial depth. Platy microcrystals are seen in the pressure solution under high magnification (1000×). The shape, optical properties, and XRD analysis of the platy grains indicate that they are clinoptilolite.

These platy microcrystals (clinoptilolite) of 10–50 µm in length are also observed in veins at 164.85 mbsf (Sample 185-1149A-19X-1, 40–42 cm), 170.68 mbsf (Sample 20X-1, 88–90 cm), and 179.51 mbsf (Sample 21X-1, 41–43 cm), Subunit IIB (Fig. F12A, F12B, F12C). The veins are recognized in two directions as a conjugate set that inclines ~45° against the bedding plane (Fig. F12A). Most of the veins cut laminations with a normal sense of displacement (Fig. F12A), and they are further cut by other larger normal faults (Fig. F12A).

Based on the above results, a schematic model of the microfabrics in Units I and II is illustrated in Figure F13.

F12. Microfabrics of Subunit IIB, p. 26.

F13. Schematic model of microfabrics, p. 27.

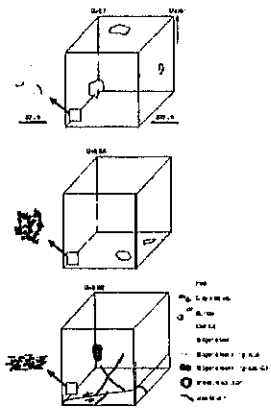

DISCUSSION

The peds in Unit I are relatively large in size (10–100 µm diameter), with porous fabric, and are composed of several kinds of particles. In contrast, those in Unit II are small-sized clay aggregations (3–30 µm diameter). The different features and scales of peds at different depths provide different formation processes, as discussed below.

How fine sediment is aggregated into a flocculated domain to form a ped plays an important role in the pore distribution and framework of the microfabric. Three characteristics, the mode of arrangement of particles, the shape and size of peds and pores, and the degree of recrystallization of minerals, systematically change downward. Together with these changes, many physical properties also change continuously downward. These relations are discussed below with the progressive compaction process.

Origin of Large Peds in Unit I

The formation processes of microfabric in argillaceous sediments through deposition to burial are physical-chemical, bioorganic, and burial diagenesis as discussed by Bennett et al. (1991). According to them, the physical-chemical processes, including bonding mechanisms by van der Waal's attraction, electrostatic attraction, and heating effects, play a major role in microfabric development during the fluvial and eolian transport stage of particulates and on their contact with a depositional interface. The bioorganic process plays an important role in marine and coastal environments during transport and sedimenta-

tion of particulates, particularly in surficial sediments. It includes three biotic mechanisms. First is a biomechanical mechanism, which is the aggregation and disturbance of particulates by planktonic and benthic animals. For example, burrow and fecal pellets are produced by this mechanism. Second is the biophysical mechanism, in which each particulate is flocculated by organic materials as marine snow. Third are the biochemical mechanisms, in which authigenic minerals are formed by bacterial activities in sediment as a formation process of framboidal pyrite. The processes of burial diagenesis drives microfabric development when overburden or tectonic stresses dominate physical-chemical and bioorganic bonding energies (Bennett et al., 1991). In Unit I, because the original sedimentary fabrics (e.g., volcanic ash layer) are completely disturbed by bioturbation, the microfabric is affected by the bioorganic mechanism, especially biomechanical processes but not by physical-chemical mechanism.

Several studies of the microfabric of Holocene sediments have been published on micrographs of features similar to the large peds described in this study. For example, Collins and McGown (1974) described regular aggregations from several kinds of marine sediments similar to the large peds. However, they used an air-drying technique that might have changed the original texture of some artifacts; exact correlation of internal microfabrics between the regular aggregation of these studies and large peds in this study is difficult. Reynolds and Gorsline (1992) observed biofloc from hemipelagic clayey sediments (Santa Monica Basin off the California coast) whose structure is similar to the large peds described in this study. The bioflocs were observed only in the sediments and rocks with bioturbation but were not observed in nonbioturbated turbidite mud and mudstone deposited under anoxic conditions. They concluded that the origin of bioflocs is due to dissolution of fecal pellets and/or pellets of benthic animals because the bioflocs could not be observed in sediments that are not affected by biomechanical processes. Therefore, it is believed that the present peds and their aggregation are the result of biomechanical processes working in pellet formation.

The large peds in Unit I are mechanically compressed in an ovoid shape at a shallower depth than 2.13 mbsf (Sample 185-1149A-1H-2, 63–65 cm). The possible mechanism of mechanical compression in such shallow burial depth is the aggregation process by benthic animals as biofloc. The large peds are clearly distinguished from the fecal pellets in texture and color by polarized microscope observations. Fecal pellets are clearer in shape and darker than peds (Fig. F8D). This confirms our conclusion that the origin of large peds is pellets of benthic animals.

Origin of Connector and Small Peds in Unit II

The connectors are long chains of clay platelets in EF contact. In the Mississippi Delta, sediments are dominated by domains of low- to high-angle EF contacts because of physical-chemical flocs (Bennett et al., 1981). The physical-chemical process in marine sediment is due to electrostatic attraction between clay platelets. EF-particle contacts dominate because the faces of clay minerals are negatively charged, whereas the edges are positively charged (Bennett and Hulbert, 1986). In general, the clay platelets at EF contacts form long chains at shallow burial depths as cardhouse fabric (Bennett et al., 1981). Therefore, the connectors in Subunit IIA are probably formed by electrostatic attraction in shallow burial depths and are preserved at the present depths.

The small peds of clay platelets at low-angle EF and FF contacts observed in this study are similar to floc described in some pelagic clays at 143 mbsf in the eastern equatorial Pacific (Bennett et al., 1981). The outer boundaries of the flocs are well defined, and their structure in transmission electron microscope images is not similar to physical-chemical flocs (Reynolds and Gorsline, 1992). Throughout deposition and burial, there are many possible processes that clay platelets are formed from low-angle EF and FF contact (Bennett et al., 1991). For example, FF contacts are constructed either by the burial compaction process of flocculated clay platelets of EF contacts (Bennett et al., 1981, 1991) or by dispersion depositional process that lack strong bonding (e.g., electrostatic attraction) at each contact point of the clay platelets (Moon and Hurst, 1984; Bennett et al., 1991).

Another mechanism of clay platelets at low-angle EF and FF contacts is clay aggregation processes by zooplankton, which produces a fecal pellet of ~100 µm diameter (Bennett et al., 1991). Small peds could form through fragmentation of such fecal pellets. Pellets of zooplankton play an important role in transporting clay platelets from the sea surface to the seabed under pelagic environments (Honjo, 1978). During sinking in seawater, they become porous and fragile because much of the organic matter (5.6–18 wt%) (Honjo, 1978) in the pellet is decomposed by bacterial activity (Honjo and Roman, 1978). In sediment-trap studies, fragmental pellets of several tens of micronmeters diameter have been described (Honjo, 1978, 1979). Some of the fragmental pellets probably further become porous and fragile by decomposition of calcareous and siliceous biogenic tests, whose contents are 10%–50% and <5%, respectively. Residue of pellets after such decomposition preserves biomechanical aggregation of clay platelets, and it is further dispersed by shear stress because of the internal flow by bioturbation and bottom-current disturbance. These fragmental fecal pellets are still connected by long chains of clay platelets in EF contact as a result of electrostatic attraction as small peds, which we saw in our samples in Subunit IIA.

Compaction Process of Units I and II

The porosity decreases steadily down to ~60 mbsf but increases to 118 mbsf at the boundary between Units I and II and then decreases steadily again down to 180 mbsf at the boundary between Units II and III. The decrease in rate from 0 to 60 mbsf and that from 118 to 180 mbsf is different, indicating different compaction processes.

In Unit I, porosity decreases from ~70% to 60% down to 60 mbsf. Magnetic fabric reflects random orientation of magnetic minerals in Unit I (Fig. F3). The size and shape of the large peds do not change with depth (Fig. F8A, F8B). In between the large peds, however, the contact of each coarse-grained particle changes from a high-angle EF contact to low-angle EF and FF contact compaction (Fig. F8). Coarse-grained particles would slide and rotate perpendicular to the maximum effective stress direction. Even through such particle rearrangement, the total direction of the particle keeps random arrangement. The size and shape of the large ped do not change during compaction. Thus, the macropores would reduce their size during early compaction in Unit I, resulting in porosity decreases in Unit I.

In Unit II, the porosity decreases from ~60% to 50% by overburden pressure are probably due to connector breakage and small ped deformation. Subunit IIA still has distinctive connectors that interconnect

the small peds, whereas they are unclear in Subunit IIB (Figs. F8, F9). The connector represents a concentration point of the effective stress in the microfabrics. As the effective stress works at the connecting edge between the peds, compaction is expected to be present by deformation and destruction of connectors, as shown by Griffiths and Joshi (1990). As a result, the macropores between the small peds would close with this connector breakage process. After the connectors are broken completely, the vertical effective stress induces the changes of shape of the small peds (Fig. F13). The contact of clay platelets in the small ped also changes from EF to FF (Fig. F9). Micropores between the clay platelets in EF contact are reduced during ped deformation in accordance with the porosity decrease. These processes would contribute to porosity decrease in Unit II.

ACKNOWLEDGMENTS

This research used samples and/or data provided by the Ocean Drilling Program (ODP). ODP is sponsored by the U.S. National Science Foundation (NSF) and participating countries under management of Joint Oceanographic Institutions (JOI), Inc. This work was supported in part by a Grant-in-Aid from the Ministry of Education, Culture, and Sports, Japan (A-10304037).

The authors gratefully acknowledge Dr. A.L. Abdeldayem (Tanta University) for carefully reading the manuscript and Dr. T. Yamazaki and Dr. H. Oda (Advanced Industry of Science and Technology) for the help in AMS and the VSM measurements. Also, thanks go to Dr. K. Ikehara (Advanced Industry of Science and Technology) for measurements of the grain size distribution, Dr. T. Takeda (Kyushu University) for many comments on the magnetic properties, and Dr. T. Itabashi (OYO Co. Ltd.) for measurement of the grain density. Dr. T. Sato (Fukada Geological Institute), who kindly revised an early version of the manuscript, is greatly appreciated.

References

Aoki, S., and Kohyama, N., 1998. Cenozoic sedimentation and clay mineralogy in the northern part of the Magellan Trough, Central Pacific Basin. *Mar. Geol.*, 148:21–37.

Anson, G.L., and Kodama, K.P., 1987. Compaction-induced shallowing of the post-depositional remanent magnetization in a synthetic sediment. *Geophys. J. R. Astron. Soc.*, 88:673–692.

Bennett, R.H., Bryant, W.R., and Keller, G.H., 1981. Clay fabric of selected submarine sediments: fundamental properties and models. *J. Sediment. Petrol.*, 51:217–232.

Bennett, R.H., and Hulbert, M.H., 1986. *Clay Microstructure:* Boston (International Human Resources Development Corp. Publ.).

Bennett, R.H., O'Brien, N.R., and Hulbert, M.H., 1991. Determinants of clay and shale microfabric signatures: processes and mechanisms. *In* Bennett, R.H., Bryant, W.R., and Hulbert, M.H. (Eds.), *Microstructure of Fine-Grained Sediments: From Mud to Shale:* New York (Springer-Verlag), 5–32.

Collins, K., and McGown, A., 1974. The form and function of microfabrics features in a variety of natural soils. *Geotech.*, 24:223–254.

Deamer, G.A., and Kodama, K.P., 1990. Compaction-induced inclination shallowing in synthetic and natural clay-rich sediments. *J. Geophys. Res.*, 95:4511–4530.

Griffiths, F.J., and Joshi, R.C., 1990. Clay fabric response to consolidation. *Appl. Clay Sci.*, 5:37–66.

Honjo, S., 1978. Sedimentation of materials in the Sargasso Sea at a 5367 m deep station. *J. Mar. Res.*, 36:469–492.

————, 1979. Material fluxes and modes of sedimentation in the mesopelagic and bathypelagic zones. *J. Mar. Res.*, 38:53–97.

Honjo, S., and Roman, M.R., 1978. Marine copepod fecal pellets: production, preservation and sedimentation. *J. Mar. Res.*, 36:45–57.

Housen, B.A., 1997. Magnetic anisotropy of Barbados prism sediments., *In* Shipley, T.H., Ogawa, Y., Blum, P., and Bahr, J.M. (Eds.), *Proc. ODP, Sci. Results.*, 156: College Station TX (Ocean Drilling Program), 97–105.

Housen, B.A., and Sato, T., 1995. Magnetic anisotropy fabrics from the Cascadia accretionary prism. *In* Carson, B., Westbrook, G.K., Musgrave, R.J., and Suess, E. (Eds.), *Proc. ODP, Sci. Results,* 146 (Pt 1): College Station, TX (Ocean Drilling Program), 233–254.

Jelinek, V., 1981. Characterization of the magnetic fabric of rocks. *Tectonophysics,* 79:63–67.

Kawamura, K., Ikehara, K., Kanamatsu, T., Fujioka, K., and Ogawa, Y. 1999. Compaction process of Pelagic clay from Parece Vera Basin. *In* Saito, Y., Ikehara, K., and Katayama, H. (Eds.), *Proc. Int. Workshop on Sediment Transport and Storage in Coastal Sea-Ocean System:* Tsukuba, Japan, 441–446.

Lambe, T.W., and Whitman, R.V., 1969. *Soil Mechanics:* New York (Wiley).

Moon, C.F., and Hurst, C.W., 1984. Fabrics of muds and shales: an overview. *In* Stow, D.A.V., and Piper, D.J.W. (Eds.), *Fine-Grained Sediments: Deep-Water Processes and Facies.* Spec. Publ.—Geol. Soc. London, 15:579–593.

O'Brien, N.R., and Slatt, R.M. 1990. *Argillaceous Rock Atlas:* New York (Springer-Verlag).

Oinuma, K., 1968. Method of quantitative estimation of clay minerals in sediments by X-ray diffraction analysis. *J. Toyo Univ. Nat. Sci.*, 10:1–15.

Reynolds, S., and Gorsline, D.S., 1992. Clay microfabrics of deep sea mud(stones), California Continental Borderland. *J. Sediment. Petrol.*, 62:41–53.

Shipboard Scientific Party, 2000. Leg 185 summary: inputs to the Izu-Mariana subduction system. *In* Plank, T., Ludden, J.N., Escutia, C., et al., *Proc. ODP, Init. Repts.*, 185: College Station TX (Ocean Drilling Program), 1–63.

Stacey, F.D., Joplin, G., and Lindsay, J., 1960. Magnetic anisotropy and fabric of some foliated rocks from S.E. Australia. *Geofis. Pura Appl.*, 47:30–40.

Stolzenbach, K.D., Newman, K.A., and Wong, C.S., 1992. Aggregation of fine particles at the sediment-water interface. *J. Geophys. Res.*, 97:17889–17898.

Takizawa, S., Kawata, T., and Ohono, Y., 1995. A method of fixation and freeze drying of soft sediments containing water. *Chishitsugaku Zasshi*, 101:941–944.

Tarling, D.H., and Hrouda, F., 1993. *The Magnetic Anisotropy of Rocks:* London (Chapman and Hall).

Velde, B., 1996. Compaction trends of clay-rich deep sea sediments. *Mar. Geol.*, 133:193–201.

Yong, R.N., 1972. Soil technology and stabilization. *Proc. 4th Asia Regional Conference on Soil Mechanics and Foundation Engineering*, 2:111–124.

Figure F1. Bathymetric map of Site 1149 study area.

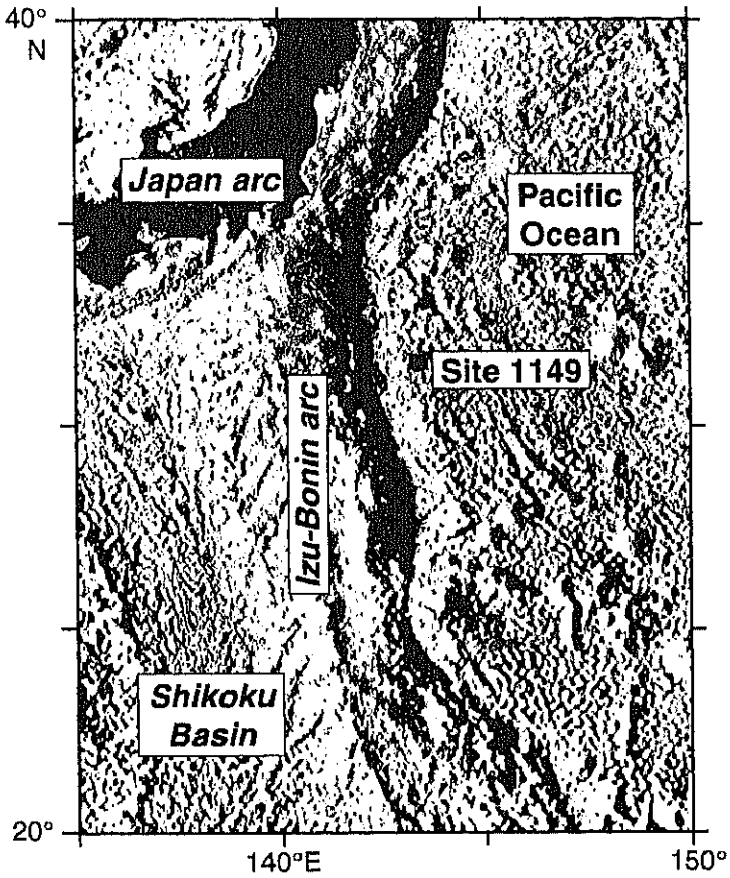

Figure F2. Comparison between both microfabrics treated by the freeze-drying and air-drying methods. Vertical views, secondary electron images at 2.13 mbsf (Sample 185-1149A-1H-2, 63–65 cm), Unit I. A. Microfabric treated by freeze-drying method. Note that fine sediments fill in radiolarian test. B. Close-up image of center of A. Clay platelets have EF contact. C. Microfabric treated by air-drying method, 60 oc, 24 hr. Volume shrinkage of sediment is 40.53%. Length shrinkage of sediment is 15.08% (vertical direction), 16.03% (lateral direction), and 16.60% (depth direction) in this micrograph. D. Close-up image of center of C. Most of clay platelets are in low-angle EF and FF contact.

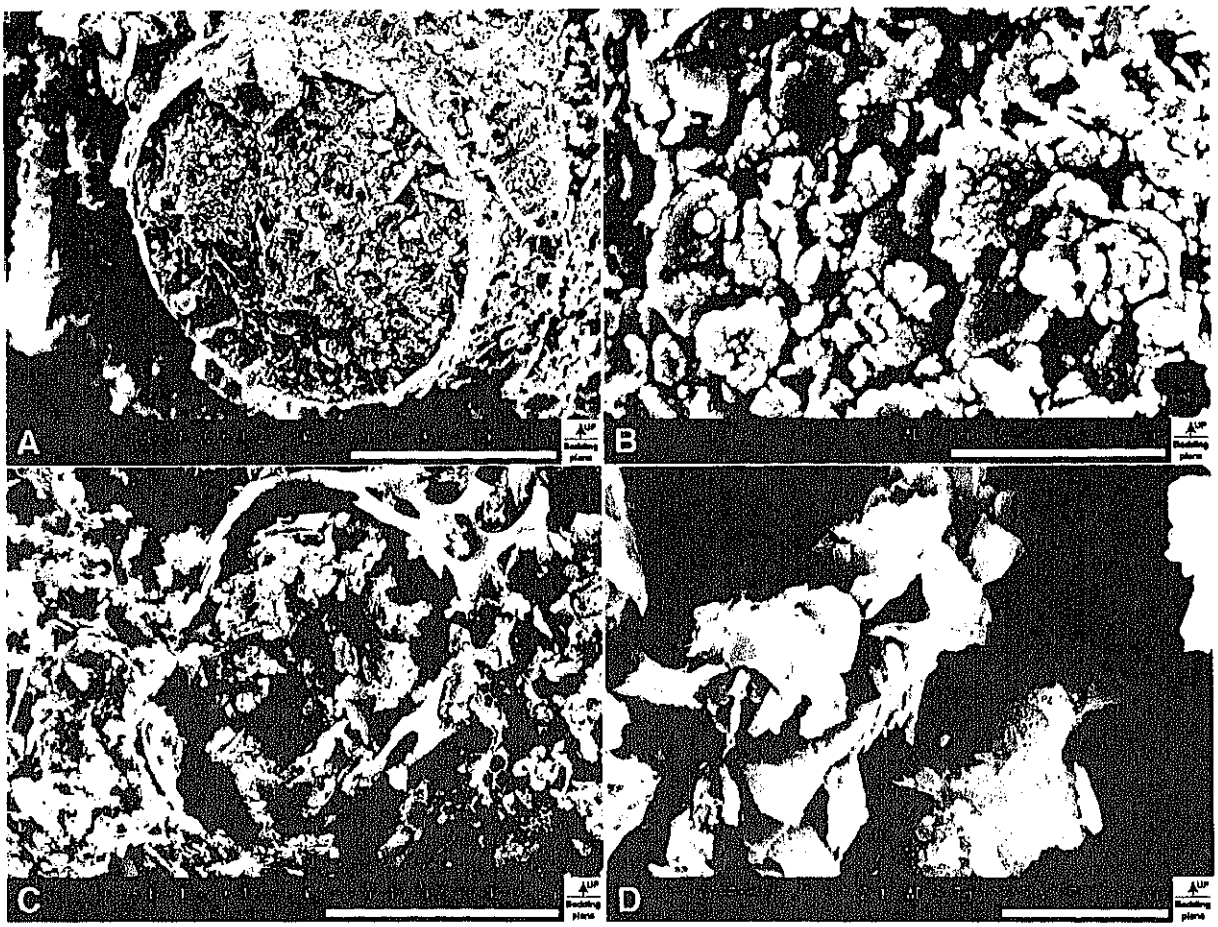

Figure F3. Profiles of magnetic susceptibility (MS), AMS parameters, and K_{min} inclination with depth. Dots and solid lines show data from Hole 1149A, and gray stars show data from Hole 1149B. From left side of figure, magnetic susceptibility profile, P' value (anisotropy degree of MS) profile, F value (foliation degree) profile, L value (lineation degree) profile, and K_{min} (minimum direction of MS) inclination profile.

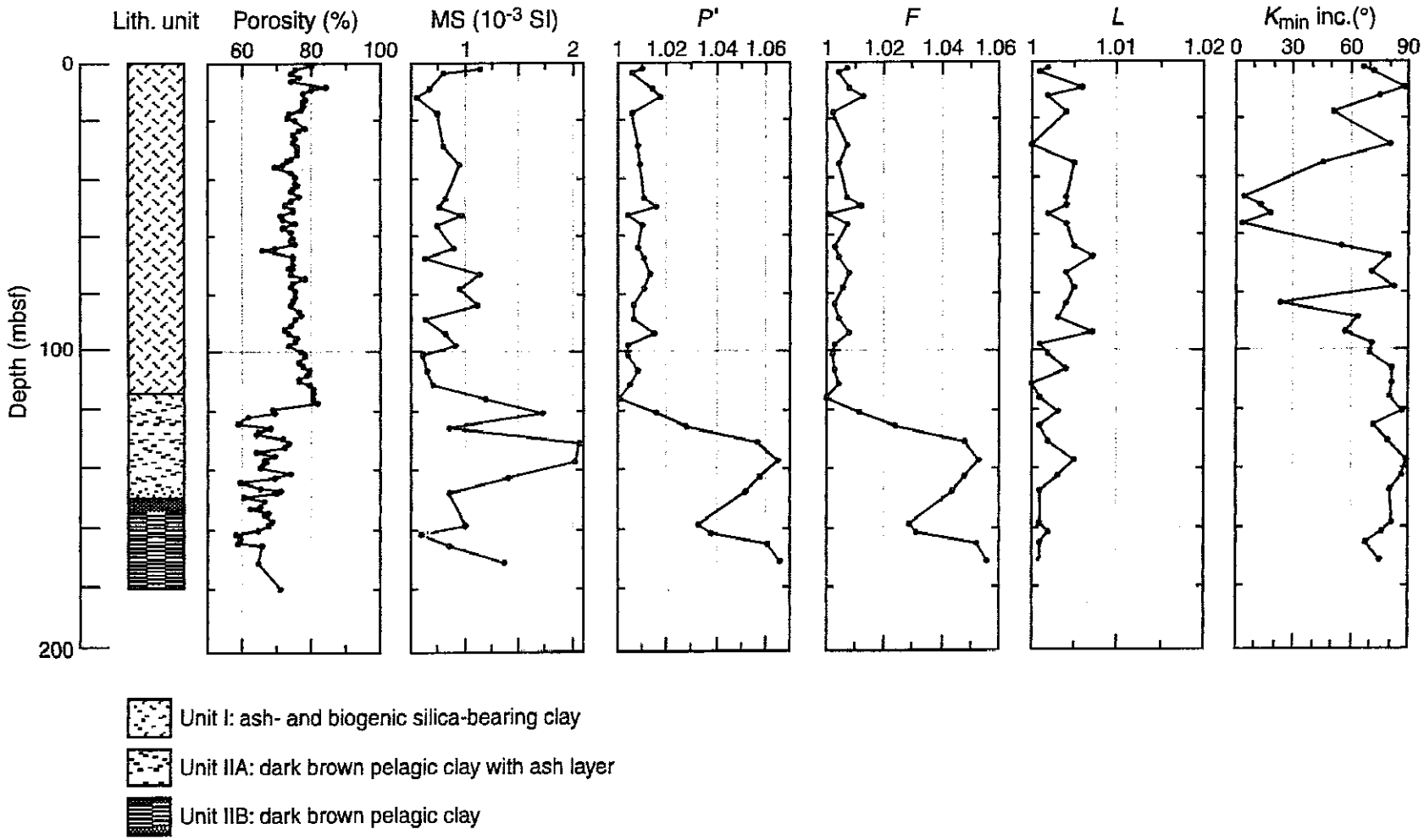

Figure F4. A. Depth vs. percentage of low magnetic susceptibility (K_{lf}) carried by paramagnetic minerals in sediments from Hole 1174B, as determined by comparing high-field and low-field susceptibilities. The majority (>90%) of K_{lf} is carried by ferrimagnetic minerals. B. Individual shape of detrital ferrimagnetic mineral grains (left) and its element composition (right) in Unit I. C. Individual shape of detrital ferrimagnetic mineral grains (left) and its element composition (right) in Unit II. K_{hf} = high magnetic fields, keV = kiloelectron volt.

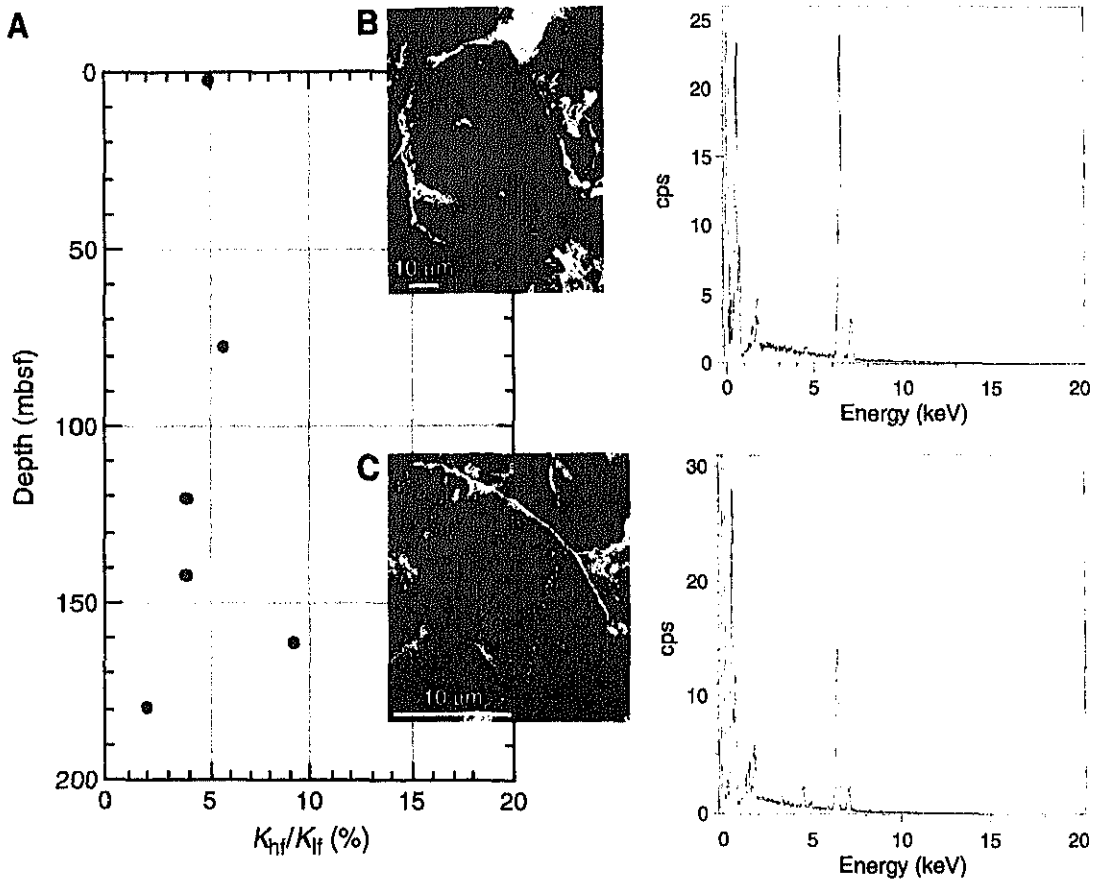

Figure F5. Grain-size distribution patterns from Unit I and Subunits IIA and IIB.

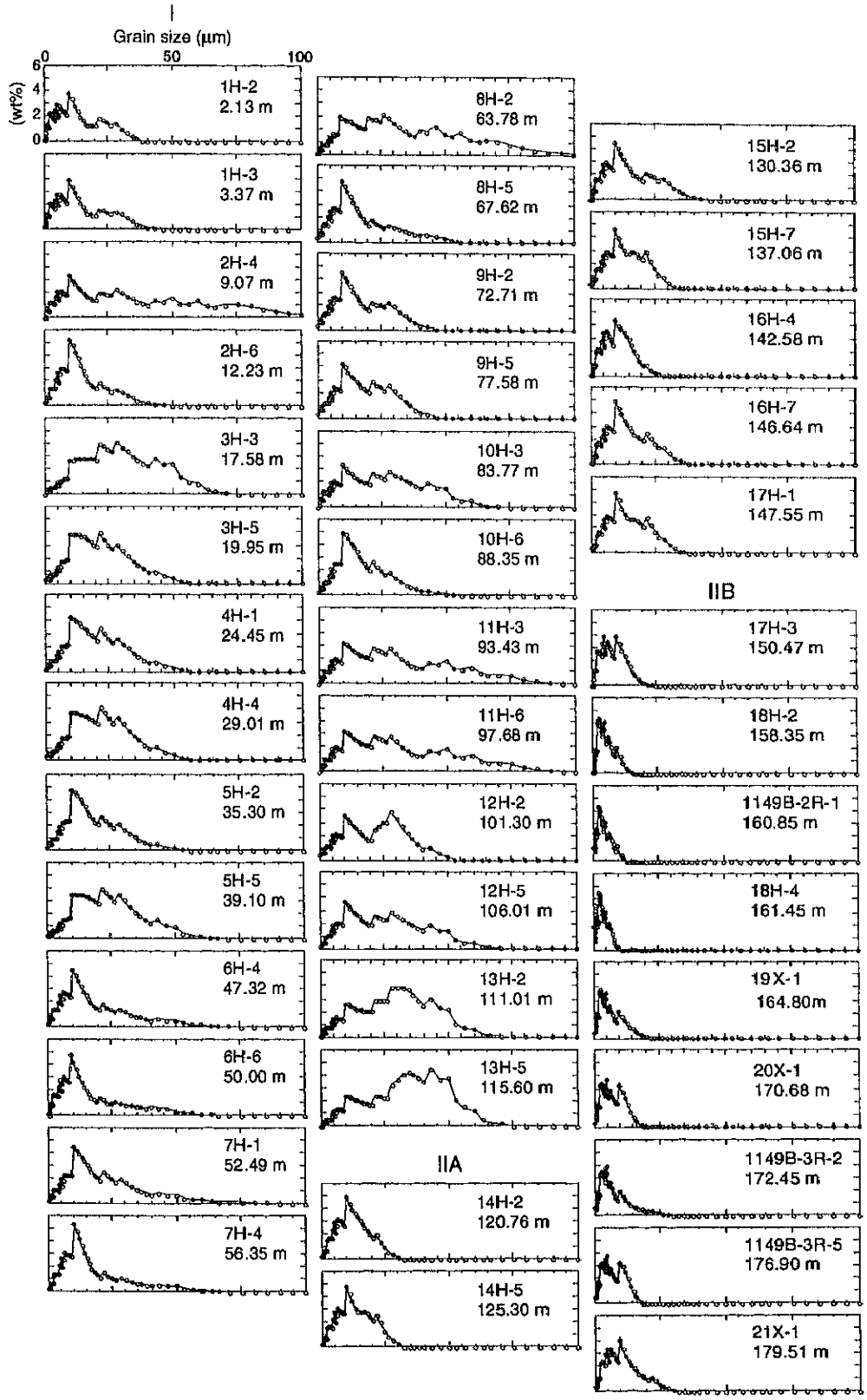

Figure F6. Results of XRD. Peaks represent smectite (Sm), illite (I), chlorite (Ch), kaolinite (K), quartz (Q), feldspar (F), zeolite (Z), and opal-CT (CT). EG = sample treated by ethylene glycol. HCl = sample treated by HCl. Not = sample not treated. d = d-spacing.

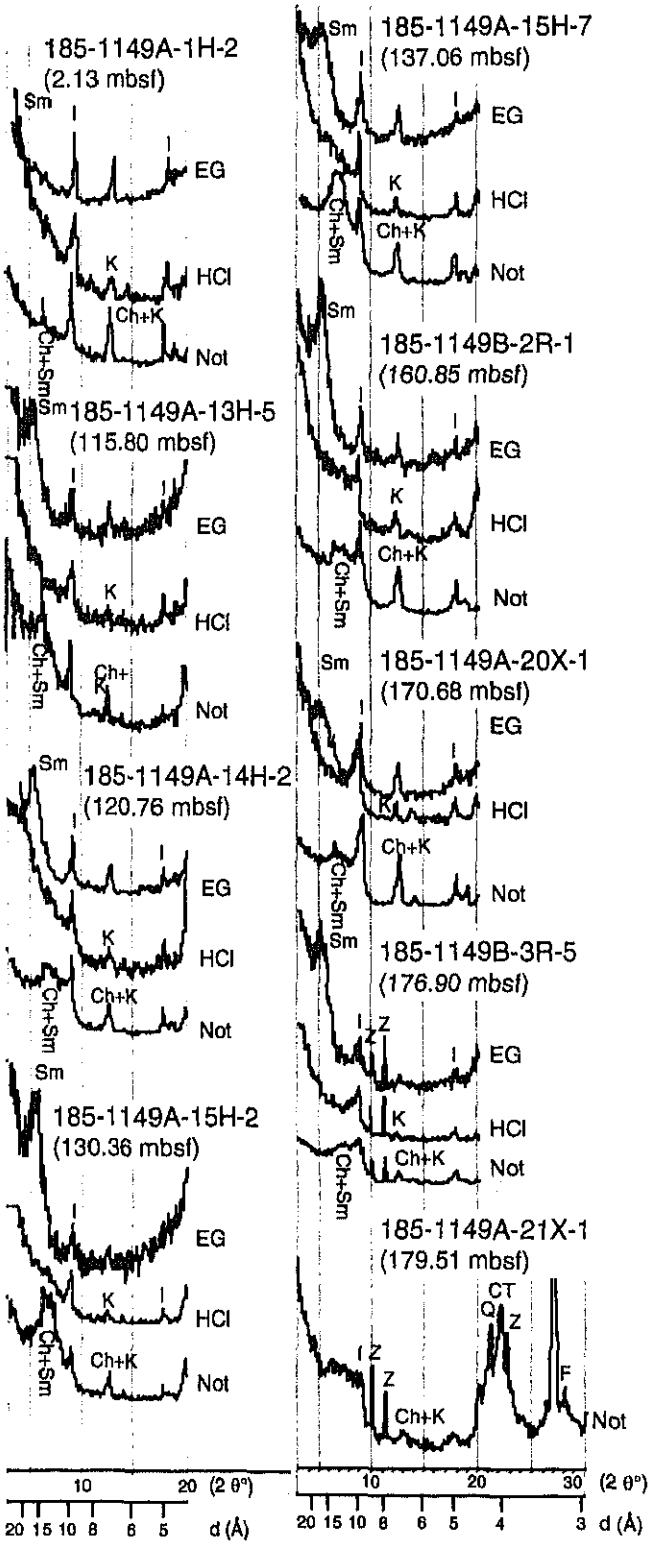

Figure F7. Ratio of clay mineral composition (smectite:illite:chlorite:kaolinite) in Units I and II.

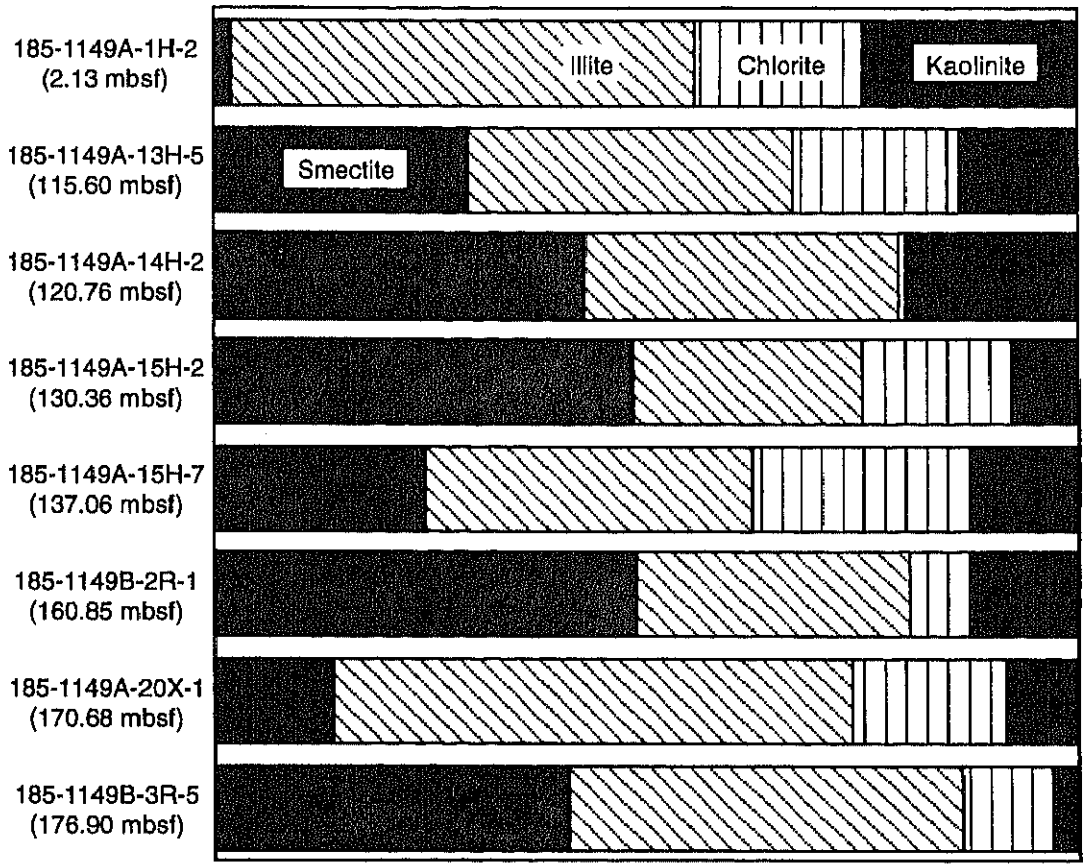

Figure F8. Microfabrics of Unit I. A. General view showing random and porous fabric from core at 2.13 mbsf (Sample 185-1149A-1H-2, 63–65 cm); vertical view, secondary electron image. B. Microfabrics from core at 52.49 mbsf (Sample 185-1149A-7H-1, 79–81 cm) showing random and porous fabric; vertical view, secondary electron image. C. Cross section from core at 2.13 mbsf (Sample 185-1149A-1H-2, 63–65 cm). Radiolarian tests in burrow are filled by fine sediments; vertical view, open nicols. D. Cross section from core at 115.60 mbsf (Sample 185-1149A-13H-5, 90–92 cm). Peds and macropores are seen in microfabric; vertical view, open nicols.

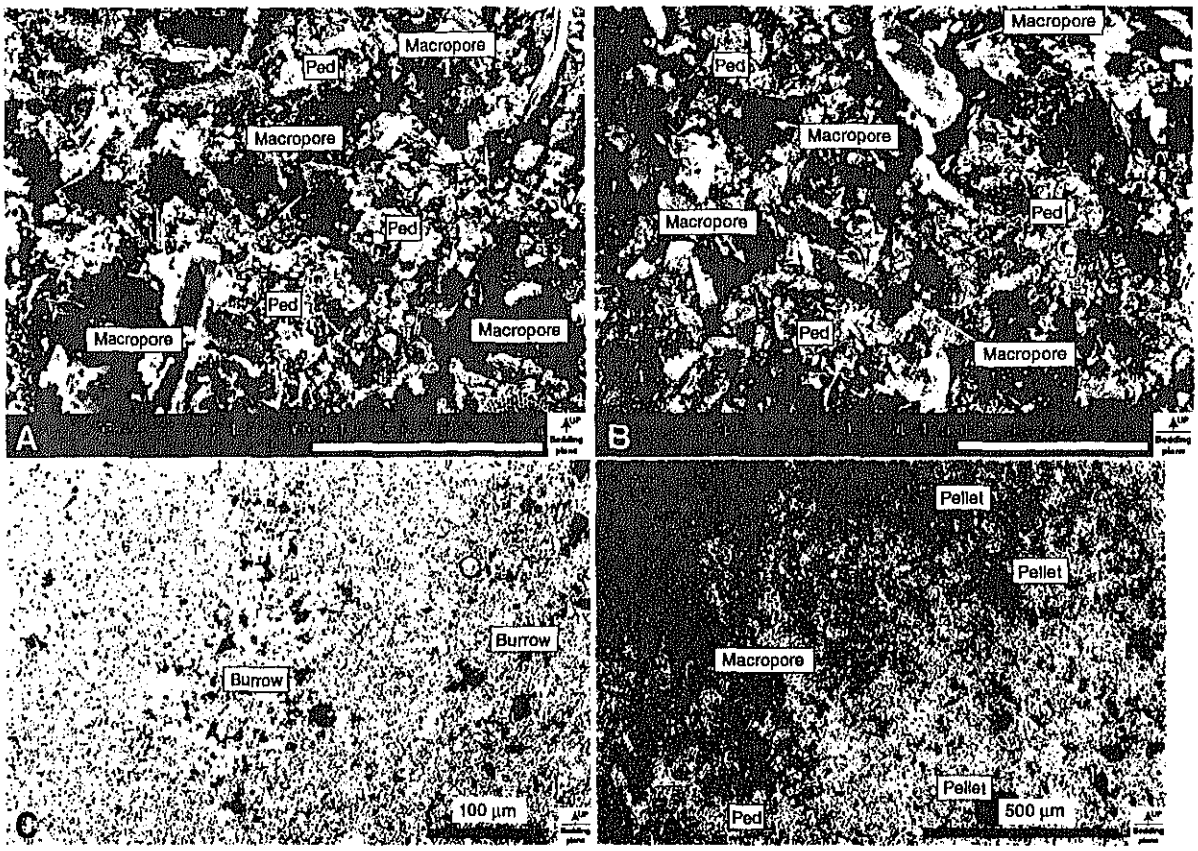

Figure F9. Microfabrics of Subunit IIA. A. General view showing random and porous fabric from core at 125.30 mbsf (Sample 185-1149A-14H-5, 110–112 cm); vertical view, secondary electron image. B. Close-up image of center of A. Peds are linked by clay platelets in EF contacts; vertical view, secondary electron image. C. Connectors, which are chain linked by each clay platelet in EF contact, at 125.30 mbsf (Sample 185-1149A-14H-5, 110–112 cm); vertical view, secondary electron image. D. Fabric showing preferred orientation of clay platelets from core at 125.30 mbsf (Sample 185-1149A-14H-5, 110–112 cm); vertical view, crossed nicols.

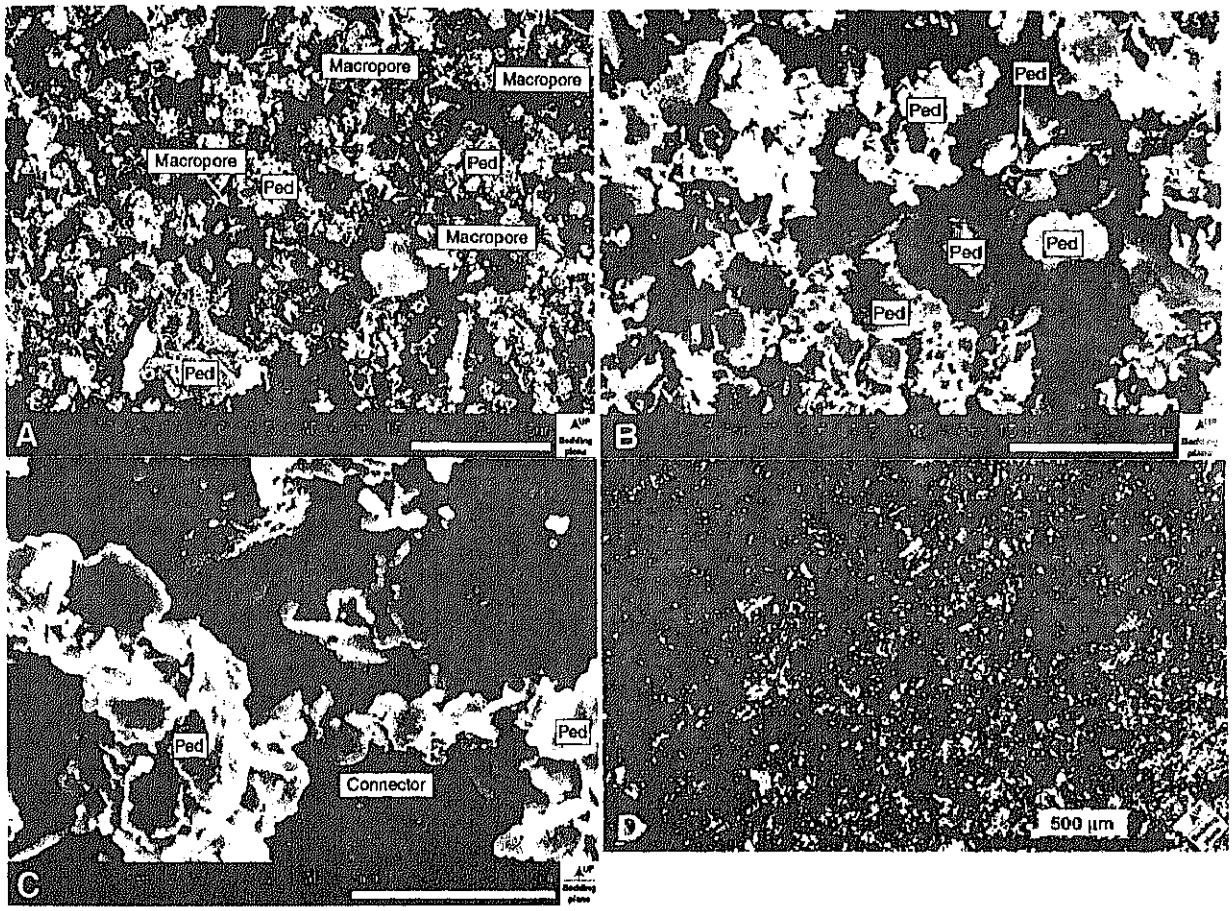

Figure F10. Microfabrics of Subunit IIB. A. General view showing random fabric of clay platelets in FF contact from core at 150.47 mbsf (Sample 185-1149A-17H-3, 77–79 cm); vertical view, secondary electron image. B. Fabric showing strongly preferred orientation of coarse-grained particles from core at 170.68 mbsf (Sample 185-1149A-20X-1, 88–90 cm); vertical view, secondary electron image. C. Close-up image of center of B; vertical view, secondary electron image. D. Fabric showing strongly preferred orientation of coarse-grained particles from core at 164.8 mbsf (Sample 185-1149A-19X-1, 40–42 cm). Note pressure solution around molding of radiolarian tests; vertical view, crossed nicols.

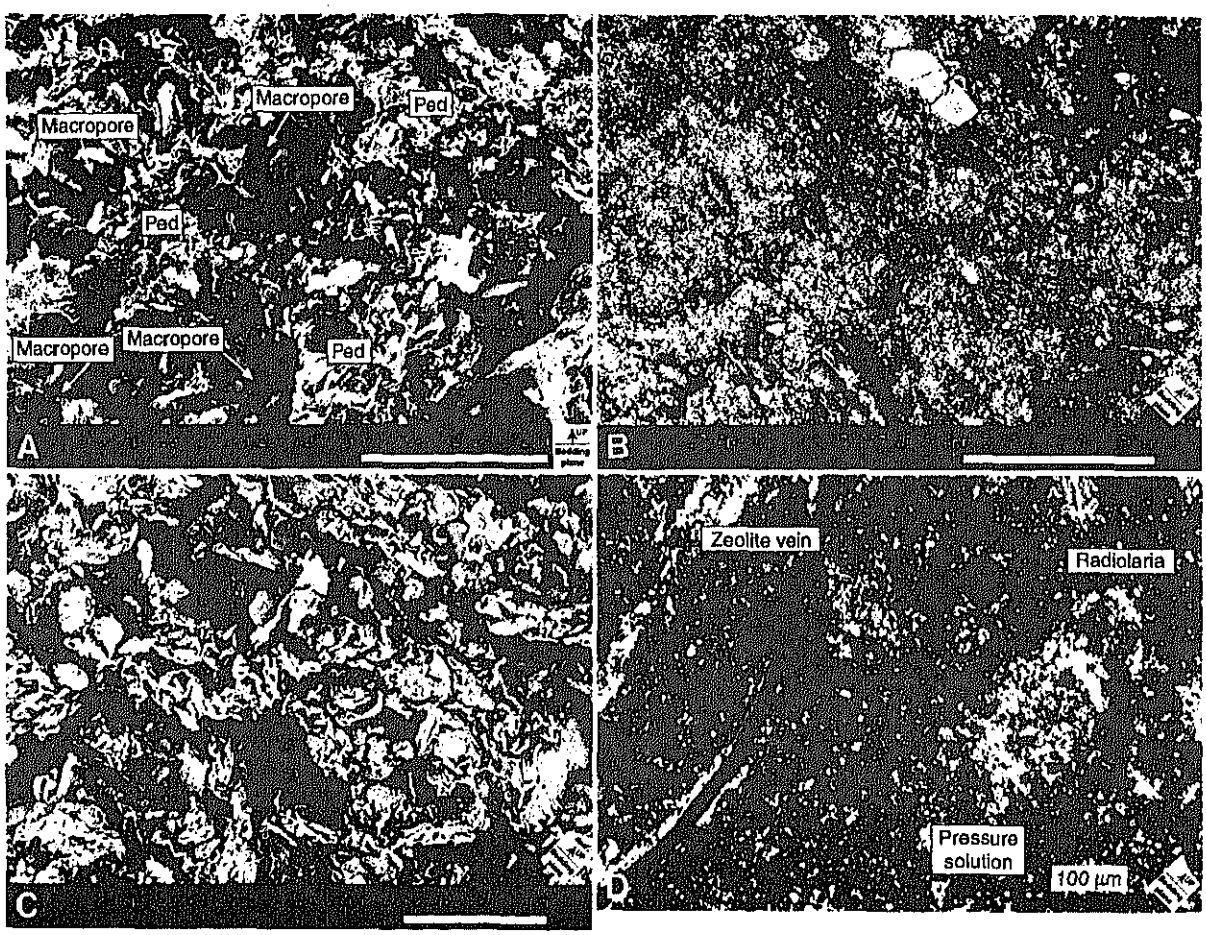

Figure F11. Palynomorphs, vertical views. A, B, C. Back-scatter images at 179.51 mbsf (Sample 185-1149A-21X-1, 41–43 cm). D. Secondary electron image at 170.68 mbsf (Sample 185-1149A-20X-1, 88–90 cm) that allows the upper direction to be shown.

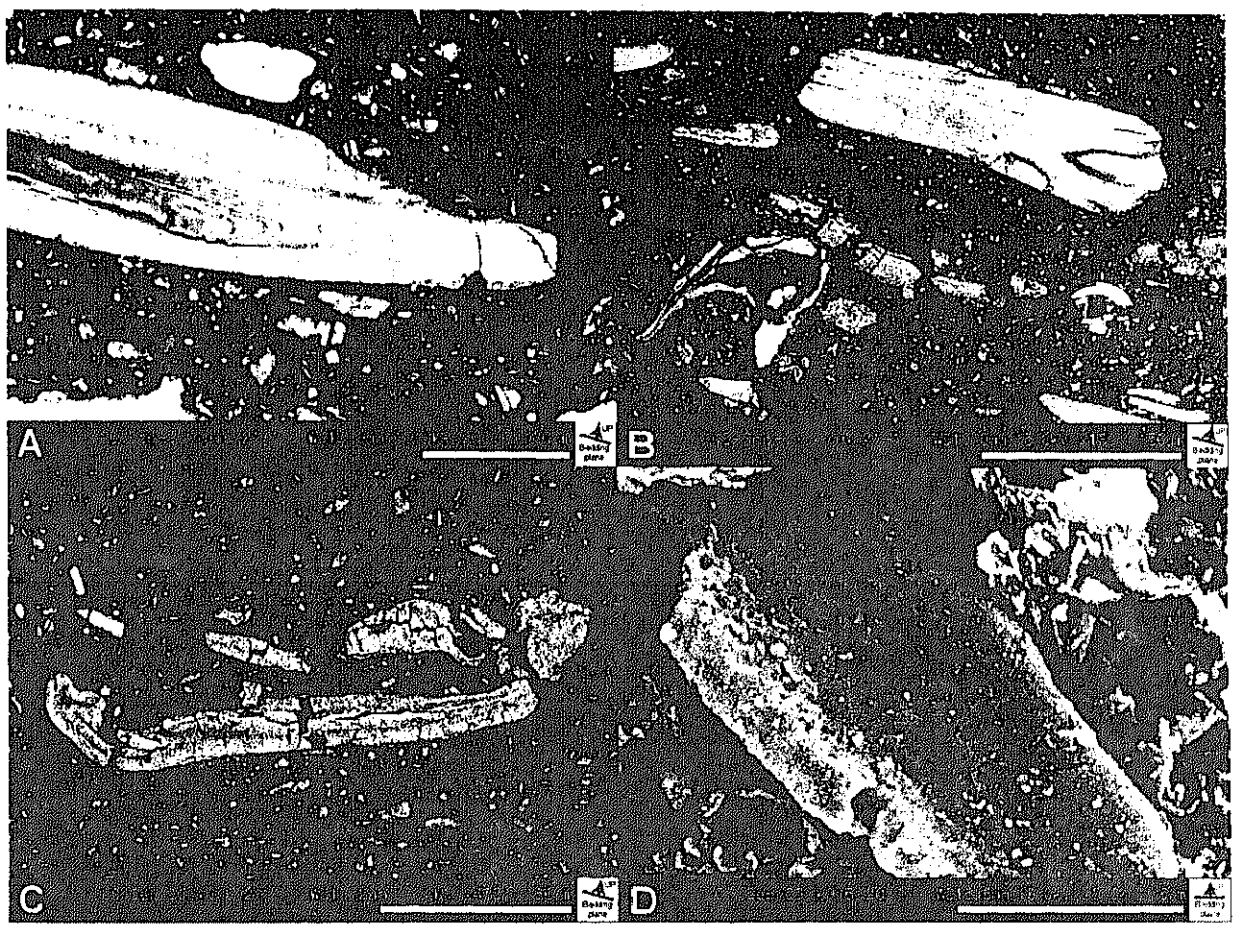

Figure F12. Microfabrics of Subunit IIB at 179.51 mbsf (Sample 185-1149A-21X-1, 41–43 cm). A. General view showing zeolite veins and faults. Zeolite veins are conjugated. B. Close-up view of zeolite vein. Microclinoptilolite grains in platy shape are seen in the vein. C. Detailed microfabric in zeolite vein observed by secondary electron image. Platy clinoptilolite grains are seen.

Figure F13. Schematic model of microfabrics in Unit I and Units IIA and IIB.

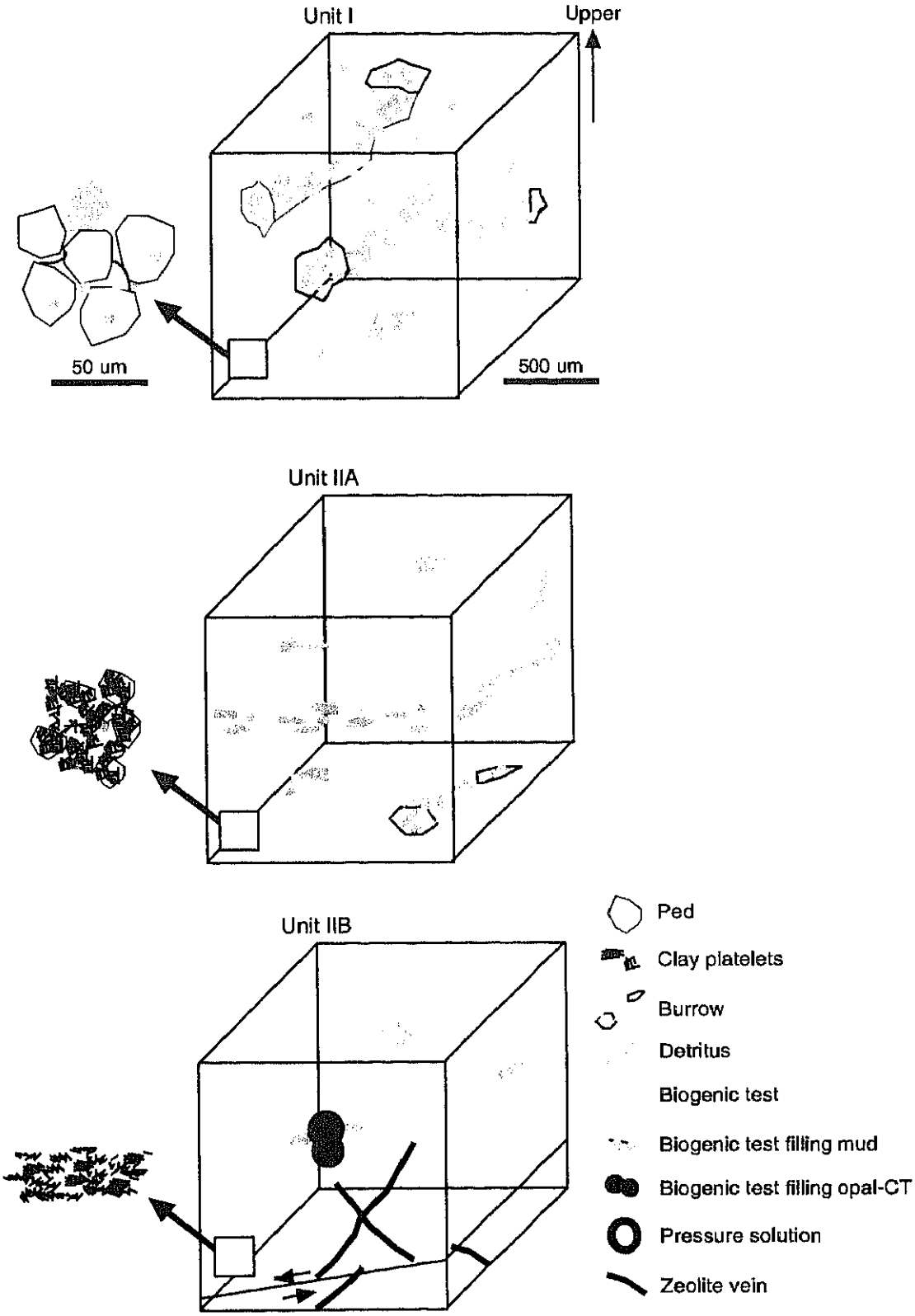

Table T1. Physical properties in Subunit IIB, Site 1149A.

Core, section, interval (cm)	Depth (mbsf)	Water content (dry%)	Wet bulk density (g/cm^3)	Porosity (%)	Void ratio
185-1149A-					
17H-3, 73–75	150.43	73.61	1.56	66.25	1.96
17H-4, 104–106	152.04	72.12	1.60	65.08	1.86
17H-5, 21–23	152.71	66.11	1.66	62.47	1.66
17H-6, 99–101	154.24	83.49	1.57	67.86	2.11
17H-7, 70–72	155.45	78.89	1.59	66.62	2.00
18H-1, 69–71	156.89	85.53	1.54	68.82	2.21
18H-2, 70–72	158.40	80.51	1.56	67.54	2.08
18H-3, 70–72	159.90	70.36	1.59	64.94	1.85
18H-4, 70–72	161.40	53.61	1.70	58.43	1.41
18H-5, 70–72	162.90	56.74	1.70	59.26	1.45
18H-6, 38–40	164.08	55.04	1.70	58.82	1.43
19X-1, 33–35	164.73	66.11	1.51	65.86	1.93
20X-1, 82–84	170.62	68.35	1.59	64.53	1.82
21X-1, 45–47	179.55	84.16	1.42	71.04	2.45

Notes: Water content and wet bulk density are data from onboard MST measurement. Porosity and void ratio are calculated by grain density 2.6 = g/cm^3.

Table T2. Magnetic susceptibility (MS) and anisotropy of MS data, Hole 1149A.

Core, section, interval (cm)	Depth (mbsf)	MS (10^{-3} SI)	P'	L	F	K_{max} Dec (°)	K_{max} Inc (°)	K_{min} Dec (°)	K_{min} Inc (°)
185-1149A-									
1H-2, 63–65	2.13	1.14	1.01	1.002	1.007	332.1	12.8	93.7	66.5
1H-3 37–39	3.37	0.81	1.006	1.001	1.004	69.21	14.6	285.31	72.2
3H-4, 37–39	9.07	0.67	1.014	1.006	1.008	298.05	1.8	142.45	88
2H-6, 53–55	12.23	0.55	1.017	1.002	1.013	153.66	13.1	357.96	75.6
3H-3, 88–90	17.58	0.75	1.006	1.004	1.002	163.62	8.7	62.92	50.5
4H-4, 131–133	29.01	0.81	1.008	1	1.007	188.64	1.5	288.34	81
5H-2, 110–112	35.30	0.95	1.009	1.005	1.004	136.55	15.8	243.35	45.6
6H-4, 62–64	47.32	0.82	1.011	1.004	1.007	287.89	13.2	18.99	4.8
6H-6, 30–32	50.00	0.76	1.016	1.004	1.012	69.19	67.4	305.09	13.1
7H-1, 79–81	52.49	0.97	1.004	1.002	1.001	300	49	188.5	17.7
7H-4, 15–17	56.35	0.74	1.01	1.004	1.007	44.6	29.1	312.9	3.1
8H-2, 108–110	63.78	0.89	1.008	1.005	1.003	218.94	14.3	330.34	55.1
8H-5, 42–44	67.62	0.64	1.011	1.007	1.004	138.48	9.2	286.58	79.2
9H-2, 51–53	72.71	1.15	1.013	1.004	1.008	41.77	2.1	137.87	70.8
9H-5, 88–90	77.58	0.95	1.011	1.005	1.006	1.06	5.5	220.56	82.8
10H-3, 57–59	83.77	1.12	1.007	1.004	1.003	220.84	21.6	120.94	23.5
10H-6, 65–67	88.35	0.62	1.007	1.003	1.004	72.55	14.6	193.65	63.2
11H-3, 73–75	93.43	0.82	1.015	1.007	1.008	210.09	24.6	75.29	57
11H-6, 48–50	97.68	0.92	1.004	1.001	1.003	175.35	11.9	303.05	70.9
12H-2, 60–62	101.30	0.61	1.004	1.002	1.002	327.78	5.3	222.68	70.3
12H-5, 76–78	106.01	0.64	1.008	1.004	1.003	98.34	7.2	250.94	81.9
13H-2, 81–83	111.01	0.71	1.005	1	1.004	26.37	5.9	250.47	81.8
13H-5, 90–92	115.60	1.19	1.001	1.001	1	142.56	3.1	33.66	80.5
14H-2, 106–108	120.76	1.72	1.016	1.003	1.011	301.01	2.9	96.41	86.8
14H-5, 110–112	125.30	0.86	1.028	1.001	1.024	231.78	16.3	76.18	72.2
15H-2, 116–118	130.36	2.06	1.057	1.002	1.048	303.62	8.3	164.62	79
15H-7, 36–38	137.06	2.02	1.065	1.005	1.053	7.46	0.9	214.06	89
16H-4, 88–90	142.58	1.41	1.058	1.003	1.048	239.69	0.2	145.69	86.8
17H-1, 85–87	147.55	0.86	1.052	1.001	1.044	141.13	1.8	40.03	80.7
18H-2, 65–67	158.35	1.01	1.033	1.001	1.029	250.75	3.3	138.55	81.2
18H-4, 75–77	161.45	0.59	1.038	1.002	1.031	325.24	8.6	197.44	76.2
19X-1, 40–42	164.80	0.86	1.061	1.001	1.052	338.38	6.2	232.48	68.3
20X-1, 88–90	170.68	1.37	1.066	1.001	1.056	107.84	4	213.84	75.6
185-1149B-									
2R-1, 25–27	160.85	0.64	1.028	1.017	1.01		43.1		39.9
3R-2, 65–67	172.45	1.52	1.017	1.001	1.014		5.9		69.9
3R-5, 60–62	176.90	1.49	1.003	1.002	1.002		12.3		33.3

Note: Dec = declination (°), Inc = inclination (°).

ELSEVIER

Marine Geology 189 (2002) 371–379

MARINE GEOLOGY
INTERNATIONAL JOURNAL OF MARINE GEOLOGY, GEOCHEMISTRY AND GEOPHYSICS

www.elsevier.com/locate/margeo

Long-lived early Cretaceous seamount volcanism in the Mariana Trench, Western Pacific Ocean

Naoto Hirano[a,*], Yujiro Ogawa[b], Kazuo Saito[c]

[a] *Doctoral Program in Geoscience, University of Tsukuba, Tsukuba 305-8571, Japan*
[b] *Institute of Geoscience, University of Tsukuba, Tsukuba 305-8571, Japan*
[c] *Department of Earth Sciences, Yamagata University, Yamagata 990-8560, Japan*

Received 13 August 2001; accepted 19 June 2002

Abstract

An alkaline volcanic rock sample, peralkaline rhyolite pillow lava, in addition to some radiolarian-bearing pelagic sedimentary rocks, were collected by the Japanese submersible *Shinkai 6500* from Quesada Seamount on the oceanward slope of the Mariana Trench. ^{40}Ar–^{39}Ar dating resulted in a plateau age of 129.3±2.6 Ma, which is approximately 10 Myr younger than the radiolarian age of the oldest intercalated tuffaceous radiolarian claystone of early Berriasian age (approximately 140 Ma). Fragments of volcanic glass that are of alkali-basalt (hawaiite) composition may indicate that this tuffaceous claystone was formed during the shield-building volcanic stage. Because the peralkaline rhyolite is a very differentiated volcanic rock and commonly erupts in the post-shield stage, we interpret that the activity lasted for a long period (approximately 10 Myr). This long-lived shield-building stage may be due to the slow moving rate of the Pacific Plate during the Early Cretaceous. © 2002 Elsevier Science B.V. All rights reserved.

Keywords: seamount; Ar–Ar age; alkali-basalt; rhyolite; post-shield volcanism; Cretaceous

1. Introduction

Most seamounts, islands and atolls on the present Western Pacific Plate were formed by submarine intra-plate volcanism mainly during the Cretaceous period (e.g. Tokuyama, 1980; Rea and Vallier, 1983; Cox, 1991; Fuller and Weeks, 1991; Larson, 1991; Haggerty and Silva, 1995). Koppers et al. (1998) named this area the Western Pacific Seamount Province (WPSP). In the WPSP region, the Magellan Seamount Chain, the Marshall–Gilbert Seamount Chain and the Marcus–Wake Seamount Chain show complicated age distributions. Although Late Cretaceous seamounts are dominant in the WPSP, some Early Cretaceous seamounts are reported, such as Himu and Hemler Seamounts (Smith et al., 1989), Ita Mai Tai Seamount (Koppers et al., 1998) and Look Seamount (Lincoln et al., 1993) (Fig. 1).

Almost all intra-plate volcanoes display a characteristic evolutionary sequence, from a voluminous alkaline or tholeiitic shield-building phase,

* Corresponding author. Present address: Earth and Planetary Science, Tokyo Institute of Technology, 2-12-1 Ookayama, Meguro, Tokyo 152-8551, Japan.
Tel.: +81 (3) 5734 2338; Fax: +81 (3) 5734 3538.
E-mail address: nhirano@geo.titech.ac.jp (N. Hirano).

0025-3227/02/$ – see front matter © 2002 Elsevier Science B.V. All rights reserved.
PII: S0025-3227(02)00445-0

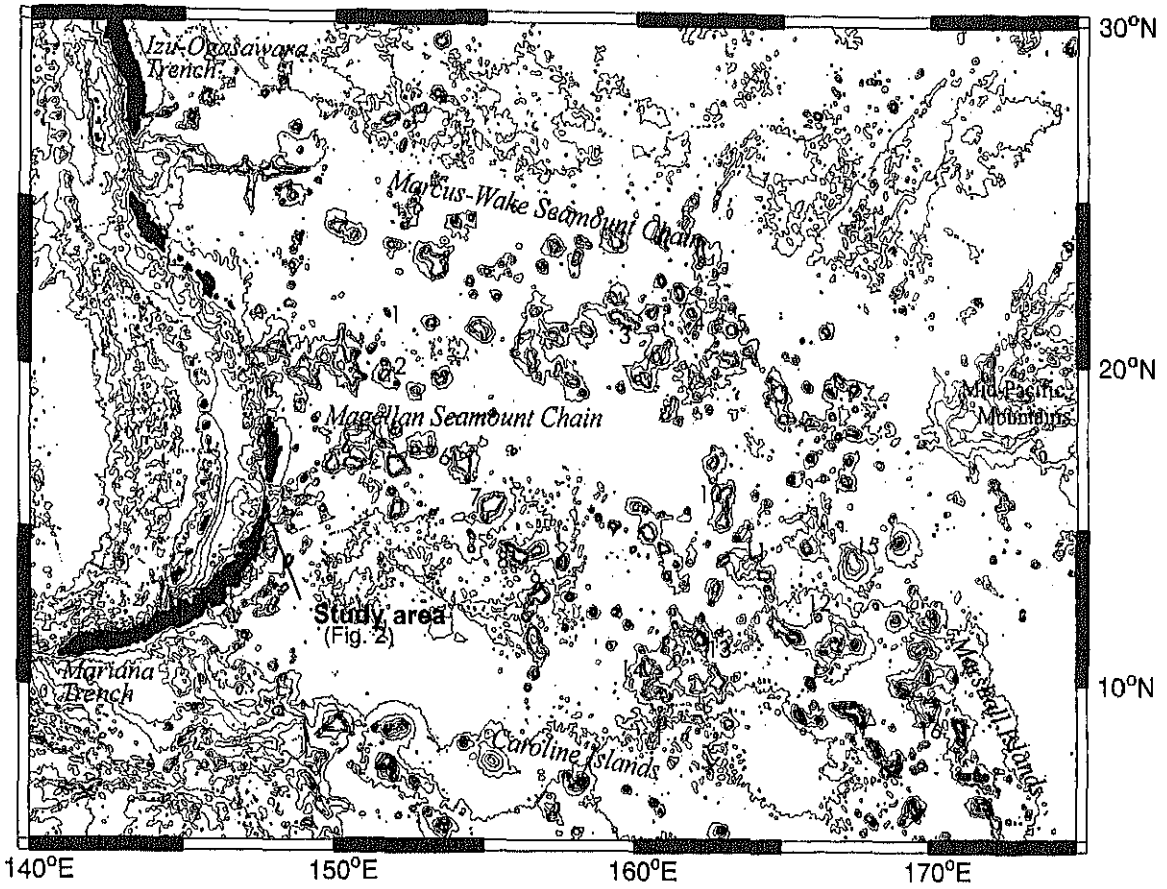

Fig. 1. The bathymetric map of the WPSP. Contour interval is 1000 m. The black areas show more than 7000 m at depth and islands. Numbers show the sites of seamounts whose ^{40}Ar–^{39}Ar ages already reported. These names, ^{40}Ar–^{39}Ar ages and rock types used for the dating are as follows; 1: Himu, 120.2±0.4 Ma*, 2: Hemler, 99.4–105.0 Ma*, 3: Lamont, 87.2±0.3 Ma (basalt) and 81.5±0.6 Ma (basalt)**, 4: Miammi, 96.8±0.8 Ma (basalt)**, 5: Wilde, 90.6±0.3 Ma (mugearite)**, 6: Vlinder, 95.1±0.5 Ma (hawaiite)***, 7: Pako, 91.3±0.3 Ma (hawaiite)***, 8: Ioah, 87.1±0.3 Ma (hawaiite)***, 9: Ita Mai Tai, 118.1±0.5 Ma (hawaiite)***, 10: North Woden, 85.3±0.4 Ma****, 11: Lobbadede, 82.4±2.4 Ma****, 12: Look, 138.2±0.8 Ma****, 13: Anewetak, 75.9±0.6 Ma****, 14: Likelep, 82.1±0.7 Ma and 75.5±0.8 Ma****, 15: Ratak (Woden-Kopakut), 82.2±1.6 Ma (hawaiite, alkali olivine basalt)*****, 16: Erikub (Lokkworkwor), 87.3±0.6 Ma (hawaiite)*****. These data refer to Smith et al. (1989)*, Davis et al. (1989)*****, Koppers et al. (1998)***, Lincoln et al. (1993)****, Winterer et al. (1993)**. This map features detailed bathymetry derived from the predicted bathymetry database (Smith and Sandwell, 1997) and are produced using the Generic Mapping Tools (GMT version 3.4) of Wessel and Smith (1991, 1998).

to post-shield stage alkaline and its differentiated phase, ultimately culminating in a post-erosional (rejuvenated) strongly alkaline stage (e.g. Batiza, 1989). A pattern of shield-building and post-shield stages has been observed in many oceanic islands; e.g. Hawaii Islands (Macdonald and Katsura, 1964), Canary Islands (Freundt and Schmincke, 1995) and Comores Islands (Strong, 1972).

Combined studies of radiometric ages, volcanic sequences and petrology of a seamount are essential for understanding the complicated age distributions of seamounts in the WPSP. In this paper we analyze the Quesada Seamount on the east side of the Mariana Trench and discuss the evolutionary history of this Early Cretaceous seamount.

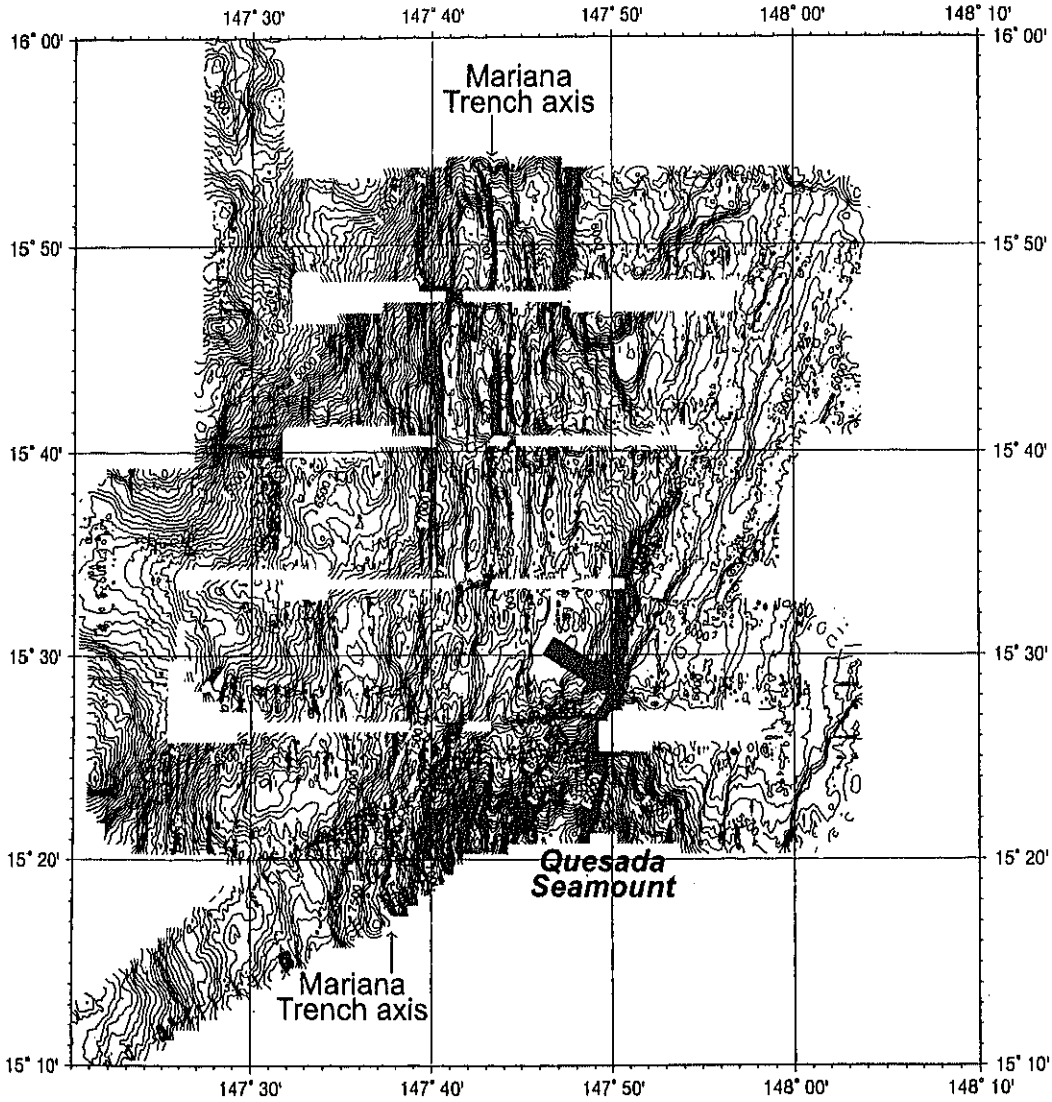

Fig. 2. Multi-narrowbeam map of the study area. The dive site is shown by an arrow. Contour interval is 100 m. Referred to Ogawa et al. (1994).

2. Geologic and tectonic setting

The seamount is located at 15°29′N and 147°50′E, and is at least 35 km in diameter and approximately 3000 m in altitude above the abyssal plain. The volcanic edifice has been disrupted by normal faulting related to horizontal extension, as the Pacific Plate subducts and bends under the Philippine Sea Plate (Ogawa et al., 1994; Smoot, 1997). The faulting produced many steep scarps composed of volcanic rocks and pelagic sedimentary rocks (Fig. 3). Two volcanic and four sedimentary rock samples were collected from these cliffs during the 181st dive of the JAMSTEC submersible *Shinkai 6500* on October 4th, 1993, at approximately 6000–6400 m depth (Fig. 3).

The volcanic rocks collected consist of pillow

Table 1
Age data for rocks collected during the 181st dive

Sample	Depth (m)	Rock	Geologic age (stage)	Age (Ma)	References
R-001	6424	radiolarian chert	late Valanginian–Hauterivian	134.5–127.0	Ogawa et al. (1994,1996)
R-002	6361	peralkaline rhyolite	Hauterivian	(129.3 ± 2.6)	This study
R-003	6316	tuffaceous radiolarian claystone	Berriasian	Ca. 140.0	Ogawa and Kawata (1998)
R-004	6284	radiolarian chert	Coniasian–Santonian	89.0–83.5	Ogawa et al. (1994,1996)
R-005	6192	radiolarian chert	Cenomanian–Turonian	98.9–89.0	Ogawa and Kawata (1998)
R-006	6035	alkali olivine basalt (altered)	?	?	

Geologic ages of samples R-001, R-003, R-004 and R-005, depth and rock's name refer to Ogawa et al. (1994), and absolute ages of stages refer to Gradstein et al. (1994).

lavas of peralkaline rhyolite (sample R-002) and pillow breccia of altered alkali olivine basalt (sample R-006). Pelagic sedimentary rocks consist of radiolarian chert (samples R-001, 004 and 005) and tuffaceous radiolarian claystone (R-003) (Ogawa et al., 1994; 1996; Ogawa and Kawata, 1998), which are obtained from the northern slope of Quesada Seamount (Fig. 2). There are no other edifices in the northern area of the dive site. The range of biostratigraphic ages and the depths of collected rocks are shown in Table 1. The oceanic plate beneath these sediments and rocks is in magnetic anomaly Chron M25 (Smith et al., 1989; Nakanishi, 1993), which is correlated to 154–155 Ma according to the scale of Gradstein et al. (1994).

3. Petrography and geochemistry

The rocks were collected from the top of the seamount down at the lower part of the scarps (R-001, R-002 and so on). However, according to the combination of ^{40}Ar–^{39}Ar ages and fossil ages, the samples are not in time-stratigraphic order (Table 1). Ogawa et al. (1994, 1996) interpreted that some normal faults may have disturbed the stratigraphic disposition (Fig. 3).

R-002 was sampled at approximately 6170 m depth from a continuous 43 m thick outcrop of pillow lava with horizontal bedding (Ogawa et al., 1994). The curvature of the trachytic structure and the foliation of vesiculation in the sample suggest that this sample is part of a pillow lava whose long diameter may be approximately 1 m or more. R-002 is a highly differentiated, high SiO_2 alkaline rock. With more than 75 wt% SiO_2 and more than 8 wt% Na_2O+K_2O it is a peralkaline rhyolite (Table 2, Fig. 4). This rock is apparently fresh, gray-white in color, and is composed of abundant sanidine ($Or_{45-43}Ab_{55-57}$)

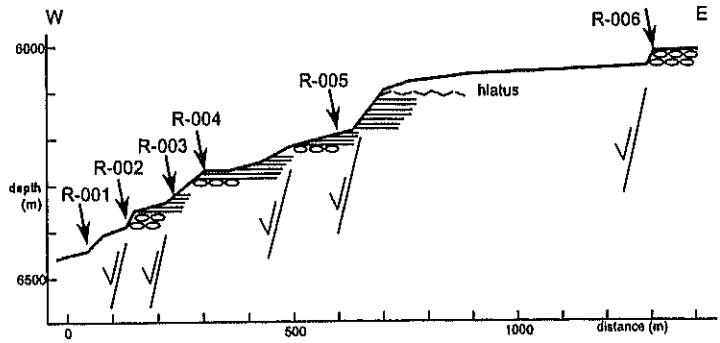

Fig. 3. W–E cross section of dive 181. Symbols of rock types are ellipses (lava), lines (chert) and dots (clay). Some normal faults inferred on the bottom of the cliff are also shown.

Table 2
Major element compositions of samples obtained by electron microprobe analysis for volcanic glasses in R-003 and by XRF analysis for bulk rock of R-002

Method:	Glass O EPMA	Glass J EPMA	Glass C EPMA	Glass F EPMA	Glass G EPMA	Glass H EPMA	Glass A EPMA	R-002 Bulk XRF
Major element (wt%)								
SiO_2	46.97	45.89	50.59	45.93	47.32	45.69	47.02	75.27
TiO_2	4.55	4.57	3.18	3.46	4.46	4.66	3.32	0.17
Al_2O_3	13.67	13.07	17.48	14.41	13.61	12.59	14.34	10.78
FeO	12.48	13.44	9.36	11.10	12.75	13.91	10.99	
MnO	0.24	0.19	0.17	0.22	0.12	0.25	0.17	3.44
MgO	4.33	4.90	3.02	6.34	4.44	4.98	6.09	0.05
CaO	8.72	10.32	9.21	11.90	9.86	10.72	10.79	0.07
Na_2O	4.19	3.47	4.12	3.37	3.44	3.54	3.75	0.12
K_2O	1.37	0.95	1.00	0.87	1.25	1.10	0.76	4.65
Cr_2O_3	0.00	0.02	0.00	0.02	0.03	0.07	0.00	–
V_2O_3	0.32	0.38	0.25	0.23	0.26	0.19	0.20	–
NiO	0.00	0.01	0.00	0.00	0.00	0.07	0.00	–
P_2O_5	0.88	0.60	0.65	0.46	0.69	0.63	0.41	0.03
LOI	–	–	–	–	–	–	–	0.59
Total	97.71	97.80	99.03	98.29	98.21	98.38	97.84	99.53

and common quartz phenocrysts with subordinate amounts of hornblende (zoning of sodic to calcic-sodic amphibole) within an aphanitic groundmass including sanidine ($Or_{40-30}Ab_{60-70}$) and opaque minerals. Some quartz phenocrysts are resorptive. Small grains of the alteration mineral zoisite occur in the groundmass, but the alteration is not pervasive.

R-003 was collected from an outcrop at approximately 6316 m depth (Ogawa et al., 1994) and is a tuffaceous radiolarian claystone composed of fresh volcanic glass, clay fragments, plagioclase (0.1–0.3 mm; $An_{80-70}Ab_{20-30}$) fragments, extremely well preserved radiolaria (Ogawa et al., 1996; Ogawa and Kawata, 1998) and foraminifera. These tuffaceous parts may be turbidites. Ogawa and Kawata (1998) reported the fossil age as early Berriasian (approximately 140 Ma). Geochemical compositions of volcanic glasses in R-003 show the Na_2O-rich alkali-basalt (Fig. 4, Table 2).

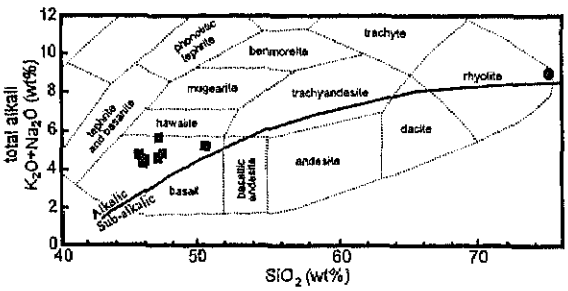

Fig. 4. The total alkali-SiO_2 diagram of non-potassic volcanic rocks (Cox et al., 1979). Volcanic fragments from R-003 and the whole rock of R-002 are squares and a circle, respectively. The dividing line between alkalic and sub-alkalic magma series is from Miyashiro (1978).

4. ^{40}Ar–^{39}Ar dating

For sample R-002, alkali-feldspar phenocrysts and groundmass were analyzed by the ^{40}Ar–^{39}Ar method. All samples were crushed into 50–100 mesh grains. These samples for dating were wrapped in aluminum foil and sealed in quartz vials under vacuum (70 mm in length, 10 mm in diameter) with flux monitors biotite (HD-B1; Hess and Lippolt, 1994, Bern4B; Flish, 1982), K_2SO_4 and CaF_2. The samples were irradiated for 24 h in an irradiation hole of the Japan Material Testing Reactor (JMTR), Tohoku University. During the irradiation, the samples were shielded by Cd foil in order to reduce thermal neutron-induced ^{40}Ar from ^{40}K (Saito, 1994). The Ar extraction and Ar isotopic analyses were done at Yamagata University. The samples were

Table 3
Ar–Ar age results

Temperature (°C)	$^{36}Ar/^{40}Ar$ ($\times 10^{-4}$)	$^{37}Ar/^{40}Ar$ ($\times 10^{-4}$)	$^{39}Ar/^{40}Ar$ ($\times 10^{-2}$)	^{39}Ar (%)	Age[a] (Ma)
K-feldspar phenocryst (R-002:peralkaline rhyolite)					$J=0.003466\pm0.000072$
600	6.94 ± 0.32	1.09 ± 0.27	3.389 ± 0.064	4.1	141.0 ± 4.0
900	3.00 ± 0.29	1.05 ± 0.41	4.026 ± 0.056	3.6	136.3 ± 3.4
1000	3.44 ± 0.30	0.39 ± 0.31	4.005 ± 0.060	4.0	135.1 ± 3.5
1100	1.21 ± 0.21	0.72 ± 0.15	4.610 ± 0.061	58.1	126.3 ± 3.0
1200	2.57 ± 0.29	3.14 ± 0.35	4.45 ± 0.059	22.3	125.4 ± 3.1
1300	3.92 ± 0.41	0.52 ± 0.28	4.094 ± 0.029	4.7	130.2 ± 3.2
1400	3.47 ± 0.38	0.53 ± 0.37	3.983 ± 0.051	3.2	135.7 ± 3.5
1500[b]	–	–	–	–	–
Total age					127.9 ± 3.2
Groundmass (R-002: peralkaline rhyolite)					$J=0.003518\pm0.000059$
600	1.26 ± 0.20	0.27 ± 0.11	4.522 ± 0.058	19.2	130.3 ± 2.7
900	1.22 ± 0.41	2.17 ± 0.20	4.518 ± 0.025	27.0	130.6 ± 2.7
1000	2.38 ± 0.39	0.13 ± 0.16	4.478 ± 0.035	13.9	127.2 ± 2.7
1100	2.64 ± 0.26	2.205 ± 0.084	4.410 ± 0.024	32.6	128.0 ± 2.3
1200	2.92 ± 0.48	0.19 ± 0.34	4.257 ± 0.051	6.7	131.3 ± 3.3
1300	15.1 ± 2.3	1.9 ± 5.0	1.715 ± 0.086	0.2	194 ± 24
1400	22.3 ± 2.9	4.8 ± 5.4	0.762 ± 0.076	0.1	264 ± 66
1500	24.3 ± 2.2	2.3 ± 2.1	0.981 ± 0.044	0.3	174 ± 39
Total age					129.7 ± 4.3
					129.3 ± 2.6[c]

All tabulated data were corrected for the mass discrimination effect and for isotopes produced from Ca and K.
[a] $(^{36}Ar/^{37}Ar)_{Ca}=(3.70\pm0.22)\times10^{-4}$, $(^{39}Ar/^{37}Ar)=(12.06\pm0.35)\times10^{-4}$, $(^{40}Ar/^{39}Ar)=(3.24\pm0.89)\times10^{-2}$.
[b] Failure.
[c] A plataeu age using 600–1200°C steps only.

incrementally heated to 1500°C in a Mo crucible by induction heating. Basically we extracted gases in eight steps from 600°C to 1500°C. Analytical methods are confirmed by Saito et al. (1991). The results of Ar analysis are summarized in Table 3. All errors are shown in 2σ.

The R-002 alkali-feldspar phenocryst probably holds the excess Ar because a U-shaped release pattern is observed when assuming a trapped atmospheric $^{40}Ar/^{36}Ar$ ratio (295.5) in the age spectrum (Fig. 5b). In this case, the central portions between 1100 and 1300°C may approximate a geologically meaningful age in the samples least contaminated by excess Ar. However, in the $^{36}Ar/^{40}Ar$–$^{39}Ar/^{40}Ar$ isochron diagram, the data indicate a relatively high $^{40}Ar/^{36}Ar$ intercept that may only be explained by an excess Ar signature with higher than atmospheric $^{40}Ar/^{36}Ar$ ratios (Fig. 5a). In the case of R-002 groundmass, on the other hand, almost all Ar gas is released in the five lower temperature fractions (99.4% at 600–1200°C). The corresponding weighted age of five fractions is 129.3 ± 2.6 Ma (Fig. 5d).

5. Discussion and interpretation

Using these volcanic ages and other sedimentary rock ages, we can illustrate the formation history of this seamount as follows. After the generation of the oceanic plate at 155–154 Ma, the tuffaceous radiolarian claystones (R-003) were deposited at around 140 Ma (Ogawa and Kawata, 1998) during a hiatus in seamount eruption (the first activity; R-003) of alkali-basalt. The last volcanic activity of this seamount is represented by R-002 groundmass, 129.3 ± 2.6 Ma, a highly differentiated alkaline rock (peralkaline rhyolite) which was erupted during the post-shield stage concurrent with the sedimentation of R-001 (134.5–127.0 Ma). Then, the volcanic edifice was covered with pelagic sediments (R-004 and R-005)

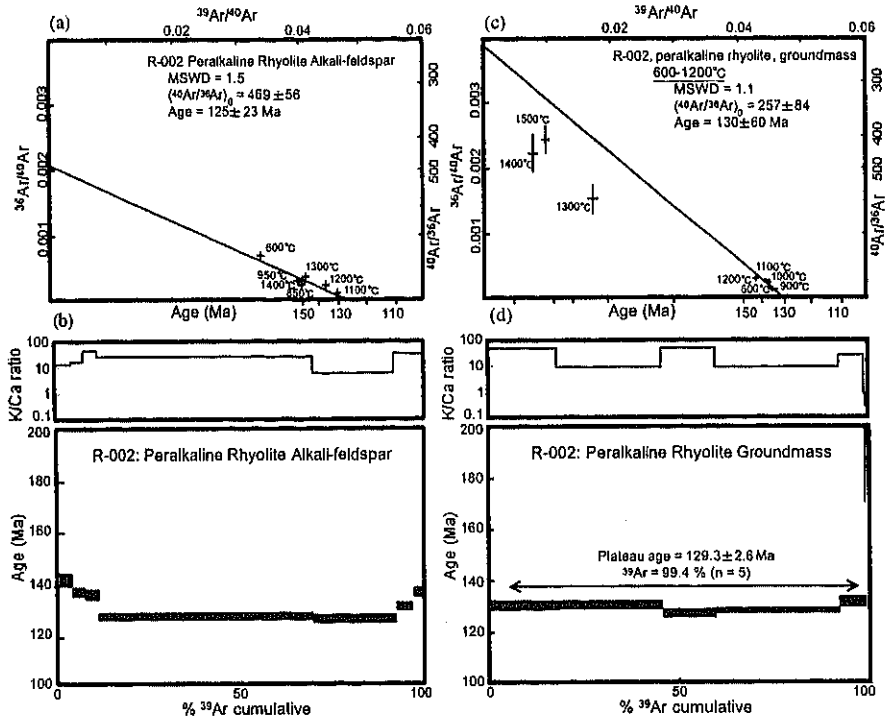

Fig. 5. Isochron diagrams and age spectra for $^{40}Ar/^{39}Ar$ incremental heating experiments on alkali-feldspar phenocrysts in the R-002 peralkaline rhyolite (a,b), and on the R-002 groundmass (c,d). The mean squared weighted deviations, MSWD = SUMS/(n-2) (York, 1969), indicates how well data fit the least-squares calculated straight line.

during the Late Cretaceous (Ogawa et al., 1994) (Table 2).

5.1. Long-lived volcanic activity of Early Cretaceous intra-plate volcanism

The shield-building period calculated from the ages between R-003 and R-002 is approximately 10 Myr, which is much longer than the Hawaiian shield volcanic period (1–3 Myr; Macdonald and Katsura, 1964; Nakamura, 1986). Such a long period of main shield volcanism suggests that this seamount remained above a hotspot for a long time. This may be attributed to either of the following two possibilities: (1) An abundant heat supply as in the superplume episode in the Early Cretaceous (Cox, 1991; Larson, 1991; Larson and Kincaid, 1996). (2) The moving rate of the Early Cretaceous Pacific Plate was slow to medium, ranging between 3 and 6 cm/yr, in contrast to the present fast moving rate (Duncan and Clague, 1985; Henderson et al., 1984). The latter reason is similar to the present setting of the Canarian hotspot in the central Atlantic Ocean, where the volcanism from the shield-building basaltic to the post-shield stage differentiated lavas has continued for as long as approximately 20 Myr after the Miocene (Freundt and Schmincke, 1995), being attributed to the slow absolute motion of the African Plate (1–1.5 cm/yr; Gripp and Gordon, 1990). The long-lived volcanism of the Quesada Seamount may reflect the slow to medium absolute motion of Early Cretaceous Pacific Plate.

6. Conclusions

We obtained ^{40}Ar–^{39}Ar ages from an Early Cretaceous seamount at the Mariana Trench oceanward slope. The peralkaline rhyolite, R-002 groundmass, has a plateau age of 129.3 ± 2.6 Ma.

Another sample, R-002 potassium feldspar phenocryst, has excess Ar. These ages suggest that this seamount has undergone a complicated volcanic history in the Early Cretaceous. The lifetime of volcanism was very long, at least 10 Myr, from alkali-basalt activity during shield-building volcanism to highly differentiated alkaline activity in the post-shield stage. In this case the long-lived petrologic sequence is similar to that of the Canary hotspot on the slow moving ocean floor. We suggest that the slow rate of plate motion of the Early Cretaceous Pacific Plate resulted in the volcanic edifice remaining above the source hotspot for a long time. Careful interpretation of the volcano-stratigraphic setting of dated samples is critical for correct interpretation of radiometric ages along the Pacific seamount chains of the Early Cretaceous.

Acknowledgements

We highly appreciate the staff of the Institute for Material Research, Tohoku University (Oarai Branch) for irradiating samples in the JMTR (Japan Material Testing Reactor). We also thank Dr. D. Curewitz of Ocean Research Institute, University of Tokyo, for improving the English. Thanks are due to the late Dr. K. Fukunaga, Mr. S. Furusawa, Miss A. Kanazawa and Messrs. T. Ohmura, M. Yamamoto and M. Ishii, Yamagata University, for their help in Ar–Ar dating. Drs. T. Ishii, H. Taniguchi and H. Sato, Ocean Research Institute, University of Tokyo, are thanked for EPMA analysis and the reviewers for their reviews.

References

Batiza, R., 1989. Seamount and seamount chains of the eastern Pacific. In: Winterner, E.L., Hussong, D.M., Decker, R.W. (Eds.), The Geology of North America Vol. N: The Eastern Pacific Ocean and Hawaii, pp. 289–306.

Cox, K.G., 1991. Earth sciences; a superplume in the mantle. Nature 352, 564–565.

Cox, K.G., Bell, J.D., Pankhurst, R.J. (Eds.), 1979. The Interpretation of Igneous Rocks. Allen and Unwin, London, 450 pp.

Davis, A.S., Pringle, M.S., Pickthorn, L.B.G., Clague, D.A., Schwab, W.C., 1989. Petrology and age of alkalic lava from the Ratak Chain of the Marshall Islands. J. Geophys. Res. 94, 5757–5774.

Duncan, R.A., Clague, D.A., 1985. Pacific Plate motion recorded by liner volcanic chains. In: Narin, A.E.M., Stehli, F.G., Uyeda, S. (Eds.), The Ocean Basins and Margins, The Pacific Ocean. Plenum, New York, vol. 7A, pp. 89–121.

Flish, M., 1982. Potassium-argon analysis. In: Odin, G.S. (Ed.), Numerical Dating in Stratigraphy. John Wiley and Sons, Chichester, pp. 151–158.

Freundt, A., Schmincke, H.U., 1995. Petrogenesis of rhyolite-trachyte-basalt composite ignimbrite P1, Gran Canaria, Canary Islands. J. Geophys. Res. 100, 455–474.

Fuller, M., Weeks, R., 1991. Geomagnetism; superplumes and superchrons. Nature 356, 16–17.

Gradstein, F.M., Agterberg, F.P., Ogg, J.G., Hardenbol, J., van Veen, P., Thierry, J., Huang, Z., 1994. A Mesozoic time scale. J. Geophys. Res. 99, 24051–24074.

Gripp, A.E., Gordon, R.G., 1990. Current plate velocities relative to the hotspots incorporating the NUVEL-1 global plate motion model. Geophys. Res. Lett. 17, 1109–1112.

Haggerty, J.A., Silva, I.P., 1995. Comparison of the origin and evolution of Northwest Pacific guyots drilled during Leg 144. In: Haggerty, J.A., Silva, I.P., Rack, F.R., McNutt, M.K. (Eds.), Proc. ODP Sci. Results 144, 935–949.

Henderson, L.J., Gordon, R.G., Engebretson, D.C., 1984. Mesozoic aseismic ridges on the Farallon Plate and southward migration of shallow subduction during the Laramide Orogeny. Tectonics 3, 121–132.

Hess, J.C., Lippolt, H.J., 1994. Compilation of K-Ar measurements on HD-B1 standard biotite, 1994 status report. In: Odin, G.S. (Ed.), Bulletin of Liaison and Informations, IGCP Project 196, Calibration of the Phanerozoic Time Scale, International Geological Correlation Programme, International 12, pp. 19–23.

Koppers, A.A.P., Staudigel, H., Wijbrans, J.R., Pringle, M.S., 1998. The Magellan seamount trail; implications for Cretaceous hotspot volcanism and absolute Pacific Plate motion. Earth Planet. Sci. Lett. 163, 53–68.

Larson, R.L., 1991. Latest pulse of earth: evidence for a mid-Cretaceous super plume. Geology 19, 547–550.

Larson, R.L., Kincaid, C., 1996. Onset of mid-Cretaceous volcanism by elevation of the 670 km boundary layer. Geology 24, 551–554.

Lincoln, J.M., Pringle, M.S., Silva, I.P., 1993. Early and Late Cretaceous volcanism and reef-building in the Marshall Islands. Geophys. Monogr. AGU 77, 279–305.

Macdonald, G.A., Katsura, T., 1964. Chemical composition of Hawaiian lavas. J. Petrol. 5, 82–133.

Miyashiro, A., 1978. Nature of alkalic volcanic rock series. Contrib. Mineral. Petrol. 66, 91–104.

Nakamura, K., 1986. Volcanology and plate tectonics (in Japanese, with English abstr.). Bull. Volcanol. Soc. Jpn. 30, 1–16.

Nakanishi, M., 1993. Topographic expression of five fracture

zones in the northwestern Pacific Ocean. Geophys. Monogr. AGU 77, 121–135.

Ogawa, Y., Kawata, T., 1998. Preservation of biogenic opal-A in Earliest Cretaceous radiolarian claystone from the western Pacific. J. Sediment. Res. 68, 435–439.

Ogawa, Y., Fujioka, K., Oshida, A., Nishimura, H., Kawata, T., Matsuoka, A., Sashida, K., Kanamatsu, T., Ito, T., 1994. Pacific Plate Jurassic to Cretaceous seamount and chert stratigraphy, rock paleomagnetism and clayey seabottom cracks (in Japanese, with English abstr.). JAMSTEC J. Deep Sea Res. 10, 123–151.

Ogawa, Y., Sashida, K., Kawata, T., 1996. Silica mineralization of Jurassic/Cretaceous radiolarian cherts and claystone from a seamount flank at the Mariana Trench oceanward slope. Sci. Rep. Inst. Geosci. Univ. Tsukuba Sect. B. Geol. Sci. 17, 1–24.

Rea, D.K., Vallier, T.L., 1983. Two Cretaceous volcanic episodes in the western Pacific Ocean. Geol. Soc. Am. Bull. 94, 1430–1437.

Saito, K., 1994. Excess Ar in some metamorphic and plutonic rocks reduction of thermal neutron-induced 40Ar by Cd shielding. Sci. Rep. Res. Inst. Tohoku Univ. A40, 185–189.

Saito, K., Otomo, I., Takai, T., 1991. K-Ar dating of the Tanzawa tonalitic body and some restrictions on the collision tectonics in the South Fossa Magna, central Japan. J. Geomagn. Geoelectr. 43, 921–935.

Smith, W.H.F., Sandwell, D.T., 1997. Global sea floor topography from satellite altimetry and ship depth soundings. Science 277, 1956–1962.

Smith, W.H.F., Staudigel, H., Watts, A.B., Pringle, M.S., 1989. The Magellan seamounts: Early Cretaceous record of the south Pacific isotopic and thermal anomaly. J. Geophys. Res. 94, 10501–10523.

Smoot, N.C., 1997. Aligned buoyant highs, across-trench deformation, clustered volcanoes, and deep earthquakes are not aligned with plate-tectonic theory. Geomorphology 18, 199–222.

Strong, D.F., 1972. The petrology of the lavas of Grande Comore. J. Petrol. 13, 181–217.

Tokuyama, H., 1980. Cretaceous volcanism in the central Pacific Ocean (in Japanese, with English abstr.). J. Geogr. Tokyo Geogr. Soc. 89, 31–49.

Wessel, P., Smith, W.H.F., 1991. Free software helps map and display data. EOS Trans. AGU 72, 441.

Wessel, P., Smith, W.H.F., 1998. New, improved version of the Generic Mapping Tools released. EOS Trans. AGU 79, 579.

Winterer, L.E., Natland, J.H., Waasbergen, R.J.V., 1993. Cretaceous guyots in the northwest Pacific: an overview of their geology and geophysics. Geophys. Monogr. AGU 77, 307–334.

York, D., 1969. Least squares fitting of a straight line with correlated errors. Earth Planet. Sci. Lett. 5, 320–324.

Available online at www.sciencedirect.com
SCIENCE DIRECT®
Fuel 82 (2003) 1271–1279
FUEL
www.fuelfirst.com

Mechanism of methane flow through sheared coals and its role on methane recovery☆

Huoyin Li[a,*,1], Yujiro Ogawa[b], Sohei Shimada[a]

[a]*Graduate School of Frontier Sciences, Institute of Environmental Studies, The University of Tokyo, Bunkyo-ku, Tokyo 113-0033, Japan*
[b]*Institute of Geoscience, University of Tsukuba, Tsukuba 305-8571, Japan*

Received 19 March 2002; accepted 14 January 2003; available online 13 February 2003

Abstract

Tectonically sheared coals are closely related with coalbed methane exploitation, and are classified into cataclastic coals and mylonitic coals in view of their deformation mechanism, either brittle or ductile. Scanning electron microscopy and reflected light microscopy observations showed that cataclastic coals possess a hierarchy of open, continuous and connecting fractures, whereas mylonitic coals always display tightly compressed and collapsed fractures. Mercury porosimetry studies also indicated that compared with normal coals, cataclastic coals possess greater porosity, more specific surface area and wider average fracture aperture; whereas mylonitic coals are characterized by narrower average fracture aperture and a great deal of specific surface area. Based on experimental data and actual site experiences, a new model of methane flow within coals was proposed. Gas flow through sheared coals, unlike normal coals—a simple dual porosity system comprising a matrix of micropores that are surrounded by cleats, also contain additional steps because of overwhelming sheared fractures and different deformation mechanisms. This model can explain why gas outbursts are always accompanied by small-scale compressively geological structures where mylonitic coals often occur, and why in such area the rate of gas extraction is unexpectedly lower, despite the presence of a great volume of methane.
© 2003 Elsevier Science Ltd. All rights reserved.

Keywords: Coalbed methane; Shear zone; Permeability; Methane extraction; Global warming

1. Introduction

A shear zone within a coal seam, which can contain a large number of fractures and therefore much gas, has long been considered as a major factor for a catastrophic failure or 'outburst' of gas and coal during coal extraction all over the world coalfields [1–3]. In order to improve the safety of production in coalmines, coalbed methane (CBM) has customarily been extracted and released to the atmosphere for a long time. This situation must, to a great extent, have aggravated global warming, because methane gas has 22 times stronger greenhouse effect than carbon dioxide gas [4].

On the other hand, a shear zone might play more positive roles in CBM prospecting and production because of its greater quantity of fractures and higher methane content. From the experiences of gas drainage in underground mines, although the rate of gas extraction within a shear zone is commonly higher than that from normal coals, the most noted local problem is that drill rods are often gripped and unable to rotate. Such drilled holes contracts rapidly, like quicksand, after drilling due to high methane pressure and powdered coals. This situation suggests that there are various deformation properties in various structural positions even within the same coal seam.

Shear zones, which are commonly named detachments, bedding plane faults or soft-coal layers, occur within compressively deformed coal basins in the world [5]. Sheared coals were classified into microstructural classes based on their particle size and textures as cataclastic-angular coal, cataclastic-granular coal, foliated coal and mylonitic coal [6]. The former two are considered to be developed in brittlely deformed parts and widely distribute in a shear zone, whereas the latter two are developed accompanying the ductile deformation and have been

* Corresponding author. Tel./fax: +81-3-5841-8950.
E-mail address: hylee@k.u-tokyo.ac.jp (H. Li).
[1] A research fellow of the Japan Society for the Promotion of Science (JSPS).
☆ Published first on the web via Fuelfirst.com—http://www.fuelfirst.com

subjected to more intensive deformation. Strong shearing also locally thickens the coal seam due to small-scale thrust lap and coal duplex which arise from a detachment zone [5], or as a result of mass transport flow of coal from areas of high stress to low stress [7]. In such areas, compressive structures, such as cleavage duplex, thrust ramp and small-scale vergent fold often appears, representing an intensive deformation environment [8].

The fact that many gas outbursts occur in shear zones has proved that sheared coals may accumulate a large volume of gas to form a high pressure gas pocket, and a higher amount of gas emission shows that sheared coals possess higher permeability by bedding-parallel migration, which can relax the pocket of high pressure gas. To explain this paradox, it is necessary to clarify the relationship between the textural characteristics and related gas flow behavior in different deformed parts within a shear zone.

This paper uses mercury porosimetry experiment and SEM observation together with in situ gas data, trying to develop a methane flow model through sheared coals with different tectonic deformations. The model is desired to offer basic materials for the project of CBM recovery in future from a geological viewpoint.

2. Geological setting of experimental samples

Bituminous rank coal samples were taken from the Lower Permian Wu coal seam, on average 4.6–5.8 m thickness, of the Pingdingshan coalfield, China. Within the Wu seam, there appears to be a widespread bedding shear zone, which has traditionally been called a 'soft-coal layer' by mining engineers because of the absence of bedding planes and the occurrence of friable coals with a thickness of 0.9–2.5 m [8]. The shear zone along the coal seam might be considered a potentially significant CBM reservoir or a 'gas river', because of its more extensively developed fractures compared with surrounding normal hard coal which is hardly disturbed and thus plays a role for sealing gas [9]. Until 1997, more than 20 outbursts have been experienced in the Wu coal seam and all have occurred within such shear zones (Table 1). The largest one burst out 144.6 t of coal and expelled 13,400 m^3 of methane. The initial gas content of the outburst coal was estimated at 92.67 m^3/t of coal, whereas the in situ gas content of the normal coal was only about 10 m^3/t of coal.

Many researches on the gas outburst have indicated that not all the areas of the shear zone possess the danger of outburst, but rather the outburst-prone areas always accompany small-scale compressively geological structures, such as cleavage duplex, thrust ramp and small-scale folds, where the thickness of the shear zone increases and foliated coal and/or mylonitic coals are always focused [8]. This phenomenon implies that such areas must have been subjected to structural or textural change into lower permeability to form a 'structural dam' or 'tectonic screen', which blocks gas migration along the bedding into the work face and consequently results in a high pressure gas pocket (Fig. 1). Reflected light microscopic observations have shown that outburst-prone coals possess overwhelming microfractures which display a more complex style and poorer connectivity compared with non-outburst sheared

Table 1
Structural state of the coals and the relationship between the amount of moved coal and emitted gas in outburst events at Wu coal seam, Pingdingsham coalfield, China

Time	Amount of moved coal (t)	Amount of emitted gas (m^3)	Specific gas emission of outburst (m^3/t)	Structural state of the coal
84.10.13	19.7	1200	60.91	Soft sooty texture
88.4.22	50	1500	30	Cataclastic-granular
88.10.7	54	1178	21.81	Cataclastic-angular
89.3.18	8	650	81.25	Fine, foliated texture
89.3.21	56	1000	17.81	Noticeably weakened by fracture
89.4.4	8	655	81.88	Highly friable, mylonitic texture
89.4.14	28	2787	99.54	Highly friable, mylonitic texture
89.7.12	6	720	120	Fine, mylonitic texture
89.7.27	30	3000	100	Fine, mylonitic texture
90.5.12	13	600	46.15	Cataclastic-granular
90.9.12	40	2240	56	Cataclastic-granular
91.4.11	144.6	13,400	92.67	Fine, foliated texture
91.5.11	55	6000	109.09	Fine, foliated texture
91.5.23	54	3487	64.57	Highly friable, mylonitic texture
92.12.15	20	390	19.50	Disturbed and very dull
93.8.26	44	2500	56.82	Highly friable
92.12.17	10	371	37.10	Cataclastic-granular texture
95.3.21	44	1580	35.91	Cataclastic-granular texture
95.12.17	20	571	33.55	Cataclastic-granular texture
97.2.21	29	1833	63.21	Foliated texture
97.4.4	550	11,300	20.54	Cataclastic-angular
97.10.7	16	633	39.56	Cataclastic-granular texture

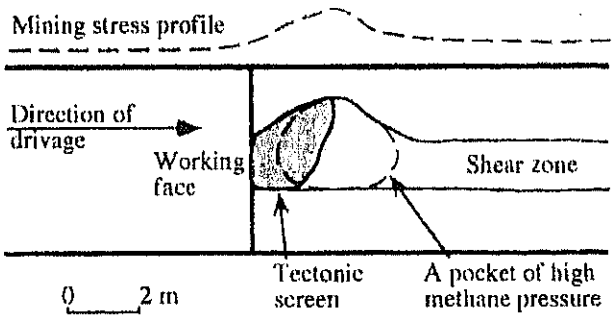

Fig. 1. Illustration of the mining stress inducing a violent outburst as a working face approaches the area of high methane pressure.

coals and normal coals. In addition, outburst-prone coals often show ductile structures, such as S–C band structure and σ-structure, representing intensively deformed environment (Fig. 2).

Based on the studies of the relationship between tectonics and gas deposit in French coalfields, Alpern [10] has proposed that intense shearing may locally transform the coal into mylonite or foliated fabric which, under ground weight or abutment pressure, makes the coal impermeable to gas, hence that part of coal is usually considered as a 'tectonic screen' against methane migration. Although the number of fissures may be very high, they are no longer connected. For this reason, gas extraction in such ductilely deformed areas becomes very difficult and the rate of gas extraction is much lower than in brittlely deformed areas (Fig. 3), despite the greater volume of gas content.

3. Pore structures of sheared coals

In order to elucidate the influence of tectonic pressure on coal properties that may be related to permeability or texture, the mercury porosity measurement was first carried out to analyze the characteristics of fractures of sheared coals. Mercury porosimetry studies on a series of coal samples exhibit various degrees of textural features for understanding: (1) porosity and specific surface areas of fractures, which, to some extent, reflect gas storage capacity, and (2) average fracture aperture, which may be related to the permeability of coals.

Eleven samples were collected and measured, three from normal coals without any visible deformation and eight

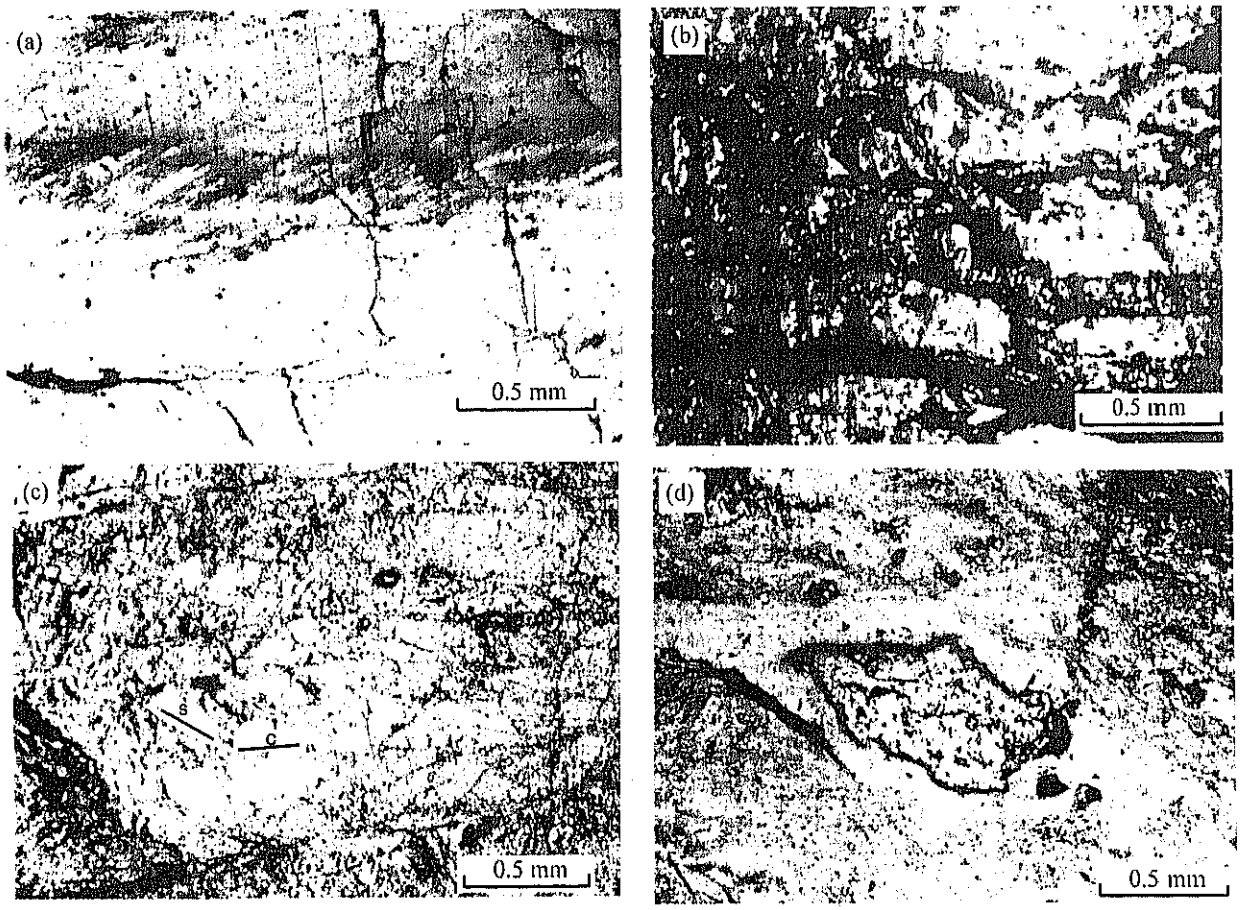

Fig. 2. Photomicrographs showing variously deformed coals under reflective microscope. (a) Normal coal exhibiting bedding plane structure and scarce cleats. (b) Cataclastic coal displaying angular structure by fractures with wide aperture. (c) Foliated coal characterized by slightly elongate shape of most grains similar to S–C structures. (d) Mylonitic coal which has been intensely sheared into σ-structures (porphyroclast is inertinite-rich coal and matrix is vitrinite-rich coal).

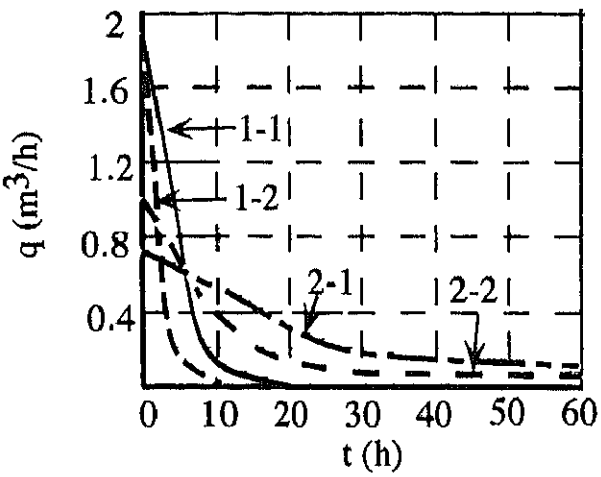

Fig. 3. The relationship between the velocity of gas emitted from the boreholes and the passage time on brittlely deformed coals (1-1,1-2) and ductilely deformed coals (2-1,2-2).

from a shear zone comprising both brittle and ductile deformation (Fig. 4). As shown in this figure, a1, b1, c1 are normal coals, whereas others are all sheared coals. In the latter, a2, a3, a4 and b2, b3, b4 are brittlely deformed cataclastic coals, and c2, c3 are ductilely deformed foliated and mylonitic coals, respectively. The bulk porosity, specific surface area, average fracture aperture and compressibility of each sample are shown in Fig. 5. From these results, following conclusions are obtained: (1) the sheared coals possess three to eight times more porosity and two to ten times more specific surface area than their normal counterparts, suggesting that the sheared coals can preserve many times more methane than their normal counterparts. (2) Within sheared coals, cataclastic coals (a2, a3, a4, b2, b3, b4) possess larger average fracture apertures representing a good condition for gas migration, whereas the foliated coals and mylonitic coals (c2, c3) show a fracture aperture even smaller than the normal coals (a1, b1, c1). This can explain why the rate of gas extraction from the foliated and mylonitic coals is always remarkably lower than that from the cataclastic coal, and also explain why the outburst of gas always occurs in the foliated and mylonitic coal areas despite the pre-drainage of gas being undertaken. (3) The compressibility analysis of various coals imply that the intensely sheared coals also contain many more smaller microfractures, which are not accessible by mercury even at very high pressure, but are accessible by gas because of the smaller molecule diameter of the latter. This tendency further indicates that some tectonically sheared coals possess a potentially significant capacity of gas storage.

4. Gas flow behavior in sheared coals: a textural consideration

Coal is known to be formed from plant materials deposited in a swamp environment through peat. The gradual accumulation of inorganic sediment above the buried peat causes the water to be driven out during consequent consolidation process of the peat. The pressure and temperature effects increase with the burial depths, promoting geochemical reactions which result in a reduction of the volatile components and a consequent increase in the fixed carbon content of the coal. During this process, a large number of gases (dominantly methane) are

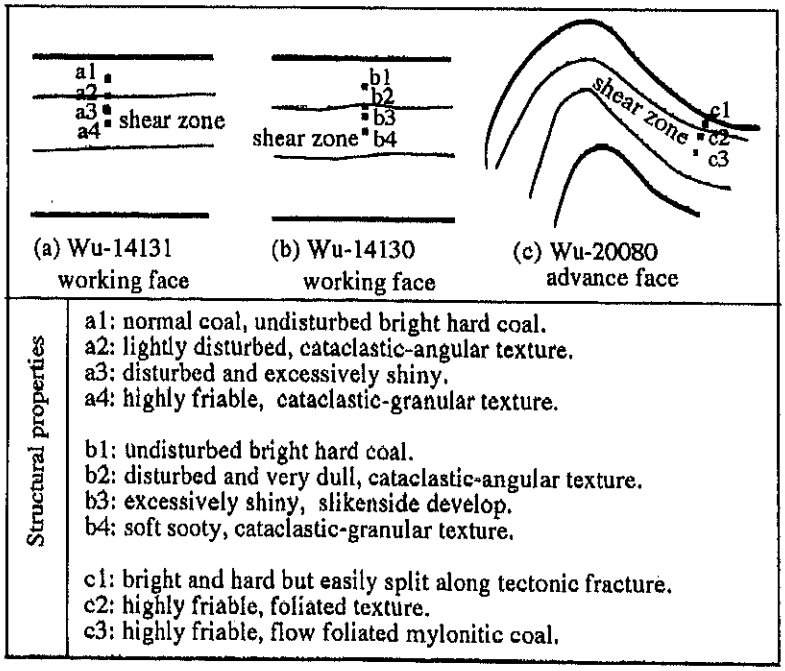

Fig. 4. Locality and structural properties of samples with (a) and (b) brittle deformation, and (c) ductile deformation, from Wu seam of Pingdingshan coalfield, China.

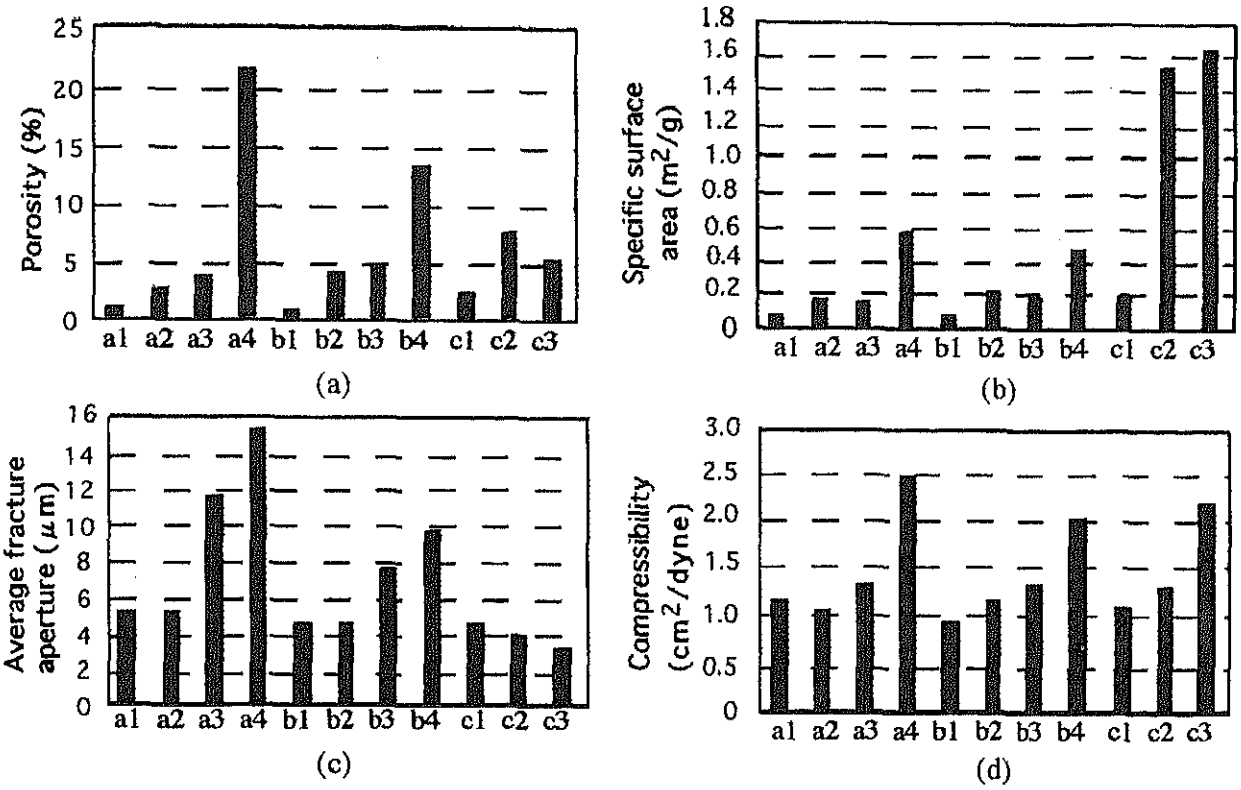

Fig. 5. Histograms indicating (a) the porosity, (b) specific surface area, (c) average fracture aperture, and (d) compressibility of samples, based on mercury porosity measurement.

also generated as increasing the effects of pressure and temperature.

The high methane reservoir potential of all coals is due to the inefficient packing of its organic structure during coalification. The density of pure carbon is approximately 2.23×10^3 kg/m^3, whereas anthracite has around 1.35×10^3 kg/m^3 and bituminous coal 1.29×10^3 kg/m^3 [11]. This density contrast is almost totally due to the microporosity created by the poor packing structure of the organic coal compounds. The bulk of the pores constituting this porosity are <0.50 nm in diameter. The small size pore precludes occupation of this space by water due to the hydrophobicity of coals, so that only other small diameter molecules such as methane (and other alkenes) can occupy this space; methane molecules have an effective diameter of 0.32 nm in an uncompressed state [11]. Methane is stored in these coal reservoirs by two ways. Firstly, gas is held in a free state in the interstitial space between the cleats. Secondly, the methane is physically adsorbed onto the surface of the pores of the coal. Harpalani and Schraufnagel [12] reported that free methane stored in this fracture accounts for less than 10% of the total gas contained in the coal and remaining 90% plus of methane is physically adsorbed onto the surface of the pores of the coal.

Present model of methane flow through a coal seam indicates that the adsorbed methane after desorbing into the gaseous phase must diffuse through the micropore structure of the coal matrix until it reaches a cleat [13], and then followed by Darcy flow through the cleat to the well (Fig. 6). The relationship between coal seam structure and gas flow behavior is usually modeled as a dual porosity system of macropores (cleat) surrounding a matrix of micropores (Fig. 7). According to this model of gas flow through coals, gas migration is governed by two main factors: (1) the distance that methane has to diffuse, and (2) the amount of gas flowing through the cleat. The former is dependent upon the cleat spacing that delineates the size of matrix blocks in the coal. The latter is dependent upon the width, length, continuity and permeability.

This dual porosity model of gas flow may well be applied to normal coals which were not subjected to the structural stress and thus display open and regular cleats. Such regular cleats are known to be formed with differential compaction and shrinkage during coalification, defining the uniform microporous blocks. During methane extraction in normal coals, methane migrates along the sequence that gas desorbs from internal coal surfaces to diffuse through the matrix and micropores to cleats, and flows through cleats and bed-parallel fractures to the well (Fig. 8a). It is evident that the growth of cleat and the amount of bed-parallel fractures influence the rate of gas migration. Previous microscopic investigations [11] have shown that on average of normal coal, 'dull

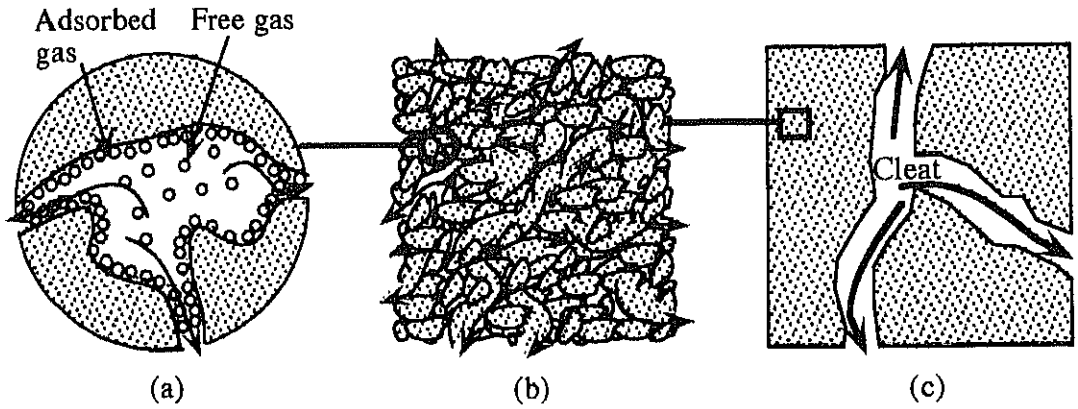

Fig. 6. Present model of methane flow through coal: (a) Desorption from the internal coal surfaces, (b) diffusion through the matrix and micropores, and (c) fluid flow in the cleats (modified from Ref. [14]).

coals' have a mean crack spacing of about 3 mm, whereas 'bright coals' are more brittle and record a mean crack spacing of around 1 mm. Thus, coal seams with higher proportion of bright macerals should have faster desorption and emission rates than more dull coals.

However, for sheared coals, because of the crushed and sized characteristics of the coal, the probable effects of maceral changes on gas emission were minimized, whereas the significance of increased fracture permeability has been shown to be far more important.

4.1. Tectonically-induced fractures of sheared coals

The nature of gas flow through sheared coals is perhaps more complex than the previous model. Mercury porosimetry studies on coals and examination of coal microstructure using SEM show that sheared coals are not simply a dual porosity system comprising a matrix of micropores that are surrounded by cleats, but possess a hierarchy of sheared fractures and microfractures at a level between the micropores and the cleat system (Fig. 2b–d). Sheared fractures firstly cut up the block of coals and are commonly connected with original cleats. As shear stress increases, the coal is further crushed into cataclastic-angular and/or cataclastic-granular, and original cleats are completely covered with sheared fractures (Figs. 2b and 9a). Locally intensive shear deformation may wrench and tightly compress the fractures, even grind coals into powder, which may plug sheared fractures. Small-scale structures, such as vergent folds, cleavage duplexes, S–C band structures and 'σ-structures' also commonly appear in such area (Figs. 2c, d and 9b). These small-scale structures are typically compressive and represent a sealing system to gas migration. The presence of sheared fractures and microstructures suggests that the flow behavior of gas through sheared coals is unlikely to be solely dependent upon the cleat system, but rather a combination of the original cleats and tectonic-induced fractures with deformation style, either brittle or ductile. The size, continuity and connectivity of the sheared fractures contribute significantly to the overall permeability, and are likely to have a major role in the flow of methane through sheared coal in both diffusion at the micropore level and laminar flow at the cleat level [14].

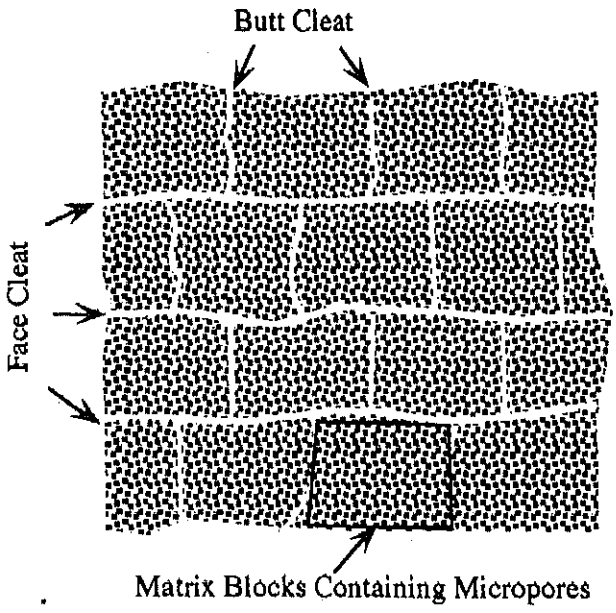

Fig. 7. Dual porosity system comprising a matrix of micropores that are surrounded by cleats (after Ref. [13]).

A number of gas desorption experiments in laboratory have proved that sheared coals commonly show faster gas emission than their normal counterpart [11,15]. On the other hand, during mining extraction, although the relative amount of gas emission is directly proportional to the thickness of shear zone in situ (Table 2), locally it does not coincide with this pattern, where usually be faced with a potential outburst risk. Moreover, the ratio of methane extraction in such an area is commonly lower and outburst coals always emit 2–10 times more gas than their normal counterparts (Table 1). These phenomena suggest that outburst-prone coals possess overwhelming microfractures, but the permeability is very low.

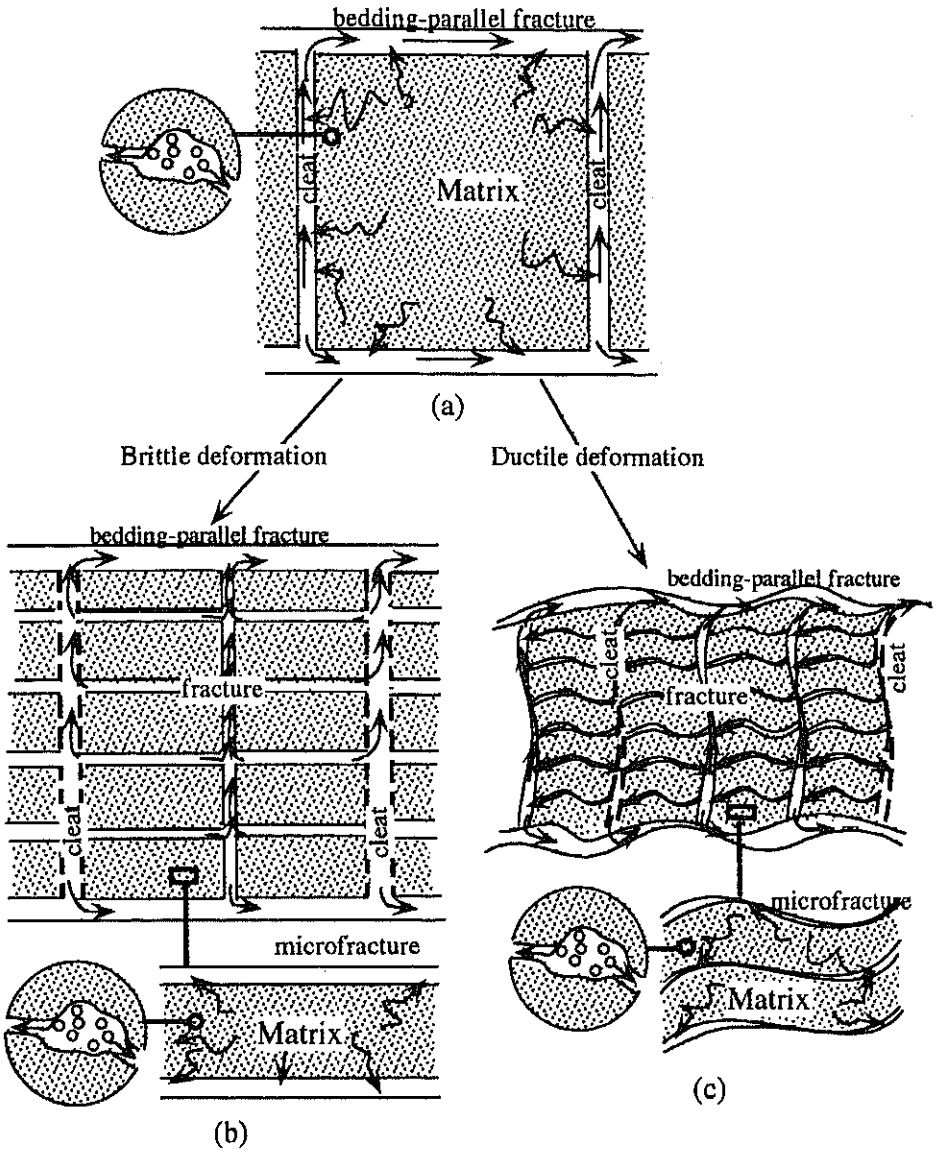

Fig. 8. A new model of methane flow through (a) a normal coal, (b) a brittlely deformed coal, and (c) a ductilely deformed coal.

4.2. *Implications of tectonic deformation on gas flow models*

In general, sheared coals formed through a brittle deformation mechanism and are called cataclastic coals. In such coals, which have a hierarchy of open, continuous and connecting fractures and cleats, the effective block size is not defined at present by the cleat spacing, but somewhere between the cleats and microfractures. The smaller the effective block size becomes, the shorter the mean diffusive distance is. This is largely because methane must be free before reaching a suitable fracture for laminar flow, and further implies that laminar flow is likely to begin at shallower levels than as identified at present by spacing of cleats. Hence, the additional steps occurring in the flow of methane through sheared coals proceed through the following steps (Fig. 8b).

Step 1. Diffusion from and through the micropores to microfractures.
Step 2. Flow of methane through microfractures to cleats or fractures.
Step 3. Gas movements through cleats and fractures to the well base.

This model shows that tectonic deformation is likely to play an important and probably significant rate-limiting role at all over the process of methane transport. A large number of brittle fractures in sheared coals will make methane migration to become faster than in normal coals. This tendency is extremely important for the development of CBM projects. Large aerial extents of such sheared coals, being widely present in a continuous matter, may not only preserve significant gas reservoirs but also increase

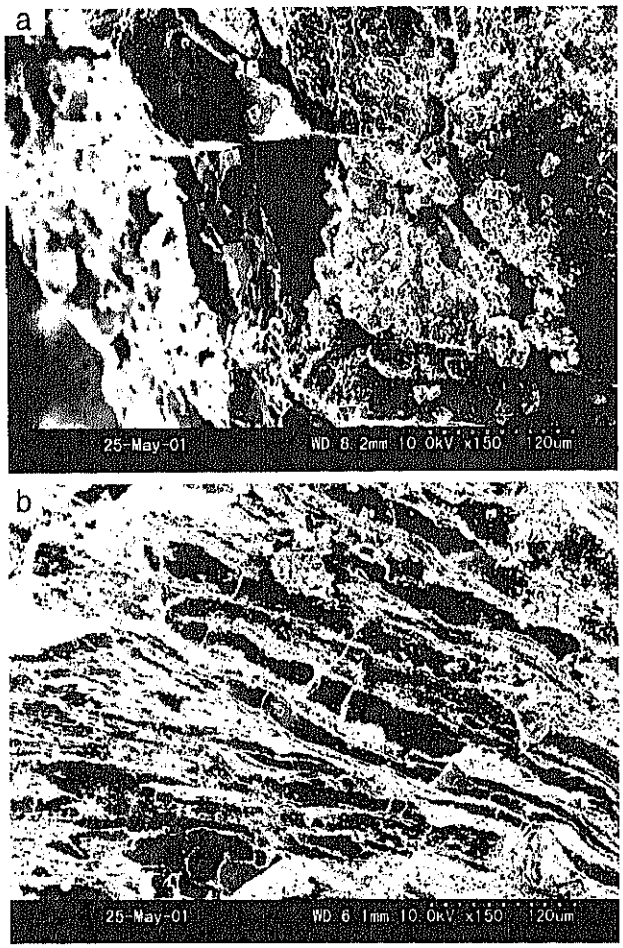

Fig. 9. SEM photos of coal samples a4 and c3 in Fig. 3. (a) Brittlely deformed coal showing a hierarchy of open, continuous and connecting fractures. (b) Ductilely deformed coal characterized by tightly compressed fractures which shows worse connectivity.

the inherent permeability. Therefore, it can be geologically considered as a 'sweet spot' for CBM exploitation.

Nevertheless, not all sheared coals are provided with the properties of faster desorption. Instead, intensively sheared coals in special structural positions, such as thrust ramp, cleavage duplex and small-scale vergent folds, which often display ductilely deformed structural appearance and are called foliated coals or mylonitic coals, are the special candidates for gas reservoir due to their low permeability with high specific surface area. Although there are overwhelming microfractures within this type of coals, almost all fractures are tightly compressed and pushed into one another to choke the conduit against methane flow. Moreover, a great quantity of windingly and tightly collapsed surfaces not only sealed original cleats for methane flow but also closed themselves (Fig. 8c). Therefore, this type of coal always shows poorer connectivity, thus results in a difficult condition for gas migration and is liable to cause a high pressure gas pocket (Fig. 1). Lower rate of methane extraction and frequent gas outburst events occur in such areas, and could be explained by this model. In such areas, artificial methods such as water infusion is necessary for relaxing stress, enlarging the aperture of fractures and consequent increasing the rate of methane recovery.

Table 2
Relationship between the relative amount of gas emission and the thickness of a shear zone in driving faces

Working faces	Depth (m)	Thickness of coal seam (m)	Thickness of shear zone (m)	Relative amount of gas emission (m^3/t)
Wu 12130	487	5.8	1.8	15.68
Wu 12130	484	5.5	1.9	16.56
Wu 14131	483	5.4	0.9	9.04
Wu 14131	485	5.3	1.1	10.45
Wu 20080	511	5.6	2.5	18.54
Wu 20080	508	5.7	2.3	17.34
Wu 20090	520	4.8	0.8	10.31
Wu 20090	521	4.9	0.6	10.55

5. Concluding remarks

Although the occurrence of a shear zone within a coal seam has long been considered as a major factor for a catastrophic failure or 'outburst' of coal and gas in a coalfield during coal extraction, it should be regarded more positively in CBM prospecting and production because of the greater quantity of fractures with higher permeability and higher methane content. Mercury porosimetry and scanning electron microscopy showed that sheared coals should not be viewed simply as a dual porosity system of micropores which are surrounded by cleats, but instead, should be viewed as having a third porosity system comprising a hierarchy of sheared fractures and microfractures, which plays a significant rate-controlling role at all over the process of methane transport.

Experiences on gas outbursts and methane drainage have proved that not all sheared coals show faster methane emission than normal coal, but some have rather slower. Sheared coals were classified into microstructural classes based on their particular size and texture as cataclastic series and mylonitic series, the former commonly occurs in a shear zone, whereas the latter is developed in a locally compressively deformed areas. Such a mode of occurrence is extremely important for the development of a CBM project, because we have to know what coals work as significant gas reservoirs due to what mechanism. Cataclastic coals, which are formed by a brittle mechanism, possess a hierarchy of open, continuous and connecting microfractures, and thus methane migration in these coals would be faster than normal coals. On the other hand, mylonitic coals, which are locally and ductilely generated in an intensively compressive environment, always display tightly compressed and broken fractures to be pushed into one another with worse connectivity for methane migration. Only this type of coal makes the real mining disaster,

because of becoming a methane reservoir due to low gas permeability to occur the gas outburst during coal production.

However, a new model of methane flow through a coal was proposed to take account into these differences between the cataclastic and mylonitic coals for the project of CBM recovery. The coal seams, previously considered economically unsuitable for CBM production due to their lower permeability, probably have a potential exploitation value if they possess continuous, brittlely deformed shear zones within them. Another important significance is that such coal seams can be utilized to preserve a vast amount of carbon dioxide with CO_2-enhanced CBM recovery project, which has been considered one of the projects protecting the earth from global warming.

Acknowledgements

This research was financially supported by a scholarship and JSPS grant-in-aid (14-02176) to H. Li, and by grant-in-aid to Y. Ogawa (Kiban A No. 13304038) from the Ministry of Education, Science, Culture, Sports and Technology of Japan. The field works were facilitated by J. Tian, Z. Liu and Y. Sun at Pingdingshan Coal, China, and mercury penetration experiment was assisted by W. Lin and M. Takahashi at Geological Survey of Japan. Their contribution was of great importance for this research and is thankfully acknowledged.

References

[1] Shepherd J, Rixon LK, Griffiths L. Int J Rock Mech Min Sci Geomech Abstr 1981;18:267–83.
[2] Dumpleton S. Mining Engr 1990;322–9.
[3] Beamish BB, Crosdale PJ. Int J Coal Geol 1998;35:27–55.
[4] Bibler CJ, Marshall JS, Pilcher RC. Int J Coal Geol 1998;35:283–310.
[5] Frodsham K, Gayer RA. Int J Coal Geol 1999;38:297–332.
[6] Cao Y. J Chin Coal Soc Suppl 1994;20:76–8.
[7] Bustin RM. Can Inst Min Met Bull 1982;75:76–83.
[8] Li H. Int J Coal Geol 2001;47:101–13.
[9] Li H, Ogawa Y. Environ Geol 2001;40:1455–61.
[10] Alpern B. Int J Rock Mech Min Sci 1970;7:67–76.
[11] Harris IH, Davies GA, Gayer RA, Williams K. Geol Soc Special Publ 1996;109:181–96.
[12] Harpalani S, Schraufnagel RA. Fuel 1990;69(5):551–6.
[13] King GR, Ertekin TM. Proceedings of the Coalbed Methane Symposium; 17–20 Aprile 1989. University of Alabama. p. 125.
[14] Gamson PD, Basil B, Johnson DP. Fuel 1993;72(1):87–99.
[15] Wang Y, Yang S. J Chin Coal Soc 1980;1:47–53.

Pseudotachylyte from an ancient accretionary complex: Evidence for melt generation during seismic slip along a master décollement?

E. Ikesawa Department of Earth and Planetary Science, University of Tokyo, Tokyo 113-0033, Japan
A. Sakaguchi Institute of Frontier Research on Earth Evolution, Japan Marine Science and Technology Center, Yokosuka 237-0061, Japan
G. Kimura Department of Earth and Planetary Science, University of Tokyo, Tokyo 113-0033, Japan, and Institute of Frontier Research on Earth Evolution, Japan Marine Science and Technology Center, Yokosuka 237-0061, Japan

ABSTRACT

Pseudotachylyte is present in the Shimanto accretionary complex in Shikoku, Japan. The pseudotachylyte occurs as a vein in a fault zone and displays flow structure, TiO_2 microlites, and other melting-related textures. The mineral assemblage of the pseudotachylyte suggests that the temperature was raised at least 450 °C above the background levels in the host rocks. This is the first direct evidence of seismogenic fault rock from an accretionary complex. The pseudotachylyte-bearing fault is a roof thrust above underthrusted mélange, which is overlain by an offscraped package of coherent units. The geologic setting of the pseudotachylyte is consistent with melt generation during seismic slip along the master décollement in the subduction zone.

Keywords: pseudotachylyte, accretionary complex, subduction, seismogenic zone, Shimanto.

INTRODUCTION

The understanding of the seismogenic process in subduction zones is an important issue of geodynamics and is one of the highest prioritized targets of the Integrated Ocean Drilling Program (Integrated Ocean Drilling Program Planning Sub-Committee, Scientific Planning Working Group, 2001). The depth range of the seismogenic zone is from ~4 to ~40 km (Savage and Thatcher, 1992). Recent hypotheses suggest that temperature controls updip and downdip limits of the seismogenic zone (e.g., Hyndman et al., 1993). Clay mineral transformation (Vrolijk, 1990) or other diagenetic mineral transformations at ~150 °C (Moore and Saffer, 2001) may coincide with the updip limit, and brittle-plastic transition of quartz and plagioclase may correlate with the downdip limits at ~350–450 °C (Hyndman et al., 1993).

The thermal conditions of the seismogenic zone encompass the range of metamorphism, from zeolite, through prehnite-pummpelyite, to blueschist or greenschist facies (Ernst et al., 1970). Many accretionary complexes exposed on land record such metamorphic range. Several features that may be related to earthquakes, such as repeated episodic fluid flow documented from crack-seal veins (Fisher, 1996) and development of ultracataclasite alternating with pressure solution creep (Onishi et al., 2001), have been found in ancient accretionary prisms. However, unequivocal geologic evidence of seismogenic activity has not been documented to date.

The clearest record of ancient seismicity in the rock is the pseudotachylyte formed by frictional melting along faults (Sibson, 1975). Fault-related pseudotachylytes have been reported from continental plutonic and metamorphic rocks (Masch et al., 1985), but never from subduction-related metamorphic rocks or accretionary complexes. Low-temperature, low-pressure conditions and the presence of abundant water within pore and intracrystal space have made finding pseudotachylyte unlikely in accretionary complexes. Instead of fusion melting, thermal pressurization may be a dominant process during seismic faulting (Mase and Smith, 1985).

In this paper we report the discovery of pseudotachylyte in an accretionary complex. The fault rocks, including the pseudotachylyte, and the geologic setting provide evidence for fusion melting along the master décollement. This discovery raises the possibility that melt generation may be more important during seismic faulting in subduction zones than previously believed.

GEOLOGIC SETTING

The Shimanto accretionary complex in Shikoku, Japan, is divided into Cretaceous and Tertiary units (Fig. 1A) (Taira et al., 1980). The Upper Cretaceous Okitsu mélange is composed of scaly black shales enclosing disrupted pillow basalts, pelagic to hemipelagic red shales, and sandstone lenses (Fig. 1B). The mélange displays a systematic fabric indicating a top-to-the-south, sinistral-reverse sense of shear, which may have been related to underthrusting (Taira et al., 1988). A roof thrust of the mélange bounds a coherent sandstone-dominated unit of the Nonokawa Formation, and the pseudotachylyte occurs within the roof thrust. Most of the bedding of the Nonokawa Formation and the foliation of the Okitsu mélange strike ENE-WSW and steeply dip northward (Fig. 1B). The age difference between the Coniacian to Maastrichtian black shale and Cenomanian-Turonian pelagic red shale in the mélange (<30 m.y.) indicates subduction of a young oceanic plate in Late Cretaceous time (Taira et al., 1980; Sakaguchi, 1999). Thermal analysis using vitrinite reflectance reveals that the maximum past temperatures of the Nonokawa Formation and the Okitsu mélange were 230 ± 30 and 270 ± 30 °C, respectively (Fig. 1A) (Sakaguchi, 1996).

EVIDENCE OF PSEUDOTACHYLYTE IN THE ROOF THRUST

The roof thrust strikes east-northeast, dips steeply to the north, and may be traced for several kilometers in the field (Figs. 1A and 2). The thickness of the fault zone of high shear strain ranges from ~2 to 5 m (Fig. 2). The shear zone consists predominantly of cataclasites, which overprint a pressure-solution cleavage (Fig. 3A). A cataclastic S-C fabric is well developed in the zone and slickenlines are observed on the C surface. Pseudotachylytes and ultracataclasites are observed along the C surface as dark veins less than a few millimeters in thickness (Fig. 3A). The structure of veins is consistent with repeated friction melting. The youngest fault vein is sharp and straight, cutting older ones that are deformed and partially incorporated into the S-C fabric (Figs. 3A and 3B). Veins have crack-filling geometry and are interpreted to have formed by melt injection into cracks (Figs. 3A and 3B). The sense of shear implied by the cataclastic S-C fabrics indicates top-to-the-south thrusting with a slight sinistral strike-slip component (Fig. 2). The kinematics are similar to those of the mélange fabric, although all the mélanges are clearly cut by the fault. Crack-sealed mineral vein networks composed of quartz, calcite, ankerite, chlorite,

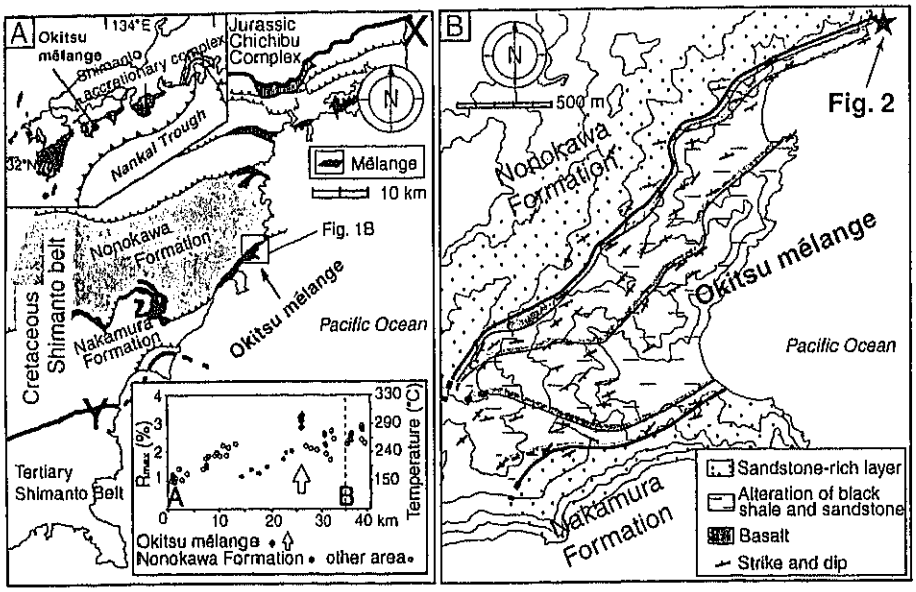

Figure 1. A: Location of Okitsu mélange (Sakaguchi, 1999), and paleothermal structure determined from maximum reflectance of vitrinite (R_{max}) along traverse X to Y on map (modified from Sakaguchi, 1999). Temperature is obtained from following approach of Barker (1988). Note repeated southward increase of R_{max} and thermal peak beyond increasing trend at place of Okitsu mélange. B: Geological map of Okitsu mélange. Map-scale structure suggests presence of composite duplexes. Disrupted layers of basalt extend over more than several kilometers, parallel to general trend of foliation of Okitsu mélange. They are significant markers that delineate geological structures that are characterized by duplex structures at large scale. Surveyed area (Fig. 2) is located near roof thrust of that structure.

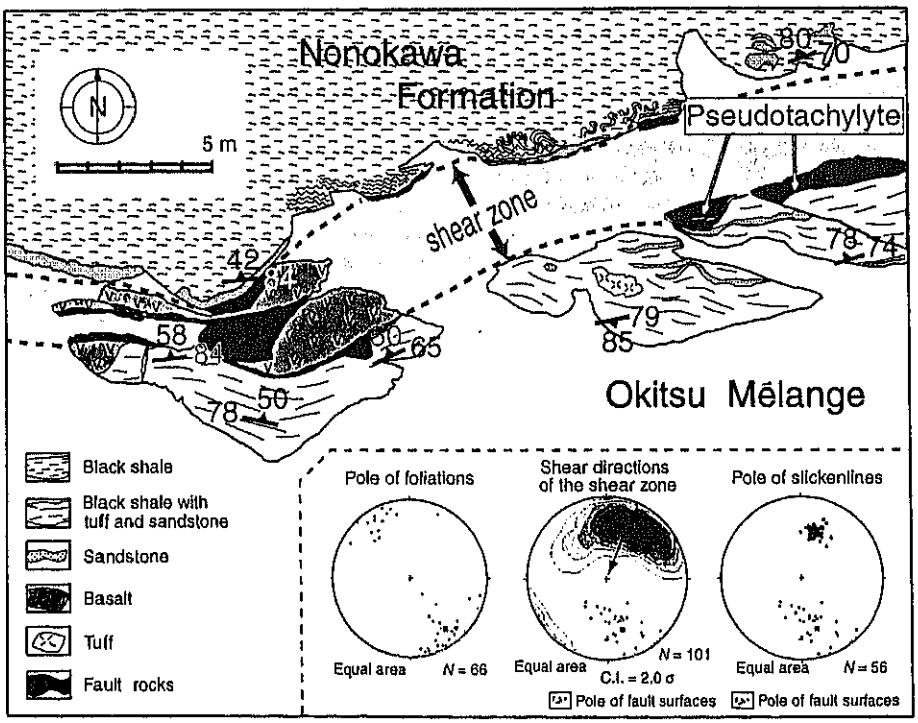

Figure. 2. Geological map of study area located at boundary between Okitsu mélange and Nonokawa Formation. Boundary is identified as shear zone ~5 m thick. Three diagrams show equal-area projection of poles of foliation, shear directions obtained from S-C fabrics of fault rocks, and slickenlines. Contour diagram illustrates density of shear directions. Arrow on equal-area projection of lower hemisphere shows sense shear of hanging-wall block obtained from asymmetric fabrics of shear zone (see Fig. 3A). Note that data of S-C fabric are consistent with slickenlines, and indicate top-to-south thrusting with slight sinistral component.

and zeolite are also developed around the fault and are incorporated into the deformation of the fault.

Several clear textures showing fusion melting are visible under the microscope.

Clasts in the fault veins. At the microscopic scale, the fault veins contain numerous clasts of quartz, feldspar, and calcite (~20% area under the microscope) derived from host rock containing several mineral veins, and abundant idiomorphic TiO_2 mineral grains within a transparent matrix (Figs. 3C and 3D). Clay minerals, which are dominant components in the host rock, are not observed as clasts in the veins. The clasts within the vein are rounded to subrounded (Figs. 3C and 3D), similar in structure to the fault-related pseudotachylytes (Lin, 1999). The rounded margins of the clasts suggest melting erosion.

Flow texture. A flow texture is visible in some of the veins (Fig. 3C). The texture is similar to that commonly observed in the glassy groundmass of extrusive rocks and has been reported from pseudotachylytes (e.g., Lin, 1993; Tanaka et al., 2001).

Injection veins. The wall of the crack-filling injection vein is sharp (Figs. 3A and 3B). The tip of the injection vein is rounded (Fig. 3E) and appears to be an embayment in the wall rocks due to melt caving resulting from corrosion.

TiO_2 microlites. Idiomorphic TiO_2 mineral grains are ubiquitous in the veins. The grain size of TiO_2 minerals varies from 0.1 to 2.8 μm and their average diameter is 0.7 μm. The size of TiO_2 minerals in the marginal part of the injection vein is smaller than that in the central part (Fig. 3D). This grain-size gradation suggests cooling from the margin to the center. Taking the idiomorphic shape and grading size distribution into account, it is suggested that the TiO_2 mineral is a microlite dropped from the melt. Previously reported microlites have shown complex shapes such as spherulitic, dentritic, and skeletal, all of which are caused by rapid chilling (Lin, 1994), but such textures are not visible in this case. Rapid cooling textures are commonly developed in the central part of the several-centimeter-thick pseudotachylyte veins (e.g., Lin, 1994). The thickness of the pseudotachylyte in this study is <~3 mm.

Matrix. Two kinds of matrices, transparent and translucent, are recognized in the veins. Under crossed-polarized light, the transparent matrix is heterogeneous, although optical homogeneity is common for glass matrix. The transparent matrix is homogeneous at high magnification under scanning electric microscope-backscattered electron (SEM-BSE) microscopy (Fig. 3G, right area). Numerous vesicles without amygdules occur in the transparent matrix

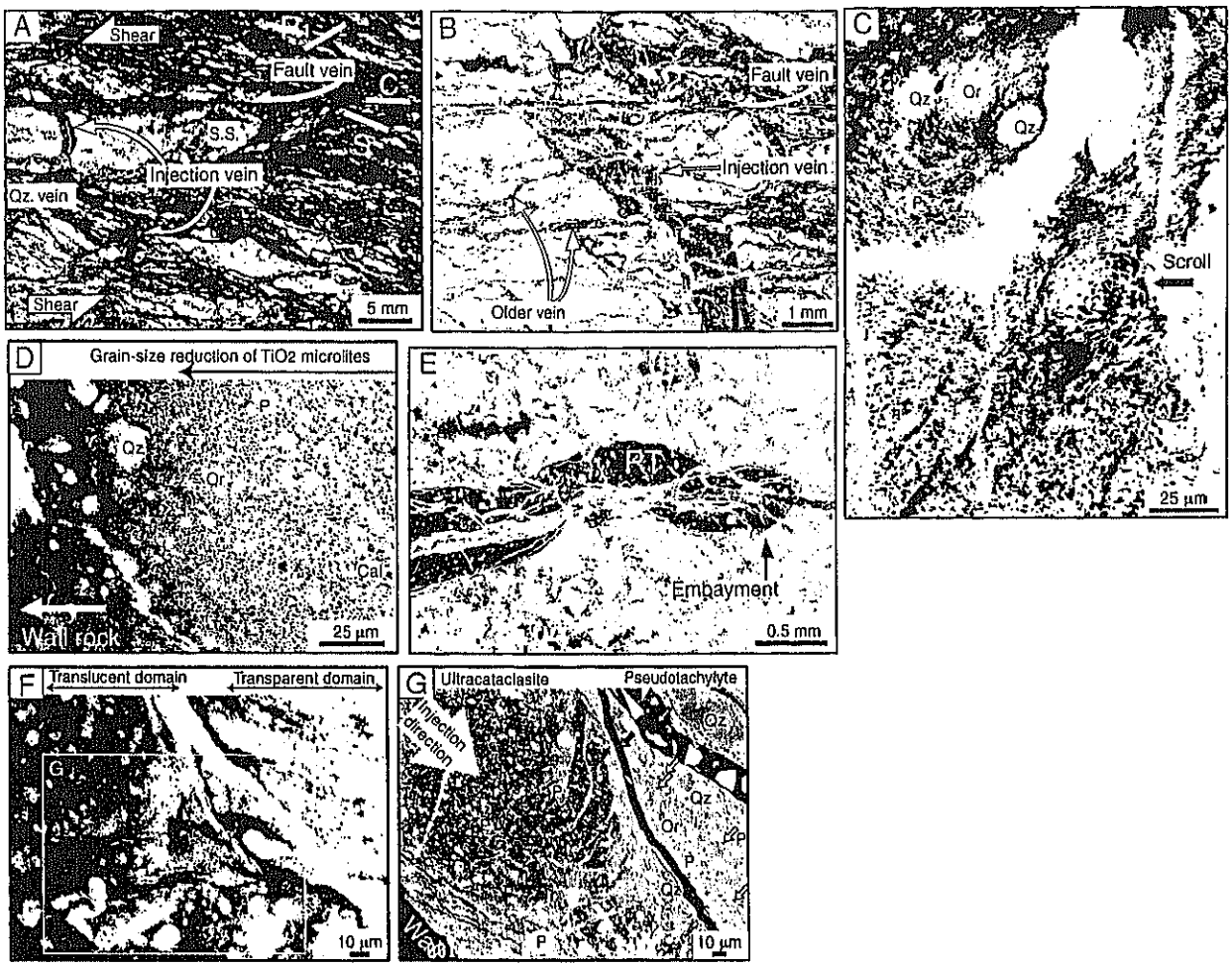

Figure. 3. Photographs of pseudotachylytes. A: Mesoscopic texture observed on polished surface of fault rock. Note that pseudotachylyte is generated on C surface and injected into host rock. Dark parts are considered to be old pseudotachylyte that underwent deformation and alteration. S.S.—sandstone, Qz—quartz. B–G: Microscopic textures observed in plane-polarized light (B–F) and by backscattered electrons (G). B: Photomicrograph of injection vein of pseudotachylyte. Appearance of young pseudotachylyte vein cutting older one shows that pseudotachylyte was repeatedly generated. Such repetition strongly suggests repeated seismicity. C: Flow texture of injection vein showing viscous behavior. Scroll aspect (red arrow) indicates turbulent flow. Dark grains are TiO_2 mineral. P—plagioclase, Or—orthoclase. D: Occurrence of pseudotachylyte at margin of injection vein. Grain size of TiO_2 mineral reduces from center of vein to margin. This occurrence accounts for appearance of chilled margin. Cal—calcite. E: Embayment dead end of injection vein suggesting wall-rock melting. PT—pseudotachylyte vein. F: Two kinds of matrices, translucent and transparent. G: Translucent and transparent matrices seen in backscattered-electron image. Vesicles are observed only in transparent matrix (pseudotachylyte) (yellow arrows). Red arrows indicate epoxy-filled cracks in thin section.

(Fig. 3G, right area). Using SEM-BSE, the translucent matrix appears to consist of fine mineral fragments (Fig. 3G, left area). No vesicle-like features are observed in this type of matrix. On the basis of these features, we infer that the transparent and translucent matrices were originally glass and ultracataclasite, respectively.

Melting temperature of the pseudotachylyte. The temperature for fusion melting is estimated by comparing the surviving mineral assemblage within the pseudotachylyte with that of the host rocks. The grains within the pseudotachylyte are dominantly plagioclase, quartz, calcite, and TiO_2 microlites without clay minerals. Preferential melting of clays transforming to illite and muscovite indicates that the temperature was higher than 650 °C (Spray, 1992). Calcite survival as a clast documents the equilibrated temperature as <740 °C (Deer et al., 1967). Taking this surviving mineral assemblage, the temperature for fusion melting is estimated to range between 650 and 740 °C, ~400–450 °C greater than the maximum temperature (230–270 °C) of the host rocks estimated from vitrinite reflectance.

DISCUSSION

The pseudotachylyte likely formed in one of three possible tectonic settings: (1) master décollement of the plate boundary, (2) out-of-sequence thrust, or (3) intracrustal seismogenic fault. The first two are related to subduction-zone seismicity, whereas the third corresponds to an intraarc event long after the lithification of the forearc.

An accretionary prism is composed mainly of offscraped and tectonically underplated units with minor slope cover sediments (Cowan, 1985; Moore and Silver, 1987). These units are deformed in various ways, and the definition of the units is partly based on difference in deformation mode. The offscraped units are characterized by an initial stage of horizontal shortening by folding and thrusting at various scales. In contrast, the underthrusted to underplated units are characterized initially by vertical flattening with horizontal shear (Fisher and Byrne, 1987; Byrne and Fisher, 1990; Kimura and Mukai, 1991). In on-land accretionary complexes, offscraped units are recognized as folded and thrusted co-

herent units, and the underthrusted to underplated units are often manifested by tectonic mélange (Fisher and Byrne, 1987; Byrne and Fisher, 1990; Kimura and Mukai, 1991; Hashimoto and Kimura, 1999; Ujiie, 1997; Onishi et al., 2001). A boundary fault that juxtaposes a hanging-wall coherent unit and a footwall mélange unit is thought to be the ancient master décollement (Byrne and Fisher, 1990).

The coherent Nonokawa Formation deformed by folding and thrusting (Taira et al., 1980) is consistent with the horizontal shortening expected for an offscraped unit. The Okitsu mélange has been interpreted as an underthrusted unit that was underplated beneath the Nonokawa Formation by the roof thrust containing the pseudotachylyte. Such a geologic setting is consistent with relationships expected for a plate boundary décollement. The sense of shear of the roof thrust is essentially the same as that of mélange, which is consistent with that of décollement in the subduction zone. Because the roof thrust cuts and overprints the fabric of mélange, the roof thrust must have been active later than the deformation of mélange. The deformation mechanisms of mélange are initially independent particulate flow and grain-scale cataclasis to later stage pressure solution (Onishi and Kimura, 1995; Hashimoto and Kimura, 1999). These mechanisms of mélange deformation represent a shallower and slower process of underthrusting than cataclasis with pseudotachylyte in the roof thrust. Therefore, the crosscutting relationship between the roof thrust and mélange indicates deformation at a different time and condition in the subduction zone; shallow and slow underthrusting is recorded by the mélange and cyclic deformation in the roof thrust at the seismogenic depth.

If the roof thrust were formed as an out-of-sequence thrust or later intracrustal fault, it would be expected to offset the older mélange fabrics more obliquely and record different kinematics. In addition, an out-of-sequence thrust would imply that the hanging-wall block was situated much deeper than before displacement. If displacement were large along the fault, a thermal inversion, i.e., hotter hanging-wall block than lower one, would be expected (Ernst et al., 1970; Peacock, 1987; Ohmori et al., 1997). The thermal difference between the Nonokawa Formation (230 ± 30 °C) and the Okitsu mélange (270 ± 30 °C) is inconsistent with such a thermal inversion. If the roof thrust was a master décollement, then it could have juxtaposed the hanging and footwall blocks without the thermal inversion. A primarily horizontal décollement would be almost parallel to the isotherm for several kilometers (Underwood et al., 1993), although an out-of-sequence thrust and intracontinental reverse fault might be highly oblique to the isotherm. Accordingly, the likely setting of the roof thrust is a master seismogenic décollement in the subduction zone.

Discovery of the pseudotachylyte in an ancient master décollement suggests that friction melt driving rupture propagation may occur in subduction zones. Although the preferred hypothesis to date has been coseismic weakening of subduction thrusts by thermal pressurization of pore fluids (Mase and Smith, 1985), our new observations suggest that melting is also a significant mechanism of dynamic weakening in subduction zones.

ACKNOWLEDGMENTS

This work was supported and helped by M. Okamura, H. Matsuoka, H. Tanaka, and the kind persons of the "Riders-inn Nakatosa." We thank P. Cummins, A. Kopf, F. Chester, and J.C. Moore for their thorough and constructive reviews.

REFERENCES CITED

Barker, C.E., 1988, Geothermics of petroleum systems: Implications of the stabilization of kerogen thermal maturation after a geologically brief heating duration at peak temperature: U.S. Geological Survey Bulletin, v. 1870, p. 26–29.

Byrne, T., and Fisher, D., 1990, Evidence for a weak and overpressured décollement beneath sediment-dominated accretionary prisms: Journal of Geophysical Research, v. 95, p. 9081–9097.

Cowan, D.S., 1985, Structural styles in mesozoic and Cenozoic Mélanges in the western Cordillera of North America: Geological Society of America Bulletin, v. 96, p. 451–462.

Deer, W.A., Howie, R.A., and Zussman, J., 1967, An introduction to the rock-forming minerals (second edition): London, Longmans, Green And Co. Ltd; 478 p.

Ernst, W.G., Seki, Y., Onuki, H., and Gilbert, M.C., 1970, Comparative study of low-grade metamorphism in the California Coast Ranges and the outer metamorphic belt of Japan: Geological Society of America Memoir 124, 276 p.

Fisher, D.M., 1996, Fabrics and veins in the forearc: A record of cyclic fluid flow at depths of <15 km, *in* Bebout, G.E., et al., eds., Subduction top to bottom: American Geophysical Union Geophysical Monograph 96, p. 75–89.

Fisher, D.M, and Byrne, T., 1987, Structural evolution of underthrusted sediments, Kodiak Islands, Alaska: Tectonics, v. 6, p. 775–793.

Hashimoto, Y., and Kimura, G., 1999, Underplating process from melange formation to duplexing: Example from the Cretaceous Shimanto Belt, Kii Peninsula, southwest Japan: Tectonics, v. 18, p. 92–107.

Hyndman, R.D., Wang, K.J., Yuan, T., and Spence, G.D., 1993, Tectonic sediment thickening, fluid expulsion, and the thermal regime of subduction zone accretionary prisms; the Cascadia margin off Vancouver Island: Journal of Geophysical Research, Solid Earth, v. 98, p. 21,865–21,876.

Integrated Ocean Drilling Program Planning Sub-Committee, Scientific Planning Working Group, 2001, Earth, oceans and life: Washington, D.C., International Working Grouping Office, p. 68–70.

Kimura, G., and Mukai, A., 1991, Underplated units in an accretionary complex-melange of the Shimanto Belt of eastern Shikoku, southwest Japan: Tectonics, v. 10, p. 31–50.

Lin, A., 1993, Grassy pseudotachylyte veins from the Fuyun fault zone, northwest China: Journal of Structural Geology, v. 16, p. 71–83.

Lin, A., 1994, Microlite morphology and chemistry in pseudotachylyte, from the Fuyun fault zone, China: Journal of Geology, v. 102, p. 317–329.

Lin, A., 1999, Roundness of clasts in pseudotachylytes and cataclastic rocks as an indicator of frictional melting: Journal of Structural Geology, v. 21, p. 473–478.

Mase, C.W., and Smith, L.S., 1985, Pore-fluid pressure and frictional heating on a fault surface: PAGEOPH, v. 122, p. 583–607.

Masch, L., Wenk, H.R., and Preuss, E., 1985, Electron-microscopy study of hyalomylonites—Evidence for frictional melting in landslides: Tectonophysics, v. 115, p. 131–160.

Moore, J.C., and Saffer, D., 2001, Updip limit of the seismogenic zone beneath the accretionary prism of southwest Japan: An effect of diagenetic to low-grade metamorphic processes and increasing effective stress: Geology, v. 29, p. 183–186.

Moore, J.C., and Silver, E.A., 1987, Continental-margin tectonics—Submarine accretionary prisms: Reviews of Geophysics, v. 25, p. 1305–1312.

Ohmori, K., Taira, A., Tokuyama, H., Sakaguchi, A., Okamura, M., and Aihara, A., 1997, Paleothermal structure of the Shimanto accretionary prism, Shikoku, Japan; role of an out-of-sequence thrust: Geology, v. 25, p. 327–330.

Onishi, C.T., and Kimura, G., 1995, Mélange fabric and relative convergence in subduction zone: Tectonics, v. 14, p. 1273–1289.

Onishi, C.T., Kimura, G., Hashimoto, Y., Ikehara-Ohmori, K., and Watanabe, T., 2001, Deformation history of tectonic melange and its relationship to the underplating process and relative plate motion: An example from the deeply buried Shimanto Belt, SW Japan: Tectonics, v. 20, p. 376–393.

Peacock, S.M., 1987, Thermal effects of metamorphic fluids in subduction zones: Geology, v. 15, p. 1057–1060.

Sakaguchi, A., 1996, High paleo-geothermal gradient with ridge subduction beneath Cretaceous Shimanto accretionary prism, southwest Japan: Geology, v. 24, p. 795–798.

Sakaguchi, A., 1999, Thermal structure and paleo-heat flow in the Shimanto accretionary prism, southwest Japan: The Island Arc, v. 8, p. 359–372.

Savage, J.C., and Thatcher, W., 1992, Interseismic deformation at the Nankai trough, Japan, subduction zone: Journal of Geophysical Research, Solid Earth, v. 97, p. 11,117–11,135.

Sibson, R.H., 1975, Generation of pseudotachylyte by ancient seismic faulting: Royal Astronomical Society Geophysical Journal, v. 43, p. 775–794.

Spray, J.G., 1992, A physical basis for the frictional melting of some rock-forming minerals: Tectonophysics, v. 204, p. 205–221.

Taira, A., Okamura, M., Katto, J., Tashiro, M., Saito, Y., Kodama, K., Hashimoto, M., Chiba, T., and Aoki, T., 1980, Lithofacies and geologic age relationship within mélange zone of northern Shimanto Belt (Cretaceous), Kochi Prefecture, Japan, *in* Taira, A., and Katto, J., eds., Geology and paleontology of the Shimanto Belt: Kochi, Japan, Rinya-Kosaikan Press, p. 179–214.

Taira, A., Katto, J., Tashiro, M., Okamura, M., and Kodama, K., 1988, The Shimanto Belt in Shikoku, Japan—Evolution of Cretaceous to Miocene accretionary prism: Modern Geology, v. 12, p. 5–46.

Tanaka, H., Fujimoto, K., Ohtani, T., and Ito, H., 2001, Structural and chemical characterization of shear zones in the freshly activated Nojima fault, Awaji Island, southwest Japan: Journal of Geophysical Research, Solid Earth, v. 106, p. 8789–8810.

Ujiie, K., 1997, Off-scraping accretionary process under the subduction of young oceanic crust: The Shimanto Belt of Okinawa Island, Ryukyu Arc: Tectonics, v. 16, p. 305–322.

Underwood, M.B., Hibbard, J.P., and DiTullio, L., 1993, Geologic summary and conceptual framework for the study of thermal maturity within the Eocene-Miocene Shimanto Belt, Shikoku, Japan, *in* Underwood, M.B, ed., Thermal evolution of the Teritory Shimanto Belt, Southwest Japan; an example of ridge-french intraction: Geological Society of America Special Paper 273, p. 1–24.

Vrolijk, P., 1990, On the mechanical role of smectite in subduction zone: Geology, v. 18, p. 703–707.

Manuscript received 10 January 2003
Revised manuscript received 4 April 2003
Manuscript accepted 5 April 2003

Printed in USA

地学雑誌
Journal of Geography
112(6) 885-896 2003

四万十付加体興津メランジュの震源断層の特徴と流体移動に伴うセメンテーションによる固着すべりのアナログ実験

坂　口　　有　人*

Observation of the Seismogenic Fault in the Okitsu Melange, Shimanto Accretionary Complex and Stick Slip of Mineral Cementation of Shear Experiment

Arito SAKAGUCHI *

Abstract

The seismogenic fault in the Okitsu Melange, Shimanto accretionary complex, Shikoku is characterized by repeated rapid slips with a pseudotachylyte formation and a concentration of vein minerals. The Okitsu Melange is composed of duplex structure of imbricated oceanic stratigraphic sequence, and the seismogenic fault is emplaced at the roof thrust of the duplex structure. Comparable fault along the seismogenic roof thrust of the duplex structure was found at the present Nankai trough, and vein mineral precipitation is expected from the fluid flow along the fault.

Some of the clasts of cataclacite were supported by a vein mineral matrix of euhedral ankerite and quartz crystals. This occurrence of vein minerals may indicate rapid precipitation due to fluid flow of super saturation with vein minerals along the fault zone. The shear strengthening with time and the stick slips were recognized by the block-slider analogue experiments which consisted of the chilled slid with ice and hot water saturated with alum on the shear surface. The result of the experiment indicates that the vein mineral precipitation make stick slip the fault.

Key words: subduction zone, pseudotachylyte, alum, stick slip
キーワード：沈み込み帯，シュードタキライト，ミョウバン，固着すべり

I. はじめに

巨大地震の多くがプレート沈み込み帯で発生しているにもかかわらず（Sholtz, 1990；ショルツ, 1993），海溝型震源断層の断層岩の地質学的分析がほとんどなされてこなかったのは，その陸上露頭が未発見であったことに起因してきた。近年になり，現世の南海トラフの地殻熱流量は非常に高いこと（Yamano *et al.*, 1984；Ashi and Taira, 1993 など），南海，東南海地震の震源領域の温度

* 海洋科学技術センター固体地球統合フロンティア研究システム
* IFREE, Japan Marine Science & Technology Center

条件がおよそ150～300℃であることが示されるようになった（Hyndman *et al.*, 1993）。一方で，南海付加体の陸上延長である四万十帯の温度圧力条件の定量化も進められ（Sakaguchi, 1996, 1999; Ohmori *et al.*, 1997），低い場所でも被熱温度は150℃に達することが明らかになってきた。そのため過去の海溝型震源断層が四万十帯のどこかに存在することが指摘されるようになり（木村, 1997; 狩野, 1999），四国西部の興津メランジュでプレート沈み込み作用に伴うシュードタキライトが世界で初めて報告されるに至った（Ikesawa *et al.*, 2003）。本論では，この興津メランジュに産する震源断層の特徴を述べるとともに，この断層露頭から推定される断層の固着メカニズムと簡単なアナログ実験を紹介する。

II. 地質概要

西南日本外帯に位置する四万十帯は，その年代，構造，温度圧力条件などが世界でも最も詳細に調査されている付加体の一つである。四万十帯は北を仏像構造線でジュラ系付加体の秩父帯と接しており，北から白亜系ユニットと第三系ユニットから構成されている。秩父帯南部から含めて，全体的に北から南へと若くなる年代特性を持ち，四国西部では白亜系ユニットは北から下部白亜系の新荘川層群と上部白亜系の大正層群。第三系ユニットも同じく北から始新統の幡多層群と中新統の莱生層群から構成される。四万十帯の大半は砂岩泥岩互層からなるタービダイトの海溝充填堆積体であるが，その一部に，浅海性の被覆堆積体や地質図スケールの剪断帯であるメランジュが挟み込まれるように分布し，そこには海洋地殻の破片がブロック状に産する。四国西部の大正層群には横波，久礼，興津の3帯のメランジュ層が分布し，いずれも剪断された黒色頁岩中に玄武岩，チャート，多色頁岩，陸源性砕屑岩の岩体をブロック状に含むことで特徴づけられ，それぞれのメランジュ毎に微化石年代に基づいて付加当時の海洋底層序が復元されている（Taira *et al.*, 1988）。これに基づく玄武岩の噴出から海溝に到達するまでの時間は，秩父帯から四万十帯の南端にかけて徐々に短くなっていき，チャートに乏しい興津メランジュが付加する頃には10 Ma以下にまで小さくなったと指摘されている（Taira *et al.*, 1988）。また，興津メランジュと同じゾーンのメランジュである四国東部の牟岐メランジュおよび九州東部の槇峰層の玄武岩体の微量元素分析は，これが典型的な海嶺起源の玄武岩であることを示しており（君波ほか, 1992），白亜紀最後期の四万十帯には，日本列島に海嶺が近づき，きわめて若いプレートが沈み込んでいたことを示している（Taira *et al.*, 1988; 君波ほか, 1992）。

四国四万十帯の熱構造は，ジルコンやアパタイトのフィッショントラック法，石炭の熟成度指標の一つであるビトリナイト反射率，イライトの結晶度，鉱物脈中の流体包有物分析などによって報告されている（坂口ほか, 1992; Hasebe *et al.*, 1993; Tagami *et al.*, 1995; Ohmori *et al.*, 1997）。その結果，低温の部分でさえ約150℃以上あり，一般にメランジュ相と海溝充填堆積体および被覆堆積体といった岩相による違いはあまり反映されない。例えばフィッショントラック熱年代法分析でも，白亜紀前期から後期までのユニット全体が約70 Maのジルコン FT 年代を示し，第三紀のユニットも約10 Maのアパタイト FT 年代が岩相や年代の違いを越える特有の傾向として報告されている（Hasebe *et al.*, 1993; Tagami *et al.*, 1995）。またビトリナイト反射率による熱構造解析では，岩相や付加年代差を超えて，北から南への単純な増加と特定の断層によって急低下するという鋸の刃のような傾向を繰り返すことで特徴づけられ，浅海堆積体でさえ150～200℃という高い温度を受けていることが示された（坂口ほか, 1992）。地質構造に依存せず，しかも浅海堆積物までが高温であったという特徴から，熱構造は付加体定置後の熱的イベントによって形成されたのではないかと解釈された。加えて鉱物脈中の流体包有物の分析がなされ，包有物中の流体の密度とビトリナイト反射率による母岩の最高被熱温度との間に相関関係があることが示された。流体密度は温度と圧力の関数で表現されることから，ビトリナイト反射率による母岩の最高温度を流体温

度の上限とすることで流体圧が求められ，当時の地温勾配が約 50 ℃/km 以上であったと推測された。そして高地温勾配の原因としては，白亜紀最後期から始新世にかけての若いプレートの沈み込みによるものではないかと提案された (Sakaguchi, 1996 ; Sakaguchi, 1999)。

一般にメランジュと周辺層との間に顕著な温度差は認められないが，若いプレートの沈み込みに伴って形成された興津メランジュのみは，周辺層よりもとりわけ高い温度を受けたことを示している。ビトリナイト反射率に基づく分析では，興津メランジュを挟む南北のユニットである野々川層と中村層がそれぞれ約 230 (± 30) ℃ とほぼ同程度の温度を受けたのに対して，その間の興津メランジュのみが約 270 (± 30) ℃ と高温であったことが示されている (Sakaguchi, 1996)。そして，興津メランジュの中でもとりわけ北の境界断層付近においてイライト結晶度が最も高いことが認められている (Sakaguchi *et al.*, submitted)。詳細は後述するが，この断層付近は鉱物脈の濃集帯が卓越しており，特に断層沿いに一段と高温の熱水が存在していた可能性が高い。そしてこの断層帯にはシュードタキライトが産し，付加体における最初の発見として報告された (Ikesawa *et al.*, 2003)。上記のように，この断層が形成された当時の地殻熱流量は非常に高かったと推測され (Sakaguchi, 1996)，それは若い四国海盆の沈み込みの影響で，トラフ底で 110～130 mW/m^2 もの高熱流量が観測されている現世南海トラフ (Yamano *et al.*, 1984 ; Taira *et al.*, 1991) と類似の温度環境であるため，南海トラフ震源断層と対比可能な断層帯と考えられる。

III. テクトニックセッティング

興津メランジュは白亜系四万十帯の他のメランジュと比較して黒色頁岩と玄武岩が卓越し，チャートなど遠洋性岩が乏しいことで特徴づけられる。黒色頁岩には若干の凝灰岩層や砂岩層がレンズ状に含まれるが，地層は一般に分断されて連続性が良くない。しかしながら地質図スケールでは，玄武岩層や黒色頁岩優勢の部層は側方に連続的に追跡可能である。これは，もとの層序は分断され一見破壊されているが，大局的には沈み込む以前の海洋底層序の順番を保存しており，メランジュの内部構造を推定する上での重要な鍵層となりうる。

詳細な地質構造調査によると，玄武岩層は側方に連続しており，これを元にメランジュ内部の地質構造を描くと，厚さ数 10 m～数 100 m の海洋底層序が少なくとも 5 回覆瓦状に繰り返される様子が描き出される (図 1) (Sakaguchi *et al.*, 2003)。これはいわゆるデュープレックス構造であり，底付けされた付加体で典型的に見られる (村田, 1991; Hashimoto and Kimura, 1999 など)。そして衝上断層に囲まれたそれぞれの海洋底層序の層はデュープレックス構造のホースと呼ばれ (Bopyer and Elliott, 1982)，その位置関係から覆瓦状構造の上下を成すルーフおよびフロア衝上断層の変位量とセンスをある程度推定することができる。このメランジュのデュープレックス構造の場合，その形態から断層の変位量はホースの長さよりも短い後背地傾斜デュープレックス (Bopyer and Elliott, 1982 ; 狩野・村田, 1998) と分類することができ，地質図上で左横ずれセンスを示す (図 1)。

興津メランジュの北の境界断層である，デュープレックス構造のルーフ衝上断層には多くのスリッケンラインやS-C構造状の変形構造が数多く見られ，それらから求められた剪断面の平均方位は N55E80N とメランジュの面構造の平均方位 N55E70N とほぼ平行であり，運動センスは 20E40N のやや東プランジの衝上センスを示す (図 1)。メランジュの剪断センスと断層帯のそれが矛盾しないことから，この断層帯が沈み込み作用に伴って形成されたものであると解釈できる。デュープレックス構造が地質図上で左横ずれセンスに見えることは，剪断センスが若干の東プランジであることから，地質体全体がメランジュおよび断層形成後の隆起過程においてやや西に横倒しになって露出しているためであると説明しうる (Sakaguchi *et al.*, 2003)。すなわちシュードタキライトを含む震源断層は，付加体の底付け作用

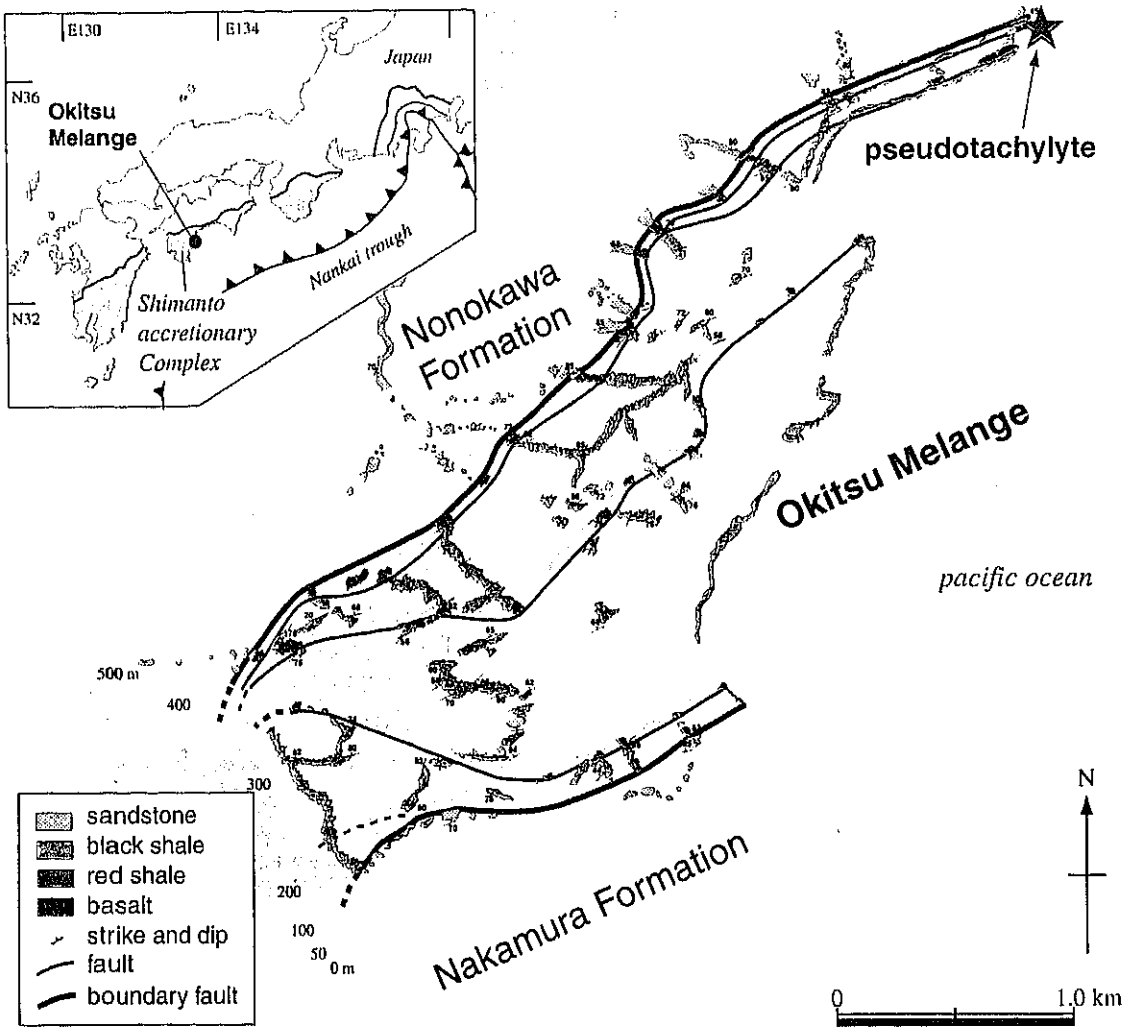
E130
E134
Japan
N36
Okitsu Melange
Nankai trough
N32
Shimanto accretionary Complex
pseudotachylyte
Nonokawa Formation
Okitsu Melange
pacific ocean
500 m
400
300
200
100
50
0 m
sandstone
black shale
red shale
basalt
strike and dip
fault
boundary fault
Nakamura Formation
N
0
1.0 km

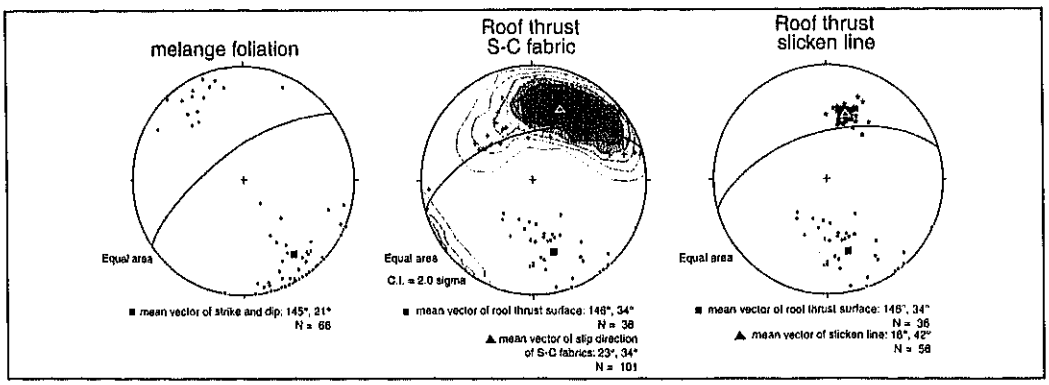
melange foliation
Roof thrust S-C fabric
Roof thrust slicken line
Equal area
Equal area
C.I. = 2.0 sigma
Equal area
■ mean vector of strike and dip: 145°, 21°
N = 66
■ mean vector of roof thrust surface: 146°, 34°
N = 38
▲ mean vector of slip direction of S-C fabrics: 23°, 34°
N = 101
■ mean vector of roof thrust surface: 146°, 34°
N = 36
▲ mean vector of slicken line: 18°, 42°
N = 58

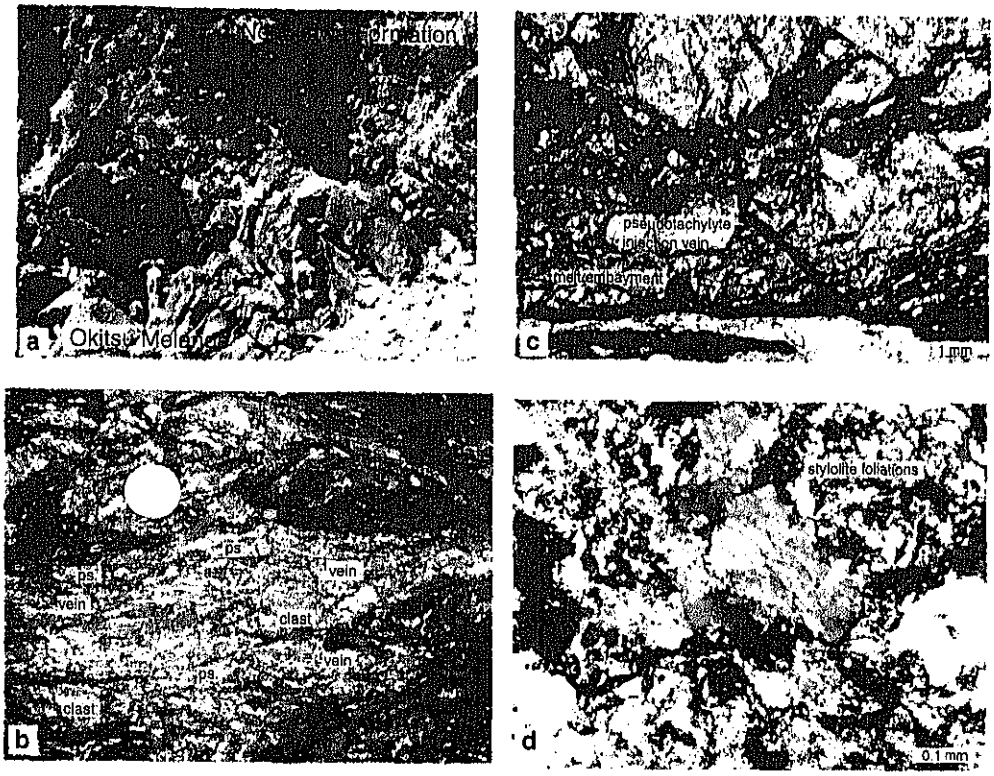

図 2 (a) 震源断層の露頭写真．断層は下盤の興津メランジュと上盤の野々川層との間に発達しており，シュードタキライトと鉱物脈が濃集することで特徴づけられる．鉱物脈は石英とアンケライトから成る．アンケライトがより多く発達する部分は，風化作用によって露頭が赤茶けて見える．
(b) 鉱物脈およびシュードタキライト脈（ps）は圧力溶解変形を被り，S-C 状構造が発達している．
(c) 古いシュードタキライトは鉱物脈と共にインターサイスミックの圧力溶解変形を受けており，それを新しいシュードタキライト注入脈が切る．断層の高速剪断が繰り返し生じていたことを示す．
(d) S-C 状構造を成す鉱物脈には，スタイロライトフォリエーションが発達しており，圧力溶解作用で変形を受けたことを示している．

Fig. 2 The seismogenic fault occurred between the hanging wall of the Nonokawa Formation and the foot wall of the Okitsu Melanges.
The fault zone is characterized by the concentration of pseudotachylyte and vein minerals of quartz and ankerites (a). Vein minerals and pseudotachylytes (ps) suffered interseismic deformation with S-C fabrics (b). Older pseudotachylytes are cut by newer ones, meaning faulting repeated (c). Stylolite foliation and amoeboidal shape of grains indicate the development of pressure solution creeping during interseismic period to make the S-C fabric (d).

図 1 興津メランジュの地質図．
海洋底層序が覆瓦状に重なりあうデュープレックス構造を成している．地質図スケールのデュープレックス構造は付加体の底付けユニットに特徴的な構造であり，震源断層はそのルーフ衝上断層に位置する．メランジュの劈開面とルーフ衝上断層の剪断面はほぼ平行である．断層帯中の S-C 状構造の複合面組織による剪断センスと断層面上のスリッケンラインの方向はほとんど同じ方向を示し，若干の東プランジだが，ほぼ傾斜方向の衝上断層である．

Fig. 1 Geologic map of the Okitsu Melange composed of a duplex structure of a imbricated oceanic stratigraphic sequences.
The seismogenic fault is placed along the roof thrust of the duplex structure. Asymmetric deformation fabric analysis shows that the sense of shear of the fault zone is similar to the sense of the fabric within the melange unit. Faulting was probably concurrent with the stage of duplexing of the Okitsu Melange.

に伴うデュープレックス構造のルーフ衝上断層に発達したと結論づけられる。

IV. 震源断層の特徴

シュードタキライトを含む震源断層は，調査地域東端の海岸に幅5～6m長さ30mにわたって非常に良い露出を示す。断層帯はデュープレックス構造のルーフ衝上断層の玄武岩層沿いに発達しており，石英やアンケライト脈が多産する。特に鉄・マンガンに富むドロマイトであるアンケライト脈の風化のために露頭全体が赤茶けた様相を呈する（図2a)。断層帯中には幅約20～30cm程度の特に強く剪断され(図2b)，かつ鉱物脈が濃集している強変形帯が少なくとも4層は発達しており，互いに分岐・融合して産し，全体としては幅5～6mになる。そういった強変形帯にシュードタキライトは産し，古いシュードタキライトや鉱物脈は，相対的に新しいシュードタキライトに切られている（図2d)。断層帯の変形は全体的には上位に向かって徐々に弱くなる片翼状の非対称構造を示し，シュードタキライトは最下位の変形集中帯に産する（図3)。これら変形集中帯が稠密に産する断層帯の上位の野々川層内にも数本の破砕帯が発達しており，これらの断層群まで含めて震源断層のダメージゾーンとすると，その厚さは約30mになる（図4)。

断層中の強変形帯は，濃集した鉱物脈と岩片およびシュードタキライトがS-C状構造を持つことで特徴付けられる。S-C状に変形した岩石は鏡下では個々の粒子境界が互いに食い込み，粒界拡散現象の進行に伴って不溶性物質が縫合線状に濃集するスタイロライトフォリエーションがいたる所に見られ，圧力溶解機構による変形を受けたことがわかる（図2d)。一方で圧力溶解変形から免れていた鉱物脈も産し(図5a)，シュードタキライト形成と交互に鉱物脈の沈澱が生じたことがわかる(図5b)。一部の石英結晶の成長面上には，微小なアンケライト結晶が含まれており（図5c)，石英結晶の成長表面に石英と共にアンケライトが析出したことを示している。一方ではアンケライトが自形を持ち，その間隙に石英が析出した部分もあり(図5d)，両者が共沈したことを示す。溶解度が全く異なる鉱物が共沈した原因としては，流体の温度・圧力が急激に低下し，両鉱物に対する溶解能力が共に急低下したとすると考えやすい。

また一部には水圧破砕を示す産状や破砕後に脈鉱物によってセメントされたと考えられる鉱物脈も見られ(図5a)，一部にはシュードタキライト脈の岩片がジグソーパズルテクスチャーを持ち，岩片はアンケライトによって支持されている産状を示すものもある（図5b)。これはシュードタキライトが冷却固結後に水圧破砕され，岩片が流体によって運搬沈澱するよりも早くアンケライトおよび石英が沈澱して岩片が支持されたもので，鉱物脈の高速沈澱の証拠ではないかと解釈される。

以上のように，断層帯はイライト結晶度が高く，鉱物脈が多産することで特徴づけられる。そしてそこでは溶解度の異なる鉱物が共沈し，破砕物が脈結晶基質によって支持されている。これらの産状は，沈み込み帯深部から流体が上昇してきたと考えれば説明可能である。つまりシュードタキライト脈も水圧破砕を受けていることから，断層の高速運動とシュードタキライトの冷却後に断層破砕帯沿いに流体が十分に速い速度で深部から移動してきたとすると，母岩との間に熱平衡に達せずに高温の熱水が断層浅部に存在しうるし，溶解度の異なる鉱物の共沈現象と多量の鉱物脈の形成も引き起こすことが可能であろう。

本断層のような底付けユニットのルーフ衝上断層における流体の存在は，南海トラフにおけるマルチチャンネル音波探査によっても報告されている。南海トラフの震源領域における詳細なイメージング結果によると，1946年の南海地震の震源領域では，南海トラフ付加体のデコルマ帯がステップダウンするとともに底付け作用が始まっている。そしてデコルマ帯上位の底付けユニットのルーフ衝上断層に強い音響反斜面が認められており，Deep Strong Reflector（DSR）と呼ばれている(Park *et al.*, 2002)。このDSRは音響特性が負であり，走向方向にも不連続でパッチ状に分布する特徴を持つ。これはルーフ衝上断層沿いの所々に音波速度が低速な領域，すなわち流体が存在して

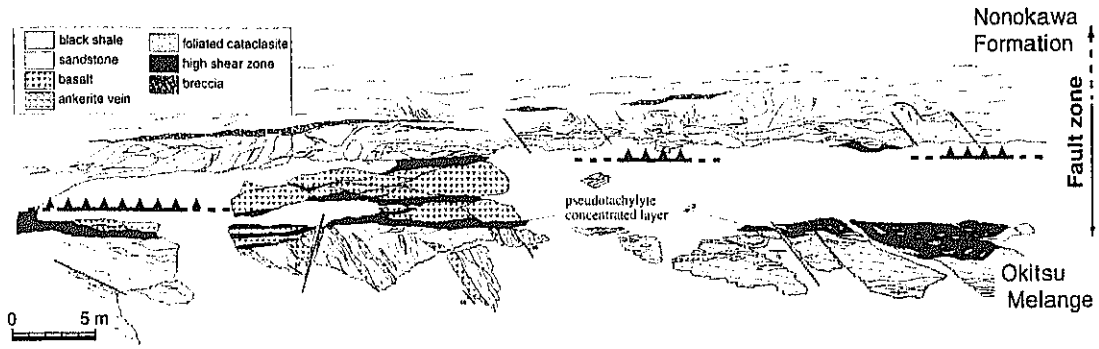

図 3　断層露頭付近のルートマップ．
鉱物脈やシュードタキライトしている強剪断帯が幾重にも枝分かれしながら発達するゾーンが幅約 5-6 m あり，その上位には幅 10 数 cm 程度の破砕帯が何層か発達し，全体としては 30 m 程度の断層帯となる．変形は下位ほど強く，最下部にシュードタキライトが良く発達する．

Fig. 3　Route map along the fault zone.
The fault zone, 30 m in thickness, is composed of a lower unit of high shear bands and an upper unit of weak deformation with some of breccia zones.

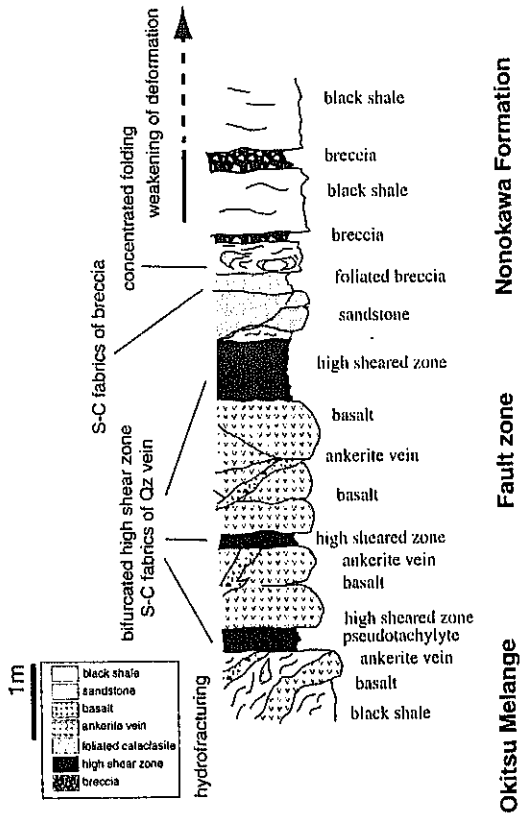

図 4　断層帯の柱状図．

Fig. 4　Column section of the fault zone.

いるためであると解釈されている（Park *et al.*, 2002）。これは震源領域における底付けユニットのルーフ衝上断層沿いに流体が存在しているという点で興津メランジュ震源断層の特徴と一致する。

V. 断層の固着モデルと簡単なアナログ実験

本論の興津メランジュの断層や南海トラフの DSR に限らず，断層沿いには流体が存在し，それによってインターサイスミックにおける破砕帯の固着が生じることは数多く報告されている（Evans and Chester, 1995; Wintch *et al.*, 1995; 藤本, 2002 など）。それは断層破砕帯が単に固結するという意味ばかりでなく，固着すべりを引き起こすか否かという，すべり挙動そのものにとっても重要な意味を持つであろうことが推測できる。

摩擦は接触表面上の微小な突起としてのアスペリティが互いに接触することによって生じ，摩擦強度は各接触エリアの剪断強度の総和によると説明されている（Borden and Tabor, 1950）。そしてこういった部分接触エリアの総面積が時間と共に増加すると仮定すれば，断層の強度回復を説明することができる。これは逆に言えば，高速で動いている場合には接触時間が短くなるため，摩擦

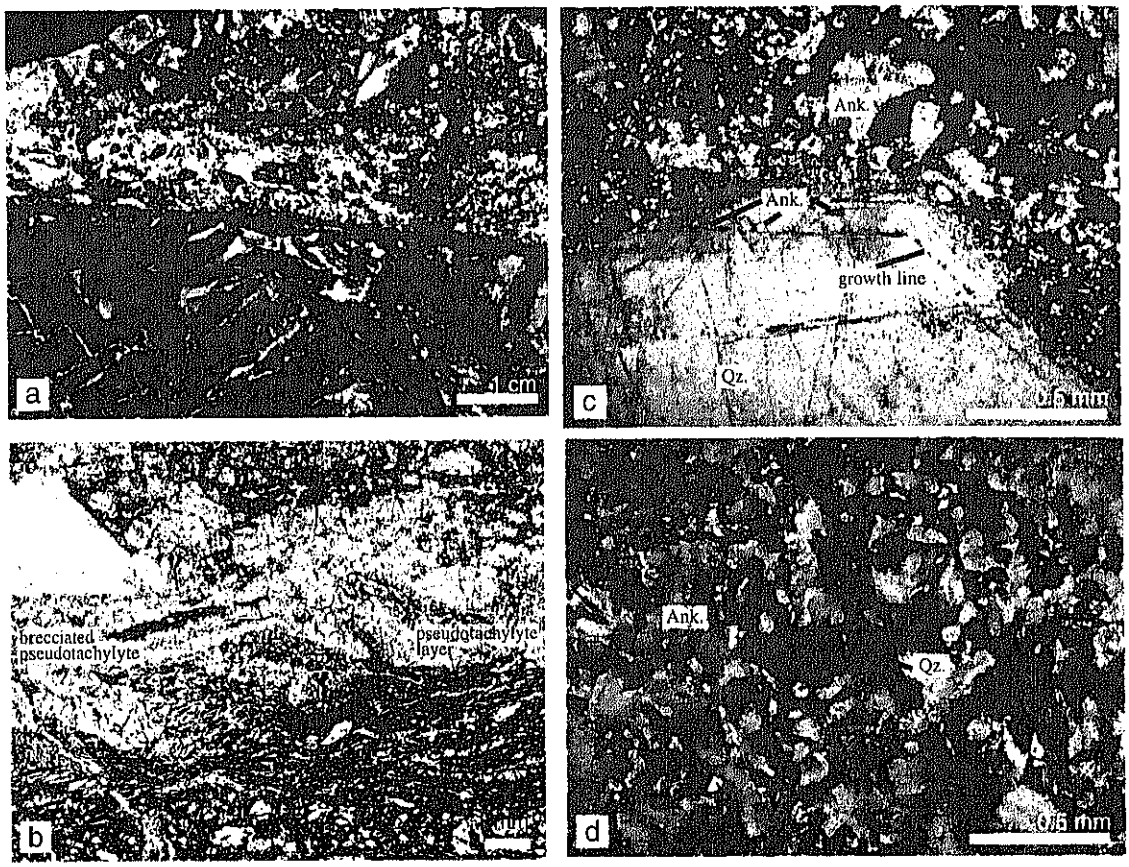

図 5 (a) 一部の鉱物脈濃集層は圧力溶解変形から免れており，水圧破砕組織が保持されている．鉱物脈はアンケライトと石英からなる．

(b) 写真下部のシュードタキライト脈は，写真中央で水圧破砕によるジクソーパズル組織を有し，破砕されたシュードタキライトの岩片はアンケライト結晶によって支持されている．破砕岩片が運搬堆積するよりも早い速度で鉱物脈が析出したと考えられる．

(c) 写真 b 左上の石英 (QZ) の拡大写真．石英の成長線に沿ってアンケライト (Ank) が取り込まれている．これは石英結晶の成長表面に石英と同時にアンケライトが析出していたと考えられる．取り込まれていたアンケライト結晶のサイズは石英外側ほど大きくなり，写真上部ではアンケライト優勢となっている．

(d) 中には逆にアンケライトが自形をとり，その隙間に石英が析出している場合もある．これらのように石英とアンケライトは同時析出したことを示す．

Fig. 5 Some of the vein mineral preserves the fabric of hydrofracturing (a), and the pseudotachylyte of the black layer has a jigsaw puzzle texture (b).

The fragments are supported by matrix vein minerals, which perhaps indicates rapid precipitation of the vein mineral before fragments drop (b). Some of the ankerites are precipitated along the growth line of the quartz grain (c) and some of the quartz is precipitated between the ankerite grains (d). The quartz and ankerites are co-precipitated, although they differ in saturation ratio. This can be explained by the rapid fluid flow from deep along the fault rupture, which maintains the super saturation condition of the fluid.

強度の低下，すなわち速度弱化が生じる。そのため，このようなアスペリティが時間と共に増加することは，固着すべりを実現する上での必要条件の一つである。そのような接触エリアの増加の機構としては，地下深部であるならばアスペリティの結晶塑性機構でイメージすることができ，部分

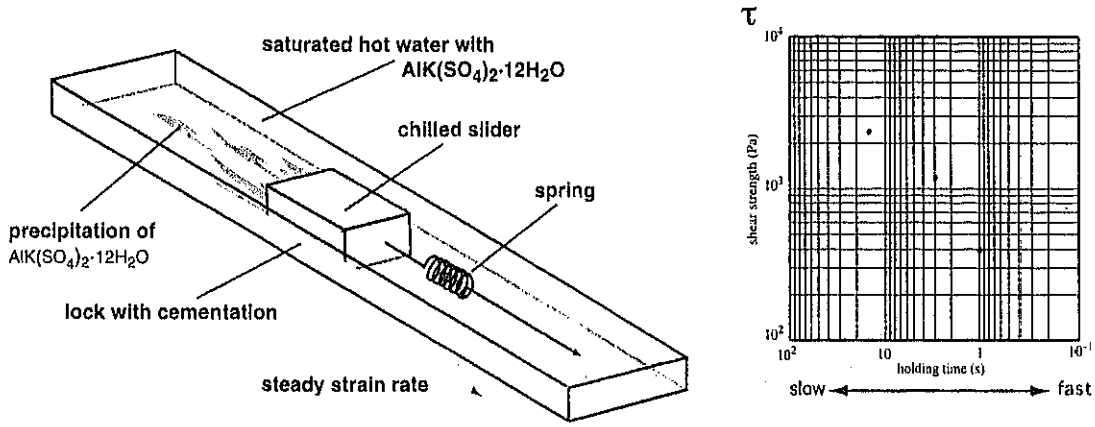

図 6　セメンテーションによる固着すべりのアナログ実験の模式図.
ブロックスライダーモデルのすべり面に鉱物が沈澱するようにしたもの．ソリ，スプリング，糸巻きと水槽から構成される．水槽には溶液平衡状態のミョウバン溶液の温水を入れる．ソリには重りと氷水を入れ，剪断中にソリの下面にミョウバン結晶を沈澱させる．それによって固着時間による剪断強度の増加と固着すべり現象を観察することができる．

Fig. 6　The concept of the analogue experiment with a blockslider model with cementation mechanism. The slider and the springs are placed into hot saturated water with alum, and the saturation ratio changes with temperature. The alum is precipitated along the shear surface of the chilled slider. Cementation due to alum precipitation causes stick slip and strengthening with time.

的に接触しているアスペリティのみが徐々に変形し，互いに噛み合っていくので，接触エリアの総和を時間と共に増加させることができる。しかし，本断層の場合は結晶塑性機構が卓越するような温度領域を経験しておらず，鏡下においても断層岩が結晶塑性変形した痕跡は認められない。そのため結晶塑性機構で説明することはできない。ところが，塑性変形でなくとも圧力溶解作用（中谷，2003 など）や部分的なセメンテーションでも同等の働きを期待することができる。断層沿いにおける鉱物脈の沈澱とそれに伴う部分的なセメンテーションが時間と共に進行し，セメンテーションエリアが増加するならば，剪断強度は時間と共に増加するであろう。脈結晶が沈澱して破砕帯をセメントして固着させるという現象は，断層帯の岩石化が進行することを意味するし，それが降伏強度を越えて破壊すれば剪断強度は大きく低下すると期待される。これは大きな速度弱化をもたらすということであると同時に，時間と共に強度回復を実現しうる。

剪断面上に脈鉱物が沈澱することによって，剪断強度が時間依存性を持つであろうこと，そして固着すべりを引き起こす様子は，例えば簡単なアナログ実験で観察することができる。実験装置は，いわゆるブロックスライダーの実験装置を水槽内にセットして，水槽には溶液平衡状態のミョウバン溶液の温水をはり，一方のソリは氷で冷やす構成からなる（図 6）。ミョウバンの溶解度は温度によって大きく変化し，とりわけ約 100℃ から 30℃ にかけては温度に対する溶解度の変化が特に大きい。冷却されたソリと水槽の底との間でミョウバン結晶が沈澱するので，これが断層帯に鉱物脈が沈澱して剪断面をセメントさせる過程に対比させることができる。実験ではソリに熱伝導度の高い材料としてアルミを用い，中に氷と水を入れてあるので底面において温度むらは少ないと考えられる。そして剪断面における沈澱と破砕の様子を観察できるように水槽底は透明アクリルにし，その下には鏡を設置してある（図 7a）。飽和ミョウバン水溶液の温度は約 70 ～ 90℃，ソリの底面は

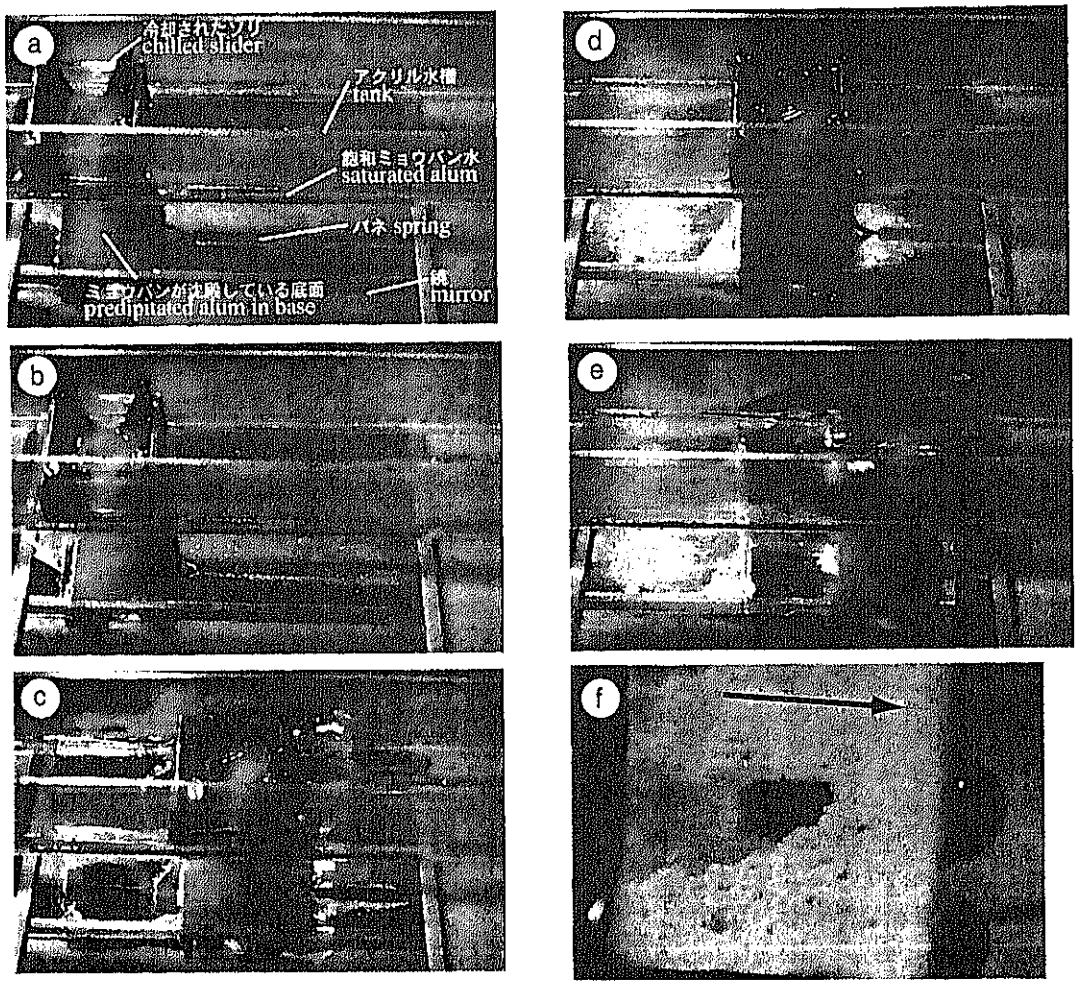

図 7　セメンテーションによる固着すべりのアナログ実験の写真.

(a) ソリの底面にミョウバン結晶が沈殿する様子を観察できるように，水槽の下に鏡が設置してある.

(b) 冷却されたソリが溶液平衡状態のミョウバン水溶液に浸されると同時にソリは固着し，次第にバネが伸びる. 加速する寸前に臨界すべりを起こすこともある（矢印）.

(c) ソリが加速すべりを引き起こし，バネの歪みは解消される.

(d) 再びソリの底面にミョウバンが沈殿し，ソリを固着させた. 水溶液の温度も低下してきており，それに従って水槽の各所でミョウバンが沈殿して白い結晶が観察される.

(e) 2回目の加速すべり.

(f) ソリの底面にはミョウバン結晶と，その表面にスリッケンラインが観察される. ソリの中央左側（すべり方向の後方）は結晶が剥離しているが，これは2回目の加速すべりの時に破砕した. この部分がより強く固着していた，いわゆるアスペリティだったのかもしれない.

Fig. 7　Photograph of the experiment.

The occurrence of precipitation along the shear surface can be observed with a mirror under a transparent experiment box (a). Chilled slider has cementation of alum adheling. Arrow shows the critical slip (b) and rapid slips (c). The slick slips are repeated (d, e), and the striation are developed on the slip surface (f).

50 mm × 50 mm で，重りと氷と水が約 180 g が入れてあり，バネ定数 20 g/mm のバネを用いて実験した。

上記の条件で一定のレートで応力をかけた場合のすべり実験と，ソリを停止させてそれから保持時間を変えて剪断応力の測定を行った。その結果，一定のレートで応力をかけた場合は固着すべりを生じた。冷却したソリを温ミョウバン水溶液に浸すとすぐに底面には白くミョウバン結晶が沈澱し(図 7b)，ソリは固着する。ソリは水槽のサイズの関係で長い距離を滑らすことはできないが，少なくとも 2 回，固着と加速すべりが生じさせることができた（図 7c，d，e)。時には加速すべりの前に緩やかな臨界すべりを観察できることもある(図 7b の矢印)。実験後にソリ底面を観察すると，ミョウバンの結晶が底面に一面に発達して，スリッケンサイドも形成された(図 7f)。またホールディング試験では，剪断応力は停止時間によって増加することとも認められ（図 6)，剪断面がミョウバンの沈澱に伴って強度回復したことを示している。また結果的には実験では固着すべりが生じているので，この現象が速度弱化性を有することも意味する。ちなみに，水槽にミョウバン水溶液を入れない場合には固着すべりや保持時間による摩擦強度の上昇は認められないので，上記の現象はミョウバン結晶の沈澱によって生じているものと考えられる。このような結晶沈澱現象による固着すべりを断層岩に当てはめるならば，鉱物脈の沈澱は，破砕物が単にインターサイスミックに膠結させられるということにとどまらず，摩擦の時間依存性を担う，すなわち固着すべりを能動的に起こす能力を有していることを意味する。

VI. ま と め

四万十帯の奥津メランジュの震源断層は，付加プリズムの底付けユニットのルーフ衝上断層で発達し，そこはシュードタキライトや破砕岩片が含まれ，鉱物脈が濃集することで特徴づけられる。脈鉱物は断層の破砕帯をセメントしており，一部の破砕岩片は基質の鉱物脈によってサポートされていることは，脈鉱物が破砕物の沈澱よりも急速に沈澱したことを示している。これが地震サイクルよりも十分に短い時間で断層を固着させたものと解釈される。

鉱物脈の沈澱，そしてそれに伴う断層強度増加が時間と共に進行するならば，摩擦の時間依存性の条件を満足させることができる。これは単にインターサイスミックに断層岩が固結したということではなく，鉱物脈によるセメンテーションが断層のアスペリティのメカニズムになりうるということを意味する。剪断面における鉱物脈の沈澱が，摩擦強度の時間依存性を満足し固着すべりを引き起こせるのかは，簡単なアナログ実験でも観察することができる。

謝 辞

地球惑星関連学会 2003 年合同大会において断層帯のレオロジーと地震の発生過程セッションに参加された多くの方々からたいへん有意義なご助言をいただいた。海洋科学技術センターの加藤愛太郎博士に摩擦理論に関してたいへん有益なご指摘を頂いた。また，このような特集に発表させて頂く機会を与えて頂いたことに深く謝意を表す。

文 献

Ashi, J. and Taira, A. (1993): Thermal structure of the Nankai accretionary prism as inferred from the distribution of gas hydrate BSRs. *Geol. Soc. Amer. Spec. Pap.*, **273**, 137–149.

Bopyer, E.L. and Elliott, D. (1982): Thrust systems. *AAPG Bull.*, **66**, 1196–1230.

Borden, F.P. and Tabor, D. (1950): *The Friction and Lubrication of Solids*. Clarenden Press Oxford.

Evans, J. and Chester, F.M. (1995): Fluid-rock iunteraction in fault of the San Andreas system: Inferences from San Gabriel fault rock geochemistry and microstructure. *J. Geophys. Res.*, **100**, 13007–13020.

藤本光一郎 (2002): 地震発生帯における流体の性状. 月刊地球，号外，**36**(沈み込み帯地震発生帯—その物質科学と深海掘削—)，53–59.

Hashimoto, Y. and Kimura, G. (1999): Underplating process from melange formation to duplexing: Example from the Cretaceous Shimanto Belt, Kii Peninsula, southwest Japan. *Tectonics*, **18**, 92–107.

Hasebe, N., Tagami, T. and Nisimura, N. (1993): Evolution of the Shimanto accretionary complex. A fission-track thermochronologic study. *In* Underwood, M.B. ed.: *Thermal Evolution of the*

Tertiary Shimanto Belt, Southwest Japan: An Example of Ridge-Trench Interaction. Geological Society of America Special Paper, **273**, 121-136.

Hyndman, R.D., Wang, K.J., Yuan, T. and Spence, G.D. (1993): Tectonic sediment thickening, fluid expulsion, and the thermal regime of subduction zone accretionary prisms the Cascadia margin off Vancouverisland. *J. Geophys. Res.*, **98**, 21865-21876.

Ikesawa, A., Sakaguchi, A. and Kimura, G. (2003): Pseudotachylyte from an ancient accretionary complex: Evidence for melt generation during seismic slip along a master decollement? *Geology*, **31**, 637-640.

狩野謙一 (1999): 付加体における震源域物質科学. 月刊地球, **21**, 38-44.

狩野謙一・村田明広 (1998): 構造地質. 朝倉書店.

君波和雄・柏木健孝・宮下純夫 (1992): 上部白亜系牟岐累層 (四国東部) 中の *in-situ* 緑色岩類の産状とその意義. 地質学雑誌, **98**, 867-883.

木村 学 (1997): プレート沈み込み帯における Mass Flux と Seismogenic Zone—OD21 に期待する科学目標—. 月刊地球, 号外, **19**(21 世紀の深海掘削への展望—ODP から OD21 へ—), 227-232.

村田明広 (1991): 九州四万十帯, 内ノ八重層の作るデュープレックス構造と内ノ八重クリッペ. 地学雑誌, **97**, 39-52.

中谷正夫 (2003): Vel. dependence of friction due to sol.-transfer healing of quartz gouge @200C and its upper cutoff velocity as low as 1E-6 m/s. 地球惑星関連合同大会講演集, I019-014.

Ohmori, K., Taira, A., Tokuyama, H., Sakaguchi, A., Okamura, M. and Aihara, A. (1997): Paleotermal structure of the Shimanto accretionary prism, Shikoku, Japan: Role of an out-of-sequence thrust. *Geology*, **25**, 327-330.

Park, J., Tsuru, T., Takahashi, N., Takane, T., Kodaira, S., Nakanishi, A., Miura, S. and Kaneda, Y. (2002): A deep strong reflector in the Nankai accretionary wedge from multichannel seismic data: Implications for underplating and interseismic shear stress release. *J. Geophys. Res.*, **107**, B4.

Sakaguchi, A. (1996): High geothermal gradient with ridge subduction beneath Cretaceous Shimanto accretionary prism, southwest Japan. *Geology*, **24**, 795-798.

Sakaguchi, A. (1999): Thermal maturity in the Shimanto accretionary prism, southwest Japan with the thermal change of the subducting slab: Fluid inclusion and vitrinite reflectance study. *Earth Planet. Sci. Lett.*, **173**, 61-74.

坂口有人・大森琴絵・山本浩士・相原安津夫・岡村 真 (1992): 輝炭反射率から見た四国四万十帯北帯の熱構造—高知県西部域を例にして—. 高知大学学術研究報告, **41**, 29-47.

Sakaguchi, A., Takami, R., Ikesawa, E. and Kanaya, T. (submitted): Tectonic setting of seismogenic fault in the ancient subduction zone, Okitsu Melange, Shimanto accretionary complex, SW Japan. *Tectonics*.

ショルツ, C.H. 著, 柳谷 俊訳 (1993): 地震と断層の力学. 古今書院.

Sholtz, C.H. (1990) : *The Mechanics of Earthquakes and Faulting*. Cambridge University Press.

Tagami, T., Hasebe, N. and Shimanda, C. (1995): Episodic exhumation of accretionary complexes: Fission-track thermochronologic evidence from the Shimanto Belt and its vicinities, southwest Japan. *The Island Arc*, **4**, 209-230.

Taira, A., Katto, J., Tashiro, M., Okamura, M. and Kodama, K. (1988): The Shimanto Belt in Shikoku, Japan - Evolution of Cretaceous to Miocene accretionary prism. *Modern Geology*, **12**, 5-46.

Taira, A., Hill, I., Fish, J. and others (1991): *Proc. ODP, Init. Repts.*, **131**, 71-269.

Wintch, R.P., Christoffersen, R. and Kronenberg, A.K. (1995): Fluid-rock reaction weakening of faut gouge. *J. Geophys. Res.*, **100**, 13021-13032.

Yamano, M., Honda, S. and Uyeda, S. (1984): Nankai Trough: A hot trench? *Marine Geophys. Res.*, **6**, 187-203.

(2003 年 10 月 17 日受付, 2003 年 12 月 5 日受理)

The nature of faulting and deformation in the Mineoka ophiolite, NW Pacific Rim

AKIKO TAKAHASHI[1], YUJIRO OGAWA[2], YASUFUMI OHTA[3] & NAOTO HIRANO[4,5]

[1]*Doctoral Program in Earth Evolution Sciences, Graduate School of Life and Environmental Sciences, University of Tsukuba, Tsukuba 305-8571, Japan*

[2]*Institute of Geoscience, University of Tsukuba, Tsukuba 305-8571, Japan (e-mail: yogawa@arsia.geo.tsukuba.ac.jp)*

[3]*Doctoral Program in Geoscience, University of Tsukuba, Tsukuba 305-8571, Japan*

[4]*Ocean Research Institute, University of Tokyo, Tokyo 164-8639, Japan*

[5]*Present address: Department of Earth and Planetary Sciences, Tokyo Institute of Technology, Ookayama, Meguro 152-8551, Tokyo, Japan*

Abstract: A belt of disrupted ophiolitic rocks occurs on the Boso Peninsula (Japan), currently located north of the oblique subduction boundary between the Philippine Sea and North American Plates, under which the Pacific Plate has been subducting westwards. This ophiolitic belt (Mineoka Belt) is composed of mafic–ultramafic rocks together with Tertiary chert and limestone and island-arc volcaniclastic rocks. Our detailed structural studies in and around the basaltic rock bodies within the ophiolite reveal three phases of deformation. The first phase is further divided into three stages, all related to oblique normal faulting associated with extensional tectonics at or near a spreading axis. Fluid pressures appear to have fluctuated in association with faulting and veining during this phase. The second phase of deformation is characterized by thrust-related shear zones with a significant strike-slip component and is probably related to the final emplacement of the ophiolite by oblique subduction–obduction processes. The third and final phase of deformation affected not only the ophiolite but also later terrigenous and island-arc pyroclastic rocks. This deformation involved large-scale transpressional dextral slip on forearc sliver faults, which are still active today.

The Boso Peninsula is located north of the oblique subduction boundary between the Philippine Sea and North American Plates, where the Pacific Plate is subducting westwards (Ogawa *et al.* 1989) (Fig. 1). In the southern part of the peninsula, an assemblage of mafic and ultramafic rocks and accompanying Tertiary chert and limestone forms the Mineoka ophiolite. This belt marks the boundary between forearc basin deposits to the north and the Miocene–Pliocene accretionary prisms to the south (Ogawa & Taniguchi 1988; Saito 1992) (Fig. 1). Although the lithologies in the Mineoka Belt have been studied earlier (Kanehira 1976; Ogawa & Taniguchi 1987, 1988), structural relationships and their tectonic implications for the ophiolitic rocks are poorly constrained because all internal contacts are faulted. Geochemical data indicate that the basaltic rocks in the Mineoka Belt include mid-ocean ridge basalt (MORB), back-arc basin basalt (BABB), within-plate basalt (WPB) and island-arc tholeiite (IAT) (Ogawa & Taniguchi 1987, 1988; Hirano *et al.* 2003). Whole-rock Ar–Ar ages of the volcanic rocks (Hirano *et al.* 2003) indicate that most tholeiitic basalts in the ophiolite are Eocene in age, whereas some alkaline varieties are of Miocene age.

In the Mineoka Belt, all contacts between the ophiolite and the adjacent Miocene sedimentary rocks are faulted, although the latter were originally deposited over the already deformed and veined ophiolitic rocks. Ophiolitic rocks are composed dominantly of serpentinized harzburgite with minor dunite (Sato & Ogawa 2001), and of mafic lavas of various ages and compositions (Ogawa & Taniguchi 1987, 1988; Hirano *et al.* 2003). In some parts of the belt, the basaltic rocks are in contact with serpentinite along cataclastic shear zones, but in other parts they are in fault contact with relatively uncompacted volcaniclastic rocks and/or continent-derived sandstone and conglomerate of mid-Miocene age (Yoshida 1974; M. M. Mohiuddin, pers. comm.) (Fig. 2). Some of the

From: DILEK, Y. & ROBINSON P. T. (eds) 2003. *Ophiolites in Earth History*. Geological Society, London, Special Publications, 218. 1–16. 0305-8719/03/$15 © The Geological Society of London 2003.

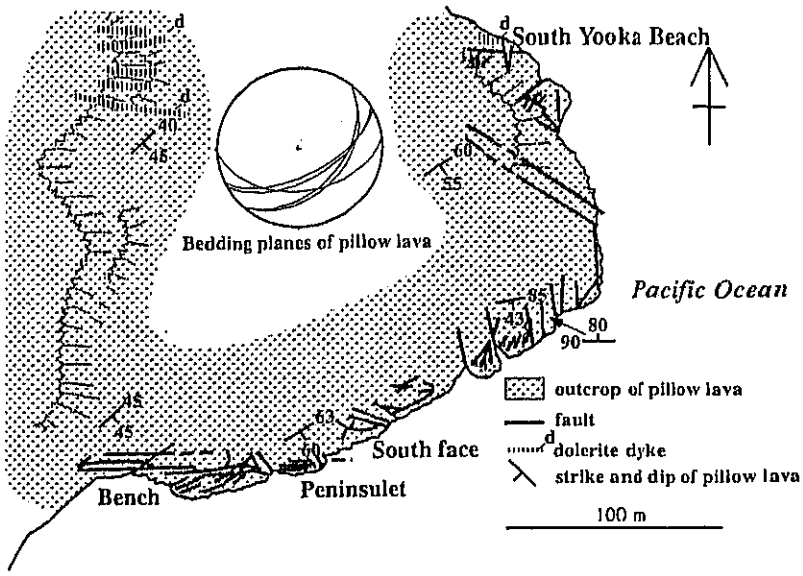

Fig. 3. Location map of the outcrops at Shinyashiki, south of Kamogawa Harbour. The strike and dip of pillow lavas are marked.

Fig. 4. Outcrop photograph showing deformation of inter-pillow calcite (Cal) and intra-pillow quartz (Qtz) formed during the first stage of precipitation; 'Bench' at Shinyashiki.

'South Yooka Beach'. Several stages of faulting, mineral precipitation and veining were identified in these areas. Precipitation of calcite and quartz predates the first-stage faulting, and is common chiefly at 'Bench' and 'South Face'. Spherical quartz aggregates, 3–5 mm across, occur in the centres of pillows, whereas calcite occurs mainly in inter-pillow spaces. The inter-pillow calcite has been deformed by shearing (Fig. 4). The intra-pillow quartz and inter-pillow calcite occur particularly around 'Bench', suggesting local hydrothermal activity before the first stage of faulting. The first stage of faulting is characterized by a foliated cataclasite, exposed at 'Peninsulet', 'South Yooka Beach' and 'South Face'. The second stage of faulting is associated with conjugate sets of zeolite veins parallel to the faults and is developed at 'Bench' and 'Peninsulet'. Faults of the third stage, represented by crushed calcite veins along dextral–oblique normal faults, are well exposed at 'Bench'. (See Table 1 for summary of the deformational events.)

First-stage faults. Faults of the first stage are characterized by discrete zones of foliated cataclasite, *c.* 5 cm wide, and rare calcite veins in 'Peninsulet' and 'South Yooka Beach' (Fig. 5). The fault planes generally strike east–west and dip steeply. Microscale crushed basalt fragments are elongated as 'fish' on the shear surfaces and show a preferred orientation under the microscope. Strong shear fabrics are common, repre-

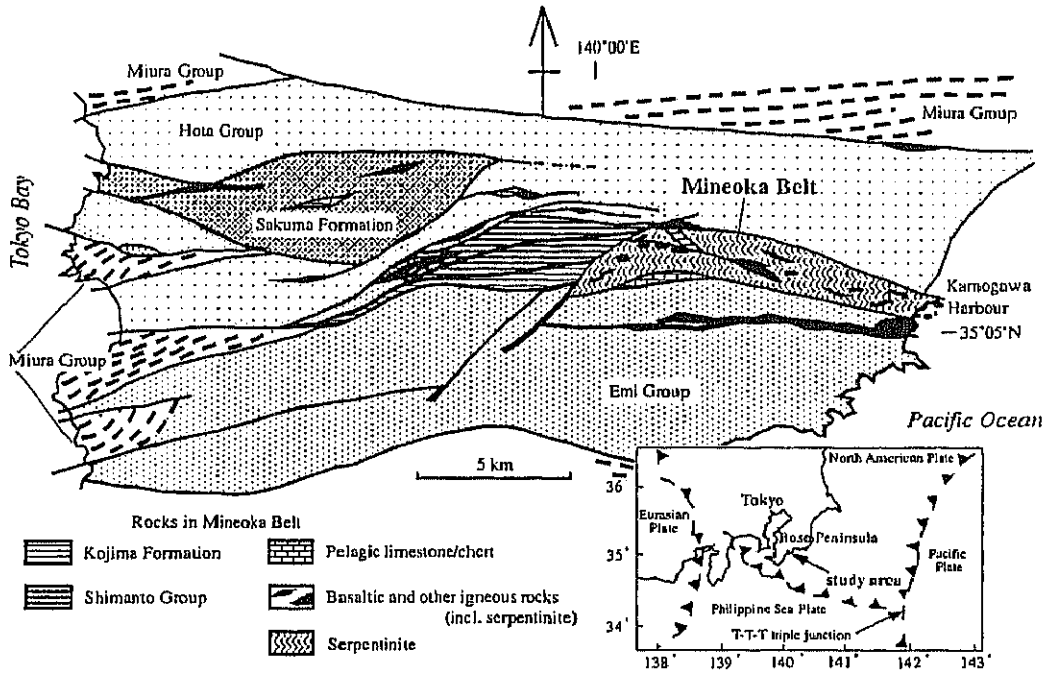

Fig. 1. Index map of the Mineoka Belt and its surroundings (adapted from Ogawa & Taniguchi 1988). The study area is the easternmost part of the Mineoka Belt.

sandstones contain serpentinite fragments (Ogawa 1983). According to Kaneoka *et al.* (1980), whole-rock Ar–Ar ages of basaltic rocks are 30–40 Ma and 40–50 Ma. These ages are generally supported by new whole-rock Ar–Ar dating by Hirano *et al.* (2003), but some alkaline basalts were found to be younger, around 20 Ma old (Hirano & Okuzawa 2002).

Ophiolitic rocks in the Mineoka Belt are accompanied by a number of other lithologies. For example, hornblende schist is exposed in the Kamogawa Harbour area and is estimated to have formed at temperatures of 500–550 °C and pressures of 500 MPa with high oxygen fugacity (Ogo & Hiroi 1991). Another rock type is weakly deformed and altered andesitic pumice exposed on Kojima Island in Kamogawa Harbour and sporadically throughout the belt (Fig. 2). These pyroclastic deposits, 12 Ma old as inferred from similar rocks exposed on the Miura Peninsula (Kanie & Asami 1995), originally were deposited unconformably on the deformed and altered ophiolitic rocks and were subsequently faulted against other lithologies (Figs 1 and 2).

In this paper, we document the different stages of faulting and veining in the basaltic rocks, and the kinematics of faulting. The data were collected from two well-exposed, large bodies of basalts in the southern part of Kamogawa Harbour, Boso Peninsula (Figs 1 and 2). These volcanic bodies contain MORB or BABB-type pillow lavas at Shinyashiki (Fig. 3) and on Benten Island (Fig. 4). The pillow lavas and dolerite dykes on Benten Island probably also contain some IAT-type basalts. Our study of the limited but well-exposed basaltic bodies in the Mineoka ophiolite offers a good opportunity for understanding the nature of shallow crustal deformation in an ophiolite and the related hydrothermal alteration during oceanic crust generation.

Fault analysis

Shinyashiki outcrops

Basalt pillow lavas are widely distributed at Shinyashiki, forming an outcrop 300 m across (Fig. 3). The pillow lavas, intruded by several dolerite dykes, are interlayered with massive flows several metres thick in the middle of the stratigraphic sequence. Pillows are commonly several tens of centimetres long, rarely up to 1 m. The sequence dips moderately to steeply to the SE. We have divided the Shinyashiki pillow lava body into four small areas (Fig. 3), which we informally name 'Bench', 'Peninsulet', 'South Face' and

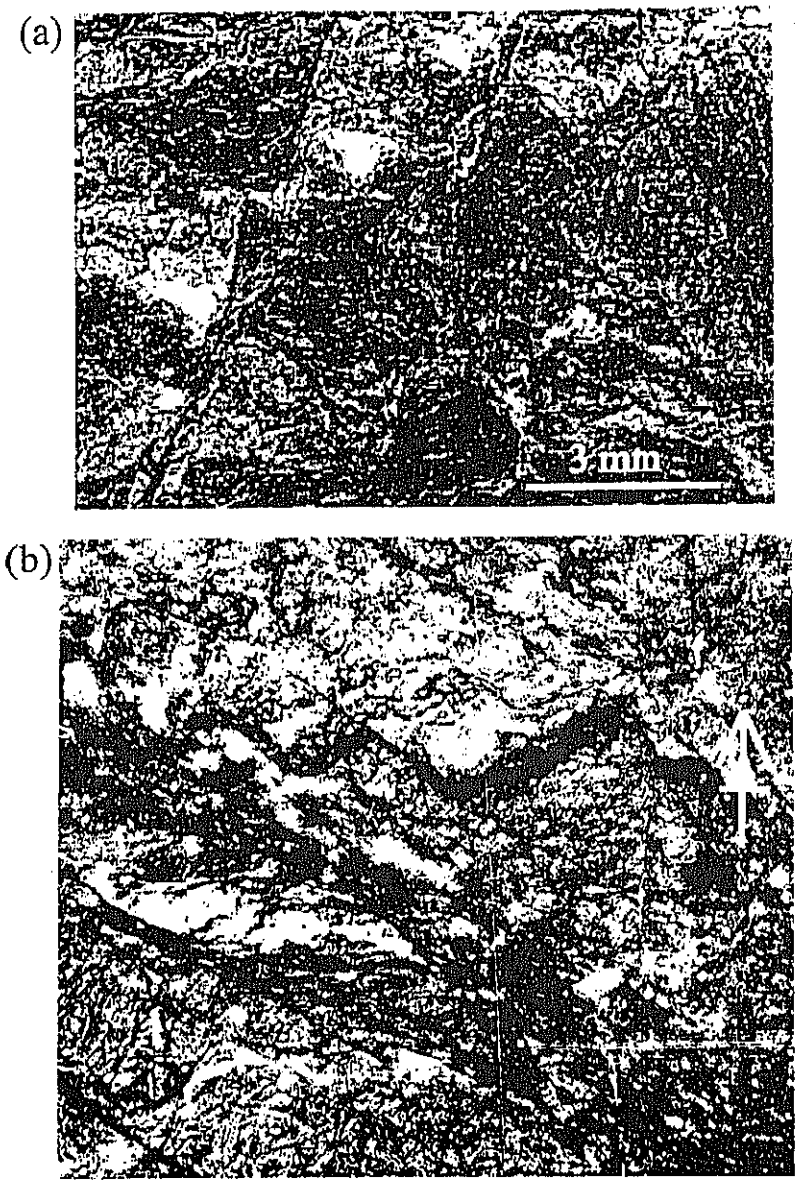

Fig. 6. (a) Polished surface of a hand sample showing first-stage faults; (b) photomicrograph of the sample in (a). Photo is 5 mm wide.

shear zone of the 'X-shaped vein' at 'Bench' (Fig. 7), and they are not crushed. In contrast, a thick analcime vein intrudes the sheared part, separating the shear zone with a straight boundary. These relationships suggest the following sequence of events: (1) shearing; (2) stilbite veining; (3) shearing; (4) analcime veining (Fig. 8). Analcime veins occur together with calcite veins and the two types occur repeatedly with further shearing.

Another example of faulting and veining is observed along a second-stage fault at 'Peninsulet'. In thin section, an analcime vein is observed to crosscut the shear zone without any offset. The vein itself is offset by the shear zone and is pulverized. The analcime has wavy extinction, indicating that shearing continued during its growth (Fig. 9). Euhedral natrolite was precipitated perpendicular to the vein wall, followed by

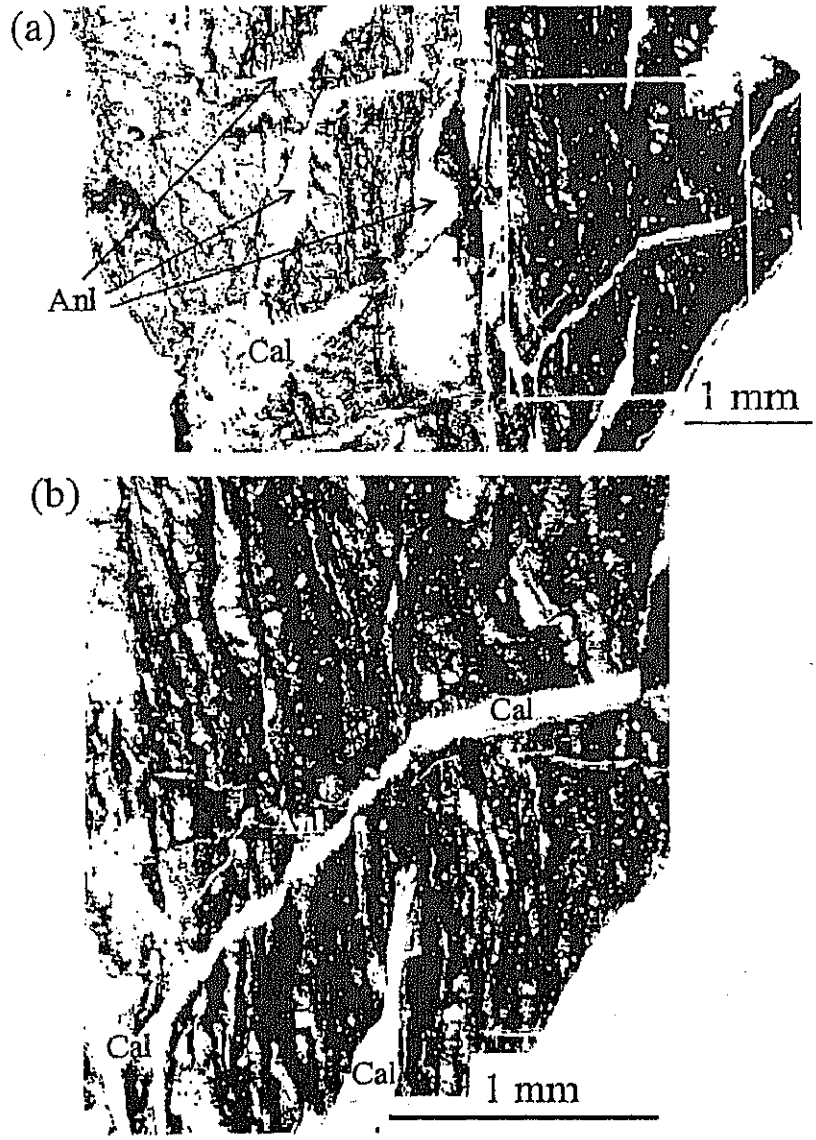

Fig. 7. (a) Mutual cross-cutting relationship of the second-stage faults in thin section; (b) close-up from 'Peninsulet', Shinyashiki. (See text for details.)

the precipitation of anhedral calcite in the centre of the vein (Fig. 9).

A fault with a shear zone of several centimetres width is exposed within the pillow lava sequence at 'South Face'. This fault curves from north–south to NW–SE and displays a normal sense of shear based on asymmetric folding of a stilbite vein (Fig. 10), which has been rotated and cataclastically deformed. These relationships suggest the following sequence of events associated with the second stage of faulting at 'Peninsulet' and 'South Face': (1) zeolite (analcime, stilbite and natrolite) vein formation; (2) crushing; (3) calcite vein formation.

Third-stage faulting. An east–west-striking fault at 'Bench' was formed in the last stage of faulting because it cuts and dislocates many other faults

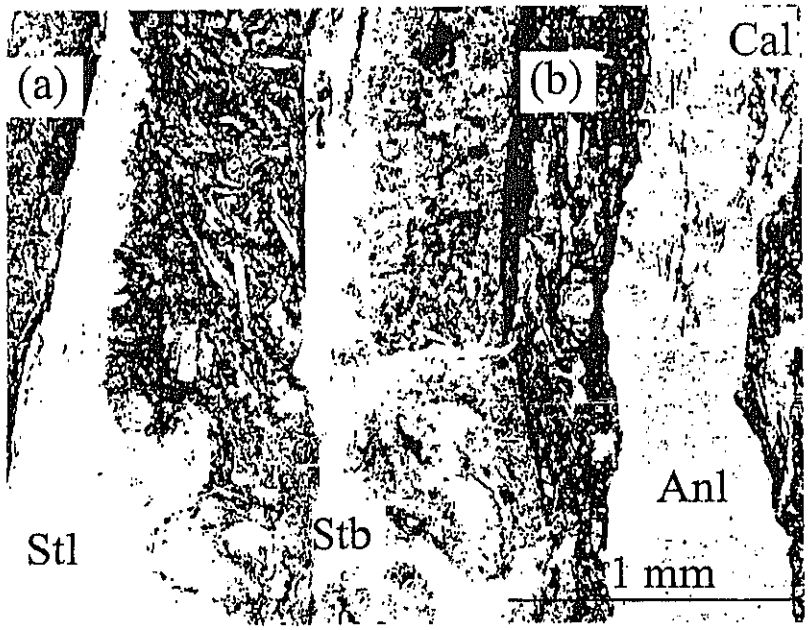

Fig. 8. Photomicrograph (plane-polarized light) of a sample from a fault zone and associated veins, showing several stages of shearing and veining: (a) shearing with stilbite vein (Stb); (b) shearing with analcime vein (Anl) and calcite vein (Cal). The dislocation of the vein by later shearing should be noted.

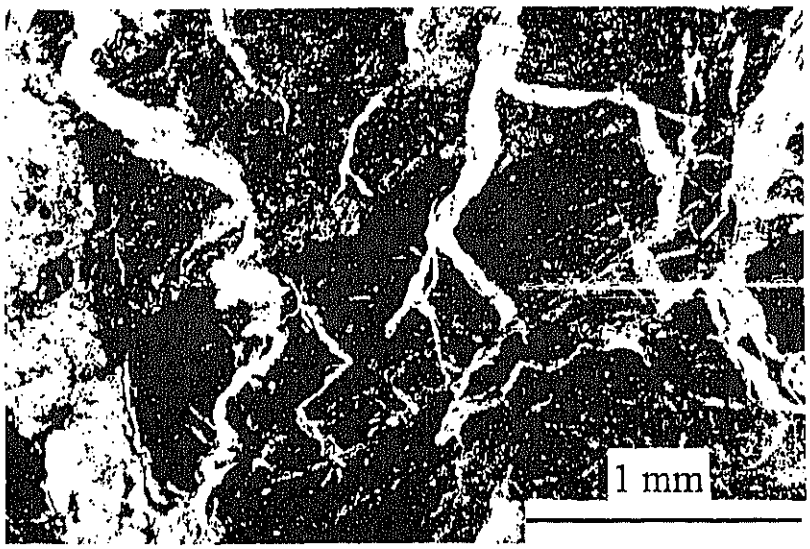

Fig. 9. Photomicrograph showing analcime (Anl) vein crosscutting the sheared, pulverized fault zone rock.

formed in the previous stages. It dips steeply southward and is up to 1 m wide. Displacement of pillow lavas shows that this fault has both normal and dextral components of movement (Fig. 11). A cataclastic zone, several centimetres wide and filled with microbreccia, occurs along the fault plane.

Microscopic observations suggest that brecciation of the host rock continued after precipitation of calcite between the breccia fragments. Some breccias are composed of aggregates of rock and mineral fragments of various sizes (Fig. 12). This style of deformation is characteristic of cataclastic

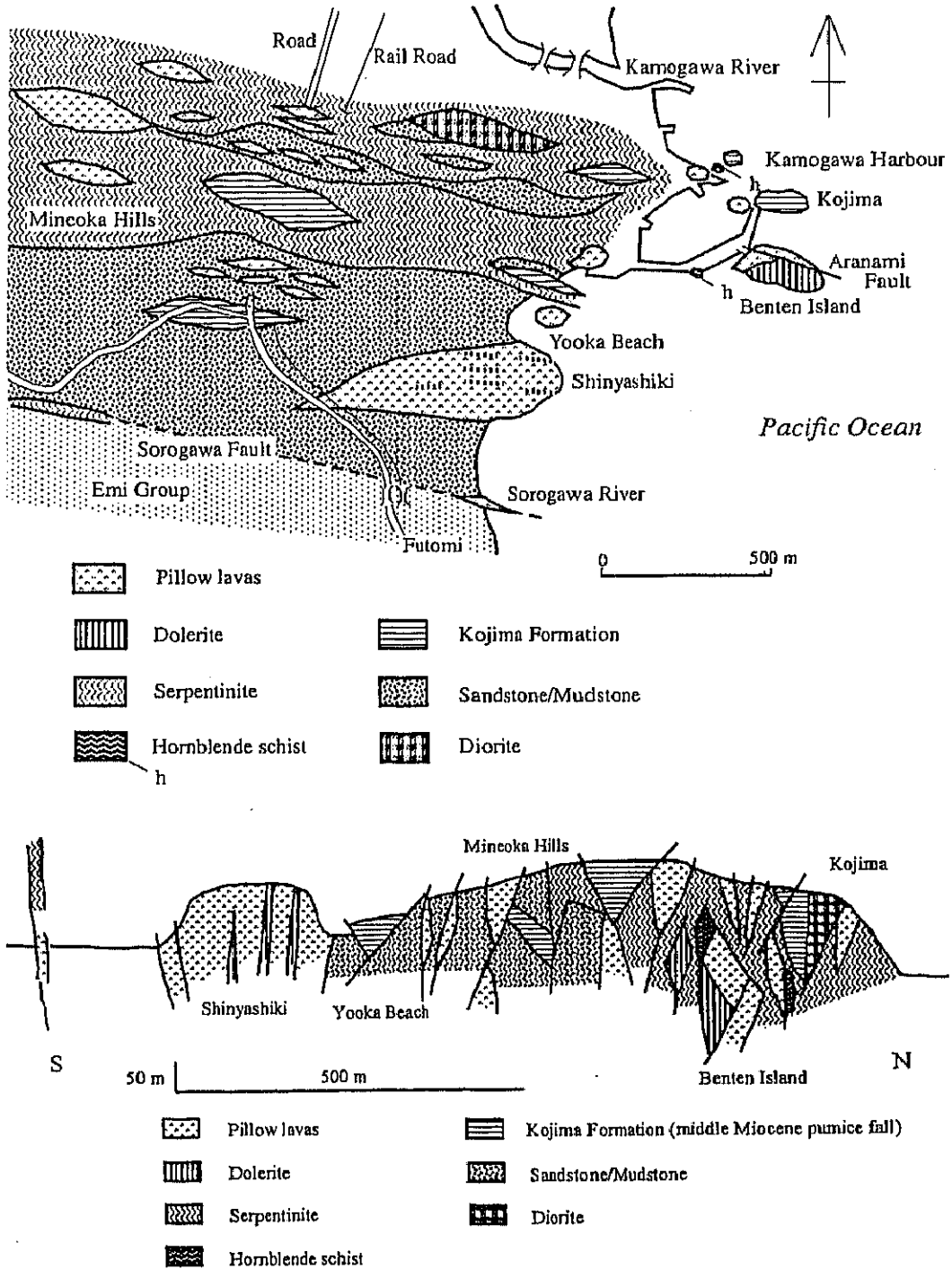

Fig. 2. General lithological map and cross-section of the study area around Kamogawa Harbour, Boso Peninsula, central Japan. Map modified from Yoshida (1974).

Table 1. *Phases and stages of faulting, veining and other events in basaltic rock bodies of the Mineoka Belt*

Stage	Strike and dip	Mode of deformation and veining	Microscopic observation
First phase			
First	East–west, high angle	Wide shear zones of foliated cataclasite	Strong shear zones of Riedel and P-shears
Second	NE–SW and NW–SE, high angle	Conjugate faults with various zeolites and calcite veins	Calcite filling in pores of euhedral zeolites
Third	East–west, high angle	Dragged pillow with brecciated fault zone of crushed calcite vein	Breccias composed of fragments of various size
Second phase			
	NW–SE, moderate dip	Dextral oblique thrust with strong shear zone without mineral veins	Microscopic and mesoscopic Riedel shears
Third phase			
	East–west, NW–SE, high angle	Large-scale dextral strike-slip without mineral veins	Shear zone with serpentinite-bearing fault

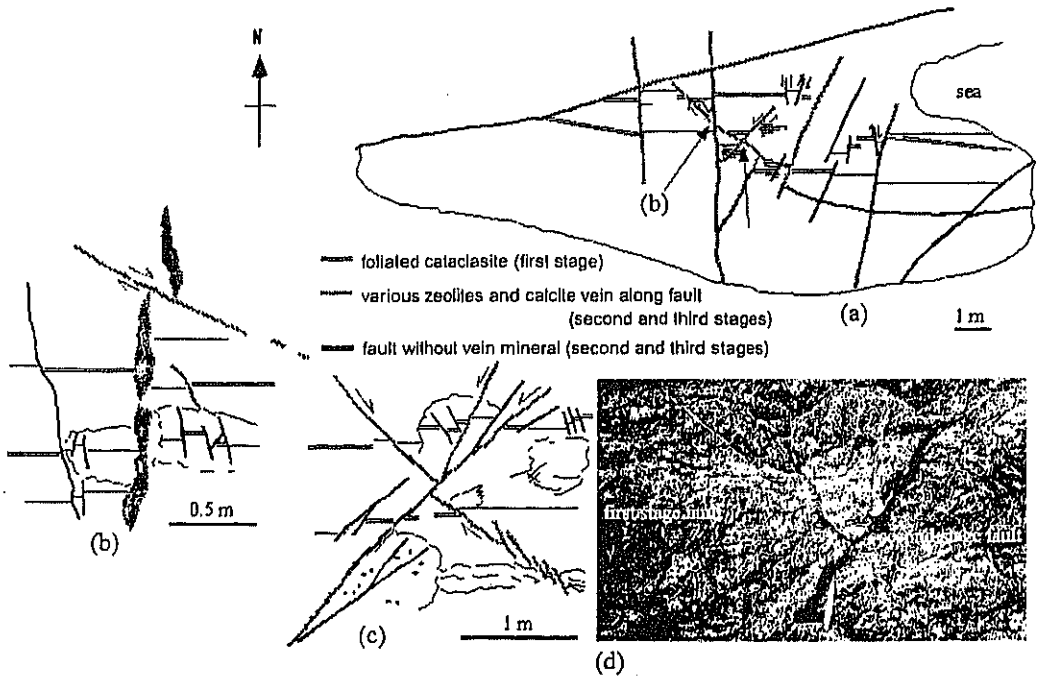

Fig. 5. (a) Plan view of 'Peninsulet' to the east of 'Bench' at Shinyashiki, showing the first-stage shear zones, which are cut by conjugate sets of second-stage faults seen in (b) and (c). (d) Photograph of area shown in (c).

sented by Riedel shears, P-shears and, particularly, duplex-like structures (Fig. 6). In general, within foliated cataclasite, calcite veins occur along the Riedel and P-shears.

Second-stage faults. The first-stage faults are cut by the second-stage faults with attitudes of N30°E or N50°W and steep dips. These NE and NW fault systems, which contain zeolite veins, crosscut each other, suggesting that they were conjugate and contemporaneous. Fault-related vein minerals are dominantly calcite and zeolites, such as analcime, stilbite and natrolite, and the veining is very complex. Calcite and analcime veins cut the

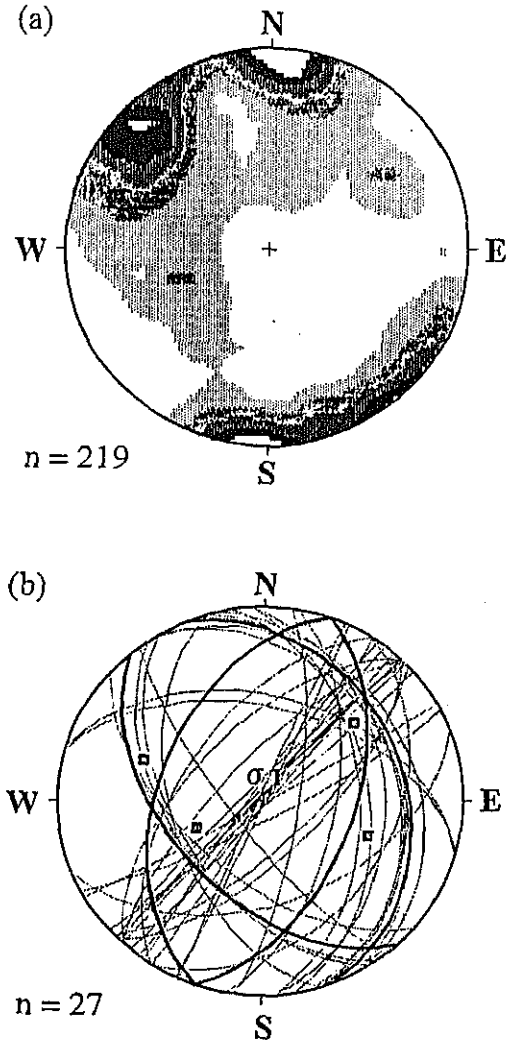

Fig. 14. Stereographic projections of second-stage faults at Shinyashiki. (a) Kamb contour diagram of all faults. (b) Three major directions of normal faults.

zeolite veins with a radial habit perpendicular to the pillow bedding.

The dolerite dykes strike N60° to 80°W and dip steeply to the south. There are two types of dolerite dykes. The first is coarse grained with rare chilled margins. These are intruded by a later group of fine-grained dykes, which occur as single dykes with chilled margins on both sides or as multiple dykes with chilled margins only on the SW side. Some basaltic dykes are intruded parallel or oblique to the dolerite dykes at various locations (Fig. 15). The dolerite dykes are strongly sheared and display several stages of veining. These rocks are altered to a slightly higher degree than those in the Shinyashiki body and the other basalts at Benten Island, as shown by the abundance of laumontite veins. Cataclastic textures are common along two fault systems, one parallel to the dyke orientation (N60°W) and the other perpendicular to it. This is similar to the second-stage conjugate faults at Shinyashiki, except that at Shinyashiki laumontite veins are rarely associated with this generation of faulting.

A Kamb contour diagram (Fig. 16) representing poles of the fault planes in the dolerite dykes shows that steeply dipping faults are dominant. Thus, the fault system in the Benten Island dolerite and the conjugate faults at Shinyashiki are both steeply dipping and have the same inferred direction of σ_1.

Faults in the N-MORB pillows in the NW part of Benten Island strike N50°E and dip steeply. These faults are characterized by euhedral analcime on both sides of the faults, followed by laumontite as the second-stage vein fill, then natrolite veining, and finally anhedral calcite (Fig. 17). Stilbite veins with calcite are parallel to the faults. These five minerals, including four zeolite types, all formed along the faults and within the pillows, suggesting changes in fluid compositions with time.

A large-scale boundary fault, called the 'Aranami Fault', occurs between the main dolerite dyke block and the black pillow lavas. This fault strikes N60°W and dips 50°SW (Fig. 18). A remarkable shear zone occurs along this fault, characterized by a lenticular (phacoidal) fabric and Riedel shears on both large and small scales (Figs 19 and 20). The faulting produced a layered mixture of red and green basalt or dolerite. R_1-shear, P-shear and Y-shear, and particularly duplex structures, indicate that progressive shearing and dislocation occurred as a result of dextral–reverse faulting. Along each shear zone, small lenticular 'fish' also indicate oblique thrusting. In thin section each 'fish' is composed of calcite lenses, crushed together with basalt and dolerite fragments. In the Aranami fault zone, early calcite was deformed by the primary R_1 and secondary shears, showing apparent dextral movement (N60°W). The small, crushed calcite fragments are concentrated along the primary R_1 shear (Fig. 20).

Discussion

In the Shinyashiki body, three main stages of faulting and associated deformation features are recognized: (1) foliated cataclastic shear zones with rare calcite veins; (2) a set of conjugate shear zones with various zeolite minerals and calcite

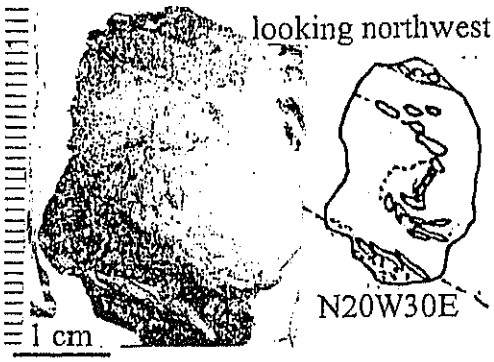

Fig. 10. Sample of a second-stage fault zone (strike N20°W, dip 30°E) at 'South Face', Shinyashiki. Deformation of the zeolite (analcime and stilbite) vein with a transposed structure should be noted. The vergence of folding suggests a normal fault.

flow without recrystallization and suggests brittle faulting.

Veins along these faults may post-date the third stage of faulting. Euhedral crystals of analcime, oriented perpendicular to the vein walls, form thick veins, which are crosscut by thin analcime veins parallel to the vein axis. The veining at 'Bench' records the following progression of events: (1) precipitation of analcime; (2) deposition of thin veins of analcime; (3) calcite precipitation, because calcite fills cavities in the euhedral analcime (Fig. 13).

The majority of the faults are subvertical with NE strikes (Fig. 14a). In the case of second-stage faults the inferred σ_1 (maximum principal stress axis) is vertical (Fig. 14b), suggesting that the conjugate fault systems at Shinyashiki were associated mainly with extensional normal faulting.

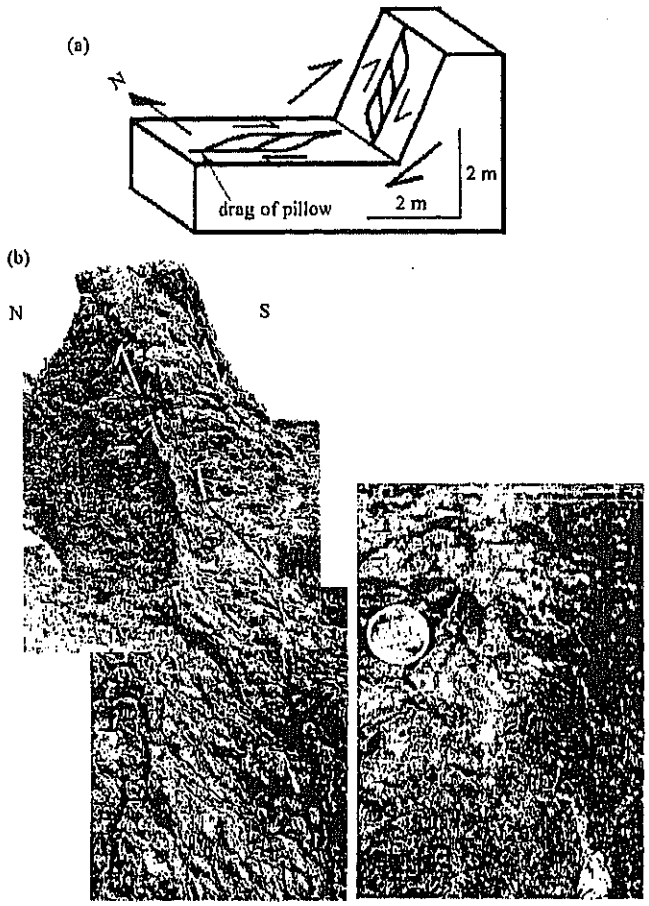

Fig. 11. (a) Schematic sketch, and (b) and (c) outcrop photographs of the eastern part of 'Bench' and Shinyashiki (view to the east). It should be noted that deformation of the pillows indicates an oblique normal fault with a dextral strike-slip component. (c) Close-up of calcite brecciation along this fault.

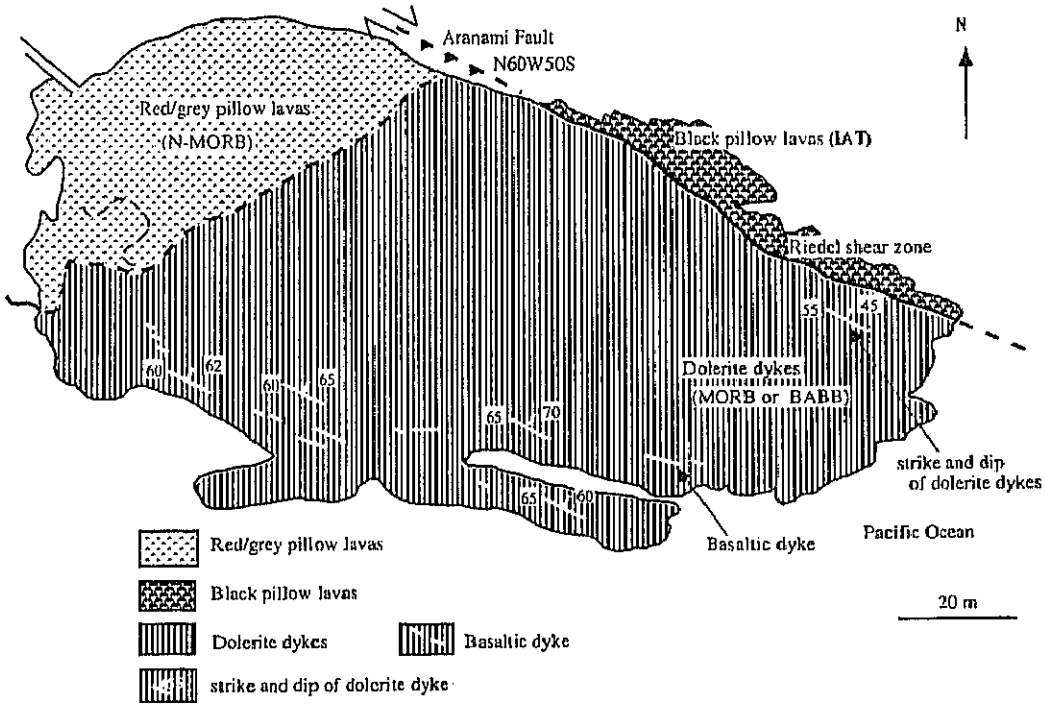

Fig. 15. Lithological map of Benten Island, Kamogawa Harbour, showing three basaltic bodies in fault contact with each other. The dolerite dykes and IAT pillow lavas occur along the 'Aranami Fault'. The strike and dip of the pillow lavas and dolerite dykes are shown. White bars in the dolerite indicate basaltic dykes.

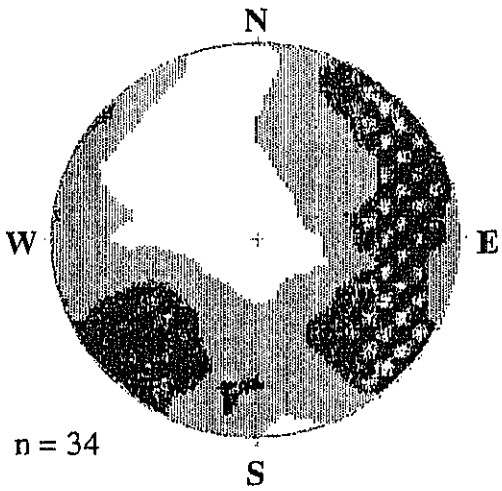

Fig. 16. Stereographic projection of faults in dolerite dyke swarms, Benten Island.

along the faults; (3) variable scales of brecciation and deformation of pillows along the faults. The first-stage shear zones indicate strain hardening, which produced the widespread cataclastic deformation without significant veining. This interpretation suggests that they formed at greater depth than the other zones and at low pore-fluid pressures because of strong frictional sliding. Microscale Riedel shears and duplex structures with a dextral sense of movement are common in the shear zones in 'Peninsulet', whereas those at 'Yooka Beach' show sinistral movement. These shear zones formed under semi-brittle or brittle–ductile transitional conditions. The second-stage faulting occurred under high pore-fluid pressures, because secondary minerals are common in fault-parallel veins. In some cases, mineral precipitation and faulting or shearing occurred repeatedly.

In the Mineoka ophiolite, the first phase of deformation consists of three stages and is represented by repeated faulting in various directions. Many of the first-stage faults are associated with shear zones and are characterized either by cataclastic deformation or by vein formation. Such a sequence of faulting may be attributed to oscillation between states of differential stress, one of frictional sliding with semi-brittle conditions under low pore-fluid pressures and the other under considerably higher pore-fluid pressures. Multiple stages of zeolite veining subparallel to the faults within the shear zones strongly suggest that fluids

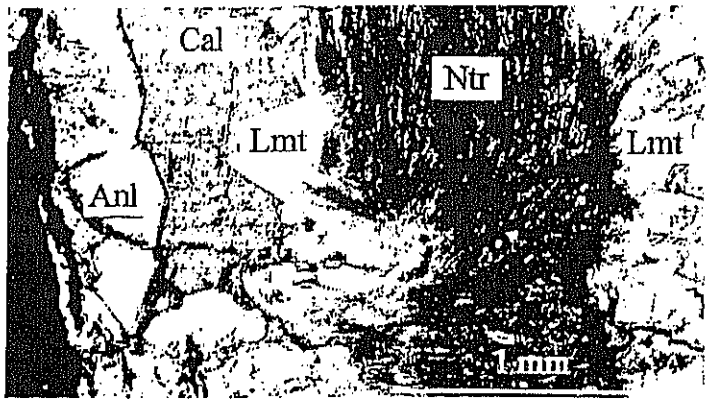

Fig. 17. Photomicrograph of N-MORB pillow lava, Benten Island, showing several stages of veining: analcime (Anl) on both sides of the fault, laumontite (Lmt), natrolite (Ntr) and calcite (Cal).

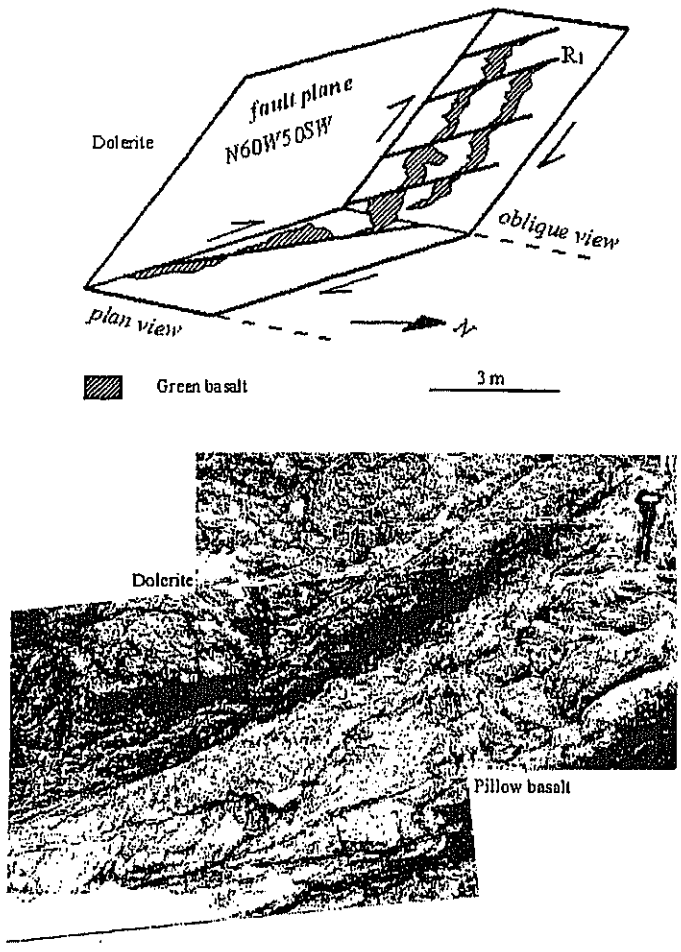

Fig. 18. Outcrop sketch of the 'Aranami Fault', Benten Island, showing Riedel shears and P-shears, with photograph of this area.

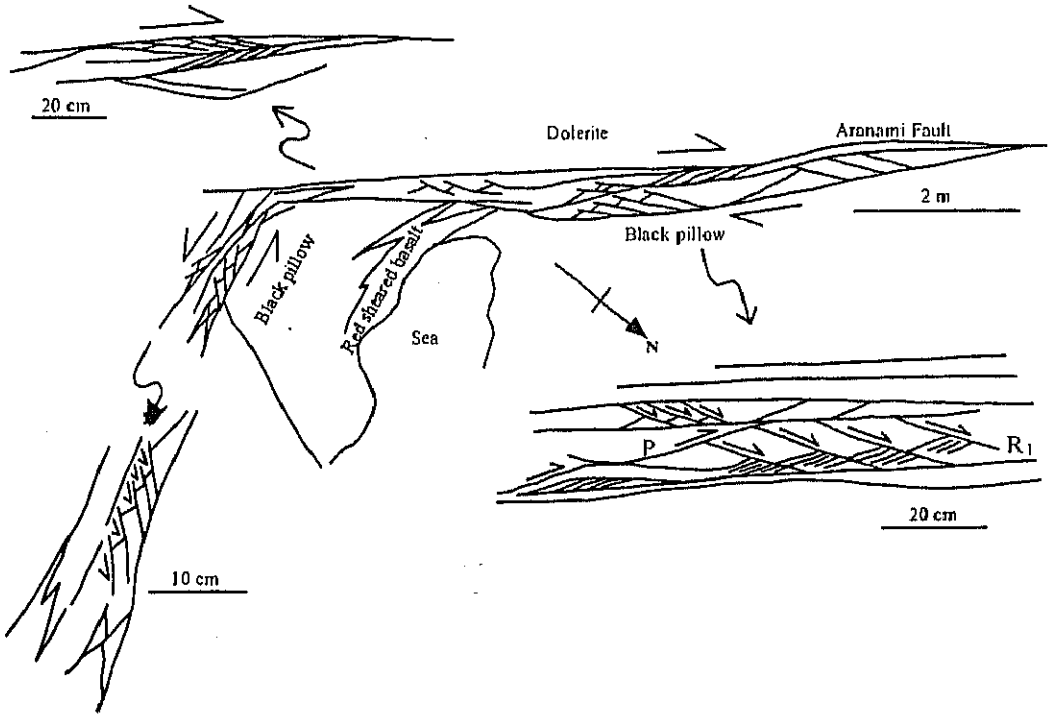

Fig. 19. Schematic diagram of deformation of the 'Aranami Fault', Benten Island.

of differing compositions percolated along the shear zones during and after their formation.

The faults in the Mineoka basalts appear to be normal faults. However, the present attitude of the normal faults may not represent their original orientation. By rotating the basalt bedding to horizontal we can restore the faults to their presumed original attitude, because the vein formation and related faulting is believed to have occurred at an early stage, just after formation of the oceanic crust formation. This interpretation is supported by the following observations. (1) Most of the pillow lavas are layered and sometimes intercalated with massive sheet flows. They strike N40° to 60°E and dip moderately to steeply. All of the lobes are more steeply inclined to the south and SE than the sheet flows, indicating that the lavas flowed in this direction. The ropy surface of one sheet lava indicates its flow in the same direction. Steeply dipping, NW-striking dolerite and basalt dykes are cut by faults with the same orientation. (2) Several stages of veining and faulting are observed and the dyking, veining and faulting occurred nearly simultaneously, indicating that they were controlled by the same tectonic processes. Clearly, the later faults of the second and third phases, with thrust or strike-slip components, are not associated with mineral veining. In addition, the pyroclastic rocks and terrigenous sediments seldom show significant veining and shearing. These features indicate that the veining and faulting was coeval with the volcanic activity and dyke intrusion, long before emplacement of the ophiolite on land. Because most of the pillow lavas and dolerite dykes at Shinyashiki and on Benten Island have MORB and BABB affinities, the deformation and veining probably occurred at a spreading axis, supporting the assumption that the deformation took place when the lava flows were still nearly horizontal.

After rotating the deformed basalts to horizontal, the normal fault systems in Shinyashiki become strike-slip faults with an inferred σ_1 trending NW–SE. The dolerite dykes on Benten Island are presumed to be in their original orientation and thus no rotation is necessary for these rocks. The second phase of deformation, represented by the Aranami Fault on Benten Island, becomes an oblique thrust that separates the IAT pillow basalt from MORB or BABB dolerite dykes. The thrust component may reflect regional convergent tectonics, related to the emplacement of the ophiolite. Rocks of the Kojima Formation, which is composed of andesitic pumice fall

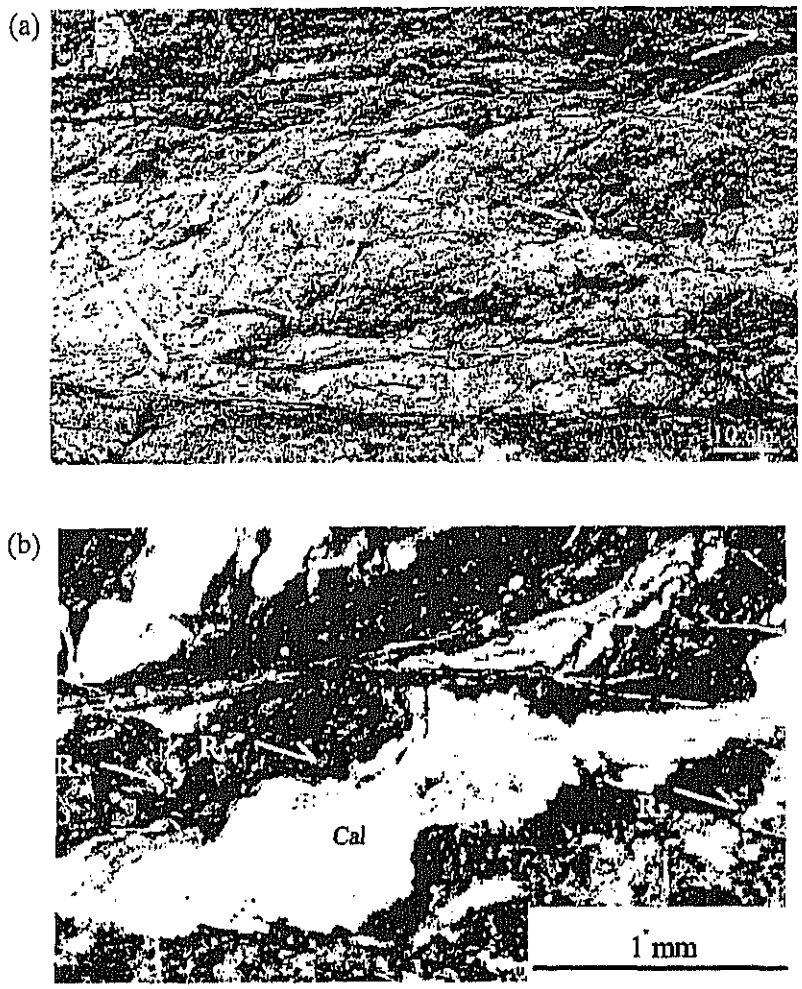

Fig. 20. Riedel shears on various scales from (a) outcrop size to (b) thin-section size along the 'Aranami Fault', Benten Island.

deposits, are neither altered nor deformed. Glassy pumice is preserved and there is no strong shear fabric (Ogawa & Taniguchi 1988). These rocks, which are widely distributed in and around the Mineoka Belt, are thought to be mid-Miocene in age (Kanie & Asami 1995). Therefore, the faulting and veining of the basaltic rocks must have occurred before the mid-Miocene. The presence of middle Miocene serpentine-bearing sandstones also supports this inferred emplacement age of the ophiolite (Ogawa 1983).

The Boso triple junction may have been situated off Boso since the Miocene (Seno & Maruyama 1984; Ogawa *et al.* 1989). The Mineoka plate, composed mainly of ophiolitic lithologies now exposed in the Mineoka Belt (Ogawa & Taniguchi 1988; Sato *et al.* 1999; Sato & Ogawa 2000; Hirano *et al.* 2003), may have been close to the triple junction; it was then emplaced onto the Honshu island arc. Following its emplacement, the ophiolitic bodies and the overlying Kojima Formation were cut by local shear zones (Fig. 2). These faults represent the third phase of deformation, beginning after the ophiolite emplacement and possibly continuing to the present. At least some of the faults that border the Mineoka Belt are thus thought to be still active.

We are grateful for discussions with Y. Dilek, G. Moore, D. Curewitz, T. Ishii, H. Sato, H. Taniguchi, A. L. Abdeldayem and N. Takahashi. Comments and revisions by three reviewers, Y. Dilek, J. Wakabayashi and F. Huot,

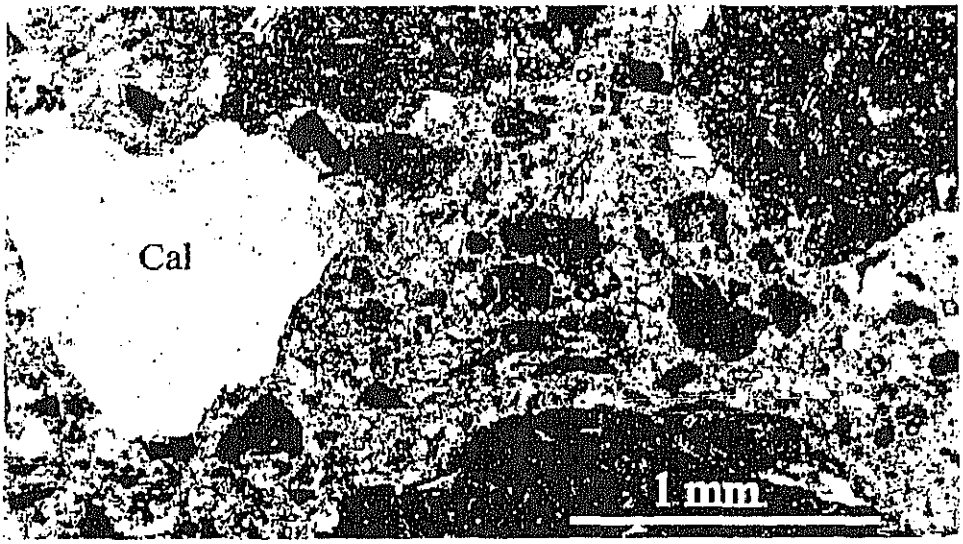

Fig. 12. Photomicrograph of a third-stage fault, showing various scales of brecciation.

Zeolite veins were simultaneously developed along the faults of the second stage. In contrast, the faulting of the third stage deformed pre-existing calcite veins of the earlier stages. This indicates that the second-stage faulting was penecontemporaneous with veining, but that third-stage faulting occurred after veining.

Benten Island outcrops

Three blocks of basalt, each with different chemistry representing potentially different tectonic settings, are present on Benten Island (Fig. 15): (1) dolerite dykes with minor basaltic dykes of MORB or BABB composition crop out on the main island; (2) black pillow lavas of IAT composition occur in the NE section; (3) red–grey pillow lavas of N-MORB composition are present in the west section (Hirano *et al.* 2003). Each segment is characterized by a specific style of faulting and veining. The dolerite has sheared laumontite veins, whereas the IAT lavas are characterized by interpillow silica and celadonite with worm-like fossils. The N-MORB pillow lavas have calcite and

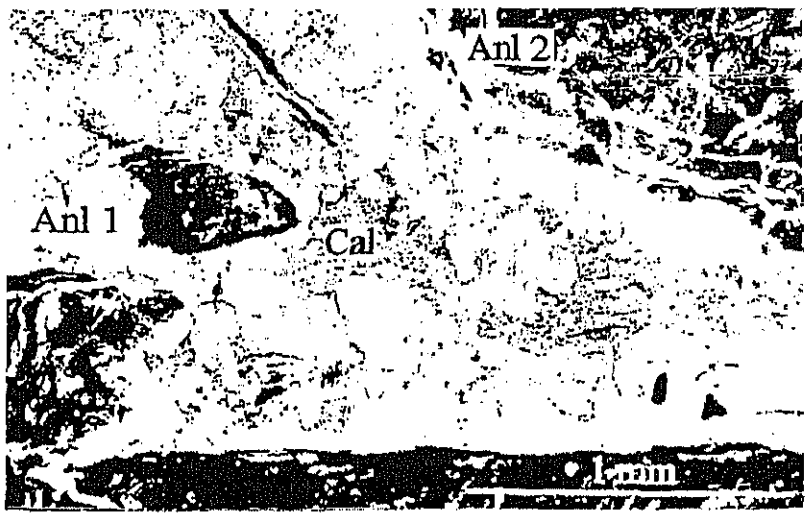

Fig. 13. Photomicrograph of a third-stage fault, showing first analcime (Anl1), second analcime (Anl2) and calcite (Cal) veins.

by three reviewers, Y. Dilek, J. Wakabayashi and E. Huot, are gratefully acknowledged. Part of this study was supported by a Grant-in-Aid from the Japan Society for Promotion of Science (A-10304037).

References

DILEK, Y. & THY, P. 1998. Structure, petrology and seafloor spreading tectonics of the Kizildag Ophiolite, Turkey. *In:* MILLS, R.A. & HARRISON, K. (eds) *Modern Ocean Floor Processes and the Geological Record*. Geological Society, London, Special Publications, **148**, 43–69.

HIRANO, N. & OKUZAWA, K. 2002. Occurrence of the sandstone included in the alkali-basalt lava flow from the western Mineoka Belt, Boso Peninsula, Japan, and its tectonic significance. *Journal of Geological Society of Japan*, **108**, 691–700.

HIRANO, N., OGAWA, Y., SAITO, K., YOSHIDA, T., SATO, H. & TANIGUCHI, H. 2003. Multi-stage evolution of the Tertiary Mineoka ophiolite at Boso TTT triple junction in the NW Pacific as revealed by new geochemical and age constraints. *In:* DILEK, Y. & ROBINSON, P.T. (eds) *Ophiolites in Earth History*. Geological Society, London, xx–xxx.

KANEHIRA, K. 1976. Occurrence of serpentinite and basalt in the Mineoka Belt, southern Boso Peninsula. *In:* EDITOR, A. (ed.) *Book Title*, Memoirs of Geological Society of Japan, **13**, 43–50.

KANEOKA, I., TAKIGAMI, Y., TONOUCHI, S., FURUTA, T., NAKAMURA, Y. & HIRANO, M. 1980. Pre-Neogene volcanism in central Japan based on K–Ar and Ar–Ar analyses. *In:* EDITOR, A. (ed.) *IAVCEI Symposium—Arc Volcanism, Tokyo and Hakone, Abstracts*. Publisher, Town, 166.

KANIE, Y. & ASAMI, S. 1995. *Biostratigraphy of the Miocene Hayama Group in the Miura Peninsula*. Report of Culture and Natural Treasures of Yokosuka City, **29**, 13–17.

MOHIUDDIN, M.M. & OGAWA, Y. 1998. Late Paleocene to middle Miocene pelagic sequences in the Boso Peninsula, Japan: new light on NW Pacific tectonics. *Island Arc*, **7**, 301–314.

OGAWA, Y. 1983. Mineoka ophiolite belt in the Izu forearc area—Neogene accretion of oceanic and island arc assemblages in the northeastern corner of the Philippine Sea plate. *In:* HASHIMOTO, M. & UYEDA, S. (eds) *Accretion Tectonics in the Circum-Pacific Region*. Terra, Tokyo, 245–260.

OGAWA, Y. & NAKA, J. 1984. Emplacement of ophiolitic rocks in forearc area: examples from central Japan and Izu–Mariana–Yap island arc system. *In:* GASS, I.G., LIPPARD, S.J. & SHELTON, A.W. (eds) *Ophiolites and Oceanic Lithosphere*. Geological Society, London, Special Publications, **13**, 291–301.

OGAWA, Y. & TANIGUCHI, H. 1987. Ophiolitic melange in forearc area and formation of the Mineoka Belt. *Science Reports, Kyushu University, Geology*, **15**, 1–23.

OGAWA, Y. & TANIGUCHI, H. 1988. Geology and tectonics of the Miura–Boso Peninsulas and the adjacent area. *Modern Geology*, **12**, 147–168.

OGAWA, Y. & TANIGUCHI, H. 1989. Origin and emplacement of basaltic rocks in the accretionary complexes in SW Japan. *Ofioliti*, **14**, 177–193.

OGAWA, Y., NAKA, J. & TANIGUCHI, H. 1985. Ophiolite-based forearcs: a particular type of plate boundary. *In:* NASU, N., KOBAYASHI, K., KUSHIRO, I. & KAGAMI, H. (eds) *Formation of Active Ocean Margins*. Terra, Tokyo, 719–746.

OGAWA, Y., SENO, T., TOKUYAMA, H., AKIYOSHI, H., FUJIOKA, K. & TANIGUCHI, H. 1989. Structure and development of the Sagami Trough and off-Boso triple junction. *Tectonophysics*, **160**, 135–150.

OGO, M. & HIROI, (?). 1991. Origin of various mineral assemblages of the Mineoka metamorphic rocks from Kamogawa, Boso Peninsula, Central Japan—with special reference to the effect of oxygen. *Journal of Japanese Association of Mineralogists, Petrologists and Economic Geologists*, **86**, 226–240.

SAITO, S. 1992. Stratigraphy of Cenozoic strata in the southern terminus area of Boso Peninsula, Central Japan. *Contributions of Institute of Geology and Paleontology, Tohoku University*, **93**, 1–37.

SATO, H. & OGAWA, Y. 2000. Sulfide minerals in peridotites as tectonic indicators for genesis of ophiolitic rocks: example from peridotite in the Hayama–Mineoka Belt, central Japan. *In:* EDITOR, A. (ed.) *Ophiolites and Oceanic Crust*. Geological Society of America, Special Papers, **349**, 427–437.

SATO, H., TANIGUCHI, H., TAKAHASHI, N., MOHIUDDIN, M.M., HIRANO, N. & OGAWA, Y. 1999. Origin of the Mineoka Ophiolite. *Journal of Geography, Tokyo Geographical Society*, **108**, 203–215.

SENO, T. & MARUYAMA, S. 1984. Paleogeographic reconstruction and origin of Philippine Sea. *Tectonophysics*, **102**, 53–84.

YOSHIDA, Y. 1974. Geology of the eastern end of the Mineoka Mountains. *Chishitsu News*, **233**, 30–36.

KANEHIRA, K. 1976. Modes of occurrence of serpentinite and basalt in the Mineoka district, southern Boso Beninsula. In: KIZAKI, Y., KURODA, N., KOSAKA, T., SHIMAZU, M., CHIHARA, K., TOKUOKA, T., HAYAMA, Y., FUJITA, Y. & YAMASHITA, N. (eds) *Studies on the Boundary Area between East and West Japan*. Memoir of Geological Society of Japan, 13, 43-50.

Multi-stage evolution of the Tertiary Mineoka ophiolite, Japan: new geochemical and age constraints

N. HIRANO[1], Y. OGAWA[2], K. SAITO[3], T. YOSHIDA[4], H. SATO[5] & H. TANIGUCHI[6]

[1]*Department of Earth and Planetary Sciences, Tokyo Institute of Technology, 2-12-1 Ookayama, Meguro, Tokyo 152-8551, Japan (e-mail: nhirano@geo.titech.ac.jp)*

[2]*Institute of Geoscience, University of Tsukuba, Tsukuba 305-8571, Japan*

[3]*Department of Earth and Environmental Sciences, Faculty of Science, Yamagata University, Yamagata 990-8560, Japan*

[4]*Institute of Mineralogy, Petrology and Economic Geology, Graduate School of Science, Tohoku University, Sendai, 980-8578, Japan*

[5]*Ocean Research Institute, University of Tokyo, Tokyo 164-8639, Japan*

[6]*Komazawa University Senior High School, Tokyo 158-0098, Japan*

Abstract: The Mineoka ophiolite in the southern Boso Peninsula is situated in a unique tectonic setting in the collisional zone between the Izu and Honshu arcs in Japan. The ophiolitic rocks are composed mainly of tholeiitic pillow basalts and dolerites, alkali-basaltic sheet flows, and calc-alkaline dioritic to gabbroic rocks. The tholeiitic basalts show variable trace element compositions ranging from mid-ocean ridge basalt to island-arc basalt, whereas the alkali-basalts have a within-plate affinity. High-Fe and -Ti tholeiitic basalt and within-plate alkali-basalt have Ar/Ar ages of 49 ± 13 Ma and 19.62 ± 0.90 Ma, respectively. Three plutonic rocks have K–Ar ages of *c.* 25, 35 and 40 Ma. These ages are inconsistent with the known ages from the Pacific or Philippine Sea Plate. We infer that the Mineoka ophiolitic assemblage was part of another Tertiary oceanic plate, the 'Mineoka Plate', which underwent island-arc volcanism in the Miocene as a result of subduction initiation at a fracture zone or a transform fault system owing to a change in the position of the Euler rotation pole of the Pacific Plate at *c.* 43 Ma. Eruption of within-plate type alkali basalts on the Mineoka Plate took place near the palaeo-Japan continental arc just before the emplacement of the Mineoka ophiolite into the Japanese continental margin.

The Mineoka ophiolite and related rocks in central Japan include mainly Tertiary mafic and ultramafic rocks with pelagic and terrigenous materials and occur in the area sandwiched between two fore-arcs of the Japan and Izu arcs (Ogawa 1983; Ogawa *et al.* 1985; Ogawa & Taniguchi 1987, 1988; Fig. 1). The Mineoka ophiolite constitutes a significant component of a fault belt (henceforth called the 'Mineoka Belt'), which lies near a trench–trench–trench (TTT) triple junction, the Boso triple junction (Ogawa *et al.* 1985; Seno *et al.* 1989), in the NW Pacific Ocean. Various kinds of mafic and ultramafic rocks are distributed in a complicated fashion together with alkali-basalt, diorite, calcareous and siliceous pelagic sedimentary rocks, and tuffaceous rocks within the Mineoka Belt. All the igneous rocks in the Mineoka Belt occur as tectonic blocks in Tertiary terrigenous clastic sediments or in serpentinite bodies (Fig. 2). Various hypotheses on the origin of these igneous rocks in the Mineoka Belt have been advanced. Ogawa & Taniguchi (1988) proposed the existence of a Tertiary oceanic plate, 'the Mineoka Plate', based on geochemical data and preliminary radiometric ages of basalts (Kaneoka *et al.* 1980), and gravity data for the southern Boso Peninsula (Tonouchi 1981). This hypothesis was supported by a recent geophysical study by Fujiwara *et al.* (1999), who reported the magnetic structures in the southern Boso Peninsula and demonstrated that the Mineoka Belt consists of fragments of an oceanic plate.

Arai and coworkers (e.g. Uchida & Arai 1978; Arai & Takahashi 1988; Arai 1991) reported petrological and mineralogical characteristics of ultramafic rocks in the Mineoka Belt and concluded that they are analogues of abyssal peridotites. Arai (1991) proposed that peridotites

From: DILEK, Y. & ROBINSON, P. T. (eds) 2003. *Ophiolites in Earth History*. Geological Society, London, Special Publications, 218, 1–20. 0305-8719/03/$15 © The Geological Society of London 2003

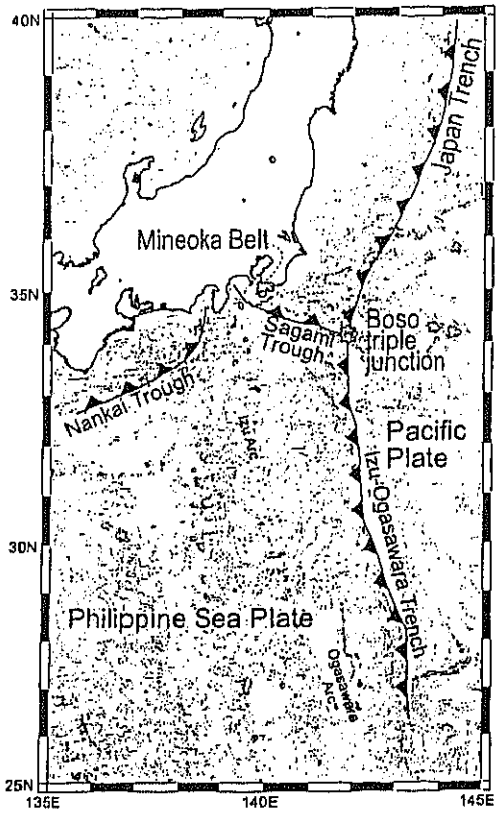

Fig. 1. Bathymetric map (500 m contour interval) of the NW Pacific and eastern Philippine Sea Plate.

beneath the Shikoku Basin intruded into the sea floor and were then accreted to the Honshu arc. Fujioka *et al.* (1995) inferred that serpentinite in seamounts of the Izu–Ogasawara–Mariana forearc area had been accreted to the Honshu arc, based on the similar mode of occurrence of serpentinized peridotites in both areas. However, Sato & Ogawa (2000) disputed the forearc serpentinite seamount origin for peridotites in the Mineoka Belt, based on petrological and mineralogical characteristics, and concluded that the Mineoka Plate hypothesis proposed by Ogawa & Taniguchi (1988) is a plausible explanation for the origin of the Mineoka ophiolite. However, the tectonic setting and evolution of the ophiolitic rocks are still unresolved.

To discuss the origin of the ophiolitic rock assemblage in the Mineoka Belt and its implications for the tectonics of the Paleogene NW Pacific area, we need precise geochemical and geochronological data from the igneous rocks. Thus, in this paper, we describe and discuss the major and trace element geochemistry and ages of the igneous rocks in the Mineoka ophiolite. We attempt to use these data to unravel the evolution of these complicated ophiolitic assemblages. Ocean-floor deformation of the Mineoka ophiolite has been documented in a companion paper by Takahashi *et al.* (2003).

Geology of the Mineoka Belt

The Mineoka Belt, defined as a 5 km wide, east–west-trending fault zone, occupies the southern

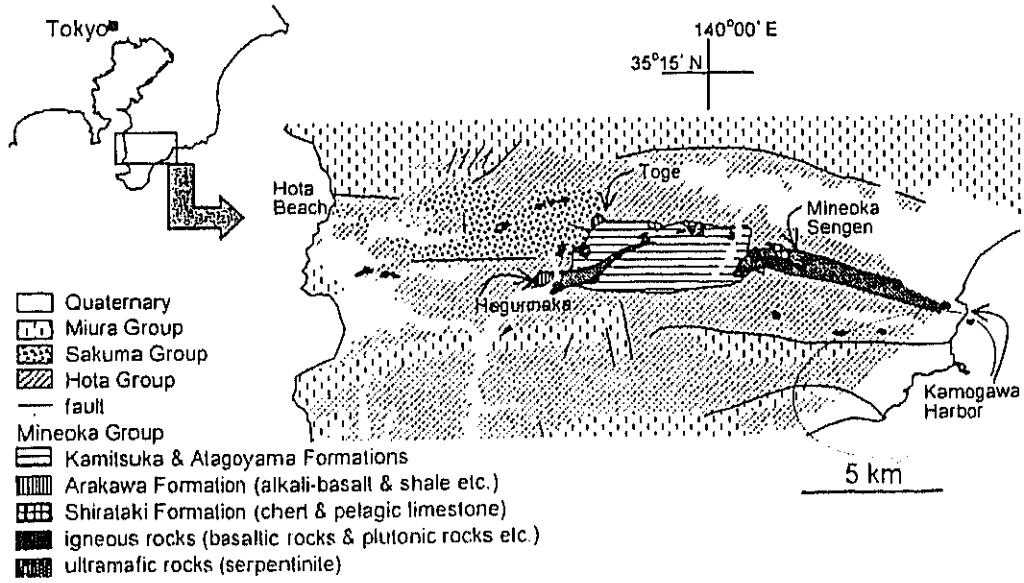

Fig. 2. Index map of the Mineoka Belt after Hirano & Okuzawa (2002).

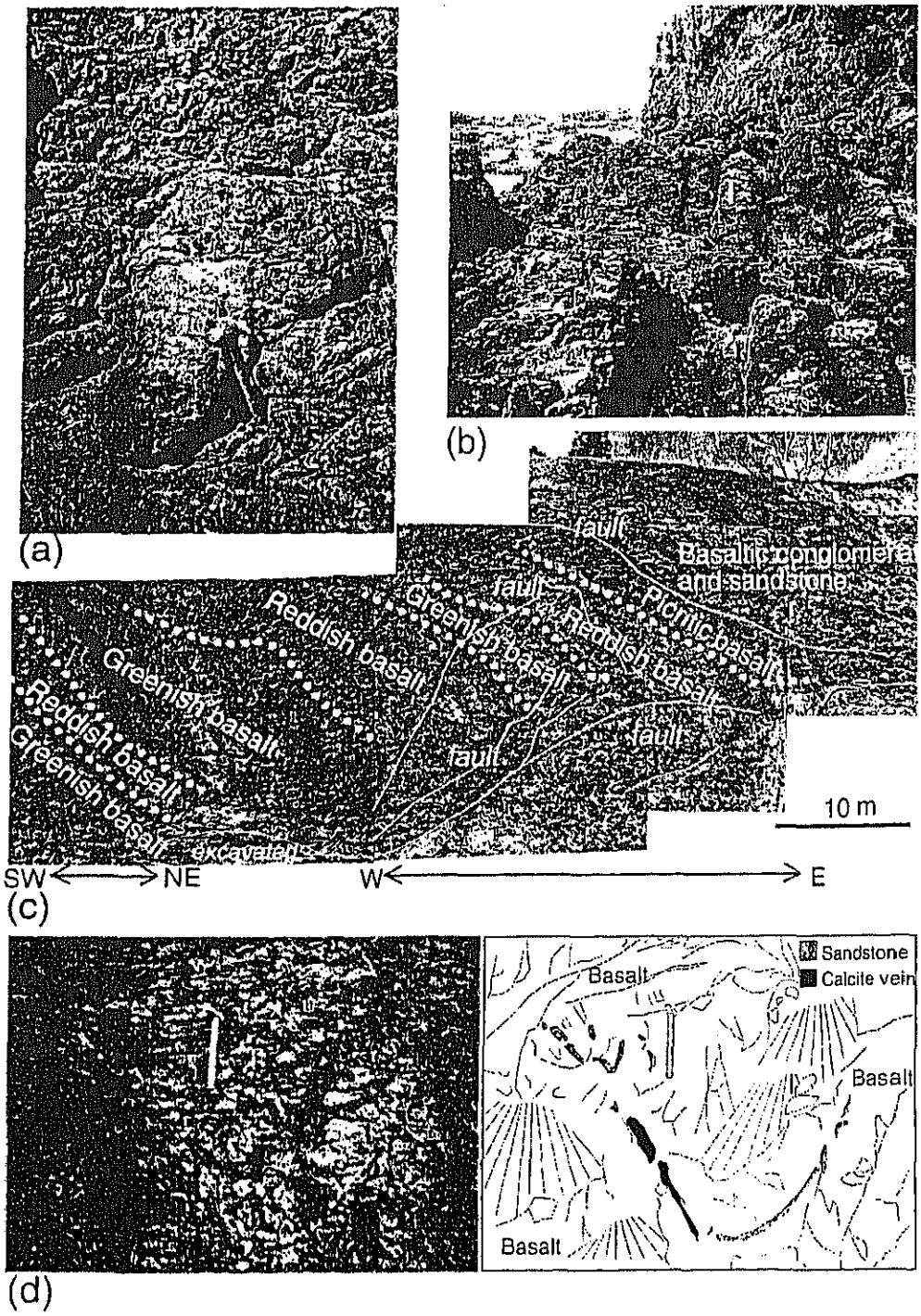

Fig. 3. Outcrop photographs: (a) tholeiite pillow basalt; (b) dolerite sheeted dyke complex; (c) alkali-basalt sheet flows; (d) sandstone inclusions in alkali-basalt lavas.

part of the Boso Peninsula in central Japan, extending from Kamogawa Harbour in the east to Hota Beach in the west (Fig. 2). Sedimentary rocks in the Izu forearc have accreted to the Japan forearc along the Sagami Trough, and several accretionary prisms have formed on the southern edge of the Mineoka Belt between the early Miocene and the present (Ogawa *et al.* 1985; Saito 1992). The forearc basin sediments cover the earlier accretionary prisms unconformably. Because the middle Miocene Sakuma Group in the western Mineoka Belt is the oldest geological unit, and because it includes clasts of the Mineoka ophiolite (Saito 1992), we infer that these rocks underwent the same processes of accretion and emplacement. The pelagic sedimentary rocks, such as limestone and chert, form an almost continuous sequence ranging in age from late Paleocene to mid-Miocene, or from 55 to 17 Ma (Mohiuddin & Ogawa 1998).

In map view, most of the igneous rocks are rounded to lozenge-shaped and range from metre to kilometre scale. They are surrounded by, or in fault contact with, the Mineoka Group (part of the Shimanto Supergroup, probably Paleogene in age: Nakajima *et al.* 1981; Ogawa *et al.* 1985; Watanabe & Iijima 1989), Hota Group (latest Oligocene to mid-Miocene: Saito 1992; Suzuki *et al.* 1996), Sakuma Group (mid-Miocene: Saito 1992) and serpentinized ultramafic bodies (Fig. 2). Basaltic rocks consist mostly of tholeiitic and rarely alkali–olivine pillow lavas (Tazaki & Inomata 1980; Ogawa & Taniguchi 1988). In the Mineoka Sengen area (Fig. 2), Cyprus-type umber deposits locally occur above the pillow basalts (Tazaki *et al.* 1980; Iijima *et al.* 1990).

Pelagic to hemipelagic and terrigenous sediments were deposited from Eocene to mid-Miocene time, and are now incorporated into the Mineoka Belt. In the Hegurinaka and Toge areas (Fig. 2), a sequence of basaltic clastic sandstone and conglomerate, micritic limestone, glauconitic shale and siliceous shale overlie alkali-basalt sheet flows (Arakawa Formation in Fig. 2) (Ogawa 1983; Takahashi 1994; Hirano & Okuzawa 2002). Basaltic clastic sediments mainly include fragments of alkali-basalts, with some fossils of benthic foraminifers, oysters and corals (Takahashi 1994; Mohiuddin & Ogawa 1996; Hirano & Okuzawa 2002). Mohiuddin & Ogawa (1996) reported mid-Eocene to early Oligocene and early to mid-Miocene foraminifers from these micritic limestones in the Hegurinaka area. Ogawa (1981) and Saito (1992) reported early Miocene radiolarians from the siliceous shale.

Tholeiitic pillow lavas are the dominant basaltic rock type in the ophiolite. They are concentrated in the eastern part of the belt as large blocks

Table 1. *Geochemical compositions of bulk-rock samples*

Sample:	BM591	BM09BT1	BM23BT2	BM25BT3	BM10SY	BM07SG1	BM08SG2	BM21SG3	BM24SG4	BM22SG6	BM29SG5
Rock type:	tholeiite	tholeiite	tholeiite	tholeiite	tholeiite	tholeiite	tholeiite	alkali-basalt	tholeiite	tholeiite	tholeiite
wt%											
SiO_2	47.88	47.92	47.88	49.48	49.83	50.75	48.65	48.61	48.03	48.05	47.89
TiO_2	3.23	1.64	1.63	1.59	2.26	2.10	1.71	2.31	2.08	1.97	1.58
Al_2O_3	11.19	14.09	14.56	14.93	14.38	13.32	13.61	11.73	13.67	14.29	14.39
Fe_2O_3	11.10	3.21	7.00	5.99	5.69	5.68	6.46	7.73	6.53	5.95	4.64
FeO	6.19	7.44	3.51	3.95	4.23	5.04	4.63	5.26	5.11	2.84	3.50
MnO	0.23	0.18	0.17	0.15	*0.18*	*0.19*	*0.22*	*0.24*	*0.21*	*0.39*	*0.14*
MgO	5.19	7.97	7.78	6.55	6.64	6.50	6.30	6.49	6.10	8.49	6.31
CaO	7.95	9.44	11.07	9.85	10.53	9.63	11.46	8.42	8.93	10.29	11.74
Na_2O	3.08	3.87	3.22	4.27	3.38	3.81	3.34	4.44	3.08	3.27	3.67
K_2O	0.20	0.26	0.11	0.29	0.38	0.54	0.59	0.54	1.25	0.10	0.89
P_2O_5	0.26	0.15	0.14	0.12	0.21	0.21	0.16	0.24	0.24	0.18	0.12
H_2O^+	2.73	3.26	1.56	1.55	1.18	1.51	2.67	2.42	2.19	1.87	4.51
H_2O^-	0.77	0.56	1.36	1.28	1.12	0.72	0.20	1.57	2.60	2.33	0.62
Total	100.00	100.00	100.00	100.00	100.00	100.00	100.00	100.00	100.00	100.00	100.00
ppm											
Ba	52.7	215	46.1	2126	31.5	43.0	46.6	71.9	224	17.5	22.2
Ce	18.1	16.6	9.3	7.0	19.7	15.7	11.2	10.0	21.5	23.4	14.3
Co	41.3	50.4	51.1	55.5	47.5	52.1	53.8	33.1	51.9	57.4	49.8
Cr	*24.7*	*336*	*356*	*386*	*136*	*101*	*290*	*15.4*	*147*	*225*	*274*
Cu	19.4	15.9	17.7	17.8	19.1	17.3	16.9	21.2	20.2	17.0	16.7
Nb	7.3	5.4	4.3	4.9	5.9	6.7	3.0	1.2	5.7	6.1	3.0
Ni	21.2	110	96.7	160	65.0	98.2	113	6.2	54.6	88.0	65.2
Pb	0.4	1.0	0.6	0.2	1.0	tr	tr	2.8	1.2	0.9	1.7
Rb	0.9	1.7	tr	0.4	3.7	6.3	13.0	0.4	17.9	tr	6.4
Sr	101	188	145	175	133	167	118	200	111	180	294
Th	2.1	tr	tr	tr	tr	tr	tr	tr	tr	tr	tr
V	348	281	357	326	271	261	305	346	374	453	346
Y	84.8	34.7	33.8	32.4	45.2	42.2	37.4	30.0	45.1	40.6	33.5
Zr	228	98.6	94.6	45.5	132	130	91.3	66.9	150	122	105

tr, trace.

(several hundred metres to 1000 m scale) in fault contact with serpentinite and terrigenous or tuffaceous clastic rocks. In the Mineoka Sengen area in particular (Fig. 2), large basalt blocks, some 100 m across, are abundant. The pillow lavas are close-packed and only rarely intruded by doleritic dykes (Fig. 3a and b). In the Benten-jima, Kamogawa Harbour, at the eastern tip of the Mineoka Belt, three blocks of pillow basalt and dolerite dykes are in fault contact (Takahashi *et al.* 2003). Alkali-basalts are distributed in the central Mineoka Belt and occur as sheet flows (Fig. 3c) or vesicular pillow basalt. Locally, some sheet flows are made of picritic lavas (Fig. 3c). Hirano & Okuzawa (2002) analysed sandstone xenoliths included in the alkali-basalt sheet flows in the Toge area (Fig. 3d), and concluded that they were picked up during eruption because the basalt is chilled against the xenoliths. The sandstone is terrigenous, mainly composed of quartz, plagioclase, datolite (a low-temperature secondary replacement mineral, borosilicate, $CaBSiO_4(OH)$) and silicic volcanic fragments, and is similar in composition to the sandstone in the Mineoka Group (Hirano & Okuzawa 2002).

Although the lavas occur with massive ultramafic rocks or Tertiary sedimentary rocks, the relative ages are unknown because they occur as tectonic blocks. Diorites and gabbros in the serpentinite are interpreted as originally intrusive plutons or dykes (Nakajima *et al.* 1981; Sato *et al.* 1999).

Petrography and geochemistry

The basaltic and other intrusive rocks from the Mineoka ophiolite were analysed by X-ray fluorescence (XRF) for major and trace elements. After excluding the altered parts and some secondary veins, all samples were split and pulverized. H_2O^- and loss on ignition (LOI) were determined at 110 and 900 °C (4 h). Specimens for analysis were prepared by mixing 3.6 g of flux (anhydrous lithium tetraborate) and 1.8 g of powdered sample and fusing the mixture into glass beads following the method of Kimura & Yamada (1996). A Rigaku RIX 2000 X-ray fluorescence spectrometer was used at the Department of Geology, Faculty of Education, Fukushima University. Analytical methods and statistical data have been given by Kimura & Yamada (1996). The results are recalculated to total 100% to insert the H_2O^- and LOI. FeO was determined by potassium permanganate titration. All geochemical data are listed in Table 1.

Based on Harker diagrams, the igneous rocks of the Mineoka ophiolite are divided into sub-alkali and alkali varieties (Miyashiro 1978) (Fig. 4a). However, Na and K may be prone to modification by alteration. To determine the original magma

BM06HS tholeiite	BM32NSGM picrite basalt	BM03HG1 alkali-basalt	BM04HG2 alkali-basalt	BM05HG3 tholeiite	BM26SK tholeiite	BM14FG gabbro	BM28SNJ diorite	BM31YD diorite	BM30RS gabbro	BM12GSCH gr.schist
49.35	41.11	41.92	47.23	47.94	48.71	47.00	59.89	58.46	49.33	48.10
1.72	1.54	2.80	3.20	2.09	1.74	0.32	0.54	0.38	1.02	1.29
13.75	7.26	11.83	13.50	13.87	14.51	25.53	17.04	18.75	14.25	14.46
4.02	6.90	6.69	4.51	4.86	5.97	1.70	2.11	2.98	3.16	4.90
6.19	4.47	5.69	6.85	6.08	3.33	2.27	3.28	2.31	5.26	5.49
0.28	0.15	0.27	0.16	0.20	0.15	0.07	0.09	0.08	0.15	0.17
7.96	24.28	11.61	8.04	7.28	7.60	4.86	3.78	3.81	8.72	8.29
9.41	5.68	9.43	8.00	9.16	10.21	9.11	6.41	7.38	9.14	11.40
4.10	0.34	2.34	3.80	4.17	3.78	4.06	4.83	3.89	4.46	2.70
0.08	0.10	0.27	0.93	0.11	0.59	0.50	0.47	0.48	0.25	0.44
0.14	0.17	0.32	0.37	0.23	0.16	0.01	0.06	0.04	0.02	0.10
2.32	7.31	5.53	2.88	2.97	2.47	4.16	1.37	1.23	4.05	2.16
0.70	0.69	1.16	0.52	1.04	0.79	0.40	0.13	0.22	0.19	0.51
100.00	100.00	100.00	100.00	100.00	100.00	100.00	100.00	100.00	100.00	100.00
42.6	43.2	224	375	46.8	73.2	16.9	91.3	80.2	92.0	42.8
10.4	27.5	35.8	41.8	18.0	16.5	tr	7.00	1.00	3.6	7.2
49.7	106	67.7	55.2	54.6	52.2	26.6	26.4	23.2	41.4	50.9
180	2849	832	146	297	340	86.7	97.3	87.0	478	338
17.3	11.0	22.6	19.6	17.9	17.3	18.0	15.9	17.2	13.2	15.2
2.7	11.4	23.1	27.6	6.4	3.8	0.05	1.0	0.9	1.0	2.1
66.3	1110	389	109	137	103	71.2	83.5	70.2	149	98.6
tr	0.3	1.2	tr	tr	2.0	tr	tr	0.3	1.1	0.3
tr	3.3	3.1	8.9	tr	6.8	2.6	1.4	1.1	tr	6.0
130	99.6	238	394	262	132	659	211	276	353	119
tr	0.1	1.5	1.1	tr	tr	tr	tr	tr	tr	tr
317	241	238	205	302	374	228	275	340	355	262
37.2	16.8	25.6	26.4	45.3	30.6	9.9	18.0	11.5	33.9	29.2
96.6	92.2	155	186	136	98.2	75.7	77.2	65.2	63.2	66.8

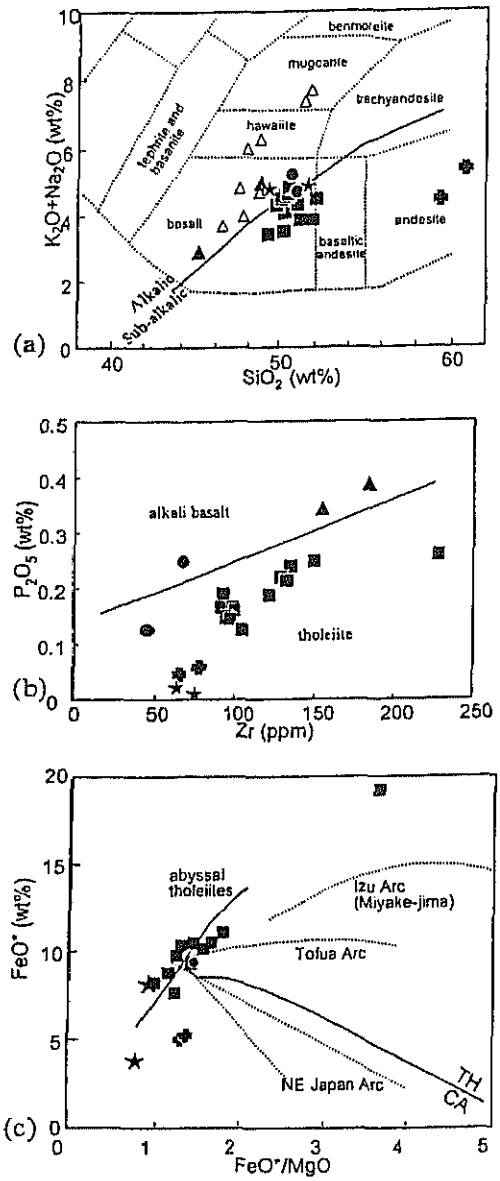

Fig. 4. (a) SiO_2–total alkali diagram. Nomenclature of *volcanic rocks is after Cox et al. (1979). Continuous line* dividing alkalic and sub-alkalic magma series is from Miyashiro (1978). Picrite basalt (BM32NSGM) is not plotted. (b) P_2O_5–Zr diagram. (c) FeO^*–FeO^*/MgO diagram (Miyashiro 1973). Continuous line and dotted *lines show the abyssal tholeiite and volcanic rocks in* several arcs (Miyashiro 1973). TH, tholeiite; AL, alkali-basalts; CA, calc-alkaline series. Squares and circles, tholeiitic basalts; triangles, alkali-basalts; stars and crosses, gabbro and diorite, respectively; open triangles, *data from Hirano & Okuzawa (2002).*

compositions, we used the P_2O_5–Zr diagram (Fig. 4b) (Winchester & Floyd 1976). Many samples, shown by squares and one circle, are 'high-alkali tholeiite', which occurs as close-packed pillow lavas and aphyric basalts in the Mineoka Belt. Also present are alkali-basalts (BM03HG1, *BM04HG2, BM21SG3*), shown by two triangles and one circle, which contain olivine and clinopyroxene phenocrysts and occur as sheeted lava flows with some picrite basalts or vesicular pillow lavas mainly in the western Mineoka Belt (Hirano & Okuzawa 2002). However, a non-vesicular, aphyric alkali-basalt sample (BM21SG3), shown by a circle, is from Mineoka Sengen, where tholeiitic basalts dominate. Another sample, BM32NSGM, not plotted in Figure 4, shows the composition of groundmass separated from the picrite basalt. Many tholeiitic samples are characterized by high FeO^* ($FeO + 0.9Fe_2O_3$) and high TiO_2 (FeO^*/MgO >1.4 wt% and TiO_2 >2.0 wt%). Tholeiitic basalts lie along the trend of abyssal tholeiite in Figure 4c.

Diorites are composed of euhedral plagioclase, subhedral to anhedral hornblende and anhedral quartz. Other minor minerals include orthopyroxene in sample *BM31-YD2 and secondary chlorite* replacing amphibole in BM28-SNJ. Gabbros are mainly composed of euhedral hornblende and anhedral plagioclase. The sample BM30RS includes rare orthopyroxene in hornblende crystals. Sample BM14FG has very high Al_2O_3 (27 wt%; Table 1), suggesting that it is a plagioclase-rich cumulate; however, it is difficult to identify the original magma type of the gabbros.

All the basaltic rocks were plotted on the discrimination diagrams of Pearce & Norry (1979) and Pearce & Cann (1973) (Fig. 5a–c) and normal mid-ocean ridge basalt (N-MORB) normalized spidergrams of Pearce (1983) (Fig. 5d–g). The *basaltic rocks fall into the fields of ocean-floor* basalts (OFB or MORB), island arc basalts (IAB or LKT; samples BM25BT3 and BM21SG3) and ocean island basalts (OIB or within-plate basalts (WPB); samples BM03HG1, BM04HG2 and BM32NSGM) (Fig. 5a and b). Alkali-basalts from the central Mineoka Belt reported by Hirano & Okuzawa (2002), are shown by open triangles in some plots and a fine line in Fig. 5e, and are the *same type of rocks as OIB of this study.*

Geochronology

K–Ar dating

Hornblende and plagioclase separates from diorites (sample BM28SNJ from the Kawaguchi region and BM31YD2 from the Yamada region) and *gabbro (BM14FG from the Futago region) were*

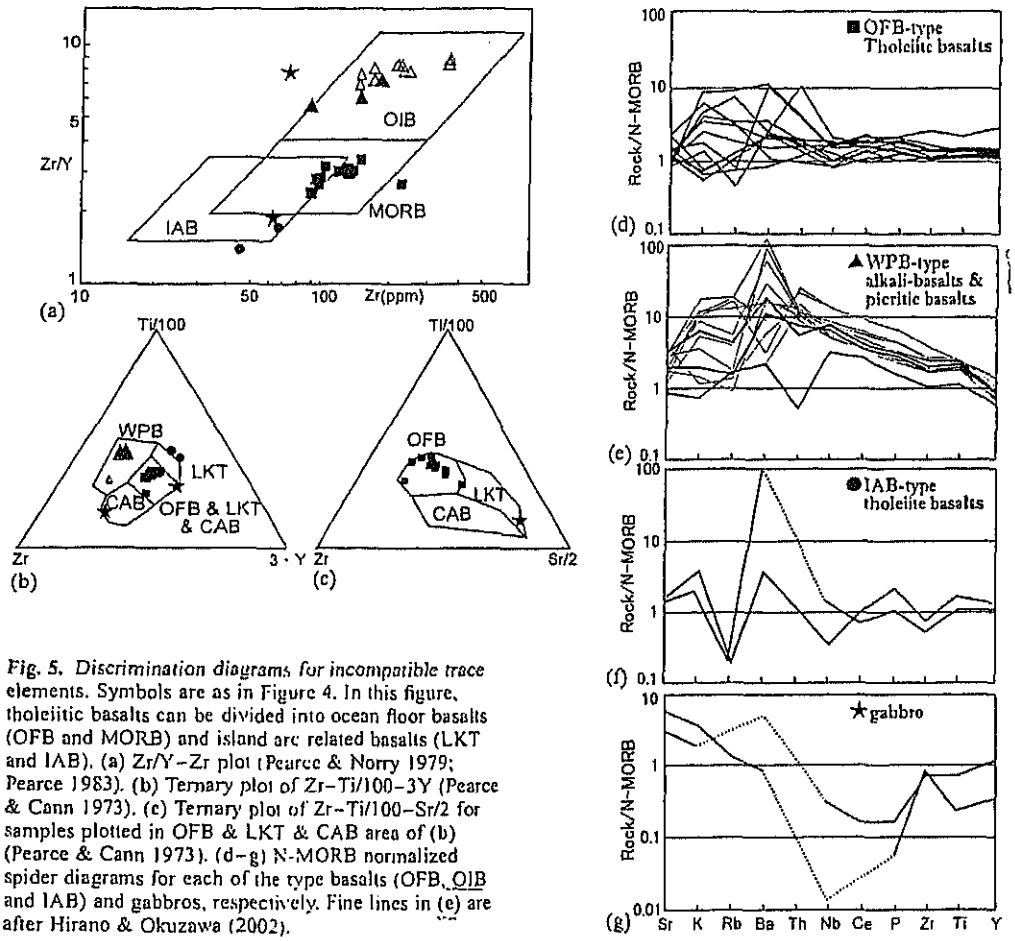

Fig. 5. Discrimination diagrams for incompatible trace elements. Symbols are as in Figure 4. In this figure, tholeiitic basalts can be divided into ocean floor basalts (OFB and MORB) and island arc related basalts (LKT and IAB). (a) Zr/Y–Zr plot (Pearce & Norry 1979; Pearce 1983). (b) Ternary plot of Zr–Ti/100–3Y (Pearce & Cann 1973). (c) Ternary plot of Zr–Ti/100–Sr/2 for samples plotted in OFB & LKT & CAB area of (b) (Pearce & Cann 1973). (d–g) N-MORB normalized spider diagrams for each of the type basalts (OFB, OIB and IAB) and gabbros, respectively. Fine lines in (e) are after Hirano & Okuzawa (2002).

analysed by the K–Ar method. The samples were crushed to 30–50 mesh and minerals were separated into mafic and felsic groups using an isodynamic separator. Hornblende was separated from the other mafic minerals by heavy liquids. Potassium analyses were carried out by XRF using a Phillips PW1404 system at the University of Tsukuba. Based on Nakano *et al.* (1997), we estimated 5% error in the potassium content. Argon isotopic analyses with ^{38}Ar spike were carried out at Yamagata University. The analytical methods have been described by Saito *et al.* (1991).

The K–Ar ages are summarized in Table 2. Experimental errors are shown as 1σ. Some of these K–Ar dates will need to be confirmed by other methods, such as Ar/Ar. From sample BM28SNJ, we obtained ages of 27.9 ± 1.8 Ma for

Table 2. *K–Ar age results*

Sample	Rock	Mineral	K (wt %)	$^{40}Ar/^{36}Ar$	Radiogenic ^{40}Ar (10^{-7} STP $cm^3 g^{-1}$)	Air content (%)	Age (Ma)
BM28SNJ	Diorite	Hornblende	0.171	405.2 ± 6.1	1.87 ± 0.08	73	27.9 ± 1.8
		Plagioclase (An50)	0.312	373.3 ± 2.6	2.95 ± 0.09	79	24.1 ± 1.4
BM31YD	Diorite	Hornblende	0.099	567.7 ± 6.0	1.59 ± 0.03	52	40.9 ± 2.1
BM14FG	Gabbro	Hornblende	0.121	455.3 ± 4.3	1.68 ± 0.03	65	35.3 ± 1.9

hornblende and 24.1 ± 1.4 Ma for plagioclase. Hara *et al.* (1989) reported a fission-track age of 34.9 ± 1.5 Ma on zircon from diorite in the Yamada area, which is from the same site as sample BM31-YD2, from which we obtained a K–Ar age of 40.9 ± 2.1 Ma on hornblende. Closure temperatures of plagioclase in the K–Ar system and zircon in the fission-track system are lower than the closure temperature of hornblende. Therefore, in plutonic rocks hornblende ages are older than plagioclase and zircon ages. The hornblende in gabbro sample BM14FG has an age of 35.3 ± 1.9 Ma.

Ar/Ar dating

Samples of tholeiitic basalt (BM591) and alkali-basalt (BM04HG2) were also analysed by the $^{40}Ar/^{39}Ar$ method. All samples were crushed to 50–100 mesh grains, were wrapped in aluminium foil and sealed in quartz vials (70 mm in length, 10 mm in diameter) under vacuum, with flux monitors biotite (HD-B1), K_2SO_4 and CaF_2. The samples were irradiated for 24 h in the Japan Material Testing Reactor (JMTR), Tohoku University. During the irradiation, the samples were shielded by Cd foil to reduce thermal neutron-induced ^{40}Ar production from ^{40}K (Saito 1994). The Ar extraction and Ar isotopic analyses were carried out at Yamagata University. The samples were incrementally heated to 1500 °C in a Mo crucible by induction heating. Gases were extracted in eight or nine steps between 600 and 1500 °C. The analytical methods have been described by Saito *et al.* (1991). The results of the Ar/Ar dating are summarized in Table 3. All errors are shown as 2σ.

Sample BM591, a tholeiite from Kamogawa Harbour, has an age of 49 ± 13 Ma (Fig. 6a). Because of the very low K in tholeiitic basalt, the error is large at the 95% confidence level. The two lower temperature fractions and the highest temperature fraction may contain excess argon and are omitted from the age determination. Sample BM04HG2, an alkali-basalt from the Hegurinaka region, yielded a good age of 19.62 ± 0.90 Ma based on three lower temperature fractions, which contain more than 88% ^{39}Ar in the gas contents (Fig. 6b).

Discussion

We discuss here the relation between the mode of occurrence, geochemistry and radiometric ages of the basaltic and other igneous rocks from the Mineoka ophiolite to verify the origin and tectonic implications of these rock assemblages. As described above, the ophiolitic rocks are composed mainly of tholeiitic pillow basalts and doleritic sheeted dykes, alkali-basaltic sheet flows, and dioritic to gabbroic rocks. Some tholeiitic basalts are Fe–Ti-basalt, and are considered to be fractionation products of oceanic tholeiite magmas (Melson & O'Hearn 1979). Such rocks are rare in island-arc tholeiites. Moreover, most of tholeiitic basalts have trace element compositions typical of

Table 3. *Ar/Ar age results*

Temperature (°C)	$^{36}Ar/^{40}Ar$ ($\times 10^{-3}$)	$^{37}Ar/^{40}Ar$ ($\times 10^{-4}$)	$^{39}Ar/^{40}Ar$ ($\times 10^{-2}$)	^{39}Ar (%)	Age (Ma)
BM591, tholeiite (J= 0.00457 ± 0.00014)					
600	25.9 ± 1.8	0.2 ± 4.5	0.24 ± 0.14	2.4	(65 ± 33) × 10
900	26.7 ± 1.6	7.5 ± 2.2	1.91 ± 0.13	10.4	89 ± 21
1000	26.3 ± 1.6	19.1 ± 1.6	4.01 ± 0.12	14.2	45.5 ± 9.7
1100	26.2 ± 1.6	19.3 ± 1.3	3.65 ± 0.19	25.7	50 ± 11
1200	30.4 ± 1.1	16.4 ± 4.9	2.32 ± 0.12	13.1	36 ± 11
1300	28.9 ± 1.6	14.5 ± 6	1.73 ± 0.11	9.3	68 ± 22
1400	27.7 ± 1.0	22 ± 10	2.778 ± 0.096	6.5	53.4 ± 9.2
1500	31.09 ± 0.86	26.1 ± 4.5	1.364 ± 0.022	7.0	48 ± 14
1550	17.7 ± 1.6	63 ± 12	2.789 ± 0.054	11.4	136 ± 14
BM04HG2, alkali-basalt (J= 0.002890 ± 0.000068)					
600	17.6 ± 2.9	5.32 ± 0.79	11.24 ± 0.25	18.7	22.1 ± 1.5
900	3.6 ± 2.9	4.07 ± 0.36	24.82 ± 0.26	48.2	18.70 ± 0.59
1000	6.4 ± 2.0	8.81 ± 0.66	21.56 ± 0.20	21.4	19.53 ± 0.70
1100	13.2 ± 3.8	20.8 ± 3.5	7.92 ± 0.24	2.7	39.8 ± 6.7
1200	27.4 ± 2.9	5.0 ± 2.4	4.69 ± 0.16	1.8	21.1 ± 7.5
1300	28.0 ± 2.3	5.2 ± 1.2	2.99 ± 0.16	2.4	29.9 ± 7.3
1400	30.3 ± 1.9	7.10 ± 0.67	1.93 ± 0.12	2.9	28 ± 10
1500	33.4 ± 2.1	4.00 ± 0.92	1.57 ± 0.11	1.9	4 ± 17

For BM591, $(^{36}Ar/^{37}Ar)_{Ca} = (8.57 \pm 0.32) \times 10^{-4}$, $(^{39}Ar/^{37}Ar)_{Ca} = (2.23 \pm 0.67) \times 10^{-4}$, $(^{40}Ar/^{39}Ar)_K = (0.43 \pm 0.90) \times 10^{-3}$. For BM04HG2, $(^{36}Ar/^{37}Ar)_{Ca} = (3.032 \pm 0.053) \times 10^{-4}$, $(^{39}Ar/^{37}Ar)_{Ca} = (8.64 \pm 0.48) \times 10^{-4}$; $(^{40}Ar/^{39}Ar)_K$ is neglected.

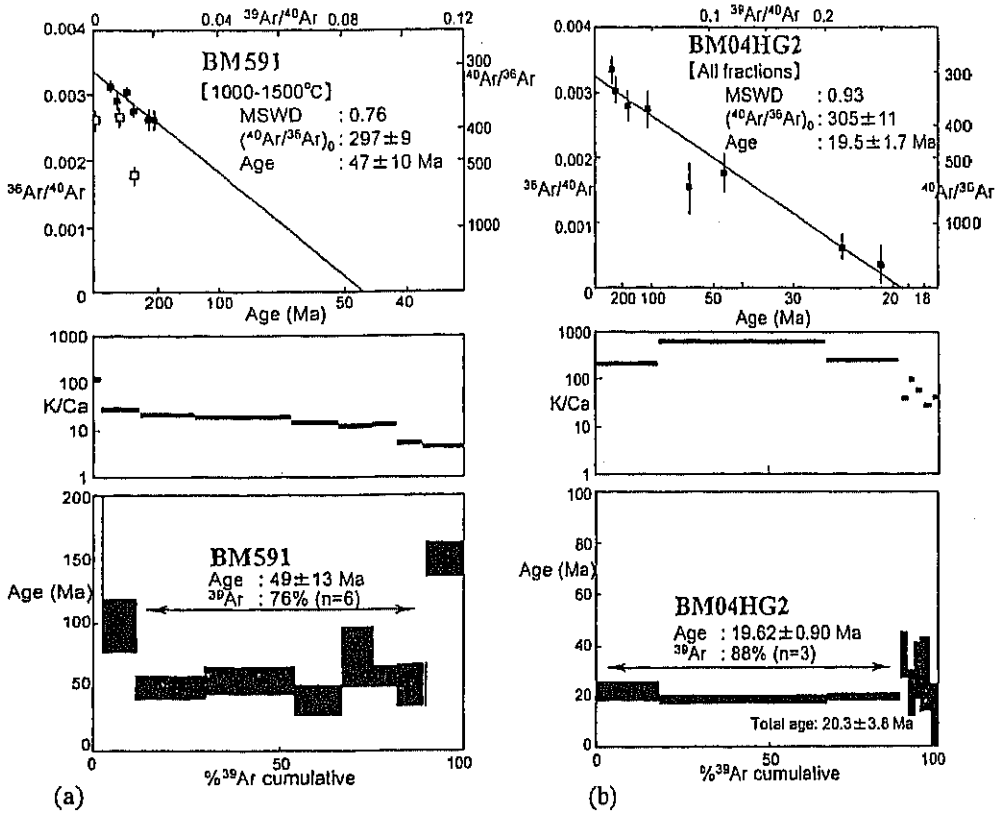

Fig. 6. Ar/Ar age results. $^{39}Ar/^{40}Ar$–$^{36}Ar/^{40}Ar$ isochrons and age spectra of sample BM591 (a) and sample BM04HG2 (b), respectively.

ocean-floor basalt. Two alkali-basalts and one picrite basalt (samples BM03HG1, BM04HG2 and BM32NSGM) have a within-plate affinity. In the central Mineoka Belt, Hirano & Okuzawa (2002) reported a sequence of sheeted lavas of alkali-basalt and picrite basalt, suggesting that these types are related. Another alkali-basalt (sample BM21SG3), one tholeiite (sample BM25BT3) and the diorites are from island arc type magmas. The original magma type of the gabbros is unknown because they are mineralogicaly heterogeneous. Ar/Ar and K–Ar dates yield ages of 49 ± 13 Ma for the tholeiite (Fe–Ti-basalts; BM591), 19.62 ± 0.90 Ma for alkali-basalts (BM04HG2), and c. 25, 35 and 40 Ma for the plutonic rocks (two diorites and gabbro). A preliminary Ar/Ar age by Kaneoka *et al.* (1980) (40–50 Ma) approximately agrees with our age for sample BM591.

The pelagic sedimentary rocks, such as limestone and chert of the Kamogawa Group, range in age from late Paleocene to mid-Miocene, i.e. roughly from 17 to 55 Ma (Mohiuddin & Ogawa 1998). Some stratigraphic gaps, possible hiatuses, are included within these successions, but the group may correspond to pelagic deposits on an oceanic plate. The mid-Eocene to early Oligocene micritic limestone (Hegurinaka Limestone; Mohiuddin & Ogawa 1998) is associated with conformable sequences of alkali-basalt, basaltic sandstone, glauconitic shale, micritic limestone and siliceous shale in the Hegurinaka area. The Hegurinaka Limestone differs in age from the Early Miocene alkali-basalt, micritic limestone (Heguri Formation; Mohiuddin & Ogawa 1998) and siliceous shale (Arakawa Formation; Saito 1992; Mohiuddin & Ogawa 1998), suggesting that it consists of tectonic blocks in fault contact with the Early Miocene sequences.

Where was the Mineoka ophiolite formed?

Previous studies suggested three models for the tectonic evolution of the Paleogene Philippine Sea Plate and the Pacific Plate. In model 1, the

Philippine Sea Plate separated from the Kula Plate and was juxtaposed with the Pacific Plate by a north–south-trending transform fault before initiation of subduction of the Pacific Plate. The TTT triple junction has remained near its present position (Matsuda 1978). Model 2 suggests that the Philippine Sea Plate and the TTT triple junction drifted eastward along the SE Japan margin (Seno & Maruyama 1984; Hall *et al.* 1995), whereas model 3 calls for southwestward drift of the Philippine Sea Plate and the TTT triple junction along the NE margin of Japan (Otsuki 1990). Koyama *et al.* (1992) presented palaeomagnetic evidence for a clockwise rotation of the Izu–Ogasawara forearc region and northeastward drift of the Philippine Sea Plate after the early Oligocene, which supports model 2. In model 2, the Paleogene island arcs, such as the Ogasawara and Mariana Arcs and Kyushu–Palau Ridge, were originally distributed along the northern margin of the Philippine Sea Plate. This requires a southward subduction of the adjacent plate in the north (Fig. 7). However, the inferred southward subduction of the Pacific Plate under these island arcs is problematic, because the Pacific Plate was moving NNW before 43 Ma (see Wessel & Kroenke 1998) (Fig. 7). To infill the area north of the Paleogene Philippine Sea Plate, there might have been another oceanic plate, the Mineoka Plate (Ogawa & Taniguchi 1988), as the counterpart of the North New Guinea Plate (Seno 1984).

In the Philippine Sea Plate at present, there are some extinct back-arc basins and active and extinct island arcs (Fig. 8). Paleogene basalts are distributed in the Ogasawara and Mariana Arcs and West Philippine Basin (e.g. Seno & Maruyama 1984). The Ogasawara and Mariana Arcs, however, did not produce Fe–Ti-basalts but rather boninite and low-Ti basalt or calc-alkaline rocks (Kuroda *et al.* 1978; Reagan & Maijer 1984). If the 49 ± 13 Ma tholeiitic basalt in the Mineoka ophiolite were part of the Philippine Sea Plate, it might have originated in the 35–60 Ma West Philippine Basin (Hilde & Lee 1984). However, the Cretaceous Amami Plateau isolated the Mineoka ophiolite from the West Philippine Basin even before the opening of the Shikoku and Parece Vela Basins (12–25 and 17–30 Ma, respectively; Okino *et al.* 1994, 1999). In addition, the Mineoka ophiolite cannot have come from the Pacific Plate, because it contains only Jurassic and Cretaceous ocean-floor basalts and seamounts (Takigami *et al.* 1989; Pringle & Duncan 1995; Hirano *et al.* 2002).

Because the ages of the igneous rocks in the Mineoka Belt are inconsistent with all known ages from the Pacific Plate and the Philippine Sea Plate, we infer that the Mineoka ophiolitic assemblage was part of another oceanic plate, designated the 'Mineoka Plate' by Ogawa & Taniguchi (1988) and Sato & Ogawa (2000).

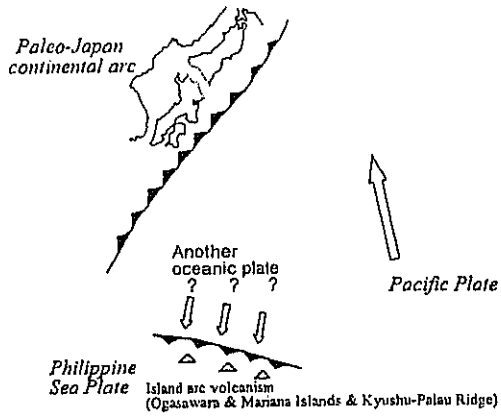

Fig. 7. Plate tectonic reconstruction of the Philippine Sea Plate before 43 Ma (Seno & Maruyama 1984; Koyama *et al.* 1992; Hall *et al.* 1995). Another oceanic plate that subducted from the north under the Philippine Sea Plate is required because the Pacific Plate had NNW absolute motion (Seno & Maruyama 1984).

Eruption environment of the OIB in the Mineoka ophiolite

Hirano & Okuzawa (2002) reported sandstone xenoliths in OIB-type alkali-basalt sheet flows in the Mineoka Belt. The sandstone is composed of terrigenous fragments such as plagioclase, quartz, acidic volcanic fragments and datolite, and is not similar to the basaltic sedimentary rocks and shale conformably deposited on the alkali-basalts (Hirano & Okuzawa 2002). The sandstone xenoliths and the Ar/Ar age of sample BM04HG2 provide important information about the geological setting of this volcanism, indicating that the Mineoka Belt alkali-basalts erupted near the palaeo-Japan arc, which was a continental arc before the Japan Sea opened around 15 Ma (Otofuji & Matsuda 1983). OIB-like alkali-basalts are reported from the Kinan Seamounts in the central Shikoku Basin (Ishii *et al.* 2000; Sato *et al.* 2003). Although the Kinan Seamounts appear to be a linear seamount chain along the palaeo-spreading centre of the Shikoku Basin, they are not of hotspot origin because they show no age progression (Ishii *et al.* 2000). These seamounts were probably formed after cessation of spreading in the Shikoku Basin. The setting of the Kinan Seamounts near the Nankai Trough may be an analogue for the alkali-basalt with sandstone xenoliths. However, the

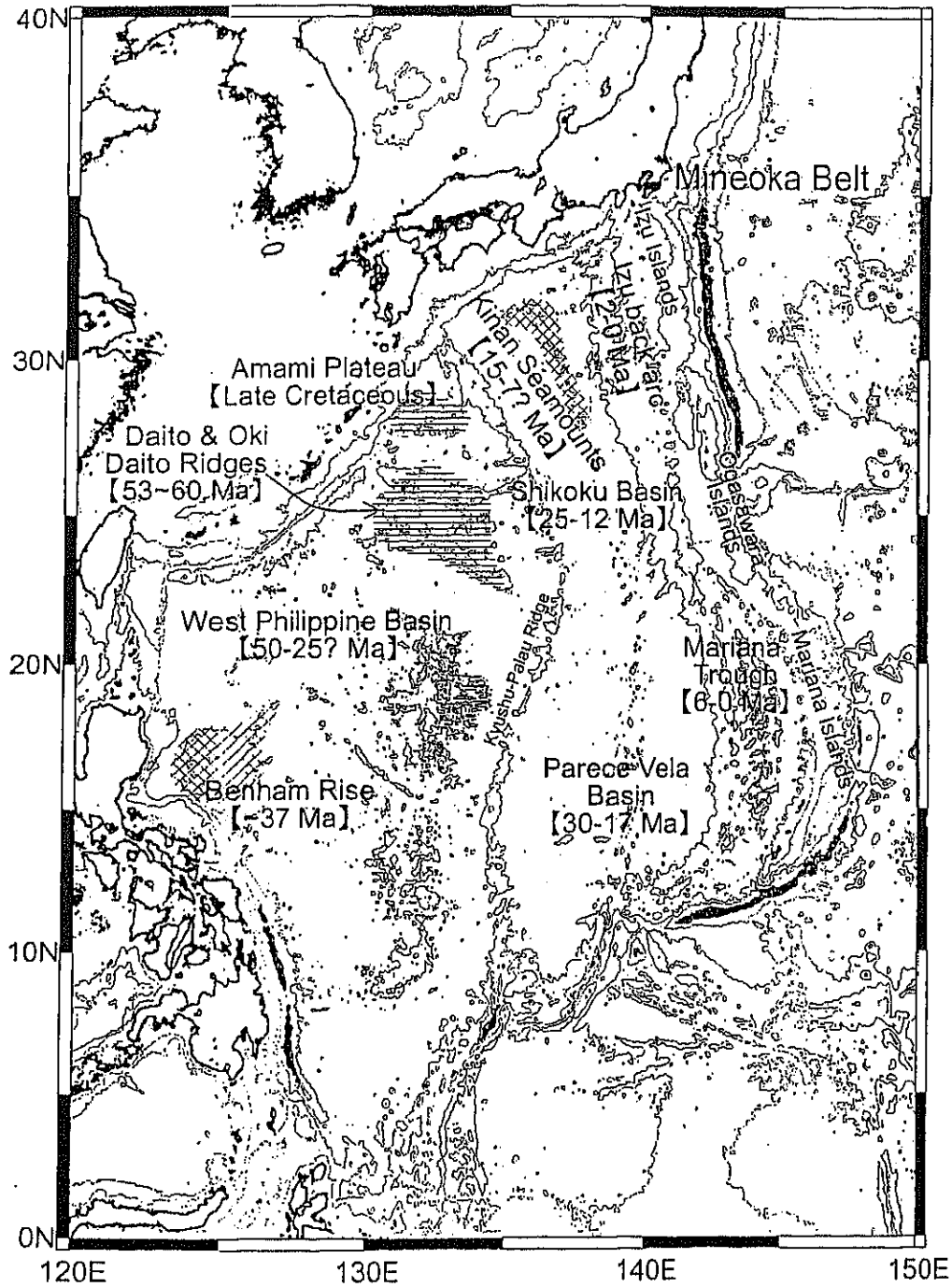

Fig. 8. Formation ages of the ocean basin and arcs shown on a 1000 m contour bathymetric map of the Philippine Sea Plate and its surrounding area. Ages are after Matsuda *et al.* (1975), Ozima et al. (1977, 1980), Marsh *et al.* (1980), Okino et al. (1994, 1999), Hicky-Vargas (1998) and Ishii *et al.* (2000).

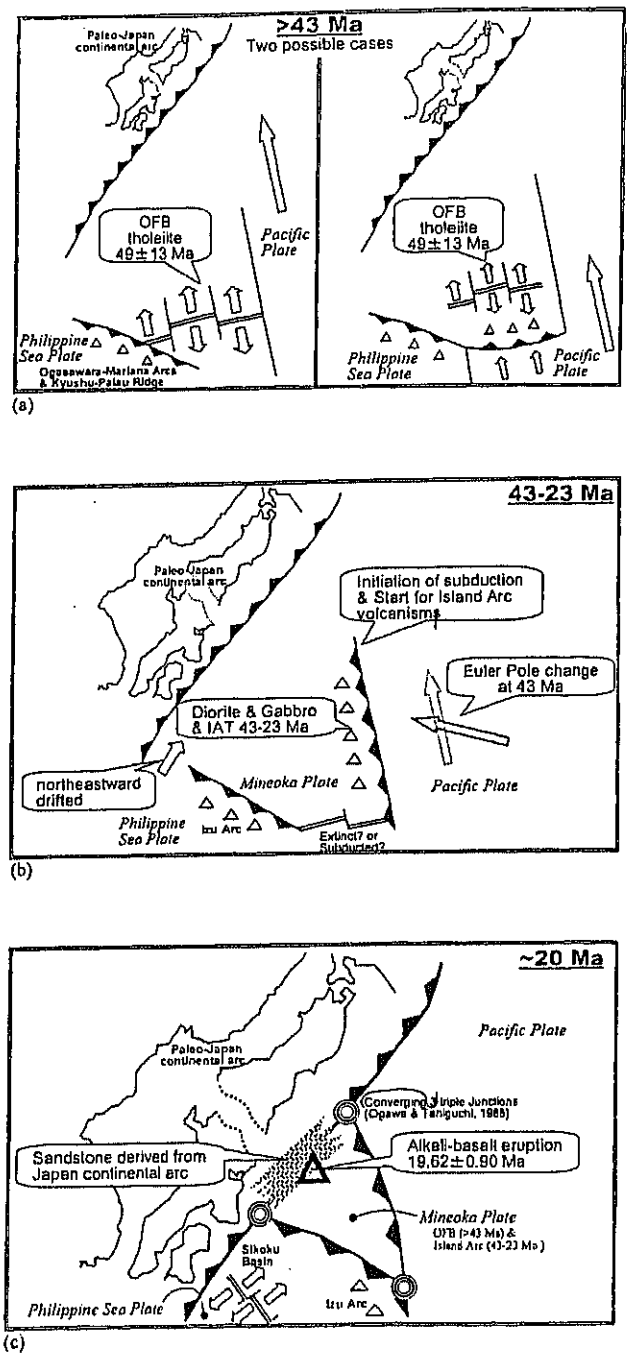

Fig. 9. Tectonic reconstruction models for the origin of the Mineoka ophiolitic rocks. (a) Formation of OFB-type tholeiite before 43 Ma. The Philippine Sea Plate had moved from the SW in Tertiary time (Seno & Maruyama 1984; Koyama *et al.* 1992; Hall *et al.* 1995). Left and right figures show the cases of MORB and BABB type tholeiite in this study, respectively. (b) Island arc stage on the Mineoka Plate after Euler pole change of the Pacific Plate. (c) Alkali-basalt erupted on the terrigenous sedimentary rocks, Mineoka Group (Hirano & Okuzawa 2002), near the palaeo-Japan Arc. The sites of three triple junctions relative to the Japanese coastline are approximate.

alkali-basalts in the Mineoka Belt are around 20 Ma old, distinctly older than the OIB-like basalts of the Kinan Seamounts. The alkali-basalt volcanism presumably occurred after the cessation of back-arc rifting in the Mineoka Arc. In that case, the Mineoka Plate might have been a back-arc basin before the alkali-basalt eruption at 20 Ma.

Conclusions

Sometime in the Eocene, probably about 49 ± 13 Ma, tholeiitic basalts were generated as ocean floor of the Mineoka Plate (Fig. 9a). However, the trace element data do not discriminate between a MORB or back-arc basin basalt (BABB) setting for the Mineoka tholeiitic basalts. The Pacific Plate had NNW absolute motion before 43 Ma (Wessel & Kroenke 1998), and at that time the very young Mineoka Plate and old Pacific Plate may have been juxtaposed either by a transform fault or by a subduction zone. The NNW-moving Pacific Plate may have subducted under the Mineoka Plate before 43 Ma (Fig. 9a).

The Mineoka Plate experienced island-arc volcanism at 25 and 40 Ma as a result of subduction initiated at a fracture zone or a transform fault system, owing to a change in absolute motion of the Pacific Plate from NNW to WNW at 43 Ma (Wessel & Kroenke 1998) (Fig. 9b). The diorites and island-arc basalts represent the products of this intra-oceanic arc magmatism (called the 'Mineoka Arc'), which may have been small, with only intermittent volcanism. Additional age dating is needed for a more detailed discussion of the Mineoka Arc. The two samples identified as island arc basalt in this study are not dated, but may also be from the Mineoka Arc. Rift volcanism associated with back-arc basin opening might have occurred within the Mineoka Plate after establishment of this island arc. Eruption of the within-plate-type alkali-basalts probably took place at around 20 Ma on the Mineoka Group near the palaeo-Japan continental arc (Fig. 9c).

These new interpretations are based on the recognition of *c.* 25 and 40 Ma island arc magmatism associated with previous ophiolitic rocks, and continent-proximal alkali-basalt formed at 20 Ma (Fig. 9). Our data and interpretations support the idea of the existence of a Mineoka Plate as previously proposed by Ogawa & Taniguchi (1988) and Sato & Ogawa (2000). We conclude that the ophiolitic rocks in the Mineoka area were derived from the Mineoka Plate, not from the Philippine Sea Plate or Pacific Plate.

We appreciate the informative and helpful discussions with Y. Dilek and M. F. J. Flower on the geology of the Mineoka Belt. We extend our thanks to M. M. Mohiuddin, N. Takahashi, K. Okuzawa and S. Oyamada for their help in the field. Thanks are due to T. Nakano, the late K. Fukunaga, and S. Furusawa, T. Ohmura and M. Ishii for their help with the Ar/Ar and K–Ar dating. We also thank the staff of the Institute for Material Research, Tohoku University, for irradiating samples for Ar/Ar dating in the JMTR (Japan Material Testing Reactor). J. Kimura, T. Asaki, R. Takashima and K. Aizawa are thanked for the XRF analyses.

References

ARAI, S. ET AL. 1991. The Circum-Izu Massif peridotite, central Japan, as back-arc mantle fragments of the Izu–Bonin arc system. *In:* PETERS, TJ. (ed.) *Ophiolite Genesis and Evolution of the Oceanic Lithosphere*. Kluwer, Dordrecht, 801–816.

ARAI, S. & TAKAHASHI, N. 1988. Relic plagioclase-bearing harzburgite from the Mineoka Belt, Boso Peninsula, central Japan. *Journal of Mineralogy, Petrology and Economic Geology, the Japanese Association of Mineralogists, Petrologists and Economic Geologists*, 83, 210–214 (in Japanese with English abstract).

COX, K.G., BELL, J.D. & PANKHURST, R.J. 1979. *The Interpretation of Igneous Rocks*. Allen and Unwin, London.

FUJIOKA, K., TANAKA, T. & AOIKE, K. 1995. Serpentine seamount in Izu–Bonin and Mariana forearcs—observation by a submersible and its relation to onland serpentinite belt. *Journal of Geography, Tokyo Geographical Society*, 104, 473–494 (in Japanese with English abstract).

FUJIWARA, T., KINOSHITA, H. & MORIJIRI, R. 1999. Magnetic structure of the southern Boso Peninsula, Honshu, Japan, and its implications for the formation of the Mineoka ophiolite belt. *Earth, Planets, Space*, 51, 413–424.

HALL, R., ALI, J.R., ANDERSON, C.D. & BAKER, S.J. 1995. Origin and motion history of the Philippine Sea Plate. *Tectonophysics*, 251, 229–250.

HARA, Y., KUSADA, T. & NIREI, H. 1989. Fission track age of diorite in Mineoka-belt. *Bulletin of Environmental Geology, Research Institute of Environmental Geology, Chiba, Japan*, 20, 65–68 (in Japanese with English abstract).

HICKY-VARGAS, R. 1998. Origin of the Indian Ocean-type isotopic signature in basalts from Philippine Sea plate spreading centers: an assessment of local versus large-scale processes. *Journal of Geophysical Research*, 103, 20963–20979.

HIRANO, N. & OKUZAWA, K. 2002. Occurrence of the sandstone included in the alkali-basalt lava flow from the western Mineoka Belt, Boso Peninsula, Japan, and its tectonic significance. *Journal of the Geological Society of Japan*, 108, 691–700 (in Japanese with English abstract).

HIRANO, N., OGAWA, Y. & SAITO, K. 2002. Long-lived Early Cretaceous seamount volcanism in the Mariana Trench, Western Pacific Ocean. *Marine Geology*, 189, 371–379.

HIROI, Y., HARADA-KONDO, H. & OKU, H. 1992.

Cuprian manganoan phlogopite in highly oxidized Mineoka siliceous schists from Kamogawa, Boso Peninsula, central Japan. *American Mineralogist*, 77, 1099–1106.

HLIDE, T.W.C. & LEE, C.S. 1984. *Origin and evolution of the West Philippine Basin: a new interpretation. Tectonophysics*, 102, 85–104.

IIJIMA, A., WATANABE, Y., OGIHARA, S. & YAMAZAKI, K. 1990. Mineoka umber: a submarine hydrothermal deposit on an Eocene arc volcanic ridge in central Japan. *In:* PARNELL, J.E., LIANJUN, Y. & CHANGMING, C. (eds) *Sediment-hosted Mineral Deposits*. Special Publication of the International Association of Sedimentologists, 11, 73–88.

ISHII, T., SATO, H. & MACHIDA, S. *ET AL.* 2000. Geological and petrological studies of the Kinan and Izu–Ogasawara–back arc–echelon Seamount Chains. *Bulletin of the Geological Survey of Japan*, 51, 615–630 (in Japanese with English abstract).

KANEOKA, I., TAKIGAMI, Y., TONOUCHI, S., FURUTA, T., NAKAMURA, Y. & HIRANO, M. 1980. Pre-Neogene volcanism in the central Japan based on K–Ar and Ar–Ar analyses. *In:* EDITOR, A. (ed.) *Abstracts 1981 IAVCEI Symposium—Arc Volcanism, Tokyo and Hakone*, Volcanological Society of Japan, Town, xx–xxx.

KIMURA, J. & YAMADA, Y. 1996. Evaluation of major and trace element XRF analyses using a flux to sample ratio of two to one glass beads. *Journal of Mineralogy, Petrology and Economic Geology, the Japanese Association of Mineralogists, Petrologists and Economic Geologists*, 91, 62–72.

KOYAMA, M., CISOWSKI, S.M. & PEZARD, P. *ET AL.* 1992. Palaeomagnetic evidence for northward drift and clockwise rotation of the Izu–Bonin forearc since the early Oligocene. *In:* TAYLOR, B. & FUJIOKA, K. (eds) *Proceedings of the Ocean Drilling Program, Scientific Results, 126*. Ocean Drilling Program, College Station, TX, 353–370.

KURODA, N., SHIRAKI, K. & URANO, H. 1978. Boninite as a possible calc-alkaline primary magma. *Bulletin of Volcanology*, 41, 563–575.

MARSH, N.G., SAUNDERS, A.D., TARNEY, J. & DICK, H.J.B. 1980. Geochemistry of basalt from the Shikoku and Daito Basins, Deep Sea Drilling Project Leg 58. *In:* KLEIN, G. DEV. & KOBAYASHI, K. (eds) *Initial Reports of Deep Sea Drilling Project, Leg 58*. US Government Printing Office, Washington, DC, 805–842.

MATSUDA, J., SAITO, K. & ZASU, S. 1975. K–Ar age and Sr isotope ratio of the rocks in the manganese nodules obtained from the Amami Plateau, western Philippine Sea. *In:* EDITOR, A. (ed.) *Symposium on the Geological Problems of the Philippine Sea*. Geological Society of Japan, Town, 99–101 (in Japanese).

MATSUDA, T. 1978. *Collision of the Izu–Bonin arc with central Honshu: Cenozoic tectonics of the fossa magna, Japan. Journal of Physics of the Earth*, 26 (Supplement), S409–S421.

MELSON, W.G. & O'HEARN, T. 1979. Basaltic glass erupted along the Mid-Atlantic Ridge between 0–37°N: relationship between composition and latitude. *In:* EDITOR, A. (ed.) *Deep Sea Drilling Results in the Atlantic Ocean: Ocean Crust*. American Geophysical Union, Maurice Ewing Series, 2, 273–284.

MIYASHIRO, A. 1973. The Troodos ophiolitic complex was probably formed in an island arc. *Earth and Planetary Science Letters*, 19, 218–224.

MIYASHIRO, A. 1978. Nature of alkalic volcanic rock series. *Contributions to Mineralogy and Petrology*, 66, 91–104.

MOHIUDDIN, M.M. & OGAWA, Y. 1996. Middle Eocene to early Oligocene planktonic foraminifers from the micritic limestone beds of the Heguri area, Mineoka belt, Boso Peninsula, Japan. *Journal of Geological Society of Japan*, 102, 611–617.

MOHIUDDIN, M.M. & OGAWA, Y. 1998. Early Miocene pelagic sequences in the Mineoka Belt, Boso Peninsura, Japan. *Journal of Geological Society of Japan*, 104, 1–12.

NAKAJIMA, T., MAKIMOTO, H., HIRAJIMA, J. & TOKUHASHI, S. 1981. *Geology of Kamogawa District. Quadrangle Series, scale 1:50,000*. Geological Survey of Japan, Town (in Japanese with English abstract).

NAKANO, T., JEON, S.R. & SUENO, S. 1997. X-ray fluorescence analysis of rock samples using Philips PW1404(1): *simultaneous determination of major* and trace elements using glass beads of GSJ igneous rock reference samples. *Annual Report, Institute of Geoscience, University of Tsukuba*, 23, 63–68.

OGAWA, Y. 1981. Tertiary tectonics of the Miura and Boso Peninsulas: ophiolite and the Izu forearc sediments trapped to the Honshu arc. *Chikyu (The Earth Monthly), Tokyo*, 3, 411–420 (in Japanese).

OGAWA, Y. 1983. Mineoka ophiolite belt in the Izu forearc area—Neogene accretion of oceanic and island arc assemblages on the northeastern corner of the Philippine Sea Plate. *In:* HASHIMOTO, M. & UYEDA, S. (eds) *Accretion Tectonics in the Circum-Pacific Regions*. Terra, Tokyo, 245–260.

OGAWA, Y. & TANIGUCHI, H. 1987. Ophiolitic mélange in the forearc areas and the development of the Mineoka belt. *Science Reports, Department of Geology, Kyushu University*, 15, 1–23 (in Japanese with English abstract).

OGAWA, Y. & TANIGUCHI, H. 1988. Geology and tectonics of the Miura–Boso Peninsulas and the adjacent area. *Modern Geology*, 12, 147–168.

OGAWA, Y., HORIUCHI, K., TANIGUCHI, H. & NAKA, J. 1985. Collision of the Izu arc with Honshu and the effects of oblique subduction in the Miura–Boso Peninsulas. *Tectonophysics*, 119, 349–379.

OKINO, K., SHIMAKAWA, Y. & NAGAOKA, S. 1994. Evolution of the Shikoku Basin. *Journal of Geomagnetism and Geoelectricity*, 46, 463–479.

OKINO, K., OHARA, Y., KASUGA, S. & KATO, Y. 1999. *The Philippine Sea: new survey results reveal the* structure and the history of the marginal basin. *Geophysical Research Letters*, 26, 2287–2290.

OTOFUJI, Y. & MATSUDA, T. 1983. Paleomagnetic evidence for the clockwise rotation of southeast Japan. *Earth and Planetary Science Letters*, 62, 349–359.

OTSUKI, K. 1990. Westward migration of the Izu–Bonin

Trench, northward motion of the Philippine Sea Plate, and their relationships to the Cenozoic tectonics of Japanese island arcs. *Tectonophysics*, 180, 351–367.

OZIMA, M., KANEOKA, I. & UJIE, H. 1977. ^{40}Ar–^{39}Ar age of rocks, and the development mode of the Philippine Sea. *Nature*, 267, 816–818.

OZIMA, M., TAKIGAMI, Y. & KANEOKA, I. 1980. ^{40}Ar–^{39}Ar geochronological studies on rocks of Deep-Sea Drilling Project sites 443, 445, and 446. *In:* KLEIN, G. DeV. & KOBAYASHI, K. (eds) *Initial Reports of Deep Sea Drilling Project, Leg 58*. US Government Printing Office, Washington, DC, 917–920.

PEARCE, J.A. 1983. Role of the sub-continental lithosphere in magma genesis at active continental margins. *In:* HAWKESWORTH, C.J. & NORRY, M.J. (eds) *Continental Basalts and Mantle Xenoliths*. Shiva, Nantwich, 230–249.

PEARCE, J.A. & CANN, J.R. 1973. Tectonic setting of basic volcanic rocks determined using trace element analyses. *Earth and Planetary Science Letters*, 19, 290–300.

PEARCE, J.A. & NORRY, M.J. 1979. Petrogenetic implications of Ti, Zr, Y and Nb variations in volcanic rocks. *Contributions to Mineralogy and Petrology*, 69, 33–47.

PRINGLE, M.S. & DUNCAN, R.A. 1995. Radiometric ages of basement lavas recovered at Lo-En, Wodejebato, MIT, and Takuyo–Daisan guyots, ODP Leg 144, northwestern Pacific Ocean. *In:* DAGER, E.L., FIRTH, J.V. & SINTON, J.M. (eds) *Proceedings of the Ocean Drilling Program, Scientific Results, 144*. Ocean Drilling Program, College Station, TX, 547–557.

REAGAN, M.K. & MEIJER, A. 1984. Geology and geochemistry of early arc-volcanic rocks from Guam. *Geological Society of America Bulletin*, 95, 701–713.

SAITO, K. 1994. Excess Ar in some metamorphic and plutonic rocks reduction of thermal neutron-induced ^{40}Ar by Cd shielding. *Science Report, Research Institute of Tohoku University*, A40, 185–189.

SAITO, K., OTOMO, I. & TAKAI, T. 1991. K–Ar dating of the Tanzawa tonalitic body and some restrictions on the collision tectonics in the south Fossa Magna, central Japan. *Journal of Geomagnetism and Geoelectricity*, 43, 921–935.

SAITO, S. 1992. Stratigraphy of Cenozoic strata in the southern terminus area of Boso Peninsula, Central Japan. *Contributions of Institute of Geology and Palaeontology, Tohoku University*, 93, 1–37 (in Japanese with English abstract).

SAITO, S., YOSHIDA, T. & AOKI, K. 1992. Geochemistry and tectonic significance of volcanic and volcaniclastic rocks in the Boso Peninsula, Central Japan. *Research Report, Laboratory of Nuclide Science, Tohoku University*, 25, 241–255 (in Japanese).

SATO, H. & OGAWA, Y. 2000. Sulfide minerals as an indicator for petrogenesis and serpentinization of peridotites: an example from the Hayama–Mineoka Belt, central Japan. *In:* EDITOR, A. (ed.) *Title*, Geological Society of America, Special Papers, 349, 419–429.

SATO, H., TANIGUCHI, H., TAKAHASHI, N., MOHIUDDIN, M.M., HIRANO, N. & OGAWA, Y. 1999. Origin of the Mineoka ophiolite. *Journal of Geography, Tokyo Geographical Society*, 108, 203–215 (Japanese with English abstract).

SATO, H., MACHIDA, S., KANAYAMA, S., TANIGUCHI, H. & ISHII, T. 2003. Geochemical and isotopic characteristics of the Kinan Seamount Chain in the Shikoku Basin. *Geochemical Journal*, 36, 519–526.

SENO, T. 1984. Was there a North New Guinea Plate? *Geological Survey of Japan Report*, 263, 29–42.

SENO, T. & MARUYAMA, S. 1984. Paleogeographic reconstruction and origin of the Philippine Sea. *Tectonophysics*, 102, 53–84.

SENO, T., OGAWA, Y., TOKUYAMA, H., NISHIYAMA, E. & TAIRA, A. 1989. Tectonic evolution of the triple junction off central Honshu for the past 1 m.yO *Tectonophysics*, 160, 91–116.

SUZUKI, Y., AKIBA, F. & KAMIYA, M. 1996. Latest Oligocene siliceous microfossils from Hota Group in southern Boso Peninsula, eastern Honshu, Japan. *Journal of Geological Society of Japan*, 102, 1068–1071 (in Japanese).

TAKAHASHI, N. 1994. 'Alkali basalt–clastic rock sequence' in the west end of the Mineoka tectonic belt, Boso Peninsula, Japan. *Journal of the Natural History Museum and Institute, Chiba*, 3, 1–18 (in Japanese).

TAKAHASHI, A., OGAWA, Y., OHTA, Y. & HIRANO, N. 2003. The nature of faulting and deformation in the Mineoka ophiolite, NW Pacific Rim. *In:* DILEK, Y. & ROBINSON, P.T. (eds) *Ophiolites in Earth History*. Geological Society, London, Special Publications, xx, xx–xxx.

TAKIGAMI, Y., KANEOKA, I., ISHI, T. & NAKAMURA, Y. 1989. ^{40}Ar–^{39}Ar ages of igneous rocks recovered from Daiichi-Kashima and Erimo Seamounts during the KAIKO project. *Palaeogeography, Palaeoclimatology, Palaeoecology*, 71, 71–81.

TAZAKI, K. & INOMATA, M. 1980. Picrite basalts and tholeiitic basalts from Mineoka tectonic belt, Central Japan. *Journal of Geological Society of Japan*, 86, 653–671 (in Japanese with English abstract).

TAZAKI, K., INOMATA, M. & TAZAKI, K. 1980. Umbers in pillow lava from the Mineoka tectonic belt, Boso Peninsula. *Journal of Geological Society of Japan*, 86, 413–416.

TONOUCHI, S. 1981. *Paleomagnetic and geotectonic investigation of ophiolite suites and related rocks occurring in the south central Honshu, Japan*. PhD thesis, University of Tokyo.

UCHIDA, T. & ARAI, S. 1978. Petrology of ultramafic rocks from the Boso Peninsula and the Miura Peninsula. *Journal of the Geological Society of Japan*, 84, 561–570.

WATANABE, Y. & IIJIMA, A. 1990. Evolution of the Tertiary Setogawa–Kobotoke–Mineoka forearc basin in central Japan with emphasis on the lower Miocene terrigenous turbidite fills. *Journal of Faculty of Science, University of Tokyo, Section II*, 22, 53–88.

WESSEL, P. & KROENKE, L.W. 1998. The geometric relationship between hot spots and seamounts: implications for Pacific hot spots. *Earth and Planetary Science Letters*, 158, 1–18.

WINCHESTER, J.A. & FLOYD, P.A. 1976. Geochemical magma type discrimination: application to altered and metamorphosed basic igneous rocks. *Earth and Planetary Science Letters*, 28, 459–469.

Appendix

Figure 10 is an index map of the sample localities, which are shown in detail in Figures 11–14.

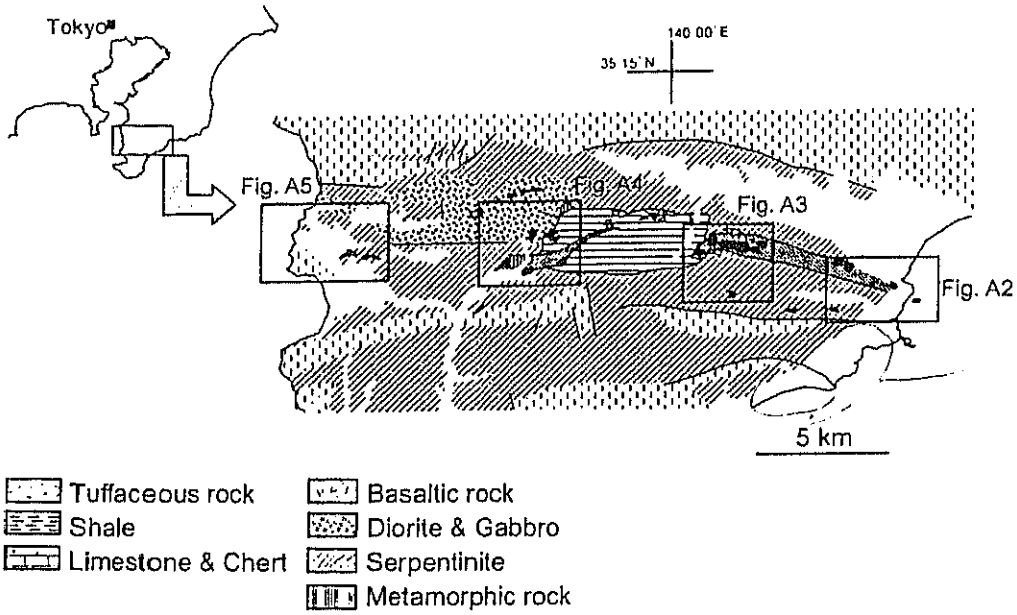

Fig. 10. Index map of the sample localities shown in Figures 11–14, and the legend for lithology for these figures. (This geological map is the same as Figure 2.)

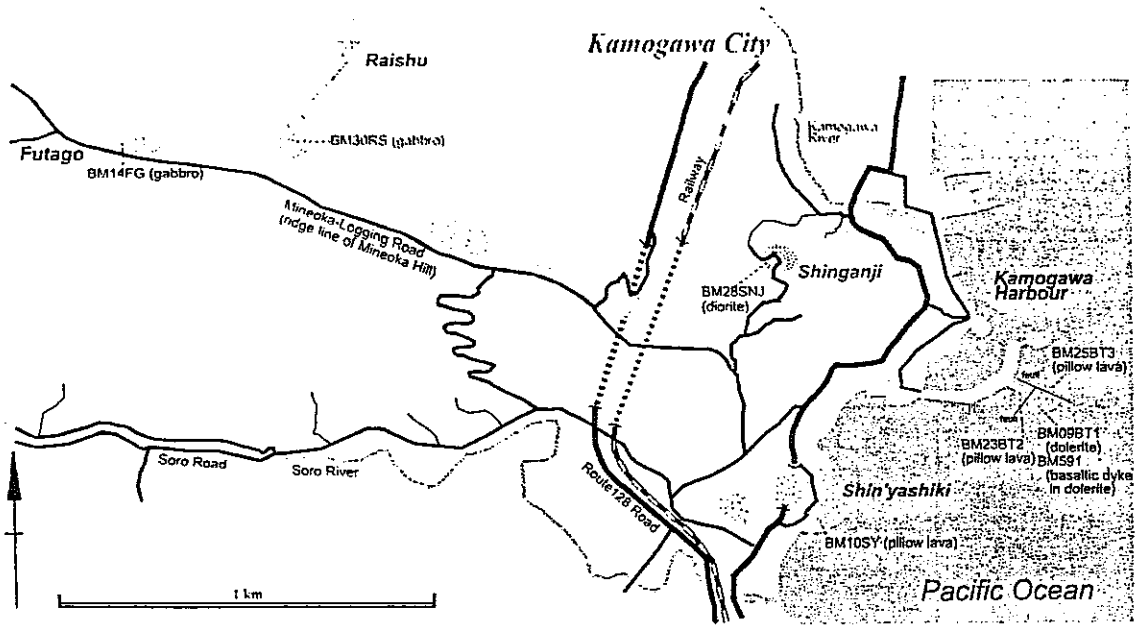

Fig. 11. Sample locality map around the Kamogawa area. BM09BT1, dolerite; BM23BT2, aphyric basalt (pillow lava); BM25BT3, cpx-basalt (pillow lava); BM591, pl-cpx-basalt (basaltic dyke in dolerite); BM10SY, aphyric basalt; BM28SNJ, hb-quartz diorite; BM14FG, hb-gabbro; BM30RS, hb-opx-gabbro.

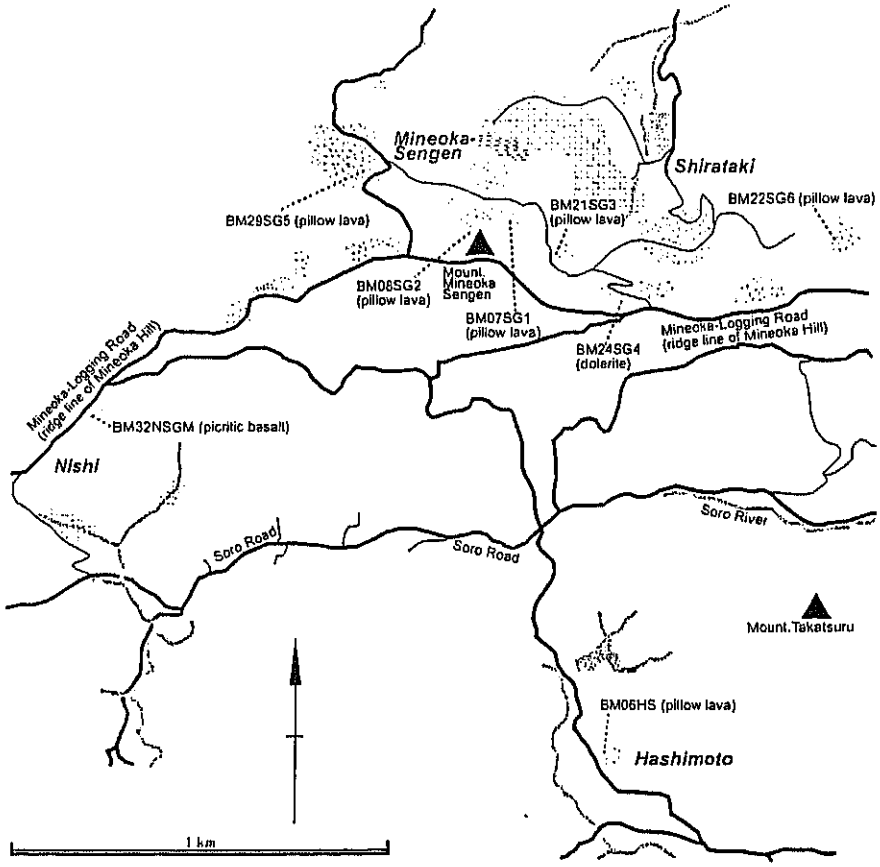

Fig. 12. Sample locality map around the Mineoka Sengen area along the logging road of the eastern Mineoka Hill. BM07SG1, aphyric basalt (pillow lava); BM08SG2, aphyric basalt (pillow lava); BM21SG3, aphyric basalt (pillow lava); BM22SG6, aphyric basalt (pillow lava); BM24SG4, dolerite; BM29SG5, aphyric basalt (pillow lava); BM32NSGM, picrite basalt (pillow lava); BM06HS, aphyric basalt (pillow lava).

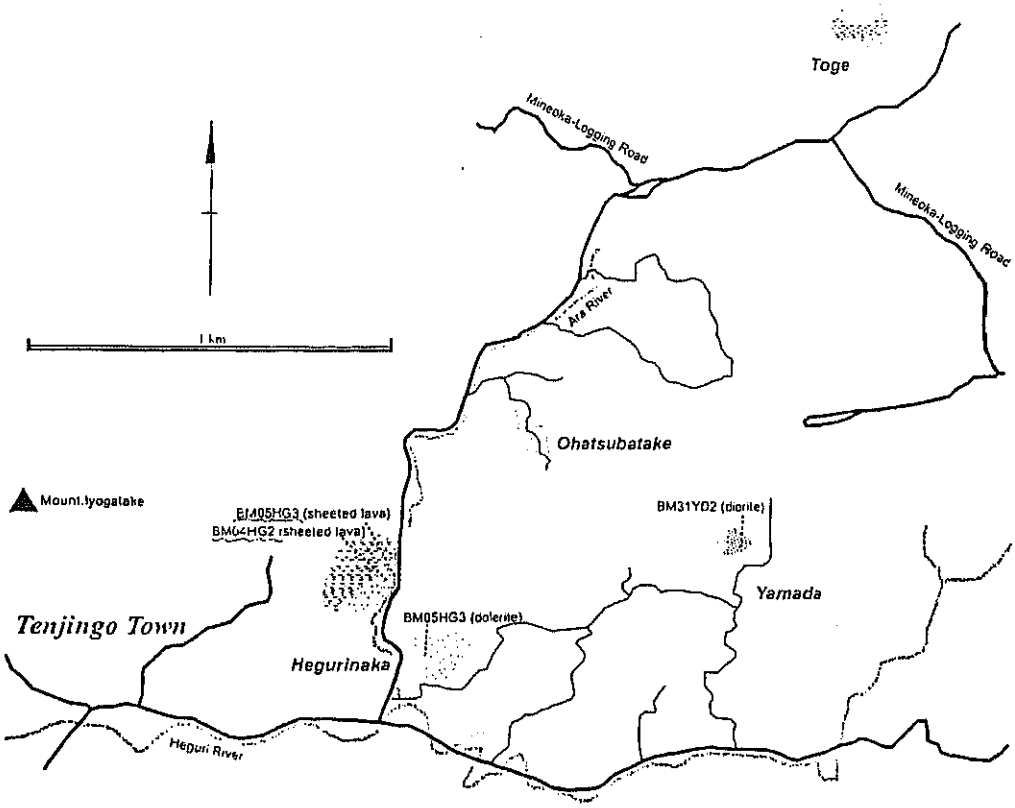

Fig. 19. Sample locality map around the Hegurinaka area in the central Mineoka Hill. BM03HG1, ol-cpx-basalt (sheeted lava flow); BM03HG1, cpx-ol-basalt (sheeted lava flow); BM05SG3, dolerite; BM31YD, hb-quartz diorite.

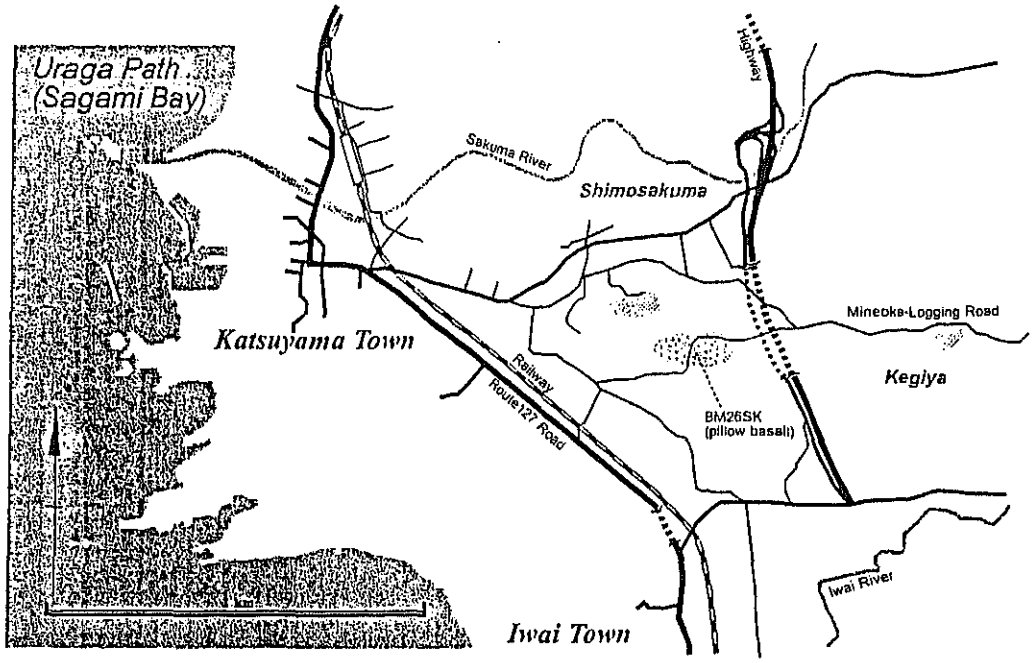

Fig. 14. Sample locality map around the Sakuma area in the western tip of the Mineoka Hill. BM26SK, aphyric basalt (pillow lava).

屋久島南西部に分布するメランジュの構造解析

遠藤良太（筑波大学生命環境科学研究科博士課程（生命共存科学専攻）2年）・
安間了（筑波大学地球科学系）

はじめに

日本列島のように海洋プレートが沈み込む地域では、陸側から運ばれる堆積物に海洋側からもたらされる堆積物が付け加わってできる「付加体」と呼ばれる特徴的な地質体が発達する。付加体では、泥質な基質部分に破断した砂岩、チャート、石灰岩、玄武岩などの岩塊がレンズ状に散在する構造が大規模に見られ「メランジュ」と呼ばれる。メランジュは、「その内部において地層としての連続性が欠如し、細粒の基質とそれに挟まれたあらゆるサイズの外来岩塊を含むブロックによって特徴付けられる、24,000分の１の地質図に表現されうる地質体」と定義されるが（Raymond, 1984）、近年では泥質基質の中に砂岩質レンズを狭在する blocks-in-matrix 構造をもつ小規模な地質体についてもこの用語が用いられるようになっている。一般にメランジュと呼ばれる混在岩の成因については、オリストストローム、テクトニック、泥ダイヤピル起源という3種類の考え方が提出されている（Cowan,1985）。このうちテクトニックメランジュは海洋プレートと付加体の境界で大規模な滑りをおこすデコルマ付近で形成されると一般に考えられている（Moore and Byrne, 1987）。デコルマは地下数百m～数km圧密を受けた高間隙水圧ゆえの低密度の堆積物から構成されており、流体の通り道として機能し（Moore, 1989; Moore and Vrolijk, 1992）、累進的変形過程で圧密と関連した歪硬化のために累進的な層厚化をしていくとされている（Moore and Byrne, 1987 ; Kimura and Mukai, 1991）。しかし、陸上のテクトニックメランジュで高い歪を受けた中心から周囲に向かって漸移的にメランジュ化している岩体は未だ認識されておらずテクトニックメランジュの形成機構については疑問の残るところが多い。

近年ではデコルマ付近では定常滑りが生じている非地震性領域から固着領域である巨大地震発生帯が挟在することからも、沈み込み帯に形成される付加体の構造解析は社会的な意義も高い。このことからメランジュの構造解析を行うことは地震発生メカニズムやプロセスを紐解く上でも重要であると考えられる。本研究目的は屋久島におけるメランジュの詳細な構造解析を行い、メランジュ形成機構を解明することとした。

地質概要

本研究地域の屋久島は九州の南端から台湾にいたるまで、南西1200 kmほどの延長をもつ琉球弧の北端に位置し、南海トラフ-琉球海溝の中軸から西へ約130 km、九州南端佐多岬から60 km南方の海上にある（図1）。島の中央部は中新世の花崗岩が貫入しており、その周囲に四万十層群堆積岩が露出している（図2）。

屋久島の四万十層群は、下位である南東側から麦生累層、船行累層、宮之浦累層、そしてこれらを傾斜不整合に覆う一湊累層の4つの累層に分けられ（図2）、断層によって区分される（橋本, 1956）。これらの一連の地層は、主として北東-北北東の走向をもつタービダイトからなるが（長浜・坂井, 1981）、砂岩の単層の層厚や含有量が異なる。本研究地域は宮之浦累層中の志戸子泥岩層の一部にあたり、屋久島内でメランジュがもっとも広範囲に分布する。岩相対比では、宮崎県に広く分布するの日南層群、種子島の熊毛層群とほぼ対比されるものと考えられ、漸新世後期から中新世前期に堆積したとされている(首藤, 1963; 佐藤・長浜, 1979)。

研究地域の地質はおもに互層1枚の厚さが7 cm～15 cm程度である黒色の泥岩優勢砂岩泥岩互層からなるが、一部砂岩優勢砂岩泥岩互層、シルト岩を含む（図3）。層理面およびメ

ランジュ中の破断した砂岩層の走向は、南北から北東-南西で、80° 前後の北落ち傾斜をもつ。メランジュは泥岩優勢砂岩泥岩互層に観察され、砂岩優勢砂岩泥岩互層およびシルト岩層には観察されない。

メランジュの構造解析

屋久島南西部の黒崎集落から栗生集落までの海岸部および中間川下流域を研究地域とし、とくに中間から栗生に向かっての約1 kmの区間は係留気球を使用した低高度（20～30 m）からの空中写真を撮影し詳細なマッピングを行った。

この写真を元に断層、層理、褶曲、剪断帯などの構造的データを記載した結果、大きく分けて堆積層が破断されつつも保存がよく、層平行な剪断帯が走る部分（zone 1, 赤色部分）と褶曲が発達する部分(zone 2, 青色部分)が交互に分布することが認識された（図4、図5）。またzone1とzone2の境界は断層によって区分される。それらzoneごとに断層、層理面のs-pole(面に垂直な軸)、褶曲軸のプランジ方向をステレオネットにプロットした（図4、図5）。

断層は層に平行に走るものと、層にゆるく斜交するものが非常に多いことが明らかになった(気球写真；図6～7)。層平行断層はzone1の場合剪断帯を伴うことが多く(図8)、剪断帯の幅は0.3～0.8 m程度である。層に斜行する断層は周囲の砂岩層を引きずりを伴うが、剪断帯はない。剪断帯内部の砂岩層は破断されており、泥質基質中にレンズ状に浮いている(Plate1⑤)。層に斜交する断層は層平行断層に切られる場合と切る場合があり、その交差関係は明瞭ではない。層理面に対する断層の角度は、15～25° 程度である。斜交する断層は剪断帯を形成しないが、引きずりによる砂岩が伸びている構造から剪断センスを判定すると、南南西-北北東方向の断層は右横ずれ断層、北北西-南南東走向の断層は左横ずれ断層である。その他の断層として、層理面に高角に入る断層があり走向は様々であるが、層平行断層と層に斜行する断層を切っていることから、より後期の断層であると考えられる。

褶曲は様々な形態のものがあるが、多くの場合根無し褶曲（Plate1①）であり、その他に指交褶曲、鞘状褶曲、キンク褶曲などがある。前述したzone2では根無しの褶曲が帯状に分布する（図9）。

石英脈について

石英脈は本研究地域の中間川以西に非常に多く観察される。分布・産状としては、1. 剪断帯、2. 根無し褶曲に集中して発達する。全体的に石英脈は選択的に砂岩層に多く発達することが多く、泥質岩にはわずかに見られるのみである。

剪断帯の内部の砂岩には、非常に多くの脈がランダムに発達しており、砂岩全体が石英化している（Plate1③・⑤）。石英脈は砂岩中にのみ発達しており、泥岩中には連続していない（Plate1⑤）。脈自体の幅は2 mm以下で、薄片観察では石英は球状の非等粒状組織を呈しており、脈の端の部分では石英粒子が細かくなることがある（Plate11③）。この石英脈は剪断帯内部にのみ発達する、ことから石英脈は剪断帯とほぼ同時期に形成されたと考えられる。

根無し褶曲中の石英脈は砂岩層に対してほぼ垂直に切るように直線的に発達している。多くの露頭で石英脈が交差することが一般的であるが、切った切られたの交差関係は、一部では観察されるものの一貫性はない(Plate1②)。また褶曲軸部にも軸面に沿って発達している様子が観察される(Plate1⑥)。

考察

断層については後期に形成されたと考えられる断層を除くと、層平行断層と層に斜交する断層が多く発達することが認識され、2種類の断層の交差関係は不明瞭である。しかしzone1とzone2の区別無く同様の断層系が発達することは、zoneごとの構造の違いに関係なく同様のメカニズムで形成された可能性が高い。

露頭観察から石英脈が砂岩層に貫入していたが、多くの場合は剪断帯内部、zone 2の根無し褶曲に集中して観察され構造(砂岩部分

にのみ)に規制されている。断層系は層平行断層と層に斜行する断層がzone 1およびzone 2の内部でも一様に発達し、zoneの境界は変形が漸移的ではなく断層にて区分される。また剪断帯内部と根無し褶曲は延性的変形であり、どちらも未固結時の変形であることから、同時期にzone1の剪断帯およびzone2の根無し褶曲が発達した可能性が高い。

まとめ

- メランジュ内部に発達する中構造はzone 1(層理の保存がよく剪断帯が発達)とzone 2(根無し褶曲が発達)が交互に繰り返し分布することが明らかになった。

- 断層系に関して
  - ・構造の発達に関係なく(zone 1, zone 2)、層平行断層と層に斜行する断層が発達する。
  - ・層平行断層と層に斜行する断層との交差関係は不明瞭で、お互い切っている。このためほぼ同時期に形成したと考えられる。
  - ・層平行断層は左横ずれセンス、層に斜行する断層は方向に関係なく、一見正断層(応力等は考慮しないで)センスをもつ。

・断層系、石英脈の産状からzone1の剪断帯とzone2の褶曲が同時期に形成された可能性が高い。

謝辞

本研究を行うにあたり、小川勇二郎教授、鈴木清史博士には野外調査の方法から論文作成に至るまで終始温かいご指導・ご助言をいただきました。

調査期間中、宿泊施設、自動車等を提供してくださった屋久島の叔母池亀和代氏および鹿児島の畠中伸一郎氏、畠中錦也氏に深い感謝の意を表します。また、遠藤は、今は亡き祖母畠中初江氏に追悼の意を表します。上屋久町環境政策課の皆さんには滞在中色々な便宜を図っていただきました。また調査地域の栗生町・中間町の方々には滞在中暖かい御支援をいただきありがとうございました。

参考文献

Cowan, D.S., 1985, Structural styles in Mesozoic and Cenozoic mélanges in the western Cordilela of north

橋本 勇, 1956, 屋久島の時代未詳層群の層序とその地質構造および種子島西部の熊毛層群に関する1, 2の事実. 九州大学教養地学研究報告., 2, 23-34.

Kimura, G., Mukai, A., 1991, Underplated units in an accretionary complex: mélange of the Shimanto Belt of eastern Shikoku, southwest Japan. Tectonics., 10, no1, 31-50.

Moore J.C., 1989, Tectonics and hydrogeology of accretionary prisms; role of the decollement zone., Journal of Structural Geology., 11, no.1-2, 95-106.

Moore, J. C., Tim Byrne, 1987, Thickening of fault zones: A mechanism of mélange formation in accreting sediments. Geology., 15, 1040-1043.

Moore, J.C., Vrolijk, P., 1992, Fluids in accretionary prisms., Reviews of Geophysics., 30, no.2, 113-135.

長浜 春夫・坂井 卓, 1981, 鹿児島県屋久島の四万十層群の堆積構造. 地質調査所月報., 23, 445-477.

Raymond, L. A., 1984, Mélanges: their nature origin, and significance. Geol. Soc. Amer. Spec. Pub., 198, 7-20.

佐藤 岱生, 長浜 春夫, 1979, 屋久島西南部地域の地質. 地質調査所., 22-30.

首藤 次男, 1963, 日南層群の地史学的研究-特に高千穂変動について. 九大理科研究報告., 6, 135-166.

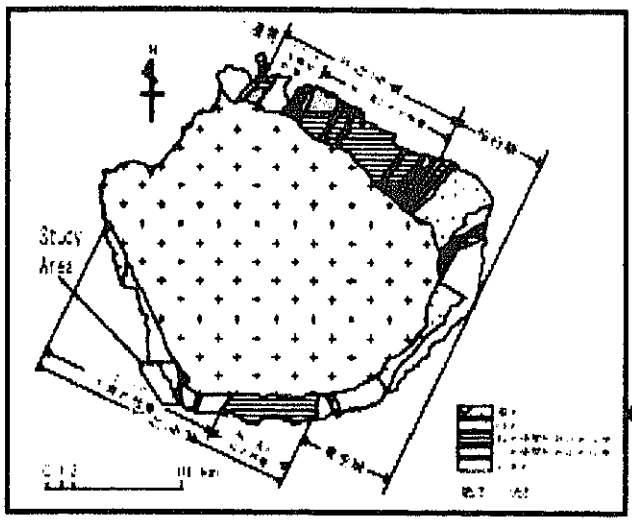

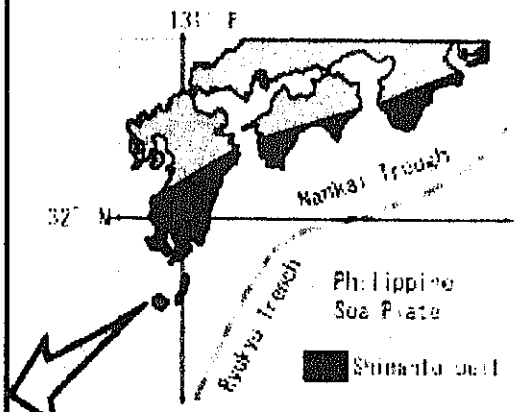

図1 屋久島位置

図2 屋久島の地質図

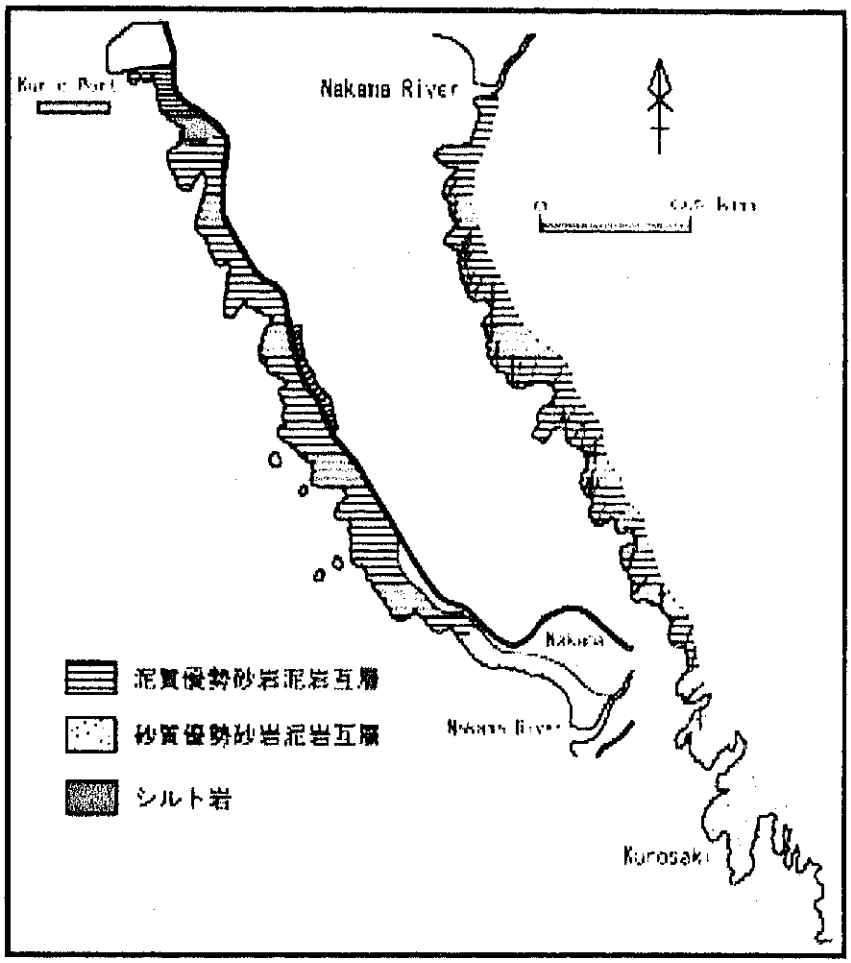

図3 調査地域の地質

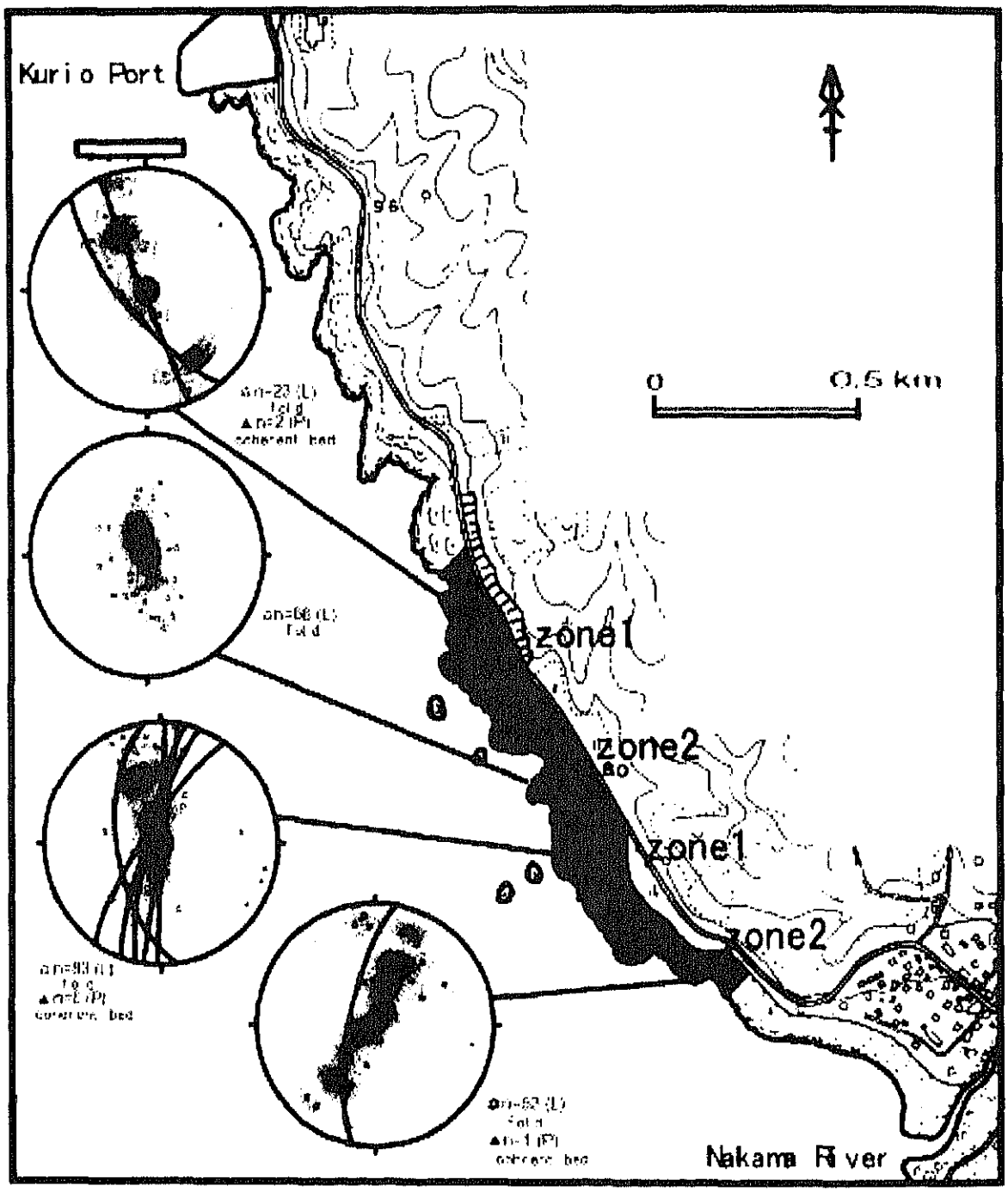

図4 層理面と褶曲軸のプランジのステレオネット

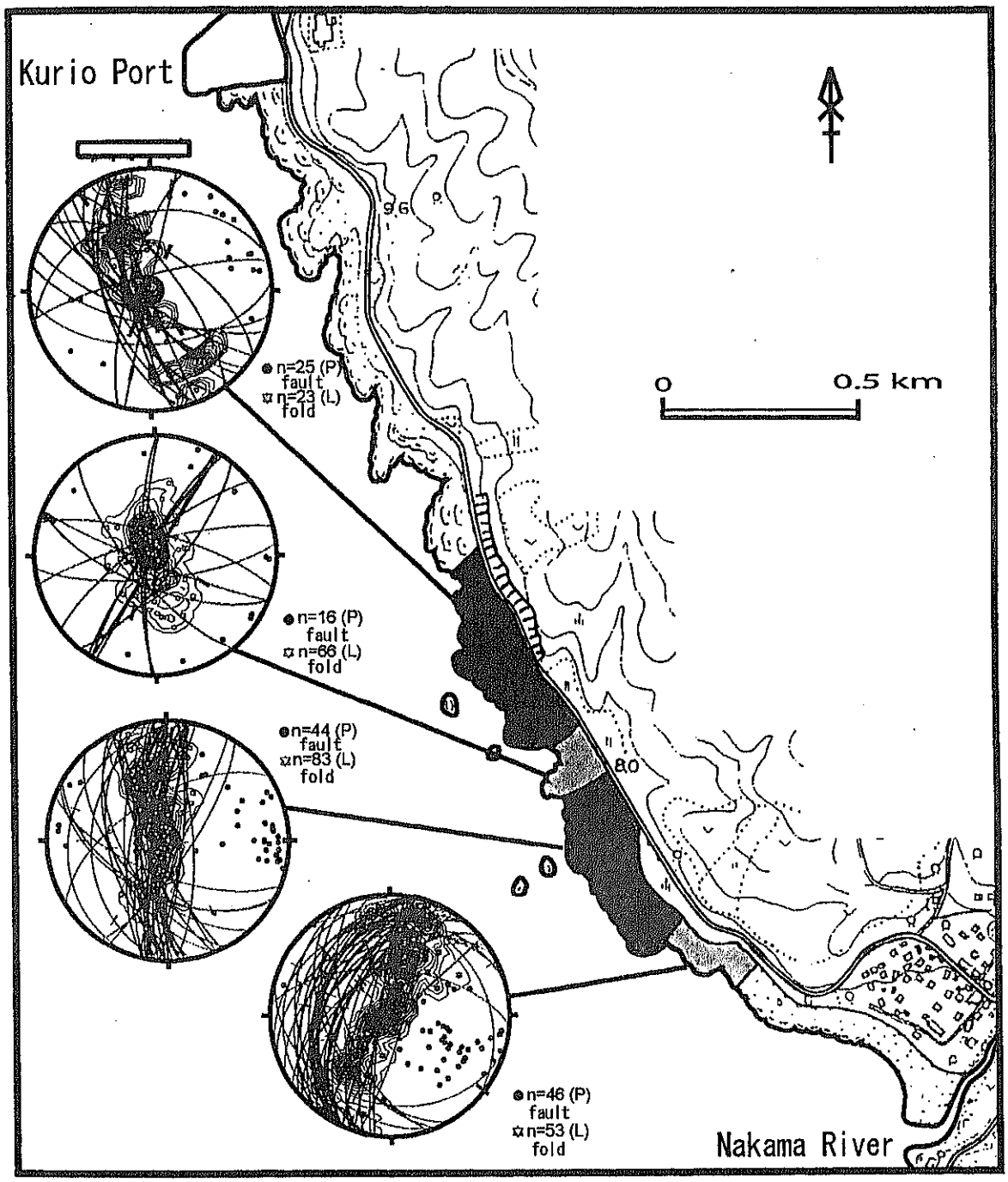

図5 断層と褶曲軸のプランジのステレオネット

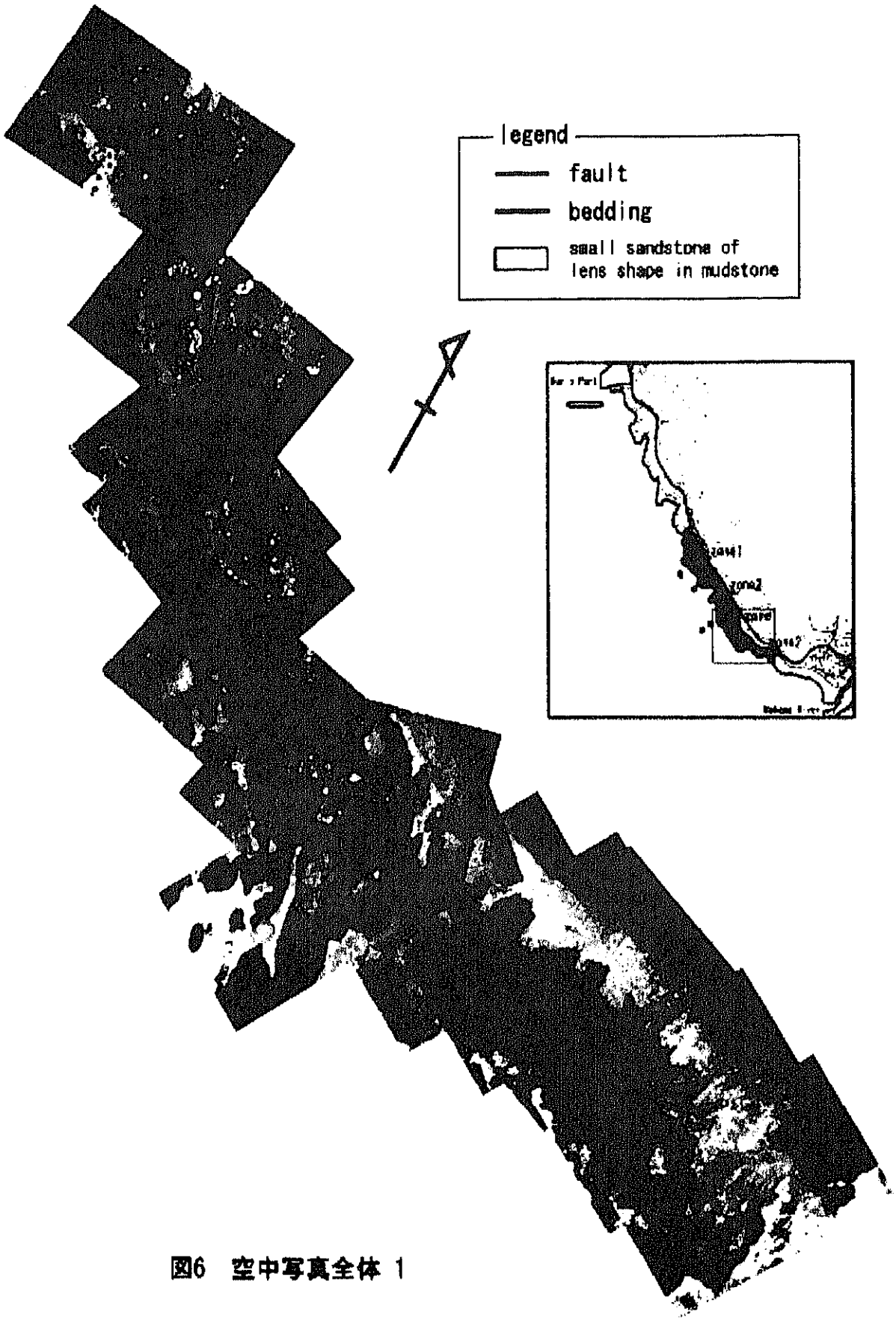
legend
fault
bedding
small sandstone of lens shape in mudstone

図6　空中写真全体 1

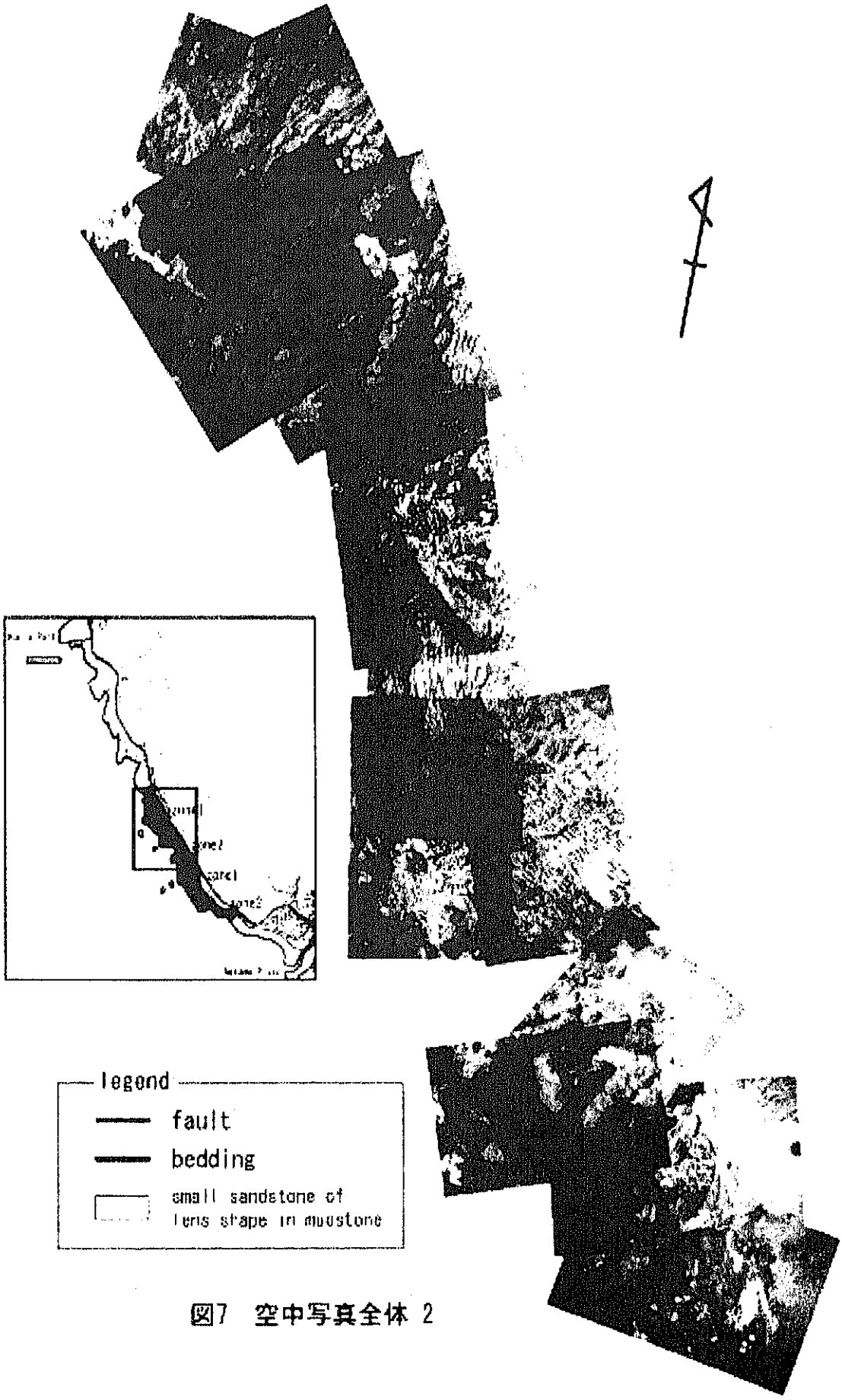
legend
fault
bedding
small sandstone of
lens shape in mudstone

図7　空中写真全体 2

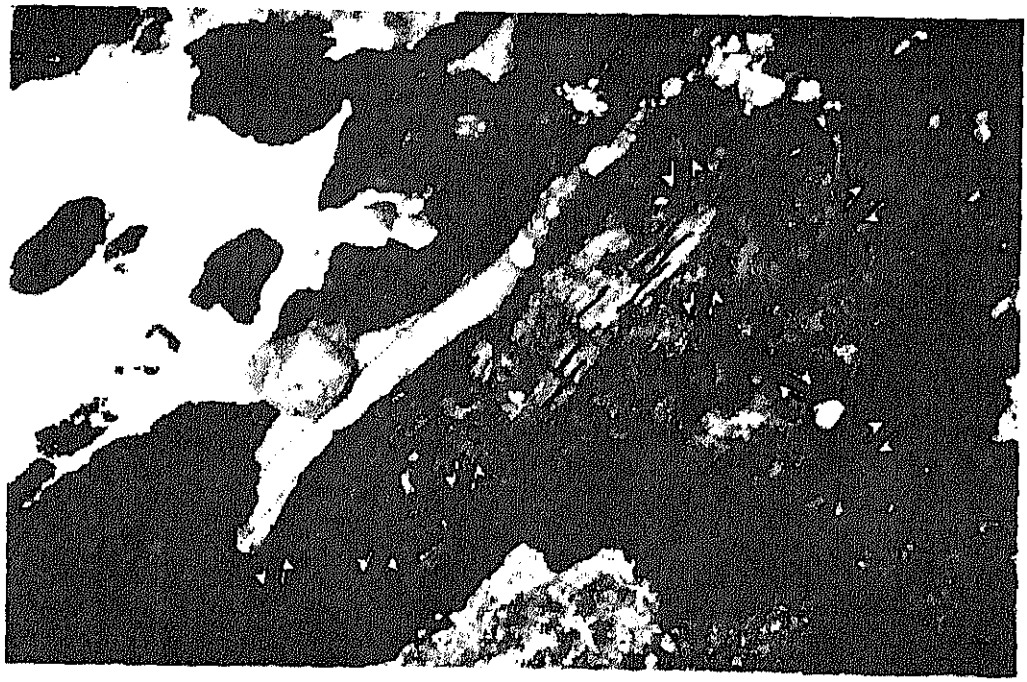

図8　zone1 層平行に剪断帯が発達している．剪断帯は弱部なので選択的に削られていく．
青線は層理面および褶曲，赤線は断層を示す．矢印は剪断センスを示す．

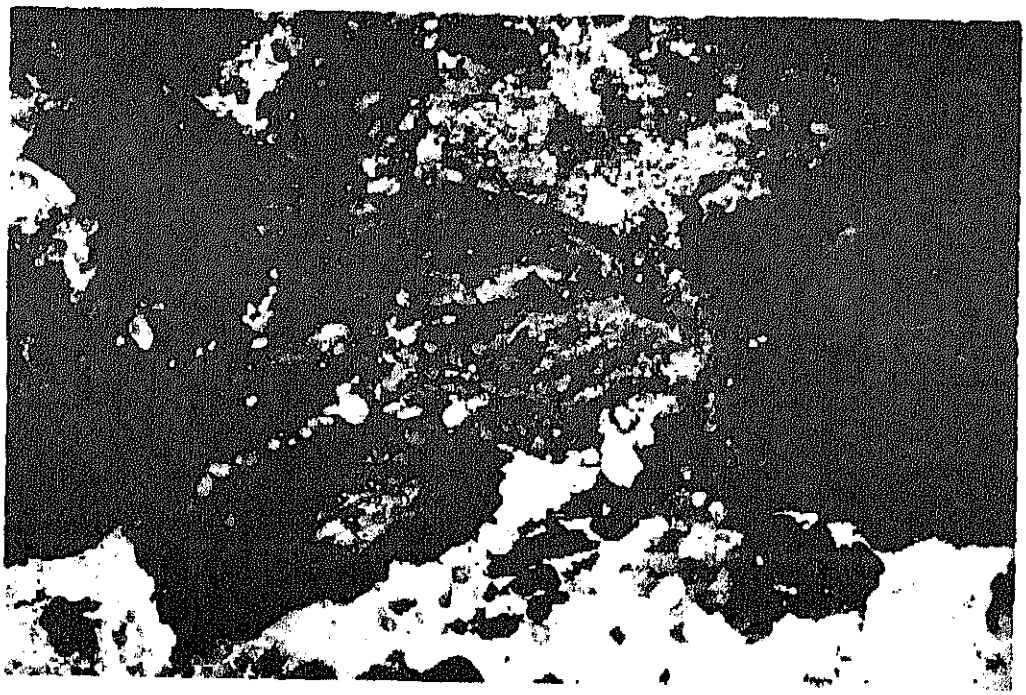

図9　zone2 層理面に平行に断層は入るものの剪断帯は発達しない．
Plate①で示した根無しの褶曲が多く発達する．
青線は層理面および褶曲，赤線は断層を示す．矢印は剪断センスを示す．

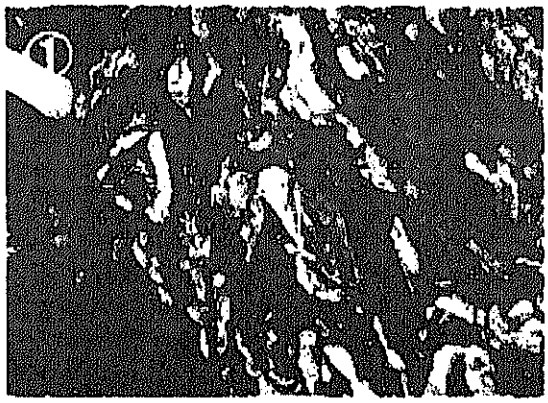

根無し褶曲 (zone2)
白色部分が砂岩層

白色部分が剪断帯．砂岩が石英にしている

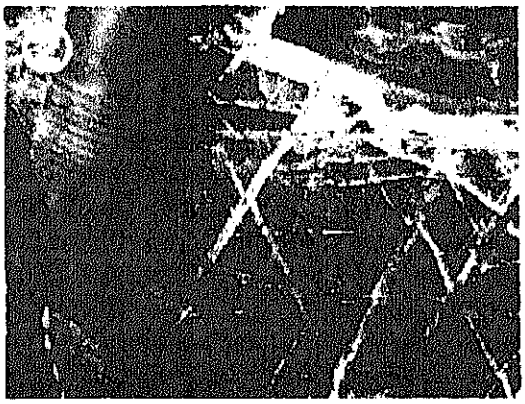

交差する石英脈

4の砂岩部分の拡写

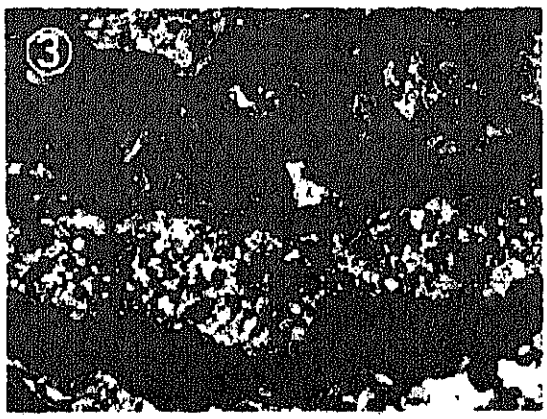

石英脈の薄片写真．石英粒子はほぼ等粒状である
黄色のスケールバーは0 01 mm

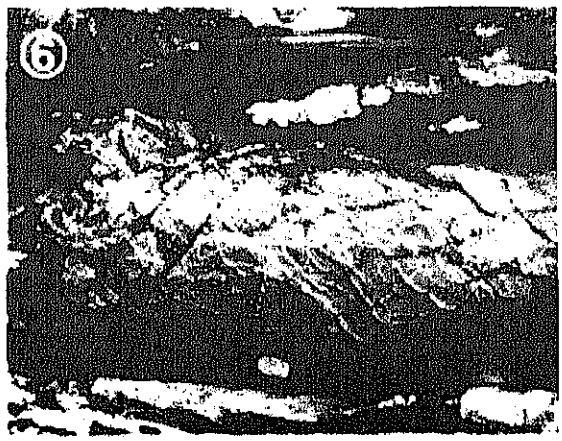

根無し褶曲に発達する石英脈
交差するものと褶曲軸部分に発達するものとがある

Plate 1.

DATA REPORT: SILICA MINERAL CRYSTALLIZATION WITH TEXTURAL CHANGE OF CRETACEOUS SILICEOUS/CALCAREOUS PELAGIC SEDIMENTARY ROCKS RECOVERED FROM THE NW PACIFIC, ODP LEG 185

Chihiro Tanaka,[1] and Yujiro Ogawa[2]

[1] College of Natural Science, University of Tsukuba, Tsukuba 305-8571, Japan (Present address: Ocean Research Institute, University of Tokyo, Nakano, Tokyo 164-8639, Japan)

[2] Institute of Geoscience, University of Tsukuba, Tsukuba 305-8571, Japan (e-mail: yogawa@arsia.geo.tsukuba.ac.jp), correspondent

ABSTRACT

Siliceous/calcareous sedimentary rocks from below pelagic sediments in the Pacific plate section collected at Ocean Drilling Program (ODP) Leg 185, Site 1149, were studied for silica mineral crystallization index, and the downhole increase of the index was confirmed. The increase was shown in relation to the textural and mineralogical change of the rocks, and the data set was presented.

INTRODUCTION

Siliceous pelagic sediments have been known to be crystallographically altered during burial diagenesis (e.g. Hesse, 1990; Behl and Smith, 1992). In order to know the systematic downhole change of silicification, the Pacific plate section obtained from Ocean Drilling Program (ODP) Leg 185, Site 1149, was checked. For collected samples of Early Cretaceous age below the pelagic sediments (which are not so highly silicified), silica mineral crystallization in the siliceous sedimentary rocks was determined by X-ray diffraction (XRD) data, and the related textural change was shown by using scanning electron microscope (SEM) photos. The methodology and results are shown below.

METHODOLOGY

All the works were held in University of Tsukuba, Japan, in 2000. We first made a thin section from each sample, mostly perpendicular to the bedding, which is demarcated by thin lamination. The rest of the samples, because some samples were separated into two or more thin laminae, they are independently numbered and checked as individual specimen (Table 1). The were partly powdered for XRD analysis, and the rest of the fragments were etched by diluted HF for several hours for the surface observation by SEM. XRD analysis was done by CuKα target with 2□□=1 min, voltage = 40 kV, current = 20 mA, from 50° to 3° 2□□. The detailed range from 69° to 67° □□□ was used for identification of silica crystallinity index after Murata and Norman (1976), as 10 × F × a/b, where F = 1.4 (tentatively), a = peak length at (212), and b = a - background height from the quintuplets for opal-CT and quartz rocks. A standard sample of Brazilian quartz was used as the index = 10. The d(101) spacing of cristobalite for eachpart of sample was also obtained. Representative SEM photos are shown in Figures 1 to 5, and the silica crystallinity data and other sample data reported onboard after Shipboard Scientific Party (2001) are shown in Table 1. Diagrams of crystallinity index and porosity (adopted to the equivalent depth of the sample from Initial Report; Shipboard Scientific Party (2001) versus depth are shown in Figure 6.

RESULTS

Samples cored below 180 meters below seafloor (mbsf), Units III and IV are already known to be composed of almost biogenic siliceous, partly calcareous, pelagic sedimentary rocks of Early Cretaceous age (Plank, Ludden, Escutia, et al., 2000; Shipboard Scientific Party, 2001). In general it has been known that the Mesozoic pelagic siliceous sediments are altered or recrystallized from porcelanite to chert descending to the cored depth, in assoiciation with a silica phase change from opal-CT to quartz (e.g. Hesse, 1990; Behl and

Smith, 1992), and as a result this tendency was generally adapted to our samples. Silica crystallinity index and opal-CT d(101) spacing from XRD data (Table 1 and Figure 6) indicate that, although locally the silica phase is higher than that below, the general trend is a downhole increase of the index and spacing. Particularly the trace of the high value are generally constant between 180 and 368.89 mbsf for Hole 1149B, until where the maximum value of index attains only 2.31, averagely only 1.48, but suddenly increases at 387,74 mbsf to 3.91, averagely 3.06. Although there are rather valuable values of index to the depth, and different in places between Holes 1149B, C, and D (Table 1), the general increase of crystalinity index is recognized, at least the enveloping trace of high value for each zone of depth (Figure 6).

Such tendency was confirmed also in the textural change seen by SEM photos in accordance with the silica crystallinity increase. As for the relation between such crystallinity increase to the textural and mineralogical change in Hole 1149B is as follows. Between 180 and 245.40 mbsf, samples have both opal-CT and quartz (chalcedony) in the cavity of sediments (including in the cavity of the radiolarian test), the latter becomes dominant downward (as shown in Figures 1 to 3), but below 387.74 mbsf, almost cavities are filled with quartz (chalcedony) (Figures 4, 5).

Porosity and other logging data can also be correlated with those tendencies of silica crystallization, but sporadic increases in porosity, in opposition to crystallinity increases, are attributed to dehydration and associated cavity increases as opal-CT converts to quartz, as well as within the quartz zone.

The obtained X-ray data are listed in Table 1 together with porosity data obtained during the cruise. This may be attributed to the higher crystallinity mineral (opal-CT and quartz) in the cavity of the sedimentary rocks. Such increase of index and crystal growth may be due to the burial diagnesis.

SUMMARY AND CONCLUSIONS

The silica index is generally increases downhole with some sporadic high and low values. The trace of the large index number (better crystallized line) increase to support the sporadic increase of the crystallinity of silica minerals.

ACKNOWLEDGMENTS

This research used usamples provided by the Ocean Drilling Porogram (ODP). ODP is sponsored by the U.S. National Science Foundation (NSF) and participating countries under management of Joint Oceanographic Institutions (JOI), Inc. Funding for this research was provided by Grant-in-Aid from Japan Science Promotion for Science (A-13304038) to Y. Ogawa.

REFERENCES

Behl, R.J., and Smith, B.M., 1992, Silicification of deep-sea sediments and the oxygen isotope composition of diagenetic siliceous rocks from the Western Pacific, Pigafetta and East Mariana Basins, Leg 129. In: Larsen, R.L., Lancelot, Y., et al., *Proc. ODP, Sci. Res.*,, 129, 81-17.

Hesse, R., 1990, Origin of chert and silica diagenesis. In: Mcllreath, I.A., and Morrow, D.W. (eds.) Diagenesis. Geological Association of Canada, *Geoscience, Canada, Reprint Series*, 4, 227-275.

Murata, K.J., and Norman, M.B., Jr., 1976, An index of crystallinity for quartz. *Amer. J. Sci.*, 276: 1120-1130.

Plank, T., Ludden, J.N., Escutia C., et al., 2000. *Proc. ODP, Init. Repts.*, 185 [CD-ROM]. Available from: Ocean Drilling Program, Texas A&M University, College Station TX 77845-9547, USA.

Shipboard Scientific Party, 2001. Site 1149. *In* Plank, T., Ludden, J.N., Escutia, C., et al., *Proc. ODP, Init. Repts.*, 185, 1-190 [Online]. Available from World Wide Web: http://www-odp.tamu.edu/publications/185_IR/chap_04/chap_04.htm.

Table 1 List of samples with d(101) spacing of crystobalite (obtained in this study), porosity (obtained onboard; Shipboard Scientific Party, 2001), and silica crystallinity index (obtained in this study).

sumple No. Hole-Core-Sect	Interval (cm)	Sub-Bottom Depth(m)	d(101) 2θ	Porosity (%)	C.I.
Brazil Quartz					10
A-21-cc-1	(41-43)	179.51	21.75		
A-21-cc-2		179.51	21.7		
A-21-cc-3		179.51	21.7		
A-21-cc-4		179.51	21.6		2.31
A-21-cc-5		179.51	21.7		2.22
A-23-1-1	(2-5)	190.92	21.9	18.00	
A-23-1-2		190.92	21.9		
B-4-1-1	(22-24)	180.22	21.7	20.70	
B-4-1-2		180.22	21.85		
B-4-1-3		180.22	21.8		
B-4-1-4		180.22	21.85		
B-5-1	(4-8)	189.44		1.80	1.48
B-6-1-1	(30-33)	199.00	21.8	16.20	
B-6-1-2		199.00	21.8		
B-7-1-1	(8-37)	203.78	21.85	20.90	
B-7-1-2		203.78	21.75		
B-7-1-3		203.78	21.75		
B-8-1-1	(10-13)	208.20		1.80	
B-9-1-1	(19-25)	217.59		2.80	1.13
B-9-1-(34)	(34-37)	217.74			1.32
B-10-1-1	(12-14)	226.92		4.10	
B-10-1-2		226.92			
B-11-1-1	(23-26)	236.53	21.85	25.00	
B-12-cc-1	(0-3)	245.40	21.8		1.37
B-13-1-1	(6-10)	254.66	21.75	17.00	1.81
B-14-1-1	(0-4)	263.80	21.8	31.50	
B-16-1-1	(55-57)	282.85	22	43.90	
B-17-1-1	(5-8)	292.05	21.8	25.70	
B-18-1-1	(63-65)	301.75		35.10	
B-18-1-2		301.75			
B-19-1-1	(29-32)	311.59		29.40	
B-20-1-1	(94-100)	321.84			
B-21-cc	(11-13)	330.61		2.30	
B-22-1-1	(32-35)	340.42		32.90	
B-22-1-2		340.42			0.99
B-22-1-3		340.42			
B-23-1-1	(3-7)	349.73		2.50	
B-23-1-2		349.73			
B-23-1-3		349.73			
B-24-1-1	(31-33)	359.51		3.70	1.48
B-24-1-2		359.51			
B-25-1-1	(19-23)	368.89		1.80	
B-25-1-2		368.89			0.69
B-26-1-1	(39-44)	378.49		4.10	
B-27-1-1	(14-16)	387.74		34.70	3.91
B-27-1-2		387.74			2.16
B-28-1-1	(9-11)	397.19		10.10	2.79
B-28-1-2		397.19			4.21
B-28-1-3		397.19			4.28
B-28-2-1	(127-130)	398.78		32.20	1.32
B-28-2-2		398.78			2.77
B-29-1-1	(81-84)	407.41		23.70	
C-1-1-1	(98-104)	237.00			
C-1-1-2		237.00	21.75		
C-1-2-1	(7-10)	237.00			1.32
C-1-2-2		237.00	22.1		1.46
C-2-1-1	(24-31)	237.24	22.1		
C-2-1-2		237.24	21.95		2.78
C-2-1-3		237.24	21.8		
C-3-1-1	(54-56)	284.14	22	44.10	
C-4-1-1	(21-24)	293.41		1.70	5.17
C-4-1-2		293.41			1.50
C-5-1-1	(7-19)	302.87		2.40	2.82
C-6-1-1	(34-42)	312.74		6.30	3.90
C-6-1-2		312.74			6.46
C-7-1-1	(0-5)	322.00			
C-7-1-2		322.00			
C-7-1-3		322.00			
C-8-1-1	(107-110)	390.00			4.67
C-8-1-2		390.00			2.48
C-9-1-1	(27-29)	398.17			
C-9-1-2		398.17			
C-9-1-3		398.17			
D-2-1-1	(23-26)	272.43		5.10	
D-2-1-2		272.43			6.01
D-3-1-1	(5-7)	281.65			6.23
D-3-1-2		281.65			1.70
D-4-1-1	(49-51)	291.34		2.20	
		291.34			
D-5-1-1	(14-16)	300.44		8.00	

7.13

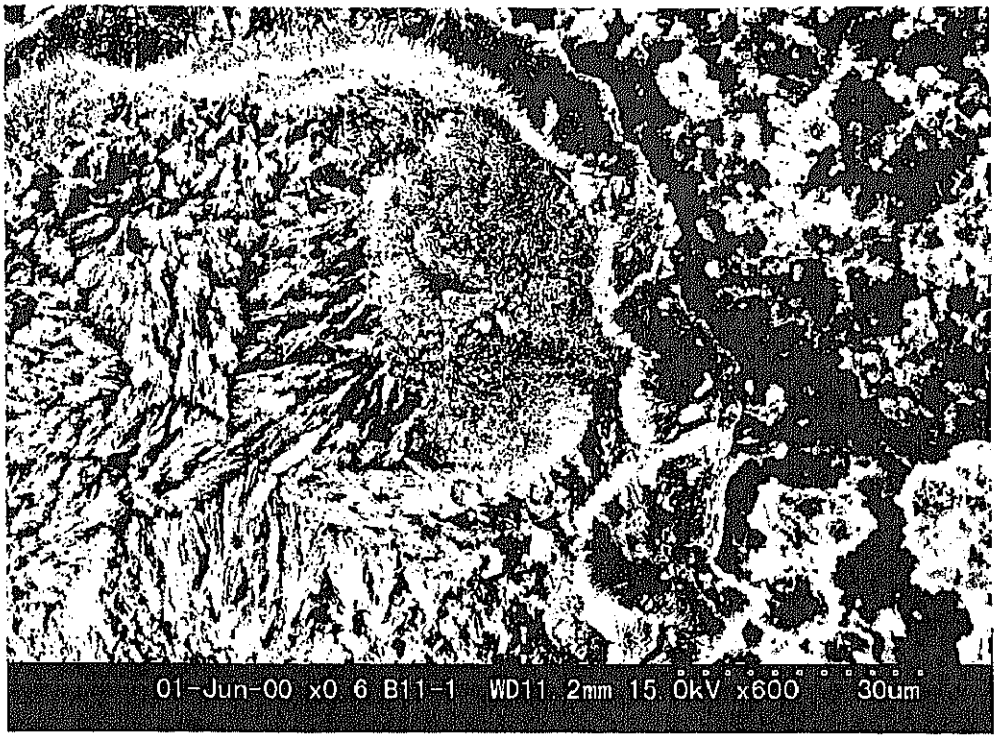

Figure 1 SEM photo of Sample 185-1149B-11R-1, 23-26 cm, (236.53 mbsf), showing opal-CT lepisphere in the center with quartz (chalcedony) on the left in a radiolarian test..

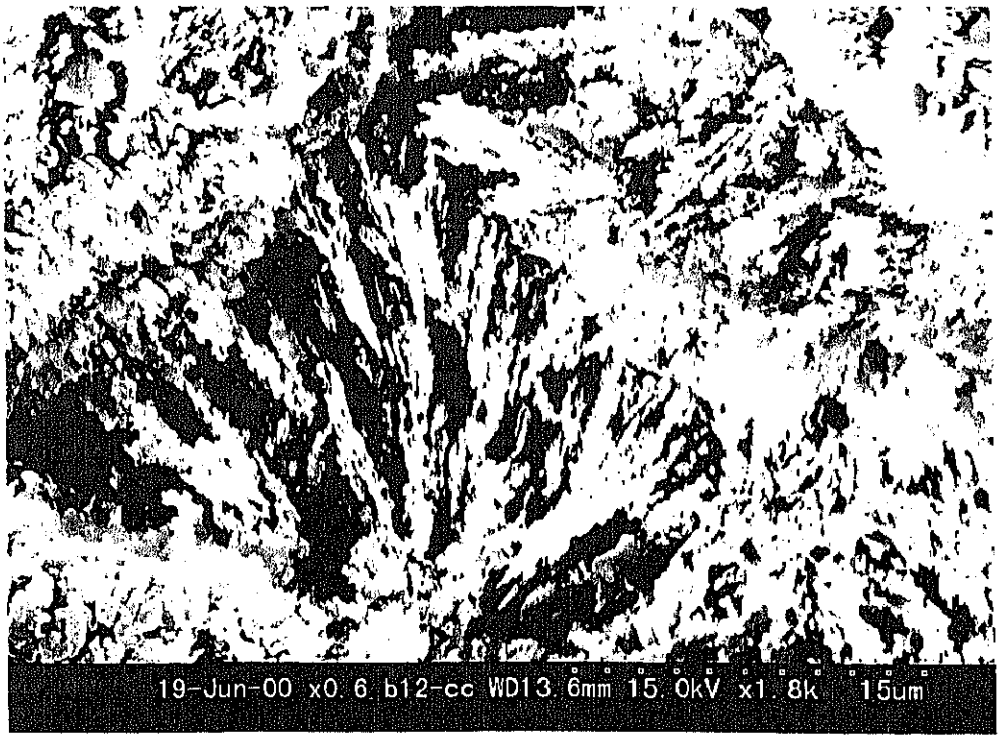

Figure 2 SEM photo of Sample 185-1149B-12R-CC, 0-3 cm (245.40 mbsf), showing quartz (chalcedony) occupying the cavities between radiolarian tests.

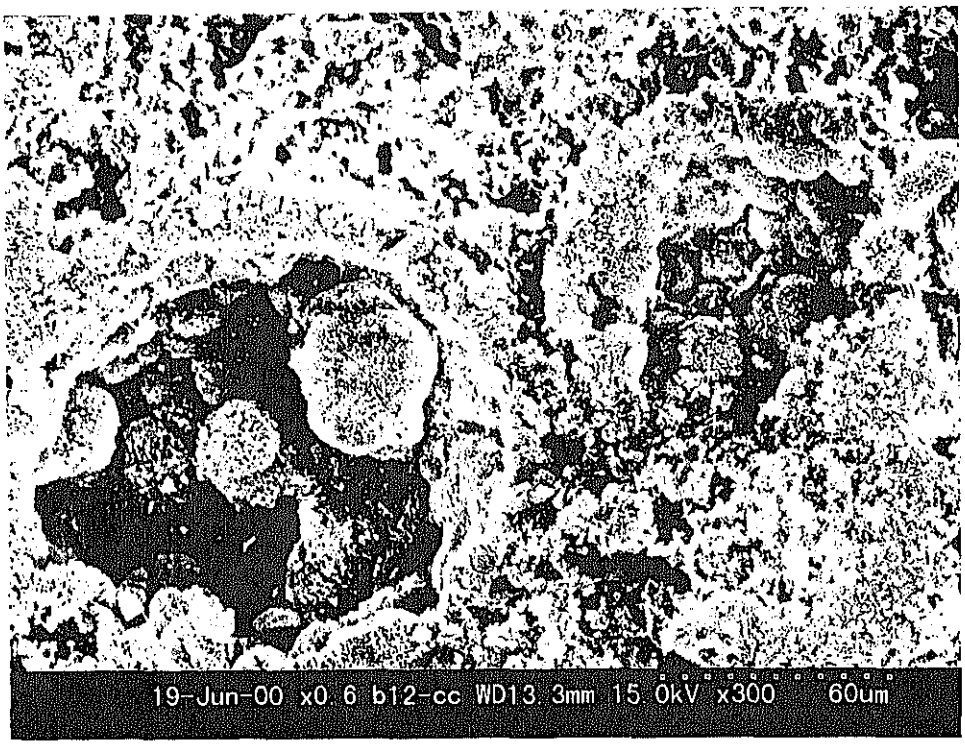

Figure 3 SEM photo of Sample 185-1149B-12R-CC, 0-3 cm (245.40 mbsf), showing opal-CT *lepisphere also occupying the cavity.*

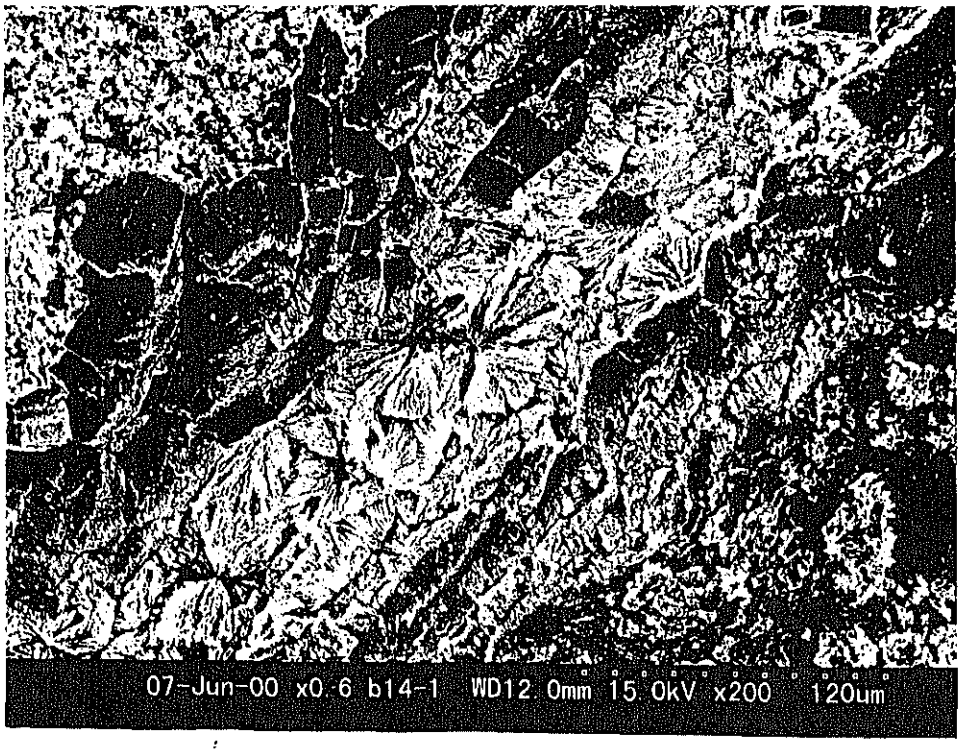

Figure 4 SEM photo of Sample 185-1149B-14R-CC, 0-4 m (263.90 mbsf), showing quartz (chalcedony) occupying a radiolarian test.

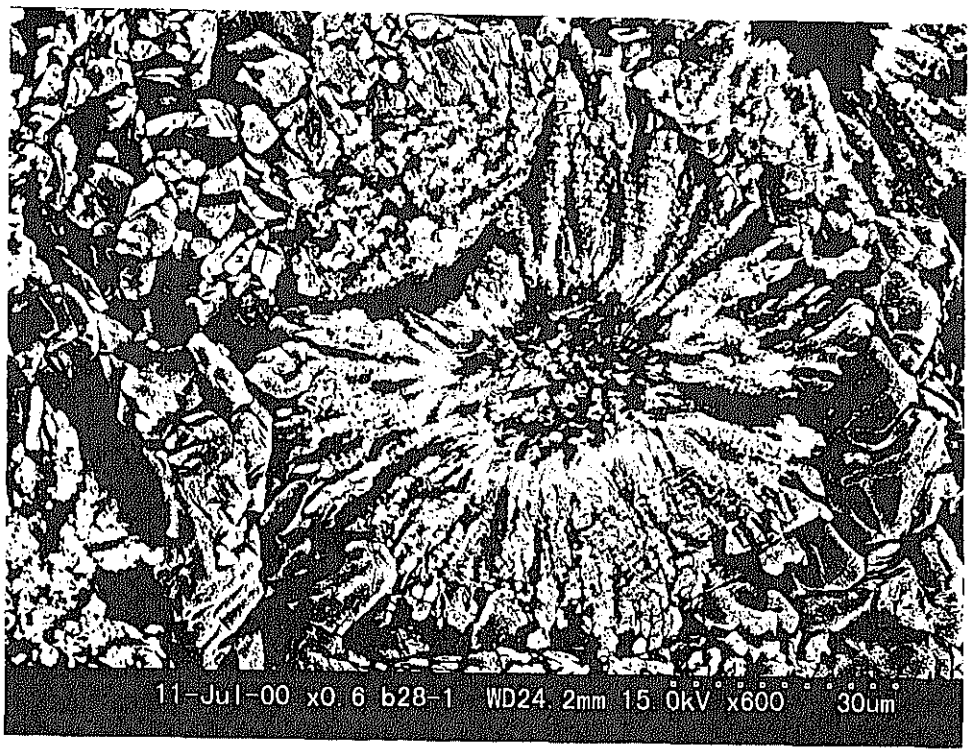

Figure 5 SEM photo of Sample 185-1149B-28R-1, 9-11 cm (397.19 mbsf), showing micro-crystalline quartz and chalcedony in the calcareous laminae.

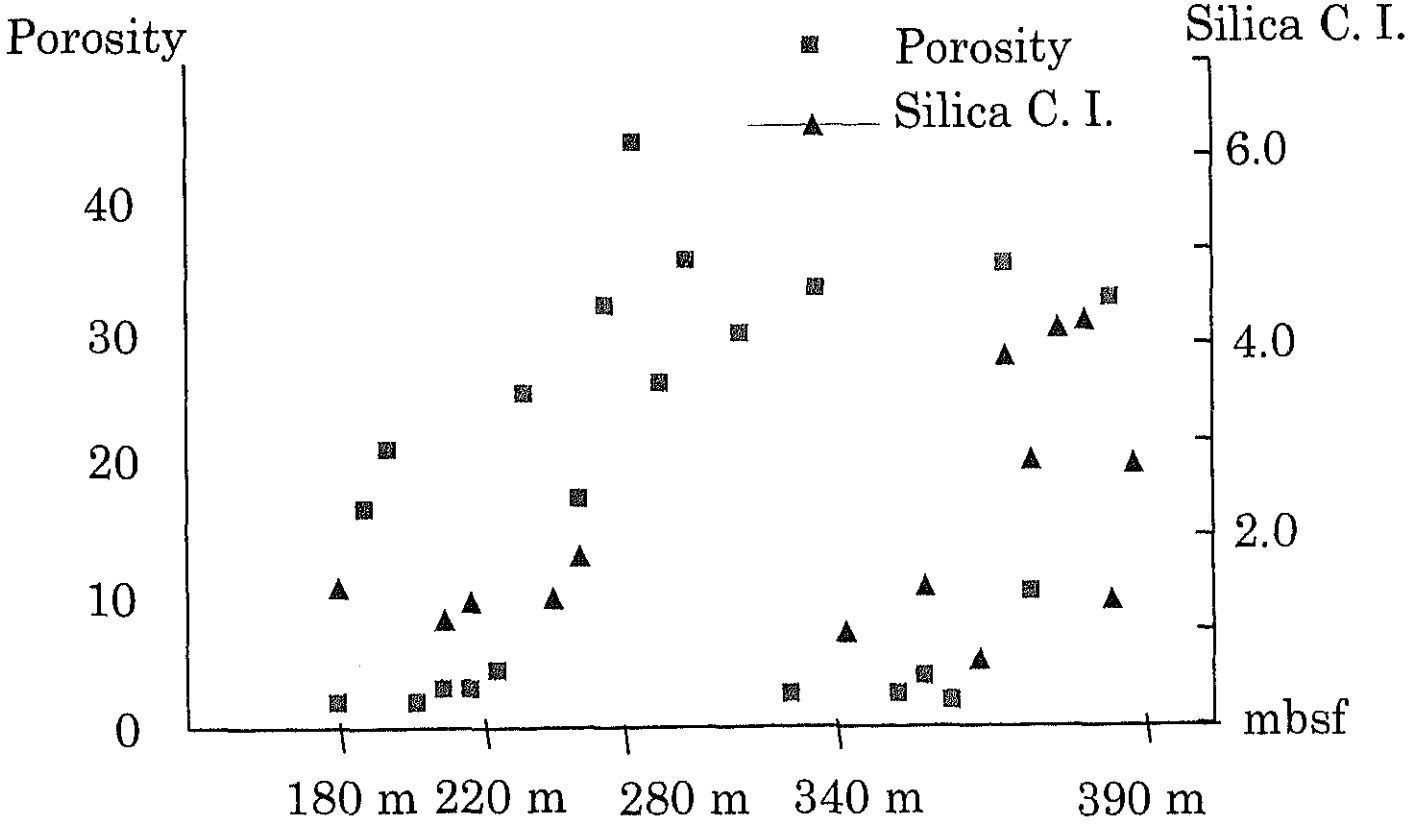

Figures 6 Diagram of porosity (after Shipboard Scientific Party (2001) to the equivalent level), and silica index of data only from Hole 185-1149B (obtained in this study) versus depth mbsf. Refer to Table 1 as well.

Discussion and reply: Control of internal structure and fluid-migration pathways within the Barbados Ridge decollement zone by strike-slip faulting: Evidence from coherence and three-dimensional seismic amplitude imaging

Discussion

Yujiro Ogawa*
Institute of Geoscience, University of Tsukuba, Tsukuba 305-8571, Japan
Peter Vrolijk**
ExxonMobil Upstream Research Company, Houston, TX 77752-2189, U.S.A.;

Keywords: accretionary prism, decollement zone, fluid migration, permeability.

*E-mail: yogawa@arsia.geo.tsukuba.ac.jp.
**E-mail: peter.vrolijk@exxonmobil.com

GSABull, 116 (2004) (in press)

Fluid flow patterns through impermeable rocks where flow is controlled by faults and fractures can be complex. In accretionary prisms the principal driving mechanism for flow is rapid burial and exists in the opposite direction from the convergence vector. DiLeonardo et al. (2002) explore the potential for flow oblique to convergence along the decollement zone in the toe area of the northern Barbados ridge accretionary prism. Using various seismic reflection data volumes to investigate basement-controlled strike-slip faults below the decollement, they infer an ENE-grain defined by faults that have propagated upward from the ocean crust but then largely become detached at the decollement. Although earlier studies identified these faults in the ocean crust (Shipley et al., 1994; Bangs et al., 1996, 1999), the combined use of amplitude (both polarity and intensity) and coherency volumes by DiLeonardo et al. (2002) further elucidated these faults and their inmpact on the subducting sedimentary column and the decollement zone. DiLeonardo et al. (2002) further suggested that this ENE-fault pattern created a component of margin-oblique fluid flow. The focus of our discussion is to further develop the question of how these faults influence flow along the decollement and whether other processes may have a comparable or perhaps greater control on flow.

Our first point is that there exists both in the amplitude map of and the coherence map sculpted from the decollement zone a secondary, N-S fabric overlooked in the DiLeonardo et al. paper (their Fig. 3). Although DiLeonardo et al. interpret a

series of NNE-trending normal faults (Fig. 10), the more regional amplitude map (Fig. 3) suggests a more northerly strike. The sense of offest is ambiguous on the inlines shown in Fig. 5, but the presence of faults appears certain from the juxtaposition of contrasting reflection dip domains (e.g., strong reflection mid-way between the basement and decollement

We suggest that there is another mechanism for deflecting flow from the overall, main fluid potential gradient opposite the plate convergence vector - high permeability in the decollement in the direction of the intermediate principle stress (sigma 2). We suggest that the phacoidal geometry of the scaly fabric in the decollement is a texture that promotes flow parallel to the deformation front, perhaps forming the dominant component of the permeability tensor. In addition, texture and geometry may exist at a broad range of scales. For example, a large-scale phacoidal fabric is suggested by repeated and thinned radiolarian stratigraphic zones in the decollement. If the interpretation of large-scale phacoidal elements is correct, then faint changes in amplitude intensity and low coherence running N-S may reflect margins of large phacoidal elements. We recognize that this interpretation is at (or perhaps beyond) the limit of the seismic reflection data, but testing of this idea could be undertaken with the existing seismic data volumes.

Further observations for the importance of this N-S structural fabric include:

- SEM pictures from the decollement zone of ODP samples, are N-S-oriented (Takizawa and Ogawa, 1999).
- A large-scale thrust duplex is also known to exist along the decollement (Shipley et al., 1997).
- Abrupt changes in amplitude polarity (e.g., Figure 2 of DiLeonardo et al., 2002).

An independent piece of information leads us to consider the relevance of N-S structural features. In a recent, important set of true triaxial compression tests using orthogonal pillar-shape (rather than cylindrical pillar-shape) rock specimens under water-pressure control (Takahashi et al., 2002), preliminary results suggest a 2x permeability increase in the direction of the intermediate versus the maximum principle stress directions (M. Takahashi's personal communication, 2003). Is the Barbados accretionary prism the first natural example of this strike-parallel flow phenomenon? Is it no longer viable to think of fluid flow through accretionary prisms in cross-sections, or is the fluid flux emanating from any point along the deformation front influenced by processes occurring somewhere along strike?

We appreciate the contribution of DiLeonardo et al. (2002) for broadening the

discussion of fluid flow streamlines in the Barbados accretionary prism. Fluid flow vectors are determined by the fluid potential field, which in turn is influenced by the distribution of overpressure processes and the heterogeneous permeability structure of the flow conduits. We draw on analog laboratory experiments to suggest another mechanism for creating strike-parallel fluid flow. Interestingly, along-strike flow does nothing to alleviate fluid pressure generated in a down-dip direction. Is there a further time-transient element to permeability in this environment that allows down-dip permeability to be greatest (e.g., Sibson et al., 1975; Moore, 1989)? Or is the 2:1 ratio of horizontal permeabilities still sufficient to alleviate the overpressure developed during subduction? Temperature and geochemical data place constraints on down-dip fluid transport (Moore et al., 1992; Kastner et al., 1998; Fisher and Hounslow, 1995). Strike-parallel flow is more difficult or impossible to detect by similar means, thus rendering any estimation of flow in this direction more challenging.

We suggest a future topic of study should be to determine the real anisotropy of permeability tensor through field (natural analogue) and laboratory tests. Particularly important is the simultaneous measurement of three-dimensional permeability, if possible. It is also important to evaluate whether the relative magnitudes of the permeability tensor change with time during deformation. Could seismically defined events result in different permeability tensors than during inter-seismic times (or alternatively aseismic high-strain versus low-strain periods). We suggest that the Barbados accretionary prism may be an excellent laboratory for testing such phenomena.

REFERENCES CITED

Bangs, N.L., Shipley, T.H., and Moore, G.H., 1996, elevated fluid pressure, and fault zone dilation inferred from seismic models of the Northern Barbados Ridge decollement: Journal of Geophysical Research, v. 101, p. 627-642.

Bangs, N.L., Shipley, T.H., Moore, J.C., and Moore, G.H., 1999, Fluid accumulation, and channeling along the northern Barbados Ridge decollement: Journal of Geophysical Research, v. 104, p. 20399-20414.

DiLeonardo, C.G., Moore, J.C., Nissen, S., and Bangs, N., 2002. Control of internal structure and fluid-migration pathways within the Barbados Ridge decollement zone by strike-slip faulting: Evidence from coherence and three-dimensional seismic amplitude imaging. Geological Society of America Bulletin, v. 114, p. 51-63.

Middleton, G.V. and Wilcock, P.R., 1994. Mechanics in the earth and environmental sciences. Cambridge University Press, Cambridge, U.K., p. 459.

Moore, J.C., 1989, Tectonics and hydrogeology of accretionary prisms: role of the decollement zone. Journal of Structural Geology, v. 11, p. 95-106.

Moore, J. C., Shipley, T. H., Goldberg, G., Ogawa, Y., and 24 others (1995) Abnormal fluid pressures and fault-zone dilation in the Barbados accretionary prism: Evidence from logging while drilling. Geology, 23, 605-608.

Shipley, T.H., Moore, G., Bangs, N.L., Stoffa, P.L., and Moore, J.C., 1994. Seismically inferred spatial pattern of fluid content of the Northern Barbados Ridge decolement: Imlications for fluid migration and fault strength: Geology, v. 22, p. 411-414.

Shipley, T., Moore, G., Tobin, H., and Moore, J.C., 1997, Synthesis of the Barbados decollement seismic reflection response from drilling-based geophysical observations and physical properties, in Shipley, T., Ogawa, Y., Blum, P. and Barr, J.M., eds., Proceedings of the Ocean Drilling Program, Scientific Results, Leg 156: College Station, Texas, Ocean Drilling Program, v. 156, p. 293-302.

Sibson, R.H., Moore, J.McM., and Rankin, A.H., 1975, Seeismic pumping - a hydrothermal fluid transport mechanism. Journal of the Geological Society, London, v. 131, p. 653-659.

Takahashi, M., Li, X., Lin, W., Narita, T., and Tomishima, Y., 2002, Permeability measurement techniques for intermediate principal stress direction: Journal of Japan Society of Engineering Geology, v. 43, p. 43-48. (in Japanese)

Takizawa, S., and Ogawa, Y., 1999, Dilatant clayey microstructure in the Barbados decollement zone. Journal of Structural Geology, v. 21, 117-122.

Research on the past-age seismogenic faults along plate boundaries in view of fluid inclusion and Raman spectroscopy

(No. 13304038)

Yujiro OGAWA (ed.)

Report of Grant-in-Aid for Scientific Research (A)(1) (2001-2004)
March 2004

CONTENTS